

RDU170377

DEVELOPMENT OF DEVELOPMENT OF A  
SENSITIVE MAGNETOMETER (EDDY  
CURRENT PROBE) PROTOTYPE FOR DEFECT  
EVALUATION IN STEEL COMPONENTS

MOHD MAWARDI BIN SAARI  
NURUL A'IN BINTI NADZRI

RESEARCH VOTE NO:

RDU170377

UMP

FTKEE

UNIVERSITI MALAYSIA PAHANG

2019

## ABSTRACT

Cracks are known as one of the defects that usually happen within a steel structure such as piping, funnel, bridges, buildings and other civil engineering structures, and can occur on the surface or subsurface of the structures. Detection of crack is crucial since cracking can cause dangerous damage to the structure which may lead to structural collapses and unfortunate events. Therefore, cracking needs to be discovered earlier before it reaches the point of fracture. Moreover, the method that is used to inspect the materials or components should not compromise the functionality of the specimen under test. It is also required that the method should provide contactless crack detection technique. Thus, for this reason, the non-destructive testing (NDT) methods are beneficial to fit those requirements as they are widely used in industries in order to control the quality of materials. Since NDT is becoming popular and necessary in certain conditions, there are few methods or techniques that have been founded in order to detect cracks based on different physics principles. Among them, magnetic method is one of the favorable methods in NDT especially in metal industries in order to evaluate the crack without causing any damage to the subject. One of the techniques based on the magnetic method, which is applied regularly to inspect metal structures, is the eddy current testing (ECT) method. This research presents the study and detailed analysis of an ECT probe's development based on AMR sensors for identifications of defects in galvanized steel plates. The probe consists of an excitation coil which is used to induce eddy current in sample plates and two AMR sensors to detect the differential magnetic response induced by eddy currents. Moreover, this probe is connected to a set/reset circuit and a homemade instrumentation amplifier circuit. In order to analyze the magnetic field distribution, which is detected by the AMR sensors, a phase sensitive detection technique by using a lock-in amplifier is applied. When the sensor probe is introduced to a metal plate with defect, the induced eddy current loops in the metal will be interfered, then it will cause changes in the magnetic field distributions. The performance of the ECT probe in the crack detection is evaluated using artificial slits on 2-mm galvanized steel plates. The performance is classified to the depth, width, length and complex shapes of slits, and the probe is used to perform line-scans and 2-D map scans above the slits' positions. By using the developed ECT probe, the magnetic response is measured on the surface and backside of the 2-mm galvanized steel plates. The output signal is detected and analyzed using imaginary components of the magnetic response vectors. The captured data show a signal change at the crack position. From the results, it can be said that the ECT probe can detect the crack as small as 0.05 mm. Furthermore, the shape of the slits can be estimated based on the distribution patterns of the differential magnetic response. It can be expected that the developed system will play an important role in the crack detection in future.

Key researchers:

Mohd Mawardi Saari (Ph.D)

Nurul A'in Nadzri (M.Sc)

Aiman Mohd Halil (Ph.D)

Email: [mmawardi@ump.edu.my](mailto:mmawardi@ump.edu.my)

Tel. No.:09-424-6119

Vote No.: RDU170377

# TABLE OF CONTENT

<b>DECLARATION</b>	
<b>TITLE PAGE</b>	
<b>ABSTRACT</b>	<b>ii</b>
<b>TABLE OF CONTENT</b>	<b>iii</b>
<b>LIST OF FIGURES</b>	<b>vi</b>
<b>LIST OF SYMBOLS</b>	<b>x</b>
<b>LIST OF ABBREVIATIONS</b>	<b>xi</b>
<b>CHAPTER 1 INTRODUCTION</b>	<b>1</b>
1.1 Background of study	1
1.2 Problem Statement	4
1.3 Objective Research	5
1.4 Scope of work	6
1.5 Significant of Study	6
1.6 Thesis Overview	6
<b>CHAPTER 2 LITERATURE REVIEW</b>	<b>8</b>
2.1 Non – Destructive Testing Evaluation	8
2.1.1 Purposes of Non – destructive Testing	8
2.1.2 Non-destructive testing methods	10
2.2 Magnetic method	14
2.2.1 Flux Leakage Measurements	15
2.2.2 Eddy Current Measurements	16
2.2.3 Eddy Current Depth of Penetration	17

2.3	Probes	25
	2.3.1 Operation Mode of Probe	25
2.4	Summary	27
<b>CHAPTER 3 METHODOLOGY</b>		<b>29</b>
3.1	Introduction	29
3.2	Eddy current principle	30
	3.2.1 Principle of operation of eddy current testing	30
3.3	System Development	33
	3.3.1 XY – Stage	35
	3.3.2 Magnetic Sensor	37
	3.3.3 Instrumentation Amplifier (INA)	38
	3.3.4 Set/Reset Circuit	40
	3.3.5 Eddy Current Testing Probe	41
3.4	Detection Technique	44
	3.4.1 Simulation of Magnetic Field Distribution Produced by A Line Current	46
3.5	Measurement Procedure	48
3.6	Preparation of sample	49
	3.6.1 Different depth of slits	50
	3.6.2 Different width of slits	55
	3.6.3 Different length of slits	56
	3.6.4 Complex shape of slits	56
	3.6.5 Backside slits	57
3.7	Summary	57
<b>CHAPTER 4 RESULTS AND DISCUSSION</b>		<b>59</b>



4.1	Introduction	59
4.2	Simulation of Magnetic Field Distribution Produced by A Line Current	59
4.2.1	Different Depth (Z)	61
4.3	Crack Detection Performance	67
4.3.1	Comparison of Different Detection Technique	67
4.3.2	Different Depth Sample	71
4.3.3	Magnetic Distribution of Rotated Probe	78
4.3.4	Different Width Sample	78
4.3.5	Different Length Sample	81
4.3.6	Complex Shape Slit Sample	85
4.3.7	Backside Detection	88
4.4	Summary	90
<b>CHAPTER 5 CONCLUSION</b>		<b>92</b>
5.1	Introduction	92
5.2	Conclusion	92
5.3	Recommendations for Future Work	94
<b>REFERENCES</b>		<b>95</b>
<b>Publications</b>		<b>100</b>
<b>APPENDIX A</b>		<b>101</b>
<b>APPENDIX B</b>		<b>103</b>
<b>APPENDIX C</b>		<b>110</b>

## LIST OF FIGURES

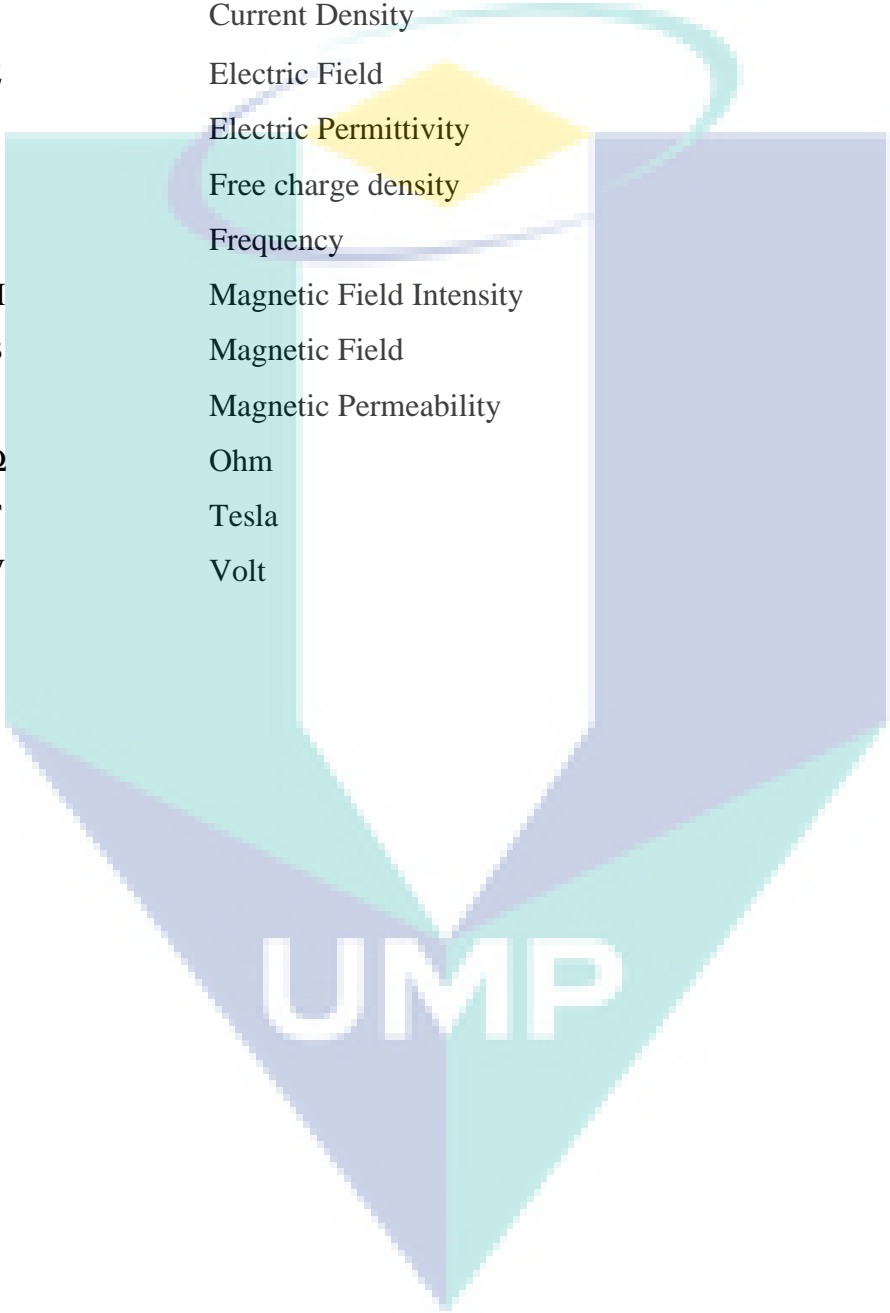
Figure 2.1	Image of visual inspection testing. (Source: <a href="https://hitechndt.com/visual-inspection.html">https://hitechndt.com/visual-inspection.html</a> )	11
Figure 2.2	Image of penetration testing. (Source: <a href="http://www.dfcvalve.com/News/Dye-Penetration-Test.html">http://www.dfcvalve.com/News/Dye-Penetration-Test.html</a> )	12
Figure 2.3	Image of magnetic particle testing. (Source: <a href="https://www.tuv.com/magnetic-particle-inspection.html">https://www.tuv.com/magnetic-particle-inspection.html</a> )	12
Figure 2.4	Image of electromagnetic testing. (Source: <a href="http://www.petroconindia/eddy-current-testing.html">http://www.petroconindia/eddy-current-testing.html</a> )	13
Figure 2.5	Illustration of radiographic testing. (Source: <a href="http://sitasndt.com/radiographic-testing">http://sitasndt.com/radiographic-testing</a> )	13
Figure 2.6	Image of ultrasonic testing. (Source: <a href="http://ultrasonic-testing.html">http://ultrasonic-testing.html</a> )	14
Figure 2.7	Illustration of the working principle of ECT.	17
Figure 2.8	Eddy current depth of penetration.	18
Figure 2.9	Absolute probe mode.	25
Figure 2.10	Differential probe mode.	26
Figure 2.11	Reflection probe mode.	27
Figure 3.1	Research Flow Chart.	30
Figure 3.2	Phase lag at the surface, $\infty$ .	31
Figure 3.3	The schematic diagram of the developed ECT probe circuit.	34
Figure 3.4	Photograph of experimental setup.	35
Figure 3.5	Photograph of XY stage.	36
Figure 3.6	Flow chart of scanning mechanism.	37
Figure 3.7	Honeywell HMC 1001	38
Figure 3.8	Magneto resistive Wheatstone bridge elements of AMR sensor.	39
Figure 3.9	AMR sensor circuit.	39
Figure 3.10	Schematic diagram of the power supply circuit.	39
Figure 3.11	Schematic Diagram of home-made Instrumentation Amplifier Circuit.	40
Figure 3.12	Schematic Diagram of Set/Reset Circuit.	41
Figure 3.13	(a) Photograph of the fabricated ECT probe. (front view).	42
Figure 3.14	Photograph of the fabricated excitation coil.	43
Figure 3.15	Photograph of the fabricated ECT probe. (bottom view).	43
Figure 3.16	Position of AMR sensors.	45
Figure 3.17	Differential vector of the measured magnetic signals.	46

Figure 3.18	Magnetic field distribution that produced by a line current in $x$ - and $y$ - direction a) $B_x$ . b) $B_y$ . c) $B_z$ .	47
Figure 3.19	a) Differential of magnetic distribution respect to position of line current in $x$ - direction. b) Differential of magnetic distribution respect to position of line current in $y$ – direction. c) Arrow map of the reconstructed current dipole.	48
Figure 3.20	Schematic diagram of experimental setup.	48
Figure 3.21	Photograph of the laser marking machine.	50
Figure 3.22	Artificial slits (defects) of depth from 210 $\mu\text{m}$ to 500 $\mu\text{m}$ on a galvanized.	51
Figure 3.23	Photograph of the 3D Measuring Laser Microscope OLS5000.	52
Figure 3.24	Image of slit when zoomed in with 3D Measuring Laser Microscope OLS5000.	52
Figure 3.25	2D image of the slit.	53
Figure 3.26	The depth of the slit that has been engraved with 3 times loop.	53
Figure 3.27	The depth of the slit that has been engraved with 6 times loop.	53
Figure 3.28	The depth of the slit that has been engraved with 9 times loop.	54
Figure 3.29	The depth of the slit that has been engraved with 12 times loop.	54
Figure 3.30	The depth of the slit that has been engraved with 15 times loop.	54
Figure 3.31	Average depth of different slits.	55
Figure 3.32	Artificial slits (defects) of width from 1 mm to 0.05 mm on a galvanized carbon steel plate.	55
Figure 3.33	Artificial slits (defects) of length from 50 mm to 10 mm on a galvanized carbon steel plate.	56
Figure 3.34	Artificial slits (defects) with shapes of letter ‘U’ , ‘M’ and ‘P’.	56
Figure 3.35	Artificial slits (defects) with depth from 1 mm to 1.8 mm on a galvanized carbon steel plate.	57
Figure 4.1	Comparison of simulation of magnetic field distribution produced by a line current.	60
Figure 4.2	Magnetic field distributions produced by a line current in $x$ - and $y$ -directions with a lift off of 1 mm a) $B_x$ . b) $B_y$ . c) $B_z$ .	61
Figure 4.3	Magnetic field distributions produced by a line current in $x$ - and $y$ -directions with a lift off of 1 mm. a) Differential of magnetic distribution respect to position of line current in $x$ - direction. b) Differential of magnetic distribution respect to position of line current in $y$ – direction. c) Arrow map of the reconstructed current dipole.	62
Figure 4.4	Magnetic field distributions produced by a line current in $x$ - and $y$ -directions with a lift off of 2 mm. a) $B_x$ . b) $B_y$ . c) $B_z$ .	63
Figure 4.5	Magnetic field distributions produced by a line current in $x$ - and $y$ -directions with a lift off of 2 mm. a) Differential of magnetic	

	distribution respect to position of line current in $x$ - direction. b) Differential of magnetic distribution respect to position of line current in $y$ – direction. c) Arrow map of the reconstructed current dipole.	63
Figure 4.6	Magnetic field distributions produced by a line current in $x$ - and $y$ -directions with lift a off of 3 mm. a) $B_x$ . b) $B_y$ . c) $B_z$ .	64
Figure 4.7	Magnetic field distributions produced by a line current in $x$ - and $y$ -directions with a lift off of 3 mm. a) Differential of magnetic distribution respect to position of line current in $x$ - direction. b) Differential of magnetic distribution respect to position of line current in $y$ – direction. c) Arrow map of the the reconstructed current dipole.	64
Figure 4.8	Magnetic field distributions produced by a line current in $x$ - and $y$ -directions with a lift off of 4 mm. a) $B_x$ . b) $B_y$ . c) $B_z$ .	65
Figure 4.9	Magnetic field distributions produced by a line current in $x$ - and $y$ -directions with a lift off of 4 mm. a) Differential of magnetic distribution respect to position of line current in $x$ - direction. b) Differential of magnetic distribution respect to position of line current in $y$ – direction. c) Arrow map of the reconstructed current dipole.	65
Figure 4.10	Magnetic field distributions produced by a line current in $x$ - and $y$ -directions with a lift off of 5 mm. a) $B_x$ . b) $B_y$ . c) $B_z$ .	66
Figure 4.11	Magnetic field distributions produced by a line current in $x$ - and $y$ -directions with a lift off of 5 mm. a) Differential of magnetic distribution respect to position of line current in $x$ - direction. b) Differential of magnetic distribution respect to position of line current in $y$ – direction. c) Arrow map of the reconstructed current dipole.	66
Figure 4.12	Line-scanned magnetic field intensity with differential technique. (a) The real and (b) imaginary of the absolute measurement $B_z$ of the magnetic response with a constant phase of the reference signal. (c) The real and (d) imaginary of the differential measurement $dB_z/d_x$ of the magnetic response with a fix location-based phase referencing technique. (e) The real and (f) imaginary of the differential measurement $dB_z/d_x$ of the magnetic response with a sensor-based phase referencing technique.	68
Figure 4.13	2-D magnetic map of the slit with 513- $\mu\text{m}$ depth (a) Absolute measurement $B_z$ of the magnetic response with a constant phase of the reference signal. (b) Differential measurement $dB_z/d_x$ of the magnetic response with a fix location-based phase referencing technique. (c) Differential measurement $dB_z/d_x$ of the magnetic response with a sensor-based phase referencing technique.	70
Figure 4.14	The imaginary components of the line-scanned magnetic field intensities with respect to different frequencies and slit depths. (a) 210 $\mu\text{m}$ . (b) 337 $\mu\text{m}$ . (c) 360 $\mu\text{m}$ . (d) 402 $\mu\text{m}$ . (e) 513 $\mu\text{m}$ .	71

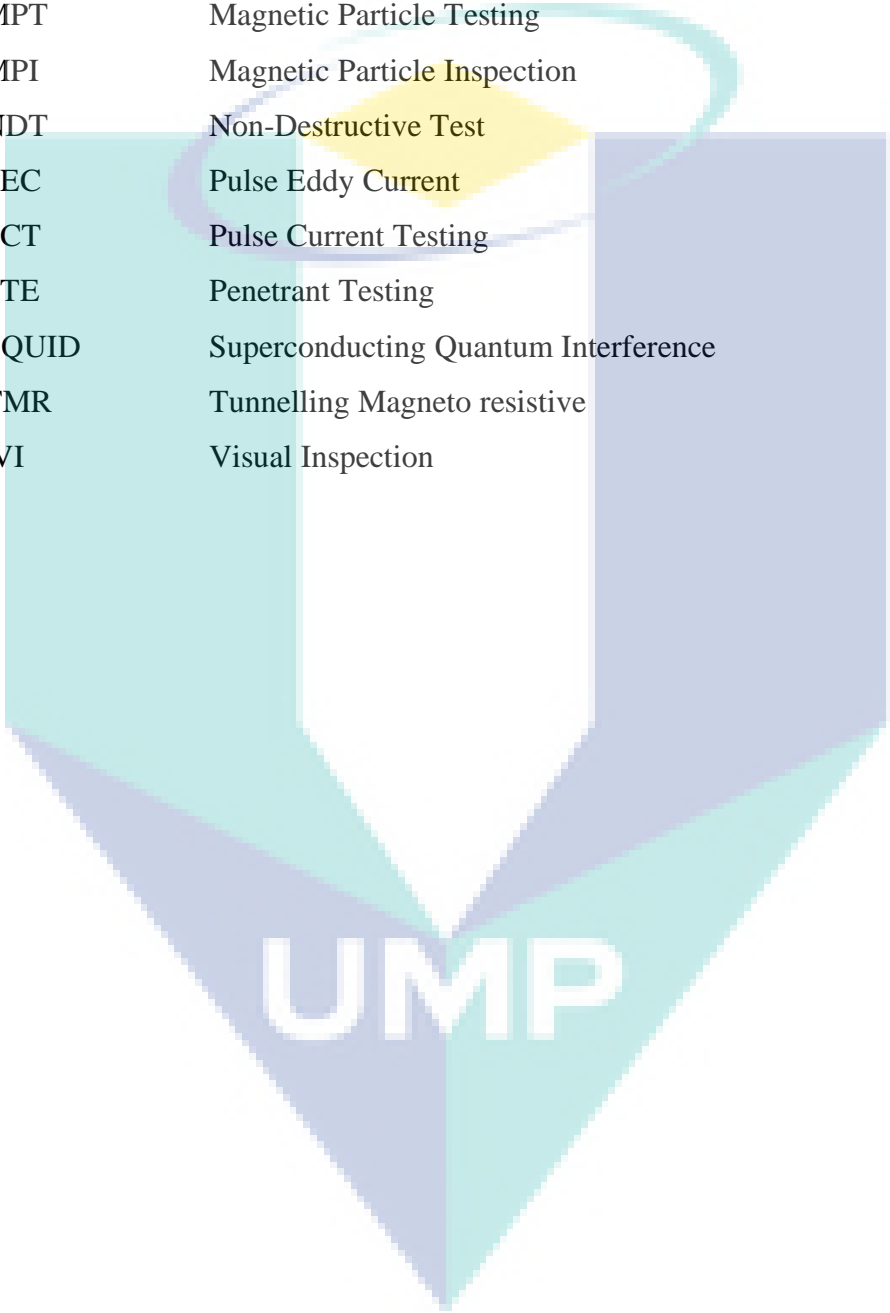
Figure 4.15	(a) The real and (b) imaginary components of the line-scanned magnetic field intensities of a slit with 513 $\mu\text{m}$ depth at different frequencies.	72
Figure 4.16	Signal difference of the different depths of slits at different frequencies.	73
Figure 4.17	2-D magnetic map distributions of different slit depths at different frequencies. (a) 1-khz. (b) 500-Hz. (c) 90-Hz.	75
Figure 4.18	Line-scanned magnetic field intensities of different slit depths with respect to different excitation field's current. (a) 1 mA. (b) 3 mA. (c) 4 mA. (d) 6 mA. (e) 8 mA. (f) 10 mA.	77
Figure 4.19	2-D magnetic map distribution after the probe has been rotated by 90 degree.	78
Figure 4.20	Line-scanned magnetic field intensities of different slit width at different frequencies. (a) 90-Hz. (b) 300-Hz. (c) 500-Hz. (d) 700-Hz. (e) 1-kHz.	80
Figure 4.21	2-D magnetic map distribution of different slit widths at 1-kHz excitation field.	81
Figure 4.22	Line-scanned magnetic field intensities of different slit lengths at different frequencies. (a) 90 Hz. (b) 300 Hz. (c) 500 Hz. (d) 700 Hz. (e) 1 kHz.	82
Figure 4.23	Signal difference of different slit lengths of slits at different frequencies.	83
Figure 4.24	2-D magnetic map distributions of different slit length at 1-kHz excitation field.	84
Figure 4.25	Correlation between real physical length of slits and estimated length in 2D image of magnetic field distribution.	84
Figure 4.26	2-D magnetic map of the steel plate with 'UMP' slits using the ECT probe.	85
Figure 4.27	2-D magnetic map of the steel plate with 'UMP' slits using the ECT probe where the letter direction is perpendicular to the ECT probe.	86
Figure 4.28	2-D magnetic map of the steel plate with 'UMP' slits using the ECT probe where the letter direction is rotated to 45° with respect to the ECT probe.	87
Figure 4.29	Line-scanned magnetic field intensities of different slit depths measured from the backside at different frequencies. (a) 90-Hz. (b) 300-Hz. (c) 500-Hz. (d) 700-Hz. (e) 1-kHz.	88
Figure 4.30	Signal difference of the different slit depths at different frequencies (backside).	89

## LIST OF SYMBOLS



A	Ampere
$\omega$	Angular Frequency
$\sigma$	Conductivity
J	Current Density
E	Electric Field
$\epsilon$	Electric Permittivity
$\rho$	Free charge density
f	Frequency
H	Magnetic Field Intensity
B	Magnetic Field
$\mu$	Magnetic Permeability
$\Omega$	Ohm
T	Tesla
V	Volt

## LIST OF ABBREVIATIONS



AMR	Anisotropic Magneto-Resistive
ECT	Eddy Current Testing
MFL	Magnetic Flux Leakage
MPT	Magnetic Particle Testing
MPI	Magnetic Particle Inspection
NDT	Non-Destructive Test
PEC	Pulse Eddy Current
PCT	Pulse Current Testing
PTE	Penetrant Testing
SQUID	Superconducting Quantum Interference
TMR	Tunnelling Magneto resistive
VI	Visual Inspection

## CHAPTER 1

### INTRODUCTION

#### 1.1 Background of study

Nowadays, Non-Destructive Test (NDT) techniques are widely used in several industries since most of the modern structures are made from the steel structures. NDT relates to the examination of materials for flaws without harming the object tested. In other words, by using NDT, after the inspection or test is completed, the part can still be used. The aim of NDT process is to inspect, test or evaluate materials, components assemblies for discontinuities, or differences in characteristics, without destroying the serviceability of the part or system. NDT provides a cost-effective of testing without causing damage to the samples. Nowadays NDT is used in manufacturing, fabrication and in-service inspections to ensure product integrity and reliability, to control manufacturing processes, lower production costs and to maintain a uniform quality level.

NDT is needed whenever we need to ensure the quality and the strength of the infrastructures. Aircraft, trains, pipelines, oil rigs, bridges and pressure vessels are examples of everyday things that are regularly examined. NDT can be used to improve the production output and to ensure the safety of the infrastructure. Besides that, a component or a whole machine can be tested many times by using NDT techniques to make sure the safety and the strength of the machine or structure. A variety of non-invasive inspection techniques has been used in scientific studies and industries to evaluate the properties of a material, component or system without causing damage to the sample (Abdullah, Mason, & Al-Shamma'A, 2013) and several NDT methods have been developed for evaluating defects in materials including internal and back side defects of the steel components. Moreover, NDT can be used to find, size and locate surface and subsurface flaws and defects.



The reason why NDT is necessary in industries is because of the safety of products. NDT is conducted to determine whether a component is compromised or in need of repair. Most of NDT methods are completely harmless to humans except for radiographic testing that needs to be conducted under strict procedures. Next, the reliability of NDT makes NDT one of the reasons why it is useful in industries. Different industries have different standards of inspections but regardless of what must be inspected, NDT is the most affordable option. The final benefit of NDT is knowing that the equipment in industries is functioning well while being able to perform a continuous inspection on them, and problems with the equipment can be identified by a simple check-up.

Currently, NDT inspection methods that are commonly used in industry are visual inspection, radiographic (X-rays transmission), ultrasonic inspection, penetrant inspection, stress measurement, acoustic emission, infrared inspections and magnetic methods. Visual inspection (VT) is easy to apply, quick and relatively inexpensive. However, this method requires a trained operator for a long inspection time (Abdullah et al., 2013; Chu & Wang, 2016). Besides, NDT often includes the X-ray scanning and ultrasound testing. The disadvantage of using this technique is, this method needs high cost of testing and requires rework after detection of any problems (Sasayama, Ishida, Matsuo, & Enpuku, 2016). NDT requires an understanding of the working principles of the used methods, their capabilities and limitations, and knowledge of the relevant standards and specifications for performing the tests, where it can give a good result when used it correctly. Materials, products and equipment may require expensive repair or early replacement due to undetected defects. This kind of defect may cause an unsafe condition, failure and loss of revenue due to unplanned shut down. Non-destructive testing can be applied to each stage of an item's construction. The materials and welds also can be examined using NDT so that their quality can be accepted, rejected or repaired.

Although there are several non-destructive techniques, this research deals specifically with magnetic methods. Magnetic methods are a promising technique for NDT of steel components since they are safe, fast and non-contact. Besides, the magnetic methods can be compacted easily since their system configuration is simple. These methods include eddy current testing (ECT) method, where ECT is widely used for the NDT evaluation of conductive materials such as metallic plates (Biegel, 2008; García-Martín, Gómez-Gil, & Vázquez-Sánchez, 2011; Ghanei, Kashefi, & Mazinani,

2013). The advantages of ECT is its ease, versatility, speed and non-contact nature. However, low-frequency measurements are required in order to avoid the skin effect caused by the high permeability of metals when using the ECT technique. It is also well known that lift-off between the coil and the test samples is strongly influenced the changes of the measured eddy current's signals.

In this research, a low-frequency ECT method is applied in order to enable a deeper detection of flaws since the induced eddy currents are governed by the skin depth effect. To achieve a highly sensitive measurement, a magnetometry system with highly sensitive magnetic sensors is developed for this NDT system, where AMR sensors (Honeywell HMC1001) are used. The AMR sensor is advantageous over coil based magnetic sensor owing to its Honeywell's Anisotropic Magneto-Resistive (AMR) technology. It is very sensitive, low field, and solid-state magnetic sensors which are designed to measure direction and magnitude of Earth's magnitude fields (DC to 1MHZ). Besides that, the magnetic sensor is easily maintained and simple to install as well.

Besides flaw detection, ECT also is used to measure thickness and conductivity measurements. The basic principle for NDT is a coil of conductive wire is used to excite magnetic field using an alternating electric current. This wire coil will produce an alternating magnetic field around itself. The magnetic field oscillates at the same frequency as the current running through the coil. When the coil approaches a conductive material, currents opposed to the ones in the coil are induced in the material and they are called eddy current. There is a wide range of ECT applications and since ECT is electrical in nature, it is limited to the conductive material and thus cannot be used in plastics. Although ECT can be applied in many ways, there are also physical limits to generate eddy currents and depth penetrations of the electromagnetic waves.

ECT method does not require the use of coupling liquids and it can examine large areas very quickly. In order to detect cracks in welding, ECT can also check metals' hardness and conductivity in various applications. Occasionally, eddy current and ultrasonic testing are being used together for having a better result of NDT.

## 1.2 Problem Statement

Nowadays, in modern construction, the steel structure is commonly used in every type of structures such as buildings, bridges, towers, etc. The important factor in developing infrastructures is the strength and quality of steels. Therefore, it is crucial to make sure all the steel products are in good condition and safe for the consumer. Commonly, the causes of failure towards the steel structures are because fatigue, machining tears, and corrosion where these can cause an accident and harmful to the structures (Marazani, Madyira, & Akinlabi, 2017). Surface and subsurface cracks are one of the defects that are essential to monitor so that fatal accidents that can cause serious injuries or loss of life can be prevented (Alpsten, 2017). A continuous inspection without causing any deterioration of samples under test is required for crack detection to ensure structural safety. Normally in the industries, visual inspection is used to inspect the defects, but it is known that this method requires a tedious process and must undergo instinctive judgments from the inspectors (Soni, 2018).

Recent reviews state that the magnetic method is one of the auspicious methods when dealing with steel structure. Because of the advancement of electronics devices and signal processing, the use of the magnetic method or specifically eddy current testing (ECT) method becomes common in metal structure (Kreutzbruck & Allweins, 2002). Generally, a common ECT probe uses a coil as a medium to detect the secondary magnetic field that is generated by the repeated eddy currents. However, the probe that uses the coil to detect defects is commonly convenient for surface defect detection only due to the frequency-dependent behaviour (Sen, Anoop, & Sen, 2017). In order to detect the existence of failures in a metal specimen using a coil probe, a high frequency is needed to allow a highly sensitive detection. The previous study stated that the sufficient frequency to generate an eddy current in a steel material ranges from 1 MHz to 2 MHz where the high frequency is used for surface analysis crack detection based on the penetration depth's,  $\delta$ , expression (M. M. Saari et al., 2019; Tondo, Porto, Villalobos, Brusamarello, & Campestrini, 2017). Furthermore, the measurement system cannot be compacted easily. Since coil probe is sensitive at high frequency, therefore it needs lots of number of turns of the induction coil to detect a magnetic field, where this can lead to the increase of the probe size. Even though this technique is promising, but to detect a small defect or crack in material especially inside the metal or backside of the metal, a low- frequency is required.

ECT is able to detect a crack in various conductive materials, either ferromagnetic or non-ferromagnetic. However, ECT method is rarely applied to ferromagnetic materials because the detected magnetic field consists of both information of the eddy current and strong magnetization signal (Tsukada, Hayashi, Nakamura, Sakai, & Kiwa, 2018). Since the magnetization signal causes trouble in finding defects on the sample, therefore, a measurement technique is needed to reduce the magnetization signal below the eddy current's signal to avoid a detection error and other magnetic noises. Because of that, ECT method is frequently operated on non-ferromagnetic material such as Aluminium because magnetization signal does not flow thus, easier to detect eddy current signal (García-Martín et al., 2011).

Cracks can exist in various shapes and sizes where the crack can develop from small scale lower than 1 mm. The size of cracks can spread and contribute to the complete fracture of components. Hence, the discovery of any cracks in their early stage will prevent any sudden fatal accidents in the future. In order to detect small sizes of cracks, a highly sensitive probe is required from the low-frequency region (Tsukada, Kiwa, Kawata, & Ishihara, 2006). Thus, the ordinary probe using coils to detect eddy current signal has been replaced by magneto resistive (MR) magnetometers. MR magnetometers are promising detector tools since they are highly sensitive and able to detect small signals produced by tiny flaws (Hamia, Cordier, Saez, & Dolabdjian, 2010).

### **1.3 Objective Research**

This study focusses on developing a sensitive AMR sensor for surface defect inspection at low frequency. The specific objectives of this study are as follows:

- I. To develop a small eddy current probe with 2D scanning mechanism using sensitive AMR sensors for detection of surface defects at a low excitation field frequency.
- II. To validate the system performance during the defect detection of sub-millimeter artificial slits by characterizing the magnetic field distributions of the induced eddy currents with regard to the length, width, depth and different shapes of the slits on ferromagnetic galvanized carbon steel plates at different frequencies of the excitation field.

## **1.4 Scope of work**

The research scopes of this project are:

- I. Development of a small eddy current probe that consists of two highly sensitive AMR magnetic sensors (HMC1001) with a phase sensitive detection technique and a small excitation coil.
- II. Characterization of eddy current response due to the different parameters of sub-millimeter artificial slits such as depth, width, length and shape on 2 mm galvanized steel plates at excitation fields less than 2 kHz.

## **1.5 Significant of Study**

The outcomes of this study can be beneficial for these institutions:

- I. Training Centre/ Institution

The prototype of this study would be one of fundamental study achievement for education purposes. Using the prototype, trainers can easily demonstrate to students on using Non-destructive test. This can also help students to get 'direct feedback' while using the equipment.

- II. Manufacture

The prototype should be a new innovative technology that can be used in industries as an alternative inspection in NDT applications.

## **1.6 Thesis Overview**

This thesis consists of five chapters including this chapter. The contents of each chapter are as follows:

### *Chapter 1*

This chapter discusses about overview of the research such as the introduction of NDT and ECT technique, problem statements and objectives of the research. Moreover, the scope of the research also has been discussed. This chapter also covers the detection of defect and cracks in metallic materials using ECT technique.

## *Chapter 2*

This chapter studies about the other methods that have been used for NDT. All the literature reviews of different NDT methods have been explained from various sources.

## *Chapter 3*

A detailed explanation about the process development of the ECT probe system is covered in this chapter. All the steps, flowchart, scanning mechanism and circuitry implementation are discussed in this chapter.

## *Chapter 4*

This chapter focuses on the results that have been obtained during the experiments conducted and the results obtained from the simulation work. The results are analysed and concluded in this chapter.

## *Chapter 5*

This chapter concludes the overall of the study. Moreover, the recommendations for future study have also been discussed in this chapter.

The logo for UWP (Universiti Malaysia Perlis) is a large, stylized shield shape. It is divided into four quadrants: top-left is light blue, top-right is light purple, bottom-left is light blue, and bottom-right is light purple. At the top center is a yellow diamond with a white outline. A white swoosh arches over the top of the shield. The letters 'UWP' are written in white, bold, sans-serif font across the bottom of the shield.

UWP

## CHAPTER 2

### LITERATURE REVIEW

#### 2.1 Non – Destructive Testing Evaluation

Non- Destructive Test has been defined as the methods that can be used to inspect a material, equipment or system without causing any damages to the system. NDT can not only check the defects without any harm to the material, but also by using practical applications of the principle of physics, NDT can measure hidden defects in the material and being contactless with the object (García-Martín et al., 2011). NDT is also used to investigate the purity of the material of the test object. Generally, NDT is implemented to industry inspection to locate and characterize conditions of the materials and defects that can cause planes to crash, trains to wrack, a pipeline to explode and many more troubling events. Besides that, NDT can also be used to test the building structures. This method can be applied frequently to the same structure and at the other times. Furthermore, NDT methods are convenient to analyze the building structures although the buildings were built a long time ago (Schabowicz, 2010).

Non-Destructive Evaluation (NDE) is a subject that usually confused with NDT. Technically, NDE is used to describe measurements that are more quantitative in nature. NDE method can be used to measure the shape, size, and location of the defects. Moreover, NDE can be used to determine the properties of materials such as the firmness, toughness and other physical characteristics.

##### 2.1.1 Purposes of Non – destructive Testing

Non-destructive tests are widely used to detect variations in structures, changes in surface, the presence of flaws or other anomalies defect, to measure the thickness of materials and coatings and to determine other characteristics of industrial products. By



applying NDT in manufacturing process, all the components, materials and structures can be examined without being harmed because the process is contactless with the component. In manufacturing process, NDT is used to:

#### **2.1.1.1 Prevent accidents and failure**

As mention earlier, NDT can identify the structural strength, fitness, and trustworthiness, and it can play an important role to make sure that all the machines and equipment are good and safe to use. Safety of the workers is the most crucial part and NDT is one of the processes to avoid any problems or unfortunate accidents by making sure that all the structure is in good condition to work on. Moreover, to add on the benefit of NDT, it can improve productivity because the employees know that their surrounding is safe.

#### **2.1.1.2 Improve product reliability**

To gain perfect and accurate results, non-destructive testing is reliable because of various methods and complementary options. NDT can check out all the given piece of equipment or machinery which can erase the risk of oversight or inaccuracy without destroying the products. Furthermore, while the product undergoes the processing technique of NDT, without affecting its performance, NDT can increase the degree of reliability of the product.

#### **2.1.1.3 Lower manufacturing cost**

NDT can help to save the time and money in many ways such as monitoring the assets' health by performing NDT inspection from time to time. If there is an unfortunate thing happens, they can replace or repair the equipment before costly problems occur. Not just that, from the test result, preventive maintenance can be taken which can save more money over the long-term, plus, there will no any waste after NDT inspection.



#### **2.1.1.4 Control the manufacturing process**

In the manufacturing industries, control is the basic concept where the process must be controlled under supervision by a trained operator so that any waste will not be produced. If there are any factors of the manufacturing process get out of control, the quality of the product will be comprised and can produce waste. To make sure the manufacturer gains a net profit without any loss, almost every NDT method is applied to assist in process control. For example, one the NDT technique is applied to a few parts to tell that when or where the cracking has occurred. If there is any mistake or problem, it can be corrected immediately. From there, cost and processing time are saved for the manufacturers.

#### **2.1.1.5 Sustaining uniform quality level**

One of the aims of the NDT technique is to improve the quality of the product. NDT can be used to make sure the highest levels of quality, right from the raw material stage until the end of the products. This secures the product consistency and conformity with buyers and industry demands.

### **2.1.2 Non-destructive testing methods**

There are numbers of NDT methods that are used frequently in the industries. NDT methods that are used to inspect components are bigger and continue to grow. To develop a better NDT method, researchers keep on finding to improve NDT by applying physics and other scientific principles. However, they are few methods that has been usually used to inspect components. These methods are visual inspection, magnetic particle testing, electromagnetic or eddy current testing, radiography, and ultrasonic testing. These methods and a few others are briefly described below.

#### **2.1.2.1 Visual Inspection (VI)**

Visual inspection technique involves using bare eyes to look for any irregularity shapes. The trained investigator will use some device such as magnifying glasses, mirrors, or borescopes to gain an accurate result and more closely to the scanning area.

The range of the procedures that the inspector will go through is from the simplest ways to very complicated ways (Abdullah et al., 2013; Chu & Wang, 2016; Gros, 1995).



Figure 2.1 Image of visual inspection testing. (Source: <https://hitechndt.com/visual-inspection.html>)

#### **2.1.2.2 Penetrant testing (PT)**

It is also known as the liquid penetrant inspection and widely used because of low-cost inspection method to check surface anomalies defects in materials such as metals, plastics or ceramics. This method might be applied for ferrous and non-ferrous materials. The first procedure for this technique is the sample objects will be coated with visible or fluorescent dye solution. Then, the excess dye will be removed from the surface and a developer is applied. The developer acts as a blotter, drawing trapped penetrant out of flaws open to the surface. By using visible dyes, bright color contrast between the penetrant and developer will come out and easy to see. To ensure the defects can be ready to be seen, with fluorescent dyes, ultraviolet light is used to make the colors more bright (Dwivedi & Sharan, 2003).



Figure 2.2 Image of penetration testing. (Source: <http://www.dfcvalve.com/News/Dye-Penetration-Test.html>)

### 2.1.2.3 Magnetic particle testing (MPT)

This method is carried out by inducing a magnetic field in a material and then rub the material with iron particles. There are two ways to rub the iron particles on the surface of materials, either dry or suspended in liquid. If there is any defects or imperfections on the surface, it will disturb the flow of current and will cause magnetism to spread out. Flux leakage field will occur at the site of damage. This provides a visible indication of the flaws (Jander, Smith, & Schneider, 2005; Lee et al., 2003).



Figure 2.3 Image of magnetic particle testing. (Source: <https://www.tuv.com/magnetic-particle-inspection.html>)

### 2.1.2.4 Electromagnetic testing or eddy current testing (ECT)

Alternating magnetic field will induce electrical currents in conductive materials. The currents that are generated in the materials is known as eddy currents. Eddy currents flow in closed-loop motions and just below the surface of the material. If there are any defects on the surface, the flow of eddy currents will be interrupted. Then

this eddy currents can be detected by a proper equipment (García-Martín et al., 2011; Sasayama et al., 2016).



Figure 2.4 Image of electromagnetic testing. (Source: <http://www.petroconindia/eddy-current-testing.html>)

### 2.1.2.5 Radiography

This method involves the use of penetrating gamma or X-radiation rays to scan the defect parts. For the source of radiation, an X-radiation generator or radioactive isotope is used. The resulting graph shows the dimensional characteristics of the material. Furthermore, this method involves formation of X-ray image projection to a 3D scene. Besides that, the testing setup is utilized with computer simulation tool while for the X-ray penetration process is based on the attenuation law. The result can be obtained from the output which includes the actual test sample's structure (Gayer, Saya, & Shiloh, 1990; Thien, Chi, & Ngoc, 2017).

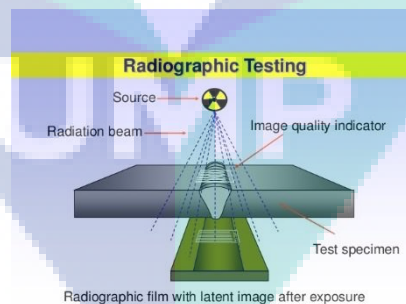


Figure 2.5 Illustration of radiographic testing. (Source: <http://sitasndt.com/radiographic-testing>)

### 2.1.2.6 Ultrasonic testing

For the ultrasonic method, it uses transmission of high frequency sound waves into the material. Pulse echo is commonly used in industry where the sound is introduced to the object and the echoes will return to the receiver and it is considered as sensitive to the defects and open cracks since it is based on the phenomenon of reflection or transmissions of sound waves (Hutchins, 1999; Nesvijski, 2000).



Figure 2.6 Image of ultrasonic testing. (Source: <http://ultrasonic-testing.html>)

### 2.1.2.7 Acoustic emission testing

The emissions are generated when a solid material is tense, then imperfections within the material will produce a blowout of acoustic energy. A special receiver is used in order to test the acoustic emissions. In addition, the study of its intensity, rate, and location can evaluate the emission sources.

## 2.2 Magnetic method

As mention earlier, NDT technique can inspect various type of materials. To be specifically, when it comes to electrically conductive materials, magnetic method is one of the promising techniques in NDT. Moreover, this is owing to its ability to inspect metallic compound as the compound is conductive and possesses strong magnetic properties. Magnetic method can be divided into two parts which is eddy current measurements and flux leakage measurements (Tsukada, Yoshioka, Kawasaki, & Kiwa, 2010).

## **2.2.1 Flux Leakage Measurements**

Flux leakage measurement consists of two methods that is magnetic particle inspection and magnetic flux leakage. These two methods are widely used in flux leakage measurement.

### **2.2.1.1 Magnetic particle inspection (MPI)**

Magnetic particle inspection or better known as (MPI) was developed in the year of 1930s by Magnflux. This method is very direct in principle. This method relies on the leakage of magnetic flux at the outer of the material in the surrounding of defects or near the surface flaws (Jiles, 1990). By using this method, to generate a magnetic field in the material, there are two main procedures which are 'yoke' and 'prod' methods. A magnetic yoke can be used by winding the yoke with a field coil. As another option, using 'prods' or in other words by using contact electrodes, where a high electric current is passed through the material. Then, a circulating magnetic field will be generated by the current. This method will give a straightforward signal of the defect's region and size of the flaws. Although MPI is a simple method, this can only be applied on ferromagnetic materials. Not only that, to produce the best output, the magnetic field must lie perpendicular to the direction of the defects. Although there is a limitation with this method, this method has the advantage to inspect the defects or flaws in the difficult area, for example, inside the pipeline. Previous study states that, this technique has shown an unsuccessful output when applying to aerospace components because of the lack of magnetization in some parts of the components (Massa, 2000).

### **2.2.1.2 Magnetic Flux Leakage (MFL)**

MFL system or magnetic flux leakage system works by detecting the flux leakage that comes out from the defects area. MPI and MFL depend on the disruption of magnetic flux in a conductive material caused by a surface flaw. For MPI method, the detection relies on magnetic powder or another tool that can be used such as magnetic recording tape (Forster, 1975; Stumm & Rotomat, 1974). However, MFL indicates the presence of a defect by the flux leakage technique where it utilizes a strong magnetic field produced by an electromagnetic yoke to saturate the magnetization of the ferromagnetic material. During the scanning process, if there is any flaws or anomalies such as cracks, the leakage of the magnetic flux will be detected by a magnetometer.



This technique was first introduced by Zuschlag (Jiles, 1990) to detect the flux leakage using a magnetometer. This technique has been successfully used for detection of the surface (Atherton, Teitsma, & Atherton, 2014) and backside crack. For example, this technique can be applied to detect flaws inside surface of long tubes and pipelines (Holt et al., 1983). Nevertheless, despite the system has no limitation on the scanning area, the use of the electromagnet yoke and high current to saturate the sample of magnetization, will cause the size enlargement of the system.

## **2.2.2 Eddy Current Measurements**

Eddy current methods for NDT is an effective method to detect defects in metal structures. There are few techniques that involve the basic principle of eddy current (Janousek, Capova, Yusa, & Miya, 2008) and those techniques depend on the identifying the eddy currents generated by an applied magnetic field and monitoring the changes of the eddy current flow (Morimoto, Araki, Satake, & Shimizu, 1992), so that the presence of the defect can be detected. Moreover, eddy current measurement technique is better than other technique because the inspection can be done without any contact (García-Martín et al., 2011) with the inspected piece. All the techniques are named as Eddy current Testing (ECT) and Pulse Eddy Current (PCT) (Auld & Moulder, 1999; Kasai, Fujiwara, Sekine, & Sakamoto, 2008). This method was increasingly developed especially in the aircraft (Kasai et al., 2008) and nuclear (Morozov, Rubinacci, Tamburrino, & Ventre, 2006) industries since the 1950s. Eddy current testing has the advantage to detect a crack in a variety of conductive material either ferromagnetic or non-ferromagnetic while other methods such as MPI limited to ferromagnetic materials only (García-Martín et al., 2011).

### **2.2.2.1 Eddy Current Testing (ECT)**

Eddy current is created from the process of electromagnetic induction. For ECT method, the magnetic field is produced from the alternating current flows in the excitation coil. If there is any conductive material brought closer to the coil, the eddy current will be induced in the sample and the flaws on the sample will make the changes of amplitude and distribution of eddy currents. The defect can be detected by measuring the amplitude changes of eddy current. Moreover, eddy current can also be used to

identify the thickness of the coating (Taylor, Pedersen, Magnusson, & Zhengsheng, 2014), checking the strength of the metal structures, conductivity, magnetic permeability, plate thickness measurement (Mercier, Lesage, Decoopman, & Chicot, 2006), surface and near-surface crack evaluation. To construct ECT system, many magnetometers have been used such as inductive coil (Slawomir, 2007), hall sensor (Vértesy & Kim, 2013), Tunnelling Magnetoresistance (TMR) sensor (Tsukada et al., 2018), anisotropic magnetoresistance (AMR) sensor (Allweins et al., 2006; He, 2017; Tsukada et al., 2006), fluxgate and superconducting quantum interference device (SQUID) (Bousack & Gmbh, 1996). A study shows that SQUID has the lowest noise compare to others sensor (Mohd Mawardi Saari et al., 2014). But this sensor is not convenient to use in the industries since to perform NDT using SQUID needs liquid nitrogen or liquid helium for the cooling. The previous study had measured the noise spectral densities (Stutzke et al., 2014) of the others commercially magnetic sensor and it showed that the AMR sensor had the lowest magnetic field noise spectrum density. Therefore, this magnetic sensor is chosen in this study. More explanations about AMR sensor will be explained in chapter 3.

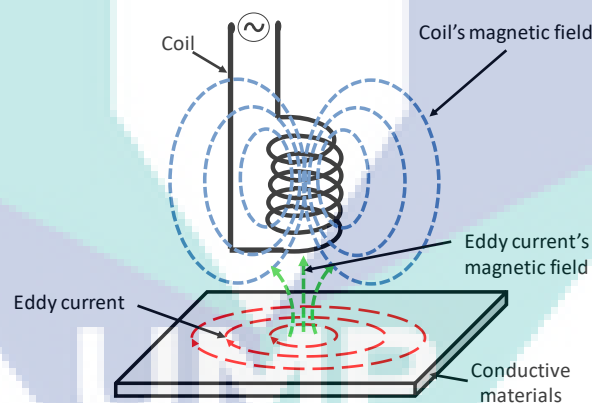


Figure 2.7 Illustration of the working principle of ECT.

### 2.2.3 Eddy Current Depth of Penetration

In eddy current testing, when applying high frequency field, eddy currents are primarily cramped to the surface of an electrically conductive material. If the frequency is tuned to a low frequency, the eddy current will penetrate inside the material where eddy current density decreases exponentially with depth.



This phenomenon is called the skin (depth) effect. The skin effect occurs when the eddy current penetrates in the material at any depth and then it produces magnetic fields which oppose the primary field. This will cause the magnetic flux to reduce and causing a decreasing magnitude of magnetic flux penetration as the depth increases. In any application, before proceeding with eddy current testing inspection, one must determine the depth of penetration. For example, if the inspection requires to inspect the surface structures, a high frequency is preferred. But if the inspection needs to inspect deep or subsurface area, then the depth of penetration must be enough to provide a high eddy current density at the possible defect depth.

Specifically, the eddy current penetrates the material is affected by the frequency of the excitation field. When the frequency decreases it can cause the depth of penetration to be deeper. Standard depth of penetration is called based on the depth where the eddy current density is decreased by 37% (Mottl, 1990). In this section the basic theory of penetration depth of eddy current will be derived and equations defining the principle parameters affecting the eddy current inspection will be investigated.

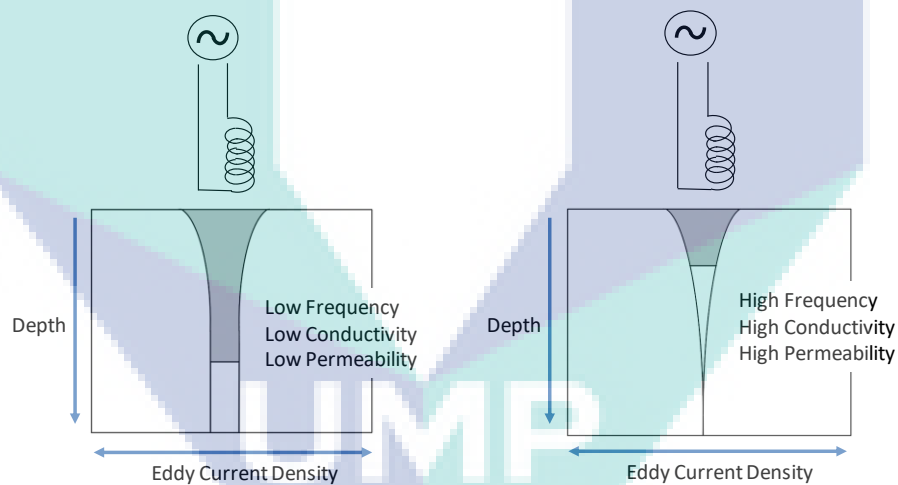


Figure 2.8 Eddy current depth of penetration.

### 2.2.3.1 Eddy Current Depth of Penetration

Derivations of electromagnetic begin with Maxwell's equations where they are given in the differential forms:

$$\vec{\nabla} \cdot \vec{D} = \rho \quad 2.1$$

$$\vec{\nabla} \cdot \vec{B} = 0 \quad 2.2$$

$$\vec{\nabla} \cdot \vec{H} = \vec{J} + \frac{d}{dt} \vec{D} \quad 2.3$$

$$\vec{\nabla} \cdot \vec{E} = -\frac{d}{dt} \vec{B} \quad 2.4$$

$$\vec{B} = \mu \vec{H} \quad 2.5$$

$$\vec{D} = \epsilon \vec{E} \quad 2.6$$

$$\vec{J} = \sigma \vec{E} \quad 2.7$$

By using Maxwell's equations, eddy currents flow in materials can be derived. When applying eddy current technique to the conductive material, the free charge density ( $\rho$ ) is zero. By combining Maxwell's equation (2.3), (2.6), and (2.7), this eliminates current and electric flux densities, giving

$$\vec{\nabla} \times \vec{H} = \sigma \vec{E} + \frac{d}{dt} \epsilon \vec{E}, \quad 2.8$$

$$\vec{\nabla} \times \vec{H} = (\sigma + \epsilon \frac{d}{dt}) \vec{E}. \quad 2.9$$

From equations (2.4) and (2.9), it suggests that  $\vec{E}$  can be eliminated by taking the curl of  $\nabla$  in equation (2.9).

$$\vec{\nabla} \times (\vec{\nabla} \times \vec{H}) = \vec{\nabla} \times \left( \sigma \vec{E} + \frac{d}{dt} \epsilon \vec{E} \right) \quad 2.10$$

$$\vec{\nabla} \times (\vec{\nabla} \times \vec{H}) = \vec{\nabla} \times \sigma \vec{E} + \vec{\nabla} \times \frac{d}{dt} \epsilon \vec{E} \quad 2.11$$

$$\vec{\nabla} \times (\vec{\nabla} \times \vec{H}) = \sigma (\vec{\nabla} \times \vec{E}) + \epsilon \frac{d}{dt} (\vec{\nabla} \times \vec{E}) \quad 2.12$$

From equation (2.4) substituting into (2.8):

$$\vec{\nabla} \times (\vec{\nabla} \times \vec{H}) = \sigma \left( -\frac{d}{dt} \vec{B} \right) + \epsilon \frac{d}{dt} \left( -\frac{d}{dt} \vec{B} \right). \quad 2.13$$

From vector calculus theory

$$\vec{\nabla} \times (\vec{\nabla} \times \vec{H}) = \vec{\nabla} (\vec{\nabla} \cdot \vec{H}) - \vec{\nabla}^2 \vec{H}. \quad 2.14$$

Now from equations (2.2) and (2.5),

$$\vec{\nabla} \cdot \vec{H} = 0, \quad 2.15$$

$$\vec{\nabla} \times (\vec{\nabla} \times \vec{H}) = \vec{\nabla} (0) - \vec{\nabla}^2 \left( \frac{\vec{B}}{\mu} \right). \quad 2.16$$

Thus, from equation (2.13),

$$-\vec{\nabla}^2 \left( \frac{\vec{B}}{\mu} \right) = \sigma \left( -\frac{d}{dt} \vec{B} \right) + \varepsilon \left( -\frac{d^2}{dt^2} \vec{B} \right), \quad 2.17$$

or

$$\vec{\nabla}^2 \left( \frac{\vec{B}}{\mu} \right) = \sigma \left( \frac{d}{dt} \vec{B} \right) + \varepsilon \left( \frac{d^2}{dt^2} \vec{B} \right). \quad 2.18$$

Sinusoidal current sources will generate eddy current which in turn create varying magnetic fields by electromagnetic induction. Assuming no material inhomogeneities, steady state conditions will conquer.

The applied magnetic field to the conductive material can be expressed by the equation

$$\vec{B} = B_z e^{j\omega t} a_z. \quad 2.6$$

Here  $\vec{B}$  is the vector-phasor representation of maximum field amplitude. Differentiating equation (2.19) yields

$$\frac{d}{dt} \vec{B} = j\omega B_z e^{j\omega t} a_z. \quad 2.20$$

Differentiating again,

$$\frac{d^2}{dt^2} \vec{B} = -\omega^2 B_z e^{j\omega t} a_z. \quad 2.21$$

Substituting into (2.18) gives

$$\nabla^2 \left( \frac{B_z e^{j\omega t} a_z}{\mu} \right) = \sigma \left( j\omega B_z e^{j\omega t} a_z \right) - \varepsilon \left( \omega^2 B_z e^{j\omega t} a_z \right). \quad 2.22$$

Rewriting equation (2.22)

$$\nabla^2 \left( \frac{B}{\mu} \right) = \sigma j\omega B - \varepsilon \omega^2 B, \quad 2.23$$

$$\nabla^2 B = \mu \left( \sigma j\omega B - \varepsilon \omega^2 B \right), \quad 2.24$$

$$\nabla^2 B = \left( \mu \sigma j\omega - \mu \varepsilon \omega^2 \right) B. \quad 2.25$$

By selecting a constant for ease of solution of the differential equation

$$a^2 = \left( \sigma \mu j\omega - \mu \varepsilon \omega^2 \right) \quad 2.26$$

And previous equation can be expressed as

$$\nabla^2 \vec{B} - a^2 \vec{B} = 0. \quad 2.27$$

To solve equation of (2.27), properties of  $\nabla$  is used,

$$\nabla^2 = \nabla \cdot \nabla, \quad 2.28$$

$$\nabla^2 = \left( \frac{d^2}{dx^2} + \frac{d^2}{dy^2} + \frac{d^2}{dz^2} \right). \quad 2.29$$

By assuming only  $z$ - components of magnetic field parallel to the surface, the equation (2.27) becomes

$$\frac{d^2}{dz^2} B_z - a^2 B_z = 0. \quad 2.30$$

Solving the differential equation gives

$$B_z = Ae^{-az}. \quad 2.31$$

Rewriting equation (2.26),

$$a^2 = j\omega\mu\sigma \left(1 - \frac{j\omega\mu\varepsilon}{\sigma}\right). \quad 2.32$$

Usually, the conductivity ( $\sigma$ ) for most metal range are from approximately  $5.7 \times 10^7 \text{ } \Omega^{-1}/m$  for copper through. Besides, for electric permittivity ( $\varepsilon$ ) for metals is approximately  $9 \times 10^{-12}$  farads/meter. Therefore, for the frequency used in eddy current testing,  $\sigma \gg \omega\varepsilon$ .

Rewriting equation (2.32) for conductive metals,

$$a = (j\omega\mu\sigma)^{\frac{1}{2}}. \quad 2.33$$

The propagation constant of a plane wave is known as  $a$ . The physical phenomenon following the real and imaginary terms contained in  $B_z$  and  $a$ .

$$B_z = Ae^{-z(j\omega\mu\sigma)^{\frac{1}{2}}} \quad 2.34$$

$$B_z = Ae^{-z \left( \frac{1+j}{\sqrt{2}} \right) \sqrt{\omega\mu\sigma}} \quad 2.35$$

$$B_z = Ae^{\left( -z \frac{\sqrt{\omega\mu\sigma}}{2} - jz \frac{\sqrt{\omega\mu\sigma}}{2} \right)} \quad 2.36$$

$$B_z = Ae^{-z \frac{\sqrt{\omega\mu\sigma}}{2}} e^{-jz \frac{\sqrt{\omega\mu\sigma}}{2}} \quad 2.37$$

From equation (2.37), the real component of the exponential term describes the exponential decay of the magnetic field as function of depth within the material while for the imaginary, and it describes a linear increase in phase angle lag from the surface with increasing penetration depth.

It shows that  $A$  is the value of  $B_z$  at the surface,  $B_z(0)$ , thus

$$B_z = B_z(0)e^{-z\sqrt{\frac{\omega\mu\sigma}{2}}} e^{-jz\sqrt{\frac{\omega\mu\sigma}{2}}} . \quad 2.38$$

To relate the induced eddy current with the penetrating magnetic field, by referring to Maxwell's equation (2.3) and neglecting displacement current with respect to condition of  $\sigma \gg \omega\epsilon$ ,

$$\vec{\nabla} \times \vec{H} = \vec{J} + \frac{d\vec{D}}{dt}, \quad 2.39$$

$$\vec{\nabla} \times \vec{H} = \vec{J}. \quad 2.40$$

Since magnetic field is applied in  $z$ -direction only, therefore:

$$\vec{H} = \frac{B_z}{\mu} e^{-z\sqrt{\frac{\omega\mu\sigma}{2}}} e^{-jz\sqrt{\frac{\omega\mu\sigma}{2}}} a_z. \quad 2.41$$

Replace equation (2.41) with

$$\vec{H} = Ka_z, \quad 2.42$$

and given that,

$$\vec{J} = J_x a_x + J_y a_y, \quad 2.43$$

the result of cross product from equation (2.40) gives

$$J_x = \frac{d}{dy} K \quad 2.44$$

$$J_y = \frac{d}{dx} K$$

Substituting (2.41) into (2.44),

$$J_x = \frac{d}{dy} \left[ \frac{B_z}{\mu} e^{\left(-z\sqrt{\frac{\omega\mu\sigma}{2}}\right)} e^{\left(-jz\sqrt{\frac{\omega\mu\sigma}{2}}\right)} \right] \quad 2.45$$

$$J_y = \frac{d}{dx} \left[ \frac{B_z}{\mu} e^{\left(-z\sqrt{\frac{\omega\mu\sigma}{2}}\right)} e^{\left(-jz\sqrt{\frac{\omega\mu\sigma}{2}}\right)} \right]$$

To conclude the equation, the real part exponential term in  $J_x$  or  $J_y$  describe the decay of eddy current with respect to depth of  $z$  while the imaginary components shows the phase lag of the eddy current when the depth of  $z$  is increased. The depth of penetration in terms of standard depth of penetration ( $\delta$ ) is defined as the depth at which  $J_x(z)$  or  $J_y(z)$  decays by  $e^{-1}$  or 36.8%. The standard depth of penetration is found by setting  $z=\delta$ .

$$\delta \left( \sqrt{\frac{\omega\mu\sigma}{2}} \right) = 1 \quad 2.46$$

Thus, yielding

$$\delta = \left( \frac{2}{\omega\mu\sigma} \right)^{\frac{1}{2}} \quad 2.47$$

or

$$\delta = \frac{1}{\sqrt{\pi f \mu \sigma}} \quad 2.45$$

As mention earlier, the sensitivity of the eddy current inspection depends on the eddy current density of the defect location where it is crucial to know the strength of the eddy current at this location. This process will help the ECT technique to produce a flaw signal.

## 2.3 Probes

### 2.3.1 Operation Mode of Probe

Probes of eddy currents come in many shapes and sizes. In fact, the probes for ECT technique can be customized according to the application which is this factor is one of the major advantages in ECT technique. To choose the best configuration of the probe, one must study the way of the coil package to best fit with the testing area. There are few types of operation of the probe in ECT. For a selection of operation mode, it must refer to the way of the coils are wired and interface with the test equipment. The mode of operation divided into three which is absolute, differential and reflection. Each of these mode operations will be discussed in more detail.

#### 2.3.1.1 Absolute Probe

Usually, absolute probe has one test coil that is used to generate the eddy currents and sense the changes in eddy current field. The principle for this mode is when the alternating current flows through the coil, it will produce a magnetic field. If a conductive material is placed near to the probe, the changing magnetic field generates eddy currents within the material. The magnetic field is then generated by the eddy current that opposes the magnetic field of the coil and it makes changes in the impedance of the test coil. Commonly, this operation is used to detect flaws, conductivity measurements, lift-off measurements, and thickness measurements. This probe is widely used because of the easy adaptability.

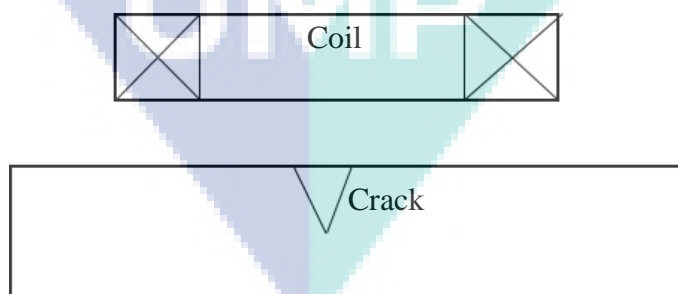


Figure 2.9 Absolute probe mode.



### 2.3.1.2 Differential Probe

The differential operation is different with the previous mode where this probe has two active coils that are wound in the opposite direction. When the coils are near to the material that has no flaws, there is no differential signal happens since they are both inspecting the same material. But the differential signal will take place when one of the coils is over a defect area and the other is over the non-defect material. However, using a differential probe can cause the signal difficult to be interpreted. As an example, if the defects are bigger than the spacing between the coils, only the leading and edges will be scanned due to signal cancellation when both sense the flaw equally (Chady, Enokizono, & Sikora, 1999; Shu, Songling, & Wei, 2007)

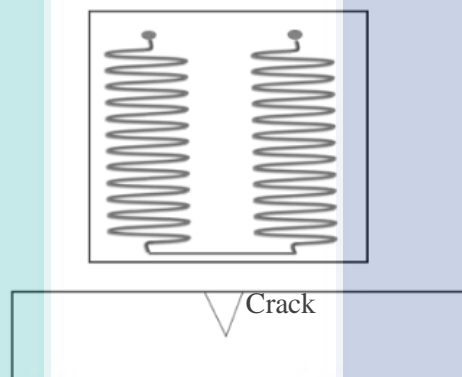


Figure 2.10 Differential probe mode.

### 2.3.1.3 Reflection Probe

Like differential probe, reflection probe has two coils but one of the coils is used to excite the eddy currents and the other is used to detect the changes in the material. The arrangement of this probe always refers to the driver-pickup probe. One of the benefits of this operation is the driver and pickup coils can be separately optimized for their own purposes. The driver coil can be made as to produce a strong flux surrounding the pickup coil, while the pickup coil can be made very small in order to detect a small defect (Auld et al., 1989).

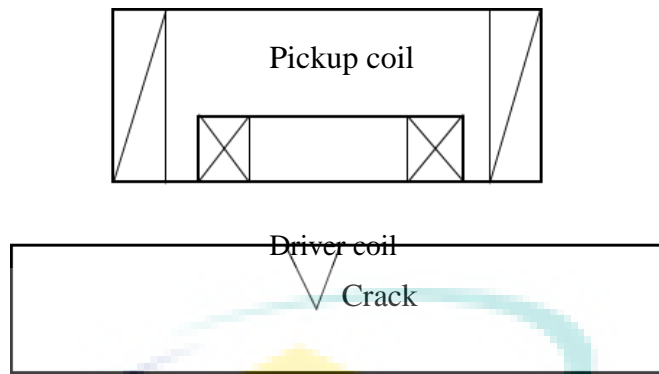


Figure 2.11 Reflection probe mode.

## 2.4 Summary

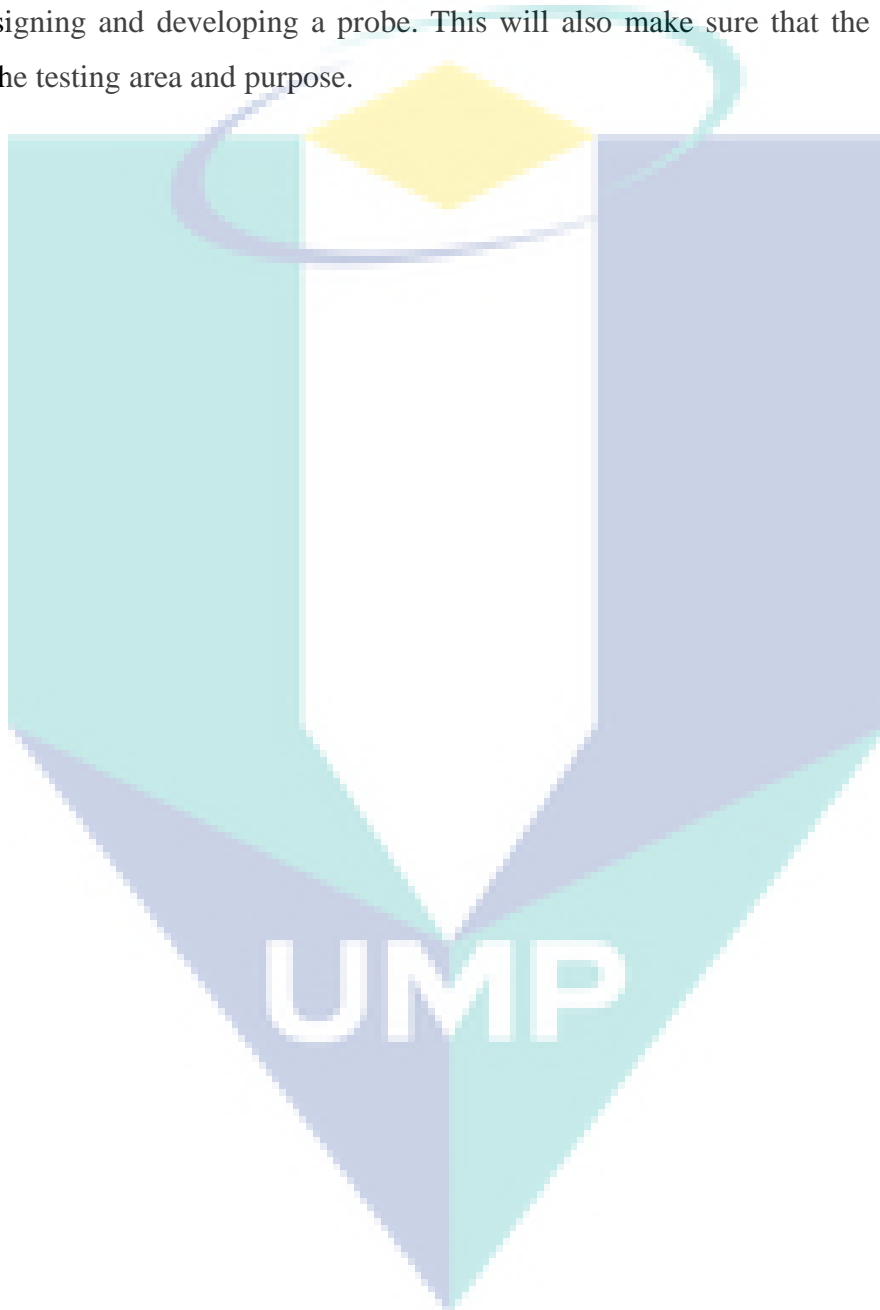
From the literature review, a variety of NDT methods that have been fabricated from a few decades ago have been discussed where all the methods are widely used for many industrial applications. Growing demands in NDT have led to advance and reliable methods where they are used in the industries with a variety of purposes. The commonly used method in the manufacturing process is the visual inspection where it requires a trained inspector to inspect the defects. Radiography is used to detect flaws but before the proceedings begin, safety precaution is required for the safety of radiations. Besides, the ultrasonic method is also ordinarily used but the produced signal is subjective and needs the expertise to evaluate it. Lastly, the most frequent method used is the magnetic methods where these methods will be focused in this research.

The magnetic methods consist of two techniques which are eddy current measurement and flux leakage measurement. The eddy current measurement is applicable for conductive materials and mostly on non-ferromagnetic materials while the flux leakage measurement, it is only applicable on a ferromagnetic material. In this research, eddy current testing method will be studied and revised so that it can be applied on a ferromagnetic material. Since it is difficult to apply the ECT method on ferromagnetic material, a proper signal analysis technique is required. By applying a phase sensitive detection technique, the eddy currents signal will be easier to be evaluated.

Eddy currents are induced in a conductive material by electromagnetic waves. When the excitation field coil approaches a conductive material, this will generate repeated and circular eddy currents. The induced eddy currents will then produce a secondary magnetic field which will oppose to the primary magnetic field. Due to the

frequency effect in eddy current testing is significant to detect flaws, therefore, the penetration depth of eddy current equation is studied and derived in this chapter.

Moreover, plenty of probes were developed with various types, designs, and sizes so that they fit and are easy to use in the desired applications. Types of the probe operation have been discussed and studied in this chapter so that it will ease the process of designing and developing a probe. This will also make sure that the probe will fit with the testing area and purpose.



## CHAPTER 3

### METHODOLOGY

#### 3.1 Introduction

There are few types of non-destructive testing methods that use the principle of electromagnetism as the basis for conducting examinations and one of the methods is known as eddy current testing. Electromagnetic induction is a process that creates eddy currents. When alternating current is applied to the conductor, such as copper wire coil, it will produce an alternating magnetic field. According Maxwell's equations, eddy currents are induced in the conductor and a magnetic field will be developed around the conductor (Drunen & Cecco, 1984). If another electrical conductor gets close to this changing magnetic field, a current will be induced in this second conductor.

According to Lenz's law, when the current is induced by this primary field within the conductive material, it will produce a magnetic field known as a secondary field in opposition to the primary field. Since our modern structures are made from conductive materials, ECT method has been applied to inspect for crack detection, material thickness measurements, coating thickness measurements, conductivity measurements and so on.

In ECT technique, the eddy currents always choose the easiest path to flow, but if cracks exist in the material, the currents will flow around the crack. The changes of eddy currents can be detected by the magnetic field produced by them. Usually, to detect the cracks, the impedance of the coil will be monitored. By using an ECT probe to scan the metallic sample surface, the position of cracks can be detected. The development of new analytical techniques based on software algorithms and adapted hardware components is increasingly important for the detection of cracks based on electromagnetic tests (Kreutzbruck & Allweins, 2002). The use of ECT systems with sensitive magnetometer for measuring the response field is suitable for detecting

backside defects where high field sensitivity is required at low frequencies. This research required both software and hardware implementations purposes. The study itself can be divided into 3 major parts which are hardware developments, interfacing of data acquisition and analysis of data. This chapter covers the detailed explanation of the development process of the ECT probe system by using a differential magnetic sensor. The design specification, the project flowchart, the scanning mechanism and circuitry implementation are explained in this chapter.

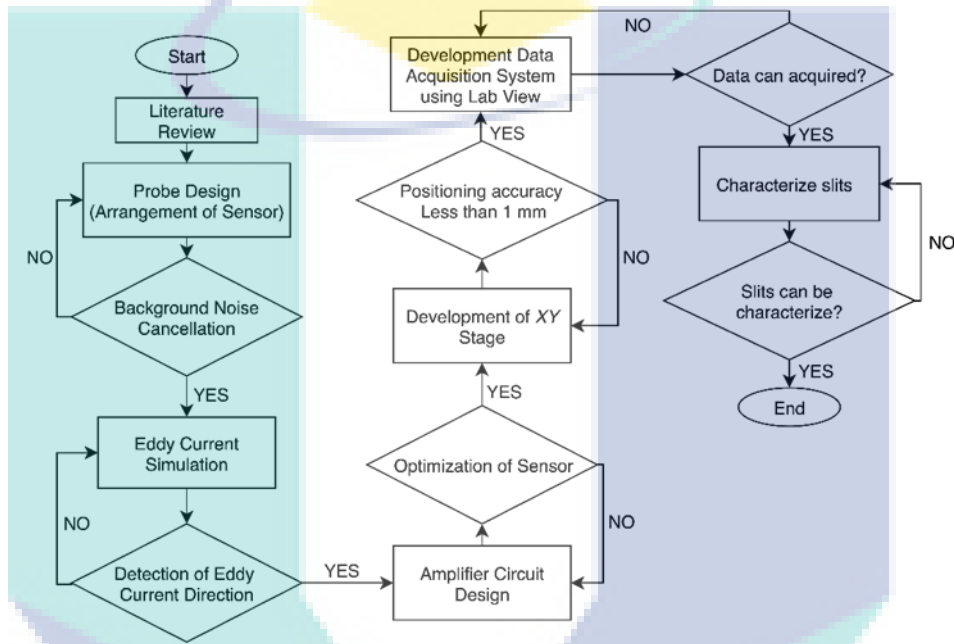


Figure 3.1 Research Flow Chart.

## 3.2 Eddy current principle

### 3.2.1 Principle of operation of eddy current testing

The aim of this section is to describe the eddy current testing principle. In this section the basic theory of eddy current will be investigated. In ECT technique, a coil is excited with sinusoidal alternating current to induced eddy currents in conducting materials. The alternating current that is applied to the coil can be described as follows where  $I_0$  is the amplitude of the alternating current:

$$I(t) = I_0 e^{j\omega t} \quad (3.1)$$

When the alternating current energizes the coil, it creates a time-varying magnetic field based on Biot-Savart's law where  $B_o$  is the amplitude of magnetic field:

$$B(t)_{apply} = B_o e^{j\omega t} . \quad 3.2$$

Here, the alternating current and magnetic field is directly proportional:  $B \propto I$ . The magnetic flux lines tend to concentrate in the middle of the coil (García-Martín et al., 2011). Based on Faraday's law, the eddy currents can be demonstrated as in the equation forms. Faraday found that a time-changing flux density of magnetic induction induces currents in an electric conductor. From the Faraday's law, the electromotive force is proportional to the time-rate change of the magnetic induction flux density  $B$ :

$$V = -N \frac{d}{dt} BS, \quad 3.3$$

Where  $N$  and  $S$  are the number of turns of a coil and  $S$  is its area. The primary magnetic field will penetrate the conductive material and it will generate repeated eddy currents when the coil is near to the ferromagnetic materials. From there, eddy currents will generate the secondary magnetic field that opposes the primary magnetic field. In this study, two sensors are located perpendicularly with the surface of a rectangular sample. The two similar sensors are excited respectively with the same frequency and a phase-delay, thus:

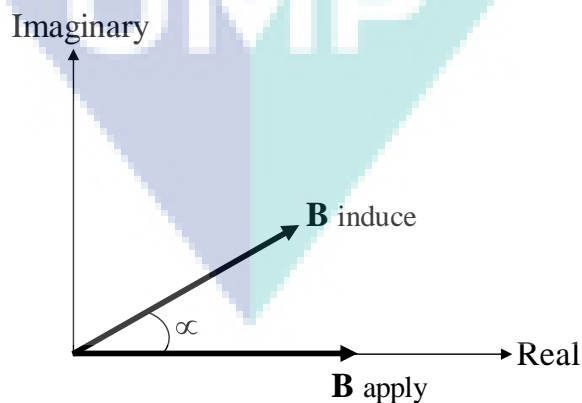


Figure 3.2 Phase lag at the surface,  $\phi$ .

$$B_{induce} = B' e^{j(\omega t + \alpha)} \quad 3.4$$

From equation (3.4):

$$B_{induce} = B' \sin(\omega t + \alpha) + jB' \cos(\omega t + \alpha) \quad 3.5$$

From equation (3.5), the first term shows the real component of magnetic field induced while the second term shows the imaginary component where the information regarding eddy currents are contained. Both components possess information regarding phase lag  $\alpha$  at the surface.

From the sensors, magnetic field vectors can be detected and calculated from two parameters which are signal amplitude and phase. The two parameters can be obtained from a phase sensitive detection using a lock-in amplifier (Tsukada et al., 2006).

The magnetic fields detected by the two sensors can be describe as follows:

$$R = \sqrt{X^2 + Y^2} \quad 3.6$$

$$R = X + jY \quad 3.7$$

$$\theta = \tan^{-1} \frac{Y}{X} \quad 3.8$$

Substitute equation (3.5) into (3.7):

$$\begin{aligned} X &= B' \sin(\omega t + \alpha) \\ jY &= B' \cos(\omega t + \alpha) \end{aligned} \quad 3.9$$

The magnitude of  $X$  and  $Y$  can be detected by the lock-in amplifier and analysed as a magnetic vector with real and imaginary components. In this section the method of producing a vector to represent eddy current flow will be presented and equations that are defining the parameters and affecting the eddy current inspection will be shown. From Maxwell's equations, electromagnetic wave derivations are started with a mathematical development given in differential form (Biddle, 1976):

$$\nabla \times \vec{E} = -\frac{d}{dt} \vec{B}_{apply} \quad 3.10$$

and,

$$\nabla \times \frac{\vec{J}}{\sigma} = -\frac{d}{dt} \vec{B}_{apply}. \quad 3.11$$

Given that,

$$\vec{B}_{apply} = \vec{B}e^{j\omega t}. \quad 3.12$$

If eddy current is assumed to accumulate on a surface, this results to a non-volumetric current where eddy current can be considered in x- and y-directions only:

$$\vec{J} = J_x a_x + J_y a_y. \quad 3.13$$

where:

$$J_x = J_{x0} e^{-\left(\pi f \mu \sigma\right)^{1/2} z} e^{j\left(2\pi f t + \alpha_0 - \left(\pi f \mu \sigma\right)^{1/2} z\right)} \quad 3.14$$

$$J_y = J_{y0} e^{-\left(\pi f \mu \sigma\right)^{1/2} z} e^{j\left(2\pi f t + \alpha_0 - \left(\pi f \mu \sigma\right)^{1/2} z\right)}.$$

From equation (3.14) it shows that the first exponential term is the decay of the induced eddy current as a function of depth,  $z$ , within the material while the second exponential shows that the phase angle delay of the induced eddy current with respect to  $z$ .

### 3.3 System Development

In this research, the ECT system is developed with numbers of components such as a sensor probe, current source for the excitation coil, lock-in amplifier, sensor circuits, and a personal computer for data acquisition and analysis. For the ECT method, using an alternating current is needed, therefore, an alternating magnetic field is



required in order to induced eddy currents in the steel materials. Eddy currents will generate a secondary magnetic field that opposes with the primary magnetic field and will be detected by the sensor. To produce the excitation magnetic field, an excitation coil is fabricated by a 0.1 mm diameter Cu wire. To produce enough magnetic field for the system, the excitation coil is formed with 60-turn square coil with dimension 11.5 mm x 11.5 mm. The schematic circuit of the developed ECT probe is shown in Figure 3.3. The two AMR sensors are separated by a 4-mm baseline and installed in the excitation coil.

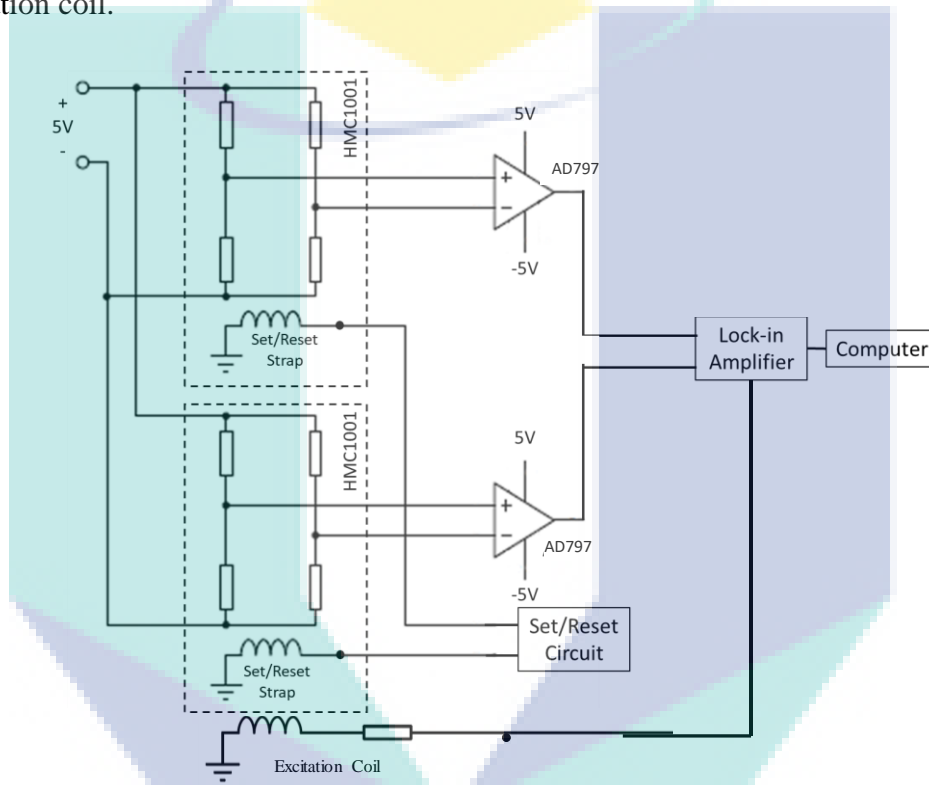


Figure 3.3 The schematic diagram of the developed ECT probe circuit.

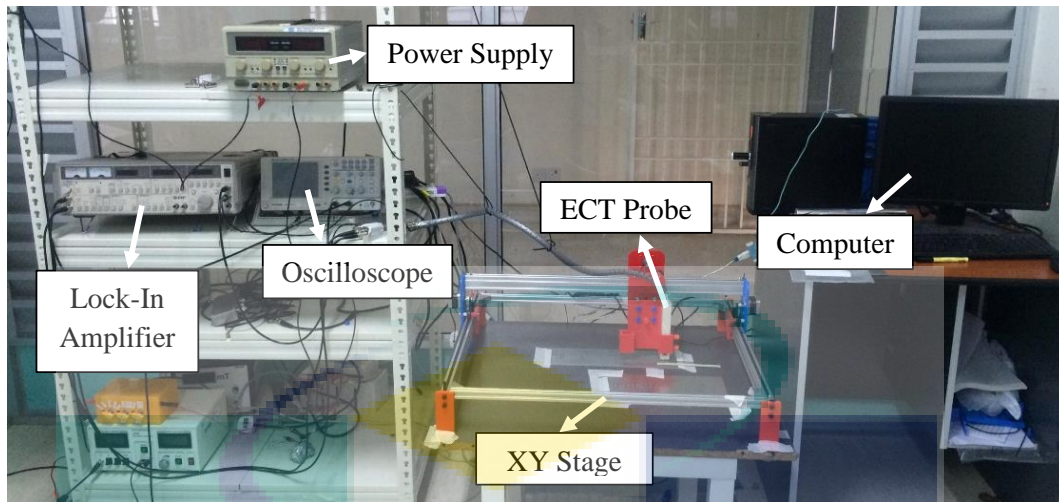


Figure 3.4 Photograph of experimental setup.

### 3.3.1 XY – Stage

For the scanning mechanism, an XY stage is used and a sample can be scanned with a maximum dimension of 45 cm × 60 cm. By using the XY stage, the position of ECT probe can be determined with 0.1-mm resolution of stepper motor. The material of the stage is made from aluminium frames and operates at a power voltage of DC 12 V. The XY stage consists of 3 stepper motors which is one motor for the X-axis and the rest are for the Y-axis. Each of the motor is controlled by a microcontroller Arduino Nano to operate accordingly.

UMP

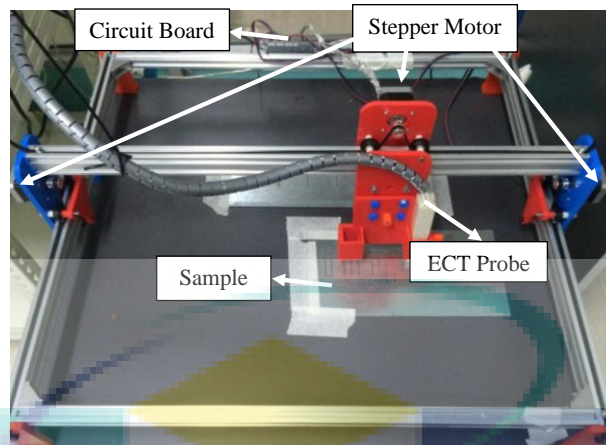


Figure 3.5 Photograph of XY stage.

A licence-free GRBL firmware is upload to the Arduino Nano to control the movement of the XY stage. The GRBL firmware runs on the Arduino Nano after uploading the firmware onto the microcontroller.

The commands that are given to the Arduino are in the form of G-code. G-code is a programming language that commonly used to control automated machine tools. The code varies according to its functions. In this study, LabVIEW is used to send over the instruction of G-code to Arduino. When the instruction has been sent to the Arduino, the arm of the XY stage can be swept in their axes by using a certain motion profile.

The output signal that is captured by the probe must be synchronized to get a reliable result. Before the experiment starts, the probe must be placed at the right position to obtain the data of the sample. The probe will pick up the data at each point according to the motion of the XY stage. Because of that, the XY stage must be set up to operate whenever the data need to be taken. When all the data are successfully taken, the collected data will produce a coordinate-based list of magnetic responses. The XY stage is arranged and programmed to map the magnetic response distributions. The flowchart of the scanning mechanism is shown in Figure 3.6.

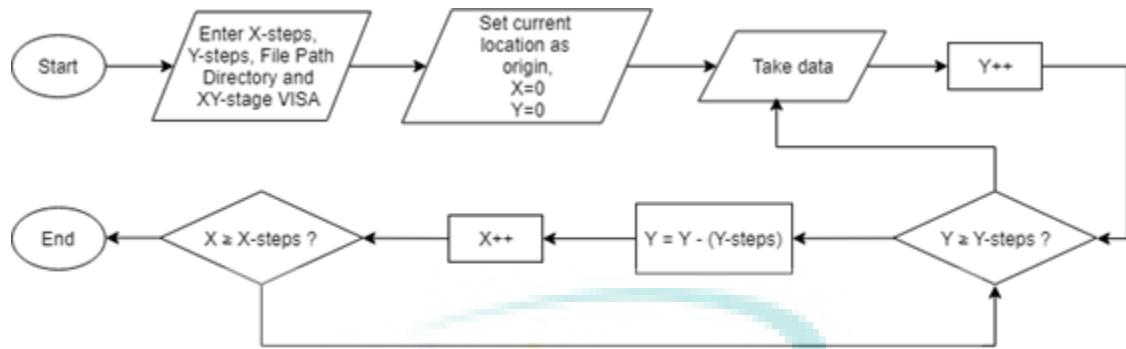


Figure 3.6 Flow chart of scanning mechanism.

### 3.3.2 Magnetic Sensor

The anisotropic magnetoresistance (AMR) sensors (Honeywell HMC1001) are used in the probe's development. One sensor consists of 4 AMR elements to form a Wheatstone bridge they are made from nickel-iron thin films deposited on a silicon wafer and patterned as a resistive strap (Stutzke et al., 2014). This AMR sensor can convert magnetic fields to a differential output voltage. When magnetic field is present, this will make a resistance change at the bridge resistance. The presence of the magnetic field will cause the resistance value in the bridge resistance to change and produce output change at the two midpoints of the bridge. When the bridge is biased with a constant voltage, the resistance change can be identified by the change of the voltage.

Moreover, this sensor is capable to sense magnetic field from  $-2$  gauss to  $+2$  gauss with a resolution of  $27 \mu\text{gauss}$ . Compare to other magnetic sensor, AMR sensor has few advantages such as small, low cost and high sensitivity. Since this research aims to detect sub-millimetre crack surface defects, the usage of small sensor is needed to improve the localization performance of the crack detection. Usually, most of low field magnetic sensors will be influenced by the large magnetic disturbing fields. A Set/Reset strap in the sensor is used in order to restore the sensitivity of the AMR elements.



Figure 3.7 Honeywell HMC 1001

The current path in the AMR elements is set to be  $45^\circ$  inclined to the anisotropy axis of the AMR elements so that a linear characteristic of an AMR sensor with respect to external magnetic field can be obtained (K. Kuijk ; W. van Gestel ; F. Gorter, 1975). When a strong magnetic field is applied to the AMR sensor, this will demagnetize the sensor (Forrest G. West, 1960). Once the AMR sensor demagnetizes, the sensitivity of the sensor will be reduced. To regain back the sensitivity, the Set/Reset strap around the AMR elements is used to reset the anisotropy direction.

The Set/Reset strap functions when a high current pulse is applied to the Set/Reset strap. This will cause the magnetization of the AMR sensor to be recovered, and the AMR sensor is set to a high sensitivity. Although the AMR sensor is small size, low cost and high sensitivity, further improvement can be attained from optimization of the driving circuit.

### 3.3.3 Instrumentation Amplifier (INA)

The AMR sensor consists of Wheatstone bridge, and a supply voltage is required to bias the sensor (He, 2017). Figure 3.8 shows the Wheatstone bridge element of the AMR sensor. The direction of the sensitive magneto resistors 1 and 3 is opposite with the sensitive direction of the magneto resistors 2 and 4. The resistance of the AMR elements changes and causes the unbalanced voltage between the two midpoints of the bridge branches when a magnetic field is applied. Therefore, an instrumentation amplifier is required so that these two points can be measured accurately and reducing the voltage loading effect.

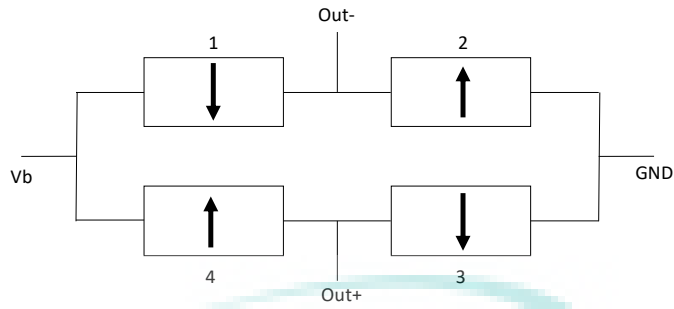


Figure 3.8 Magneto resistive Wheatstone bridge elements of AMR sensor.

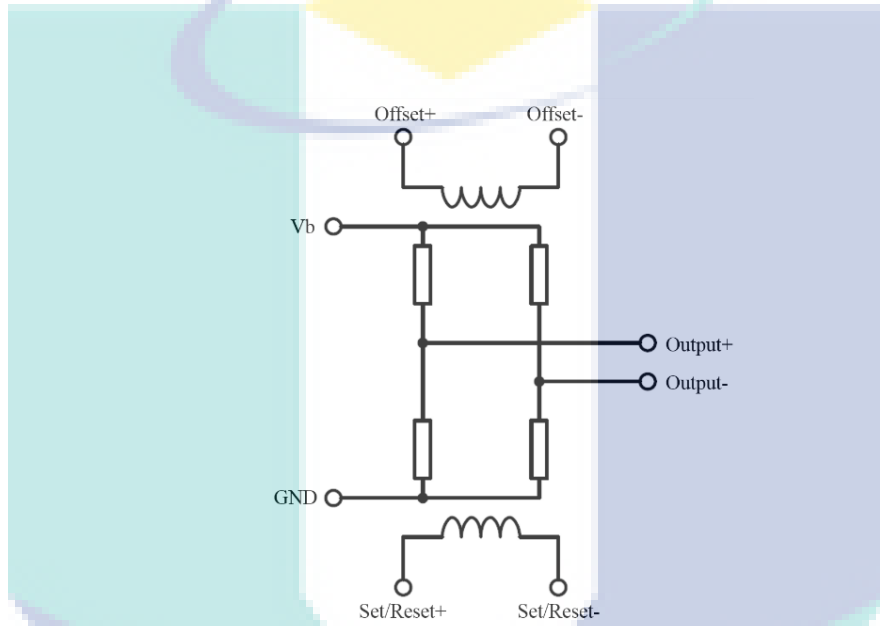


Figure 3.9 AMR sensor circuit.

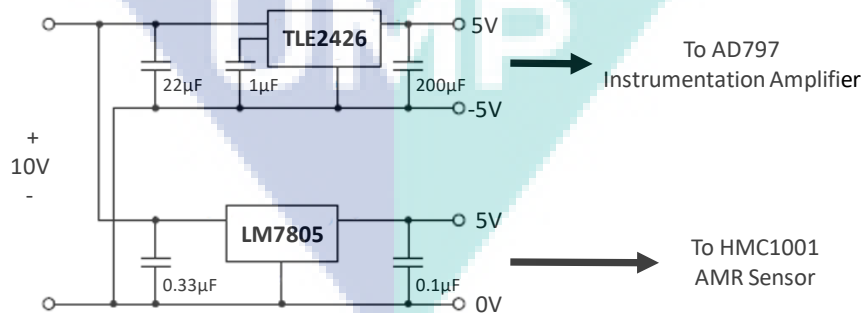


Figure 3.10 Schematic diagram of the power supply circuit.

The bridge output of the AMR Wheatstone bridge is measured by an instrumentation amplifier (INA) to reduce the loading effect. A high sensitivity detection unit is obtained by fabricating a home-made INA by using 3-operational

amplifier topology. AD797 operational amplifiers are used to achieve a low noise INA. To secure a wide dynamic range of the INA frequency response, a gain of 99 is chosen. This will also cause a satisfactory amplification output between  $-5\text{ V}$  and  $5\text{ V}$ . A voltage rail splitter of TLE2426 is used to power the instrumentation amplifier and by applying a linear voltage control, the AMR sensors are biased at  $5\text{ V}$ . Finally, the lock-in amplifier is used to process the signal that comes from the instrumentation amplifier for a phase sensitive detection.

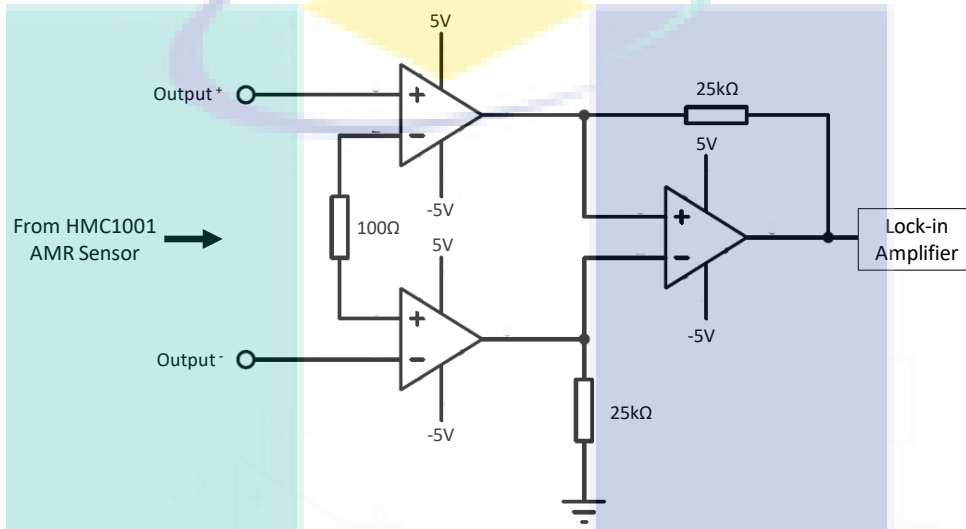


Figure 3.11 Schematic Diagram of home-made Instrumentation Amplifier Circuit.

### 3.3.4 Set/Reset Circuit

To restore the high sensitivity of the AMR sensor, a simple Set/Reset method is used in this system. A Set/Reset circuit is developed to apply a high current pulse into the Set/Reset strap so that the sensitivity of the AMR sensors is maintained during measurements. If a strong external magnetic field is applied to the sensor, the sensor is possible to be strongly magnetized and saturated. In order to recover the sensitivity, this requires the AMR sensor to be demagnetized by having a set or reset. Besides that, the set or reset is necessary to enhance the magnetic domains of the AMR elements for the most sensitive performance. Plus, the domains for extraction of bridge offset can be flipped under changing temperature conditions. Figure 3.12 shows the output of a voltage divider consisting of two  $3\text{-k}\Omega$  resistors is fed to a push button that are connected to ground at the other end.

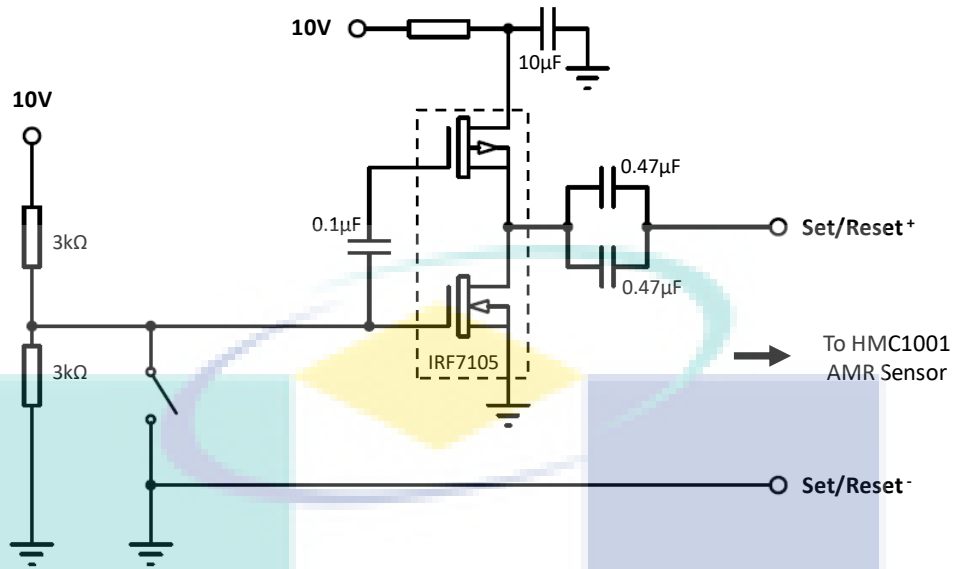


Figure 3.12 Schematic Diagram of Set/Reset Circuit.

The required voltage supply for this circuit is 10 V. The signal source to perform set/reset is the voltage pulse of 5 V. The 5-V pulse can fully turn off/on of the MOSFET IRF7105. To give the pulse, a mechanical switch is used to set and reset the circuit. The IRF7105 contains both N-channel and P-channel MOSFET and has the electrical characteristics needed in this circuit.

### 3.3.5 Eddy Current Testing Probe

The main objective of the ECT probe in this research is to detect a surface flaw. Therefore, a small size of an ECT probe is advantageous because it can be used to measure a small or a difficult shape of cracks. Since AMR sensor is relatively small, this gives advantages in developing the ECT probe while resolving the magnetic noise problem in conductive materials.

Firstly, before proceeding to design the ECT probe, the designer needs to make sure that the size of the probe will fit with the size of the testing surface. Not only that, the probes must be able to produce eddy currents that will be disrupted by cracks. After taking all this into consideration, then they can proceed to develop the ECT probe. There are few types of operation mode in ECT such as absolute, difference, reflection and hybrid modes.



The operation mode can be referred by the way of the coils or sensors are wired and interfaced with the test equipment. In this study, two AMR sensors with each in absolute mode are used and combined to form a differential technique. This results to a dual-channel sensor probe. The dual-channel sensor probe consists of two AMR sensors that have been inserted inside an excitation coil. The two AMR sensors are attached together and separated by a 4-mm baseline to detect the differential signal. One excitation coil with a dimension of 11.5 mm × 11.5 mm is used to produce a magnetic field. Figure 3.13 below shows the structure of the ECT probe. During the experiment, a metal plate is placed 1 mm below the sensor probe, as shown in Figure 3.13. In the experiment, sinusoidal currents with an amplitude  $I_0 = 4$  mA and few values of frequencies are supplied to the excitation coil. The output voltage of the AMR sensors is amplified with the amplifier and then connected to the lock-in amplifier.

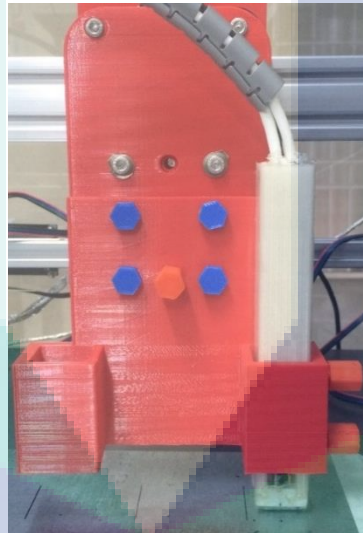


Figure 3.13 (a) Photograph of the fabricated ECT probe. (front view).

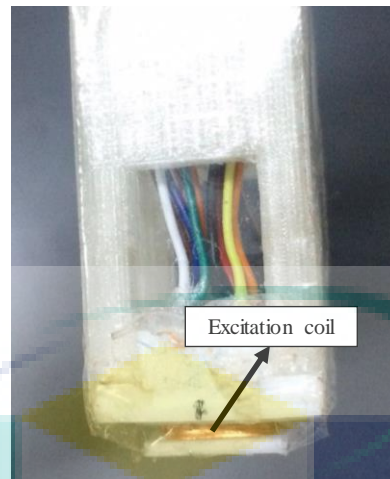


Figure 3.14 Photograph of the fabricated excitation coil.

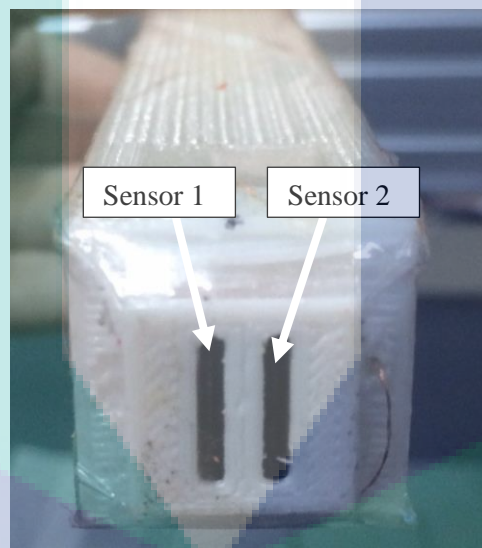


Figure 3.15 Photograph of the fabricated ECT probe. (bottom view).

During the detection process, the ECT probe is set to be 1 mm higher from the test surface. As mention earlier, the size of the probe is determined by the proposed use of the ECT probe. If the probe has a large size, that means that it is useful to test big area. However, this limits the ability to detect small defects. Hence, the size of the ECT probe should be designed properly, and the resolution of the probe for defects should meet with the size of defects (Biddle, 1976).

### 3.4 Detection Technique

In this study, the new differential eddy current testing sensor is proposed which consists of two magnetic sensors with the excitation coil. In the beginning, this research started with an AMR sensor which means it only contained a single absolute probe. This sensor module was used in the first attempt of the study to integrate the magnetic field sensor into the ECT probe. Due to some specific issues such as, when the scanning process was conducted, it is found that the measured signal contained metal and background signals which could be assumed as noises. By using one sensor, it was observed that the background signals interfered during the scanning process.

For this reason, to make sure the background signal fades away, a new method is proposed by using two magnetic sensors. This method is called as differential analysis using dual-channel sensor probe. The output signal is analyzed using a component of magnetic vector,  $\vec{B}$  which is  $B_z$  through the lock-in detection. In the lock-in detection, a reference signal for the phase sensitive detection is required.

In a conductive material, if the magnetic and the physical properties are in the same conditions, then the reference signal will remain the same at all locations of the material. Unfortunately, if there is a distribution in the magnetic properties in the material, then the reference signal will be different in each location since the eddy current is related to conductivity,  $\sigma$  and permeability,  $\mu$  of the material. The reference signal is used to measure the phase delay of the eddy currents. Due to this, it can cause false detection even there is no crack in the material if the phase signal is incorrect.

To improve this kind of obstacle, instead of using location as the reference technique, sensor 1 is proposed as the reference signal which means that the reference signal will change according to location of sensor 1. By this technique, the dependency of distribution of the magnetic properties can be reduced. However, the disadvantage of using this method is the data of the absolute reading and the local data of the properties of magnetic and physical properties of the sample are lost because of the differential technique. But in this study, this will not be an issue because the interest of this study is to identify the change of eddy currents due to crack or defects in materials.

Moreover, the arrangement of the two sensors plays an important role during the scanning process. Figure 3.16 shows the arrangement of the sensors in the ECT probe where the sensitive axis of the sensors is located at the centre of sensors that move horizontally. If the sensors are arranged as shown in the Figure 3.16 (a), the probe will

detect signal in a same direction where the magnetic vector signal cannot be cancelled due to the different lift-off. But if the sensors are arranged according to the Figure 3.16 (b), surely there is no differential signal will take place. Because of that, the arrangement of the sensors has been selected as in the Figure 3.16 (c). This arrangement can detect the difference of magnetic fields between two locations to achieve the differential technique.

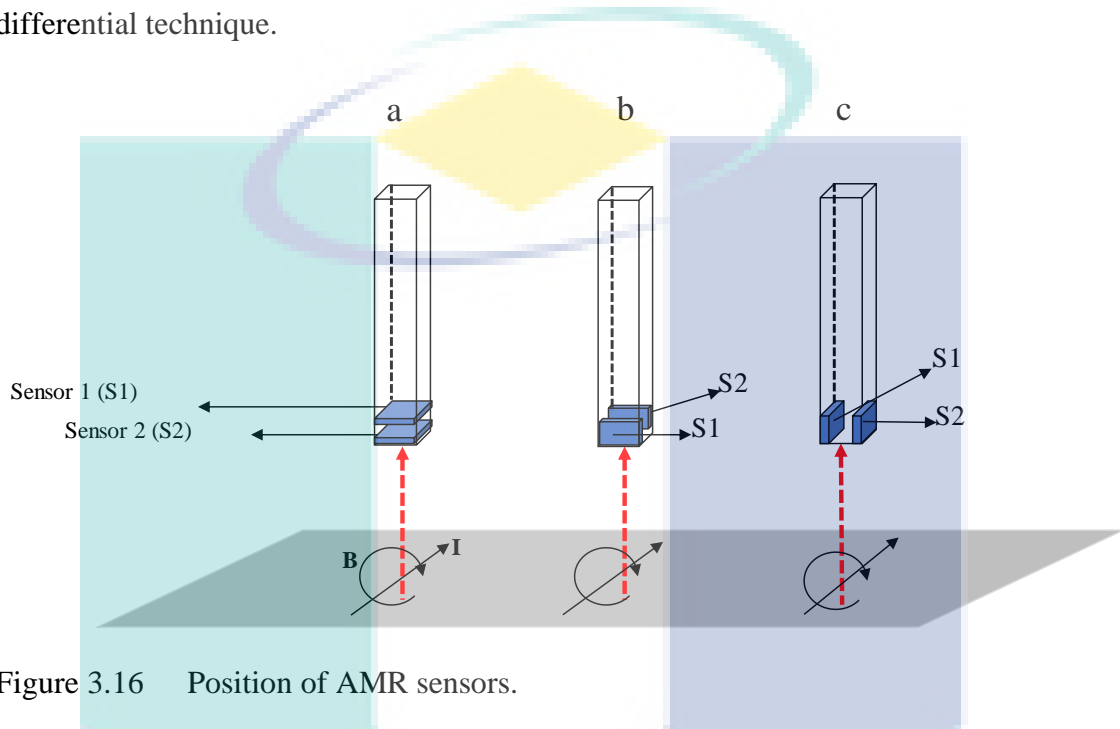


Figure 3.16 Position of AMR sensors.

During line scanning of the cracks, the probe runs in the direction of the  $x$ -axis. This probe works as detection of eddy current when the eddy current stumbles upon something else. The detected signal will change by following the flow of the current. For an explanation, a current that is in  $y$ -direction will produce two magnetic fields in  $x$ - and  $z$ - directions,  $B_x$  and  $B_z$ , respectively. If the crack in the material is in  $y$ -direction, this will block and redirect the current to the  $y$ -direction. According to Maxwell equation, the  $y$ -directed current can be determined by measuring the magnetic fields that are perpendicular to current. To proof this, Maxwell equations have been derived in the next paragraphs and a theoretical simulation is performed to facilitate the understanding.

During the scanning process, an AC magnetic field will be applied to the conductive samples. Then, a magnetic response from sensor 1 ( $S_1$ ) will be produced. In  $S_1$ , the signal consists of a large magnetization signal  $S_{mag,1}$  due to the magnetization curve M-H characteristic (M M Saari et al., 2015) and small eddy current induced signal

$S_{eddy,1}$ . As mentioned earlier, the output signal will be analysed using the lock-in amplifier with two components (real part,  $S_{mag}$ ; imaginary part,  $S_{eddy}$ ). If there is an anomaly shape presents in the sample, a phase delay in  $S_{eddy,1}$  will come out where the delay is from the induced eddy current that takes a longer path to enclose its loop. At that point, by using  $S_1$  as the reference signal, the intensity of the differential vector  $S_{eddy,1} - S_{eddy,2}$  is calculated. Since  $S_{mag,1}$  is diminished by the means of difference between the sensors, the phase delay of the small eddy current can be identified. It should be emphasized that the baseline of the sensor and the size of the excitation coil have a huge effect to  $S_{mag,1}$  since the magnetic properties' distribution may exists over the sample.

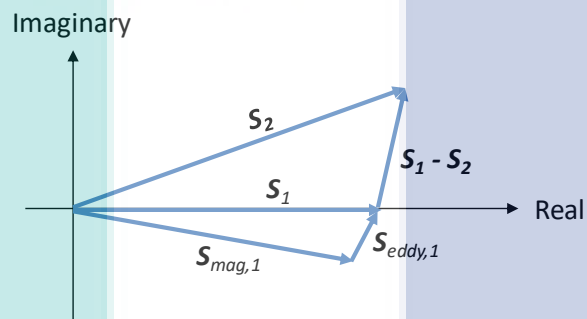


Figure 3.17 Differential vector of the measured magnetic signals.

### 3.4.1 Simulation of Magnetic Field Distribution Produced by A Line Current

To verify the distribution of magnetic field produced by a line current, a simulation is performed. Figure 3.18 below shows the simulation of magnetic field distribution that is produced by a line current having  $x$ - and  $y$ - directions.

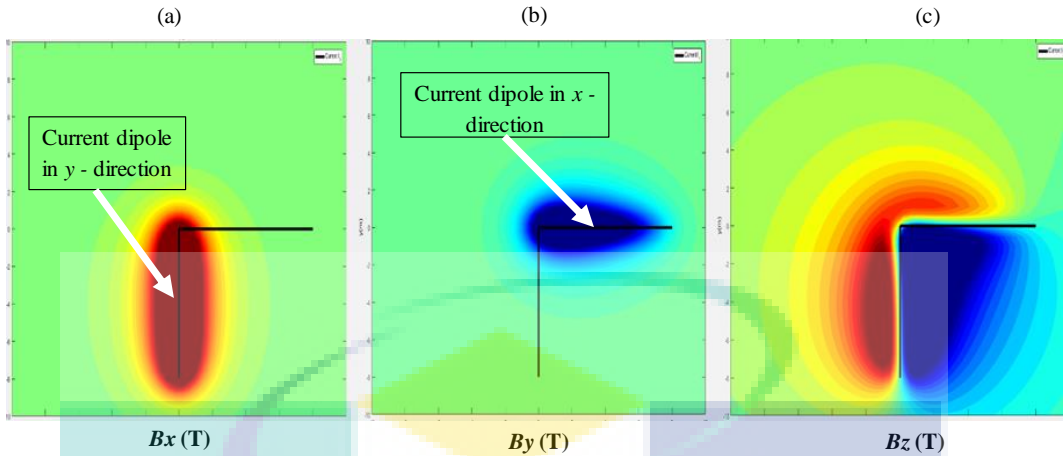


Figure 3.18 Magnetic field distribution that produced by a line current in  $x$ - and  $y$ -direction a)  $B_x$ . b)  $B_y$ . c)  $B_z$ .

In the simulation, the current dipole is created in  $x$ - and  $y$ -directions. From Figure 3.18, the current dipole is shown as the black line. According to Bio Savart's law, the current dipole will create a magnetic field where  $B_x$ ,  $B_y$  and  $B_z$  is the components of the magnetic field. From the Figure 3.18 (a) and (b), it can be shown that each direction of the current dipole has their own magnetic field distribution characteristics. While, for Figure 3.18 (c) it shows that the magnetic field distribution  $B_z$  covers all areas for both  $x$ - and  $y$ -directions. Therefore, it can be concluded that it is more convenient to take  $B_z$  into consideration during the probe development as it can cover different direction of the current.

Figure 3.19 (a) and (b) show the differential of magnetic distribution  $B_z$  with respect to the current dipole. Similar with Figure 3.19 (a) and (b) where each of the current dipole has their own magnetic distribution characteristics. The differential signal of the  $B_z$ -component is equivalent to a gradient of  $\Delta B_z/\Delta x \approx \partial B_z/\partial x$  or  $\Delta B_z/\Delta y \approx \partial B_z/\partial y$ . Figure 3.19 (c) shows the arrow map where the  $a_x$  and  $a_y$  are unit vectors. From this figure it shows clearly that the location and direction of current in every direction can be estimated by the vector  $\mathbf{a}$ , which can be determined by measuring  $\partial B_z/\partial x$  and  $\partial B_z/\partial y$ .

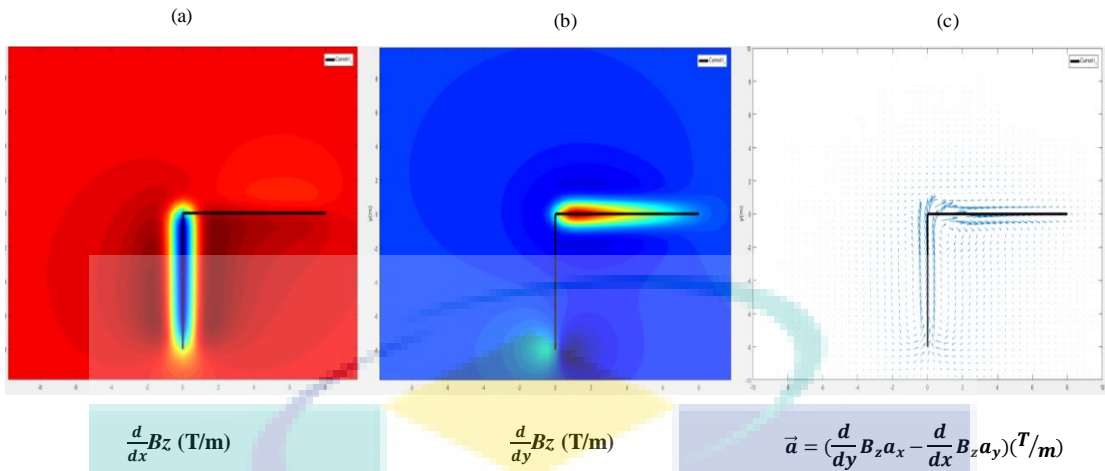


Figure 3.19 a) Differential of magnetic distribution respect to position of line current in  $x$  - direction. b) Differential of magnetic distribution respect to position of line current in  $y$  – direction. c) Arrow map of the reconstructed current dipole.

### 3.5 Measurement Procedure

The ECT system works by supplying current to the excitation coil and producing the excitation magnetic field (primary magnetic field  $B_{primary}$ ) in order to induce Eddy's currents in steel components. If the coil is placed near to the sample, eddy currents will be generated in the conductive material. Then, these eddy currents will generate secondary magnetic fields  $B_{secondary}$  where these magnetic fields are detected by the sensors.

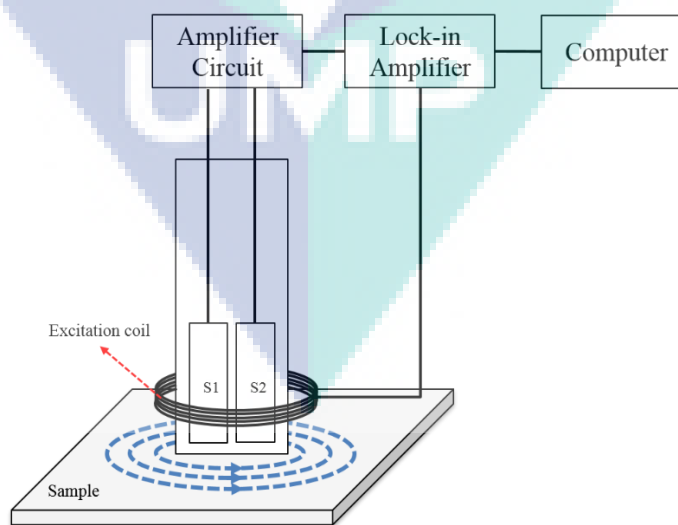


Figure 3.20 Schematic diagram of experimental setup.



If there is any flaw in the sample, this will cause a change in eddy current where it can be measured by change in the phase and amplitude of the measured signal of the secondary magnetic fields. This translates to a different response of secondary magnetic fields according to the flaw characteristics. The AMR output signal will be detected through the lock-in amplifier and the magnetic field distribution of the sample will be captured and recorded in LabVIEW. The lock-in amplifier will give two outputs which are the magnitude of real (in-phase) and imaginary (out-of phase) components of the detected magnetic responses. The image mapping of the magnetic response characteristics will be constructed in LabVIEW and the result will be analyzed to identify the property of the flaw.

### **3.6 Preparation of sample**

To evaluate the effectiveness of the ECT probe, artificial slits are laser-engraved on a 2-mm galvanised carbon steel plate. The galvanized carbon steel plate has been widely used in industries because its good performance to withstand rusting. However, the galvanized steel plate is a ferromagnetic material where a previous study claimed that ECT technique was difficult to apply to ferromagnetic materials (Tsukada et al., 2018) because the magnetic field responses contain both eddy current and strong magnetization signals. The test samples are 2-mm thick with different slit-like artificial cracks. Few types of samples are prepared to evaluate the crack detection performance. A fibre laser marking machine is used to create the artificial slits as shown in Figure 3.21. This machine has been designed for direct parts marking and unique identification applications on metals.



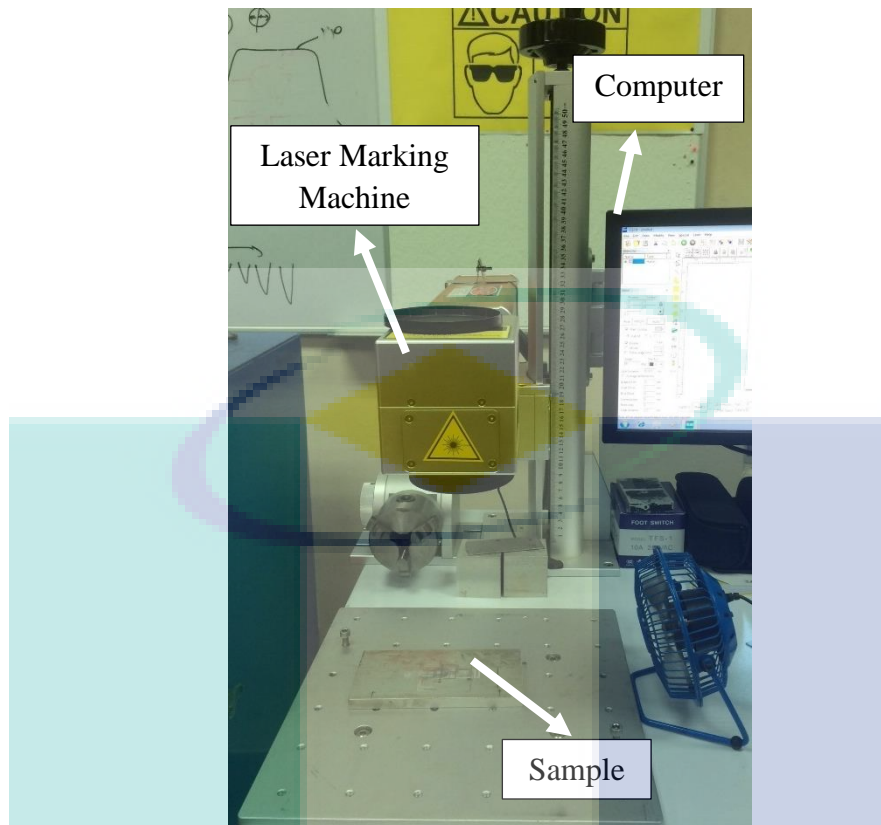


Figure 3.21 Photograph of the laser marking machine.

### 3.6.1 Different depth of slits

The first sample is engraved to form artificial slits with different depths. Before the laser marking machine starts to engrave the sample, the parameters of the machine need to be set up first. For the whole process of the engraving, the parameters are the same. The frequency, power, and speed have been set to 20 kHz, 70% and 500 mm/s, respectively. In this case, the only difference is the depth of the slits where the laser marking machine needs to set the different numbers of engraving loops and the width of slits is set to 0.2 mm.

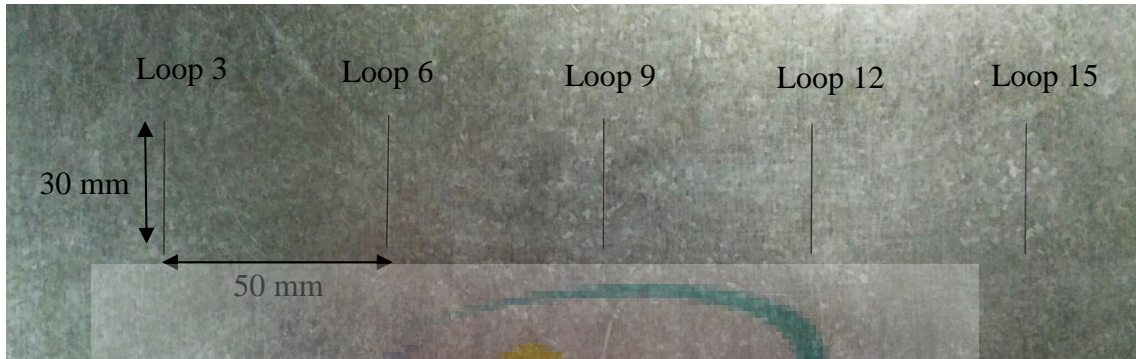


Figure 3.22 Artificial slits (defects) of depth from  $210\ \mu\text{m}$  to  $500\ \mu\text{m}$  on a galvanized.

Figure 3.22 shows the artificial slits with different depths. The difficulty of using the laser-engraving machine is the depth of the slits cannot be directly measured. Therefore, to measure all those slits, a special equipment is used which is 3D Measuring Laser Microscope OLS5000 by Olympus. This microscope can not only measure the depth, but it can perform a laser light scan over the surface of the sample where it can provide the enlarged images of micro-scale features and capture the shape measurements of the surface roughness, steps, and other features. Figure 3.23 shows a photograph of the 3D Measuring Laser Microscope OLS5000. To investigate the depth of each slit, this equipment is used. Figure 3.24 shows the features and the surface roughness of the slit.

From the Figure 3.24, it shows that the slits are uneven, and this might be due to the engraving process. From Figure 3.25, it shows the depth of the slit, and since the slits are uneven, therefore, the deepest slit is chosen as the depth of the engraved slits. From the Figure 3.26, the depth can be identified as  $210.06\ \mu\text{m}$  where this is the least depth compare to other slits. This slit takes only 3 loops of the laser engraving machine to engrave the slit. Next, Figure 3.27 shows that the depth of the slit is  $337.371\ \mu\text{m}$  while Figure 3.28 shows the depth of slit of  $360.176\ \mu\text{m}$ .

If the laser engraves the slit for 12 loops, the depth has been measured to be  $402.512\ \mu\text{m}$  as shown in Figure 3.29. Finally, the last slit is engraved 15 loops and the depth are given by  $513.925\ \mu\text{m}$ . From all the figures, the depth is not consistent since the slits are uneven. Therefore, Figure 3.31 shows the average of the depth of each single slit.



Figure 3.23 Photograph of the 3D Measuring Laser Microscope OLS5000.

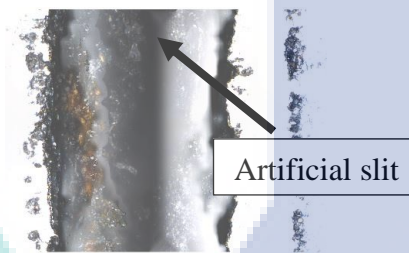


Figure 3.24 Image of slit when zoomed in with 3D Measuring Laser Microscope OLS5000.

UMP

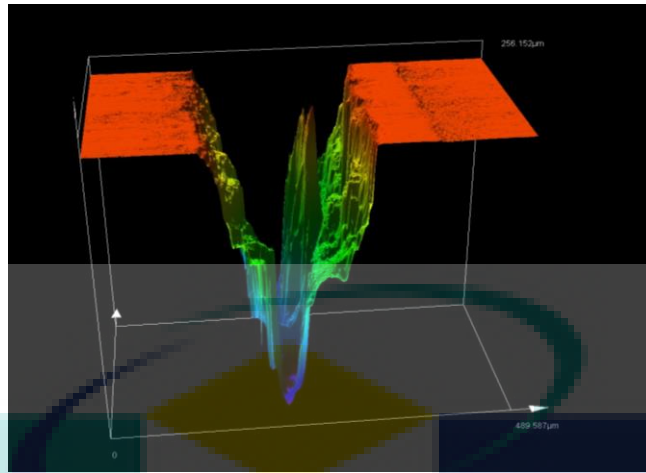


Figure 3.25 2D image of the slit.

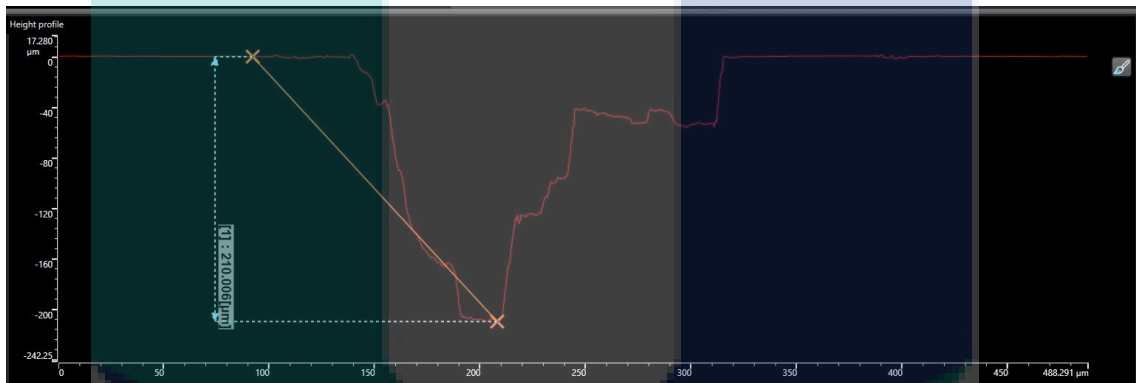


Figure 3.26 The depth of the slit that has been engraved with 3 times loop.



Figure 3.27 The depth of the slit that has been engraved with 6 times loop.

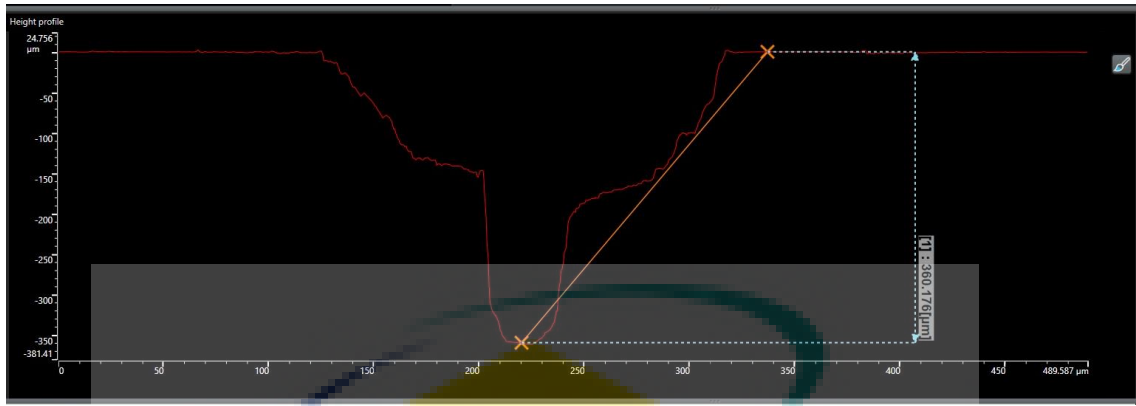


Figure 3.28 The depth of the slit that has been engraved with 9 times loop.

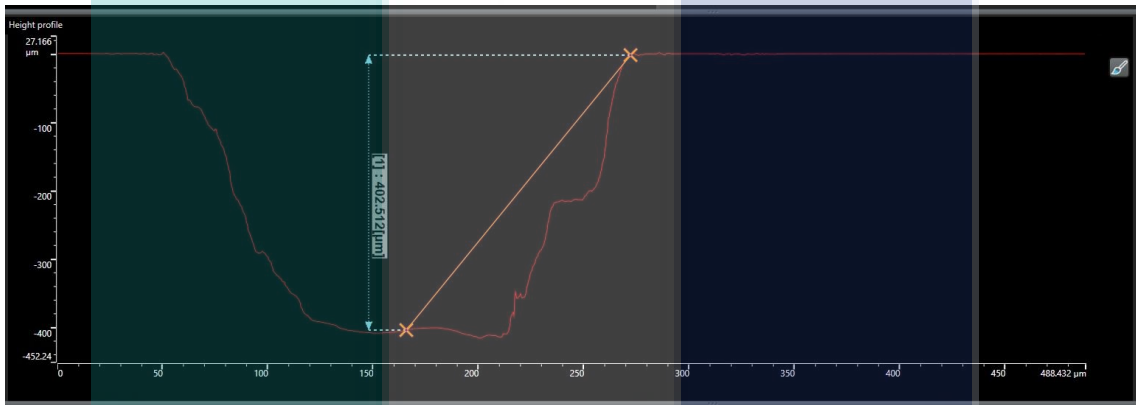


Figure 3.29 The depth of the slit that has been engraved with 12 times loop.

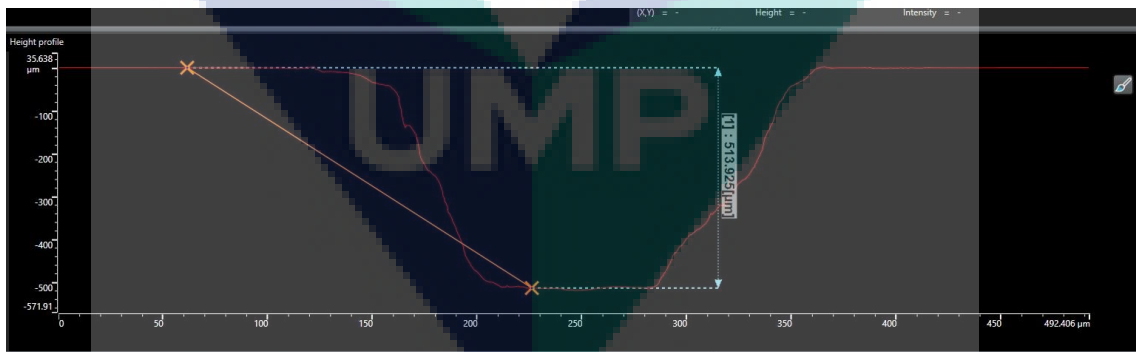


Figure 3.30 The depth of the slit that has been engraved with 15 times loop.

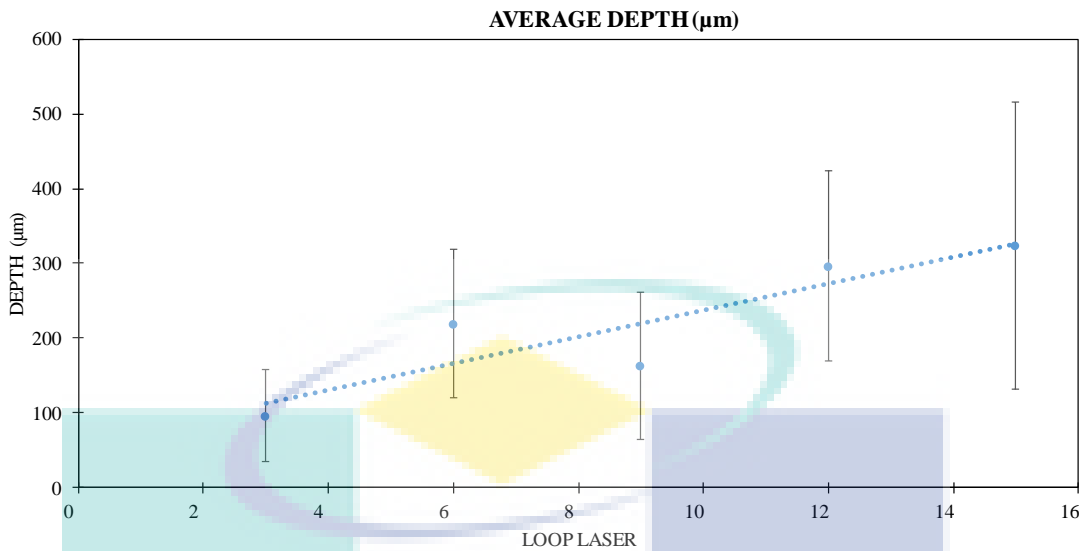


Figure 3.31 Average depth of different slits.

### 3.6.2 Different width of slits

Figure 3.32 shows slits on top of one of the samples where they are separated by an interval of 30 mm. This slit is engraved with different width but same depth. The width of the slits starts from 0.5 mm to 1 mm. These artificial slits are engraved on a 2 mm galvanized carbon steel plate. The parameters of the laser engraved machine are still the same with the previous sample. The red horizontal dashed line as in Figure 3.32 shows the line scanning direction of the ECT probe.

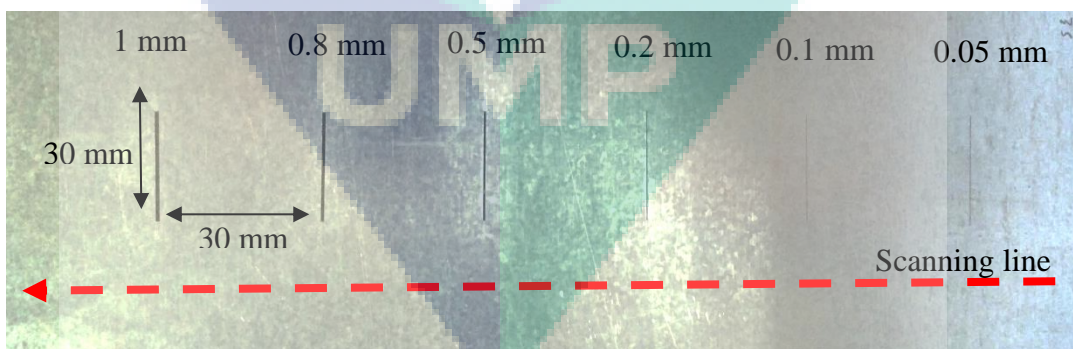


Figure 3.32 Artificial slits (defects) of width from 1 mm to 0.05 mm on a galvanized carbon steel plate.



### 3.6.3 Different length of slits

The third sample is engraved with the slits that have different length as shown in Figure 3.33. The depth and width of each slits are made to be same in which the depth is engraved for 15 loops and the width is set to be 0.2 mm for all slits. The length of slits is from 10 mm to 50 mm.

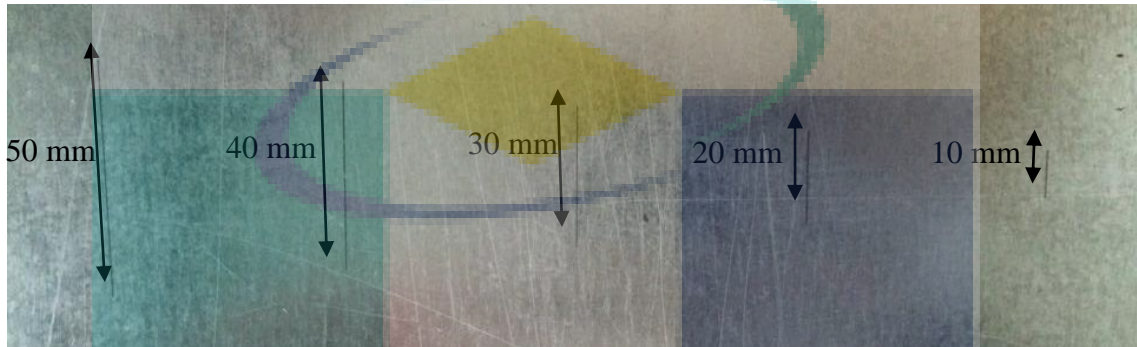


Figure 3.33 Artificial slits (defects) of length from 50 mm to 10 mm on a galvanized carbon steel plate.

### 3.6.4 Complex shape of slits

Different from other samples, the next sample is engraved with a complex shape of slits where it is a combination between the  $x$ - and  $y$ -directed (axial and circumferential) slits. The slits are engraved with the letter 'U', 'M', and 'P' as shown in Figure 3.34. The width of each slit is 1 mm. Each of the letters is separated by an interval of 30 mm.



Figure 3.34 Artificial slits (defects) with shapes of letter 'U', 'M' and 'P'.

### 3.6.5 Backside slits

The final sample has a different depth of slits, but it is different from the previous one because this time the depth is engraved deeper where this sample is intended for backside slit detection's purpose. The depth of the slits is from 1.0 mm to 1.8 mm and it is engraved on top of a 2-mm galvanized carbon steel plate. Each of the slits has 1-mm width and separated by an interval of 30 mm while the length of the slits is 30 mm as shown in Figure 3.35.

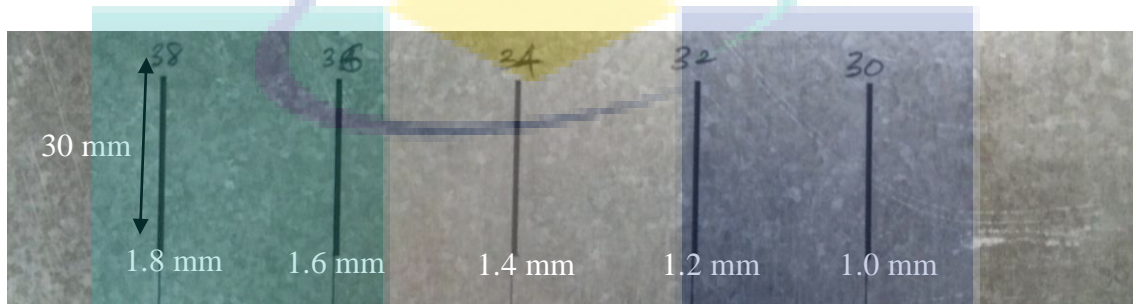


Figure 3.35 Artificial slits (defects) with depth from 1 mm to 1.8 mm on a galvanized carbon steel plate.

## 3.7 Summary

This chapter focuses more on developing an ECT probe where the principle of operation of eddy current testing is investigated and the equations that define the parameters affecting the eddy current are derived and studied. The developed probe consists of two AMR sensors where these sensors are chosen as a detector device because of their small size which is given by  $11 \times 4 \text{ mm}^2$ . The small size of the sensor is beneficial to develop a small probe to detect narrow cracks so that localization performance of the crack detection can be improved. The most important point which makes these sensors suit to the probe is because their sensitivity. They can detect one part of 10 thousand parts smaller than earth magnetic field using 1-Hz frequency bandwidth. The differential detection technique is implemented to reduce strong magnetization signal caused by the ferromagnetic materials.

For the hardware development, the measurement circuits are designed where they contain the homemade instrumentation amplifier, power supply circuit and set/reset circuit. The set/reset circuit is implemented so that the sensitivity of the AMR sensors can be maintained. To measure the output of the AMR sensors, the homemade



instrumentation amplifier is used to measure the voltage difference between the two midpoints of the sensor's bridge. The output signal from the instrumentation amplifier will be analysed by the lock-in amplifier. Finally, for data acquisition and analysis, Lab view is used to interact with the lock-in amplifier.

To determine the optimum arrangement of the sensor, the simulation of magnetic field distribution produced by the line current is conducted by using Bio Savart's law. Based on the simulation, the ECT probe is developed where the two AMR sensors are positioned side by side with the distance of 4 mm. Then, the sensors are inserted into the excitation coil with an  $11.5 \times 11.5 \text{ mm}^2$  area and 60 turns. The probe is attached to the XY stage to obtain the map of the magnetic responses across the slits' area. A set of samples with different parameters of artificial slits is prepared using the laser engraving machine to study the performance of the ECT probe during surface and backside scanning.

The logo of UMPA (Universiti Malaysia Perlis) is a large, stylized shield shape. It is divided into four quadrants by a white cross. The top-left and bottom-right quadrants are light blue, while the top-right and bottom-left quadrants are light purple. The letters 'UMPA' are written in white, bold, sans-serif font across the center of the shield.

UMPA

## CHAPTER 4

### RESULTS AND DISCUSSION

#### 4.1 Introduction

The performance of the ECT probe will be discussed in this chapter where the detection of artificial slits is used as a preliminary step before advancing to assess real cracks or flaws in steel parts. This chapter focusses on the analysing of the output signal from the ECT probe system to estimate and visualize the parameters of the artificial slits with respect to different measurement parameters.

#### 4.2 Simulation of Magnetic Field Distribution Produced by A Line Current

This section will explain more about the theoretical verification of the developed probe. Therefore, for a more understanding on the magnetic distribution produced by a line current that flows in  $x$ - and  $y$ - directions, a simulation work has been done. As a first step towards finding the solution to estimate the eddy current strength and direction, a basic current element used in the eddy current technique was used to simulate the current sources in the metal. This section focusses on reproducing the current map by simulating the dipole current. Moreover, this study would show the effect of lift-off by manipulating the distance between the probe and the line current where the lift off,  $z$  was fixed from 1 mm to 5 mm and the difference can be shown from Figure 4.1.

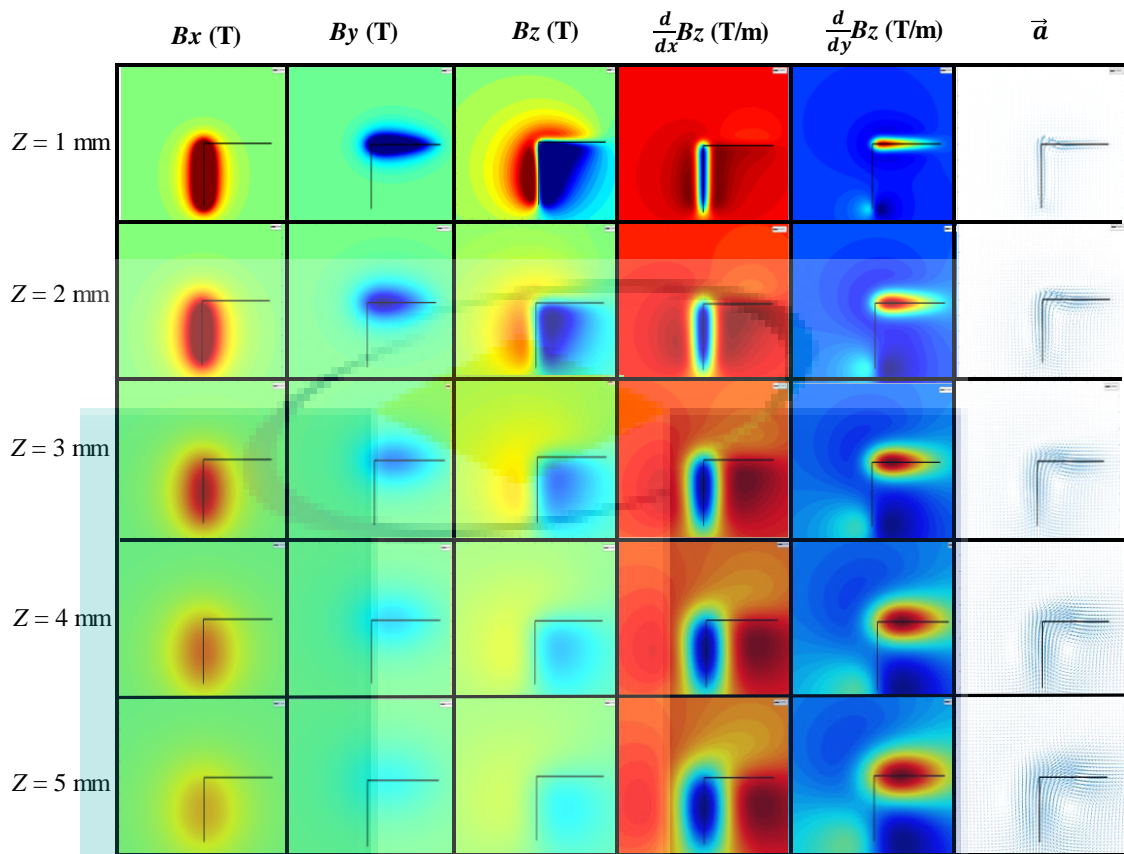


Figure 4.1 Comparison of simulation of magnetic field distribution produced by a line current.

From the simulation, a conclusion can be made where the nearer the detection unit to the material, the easier the sensor could detect the changes of eddy current. The detection sensor focused more on crack area when the probe was near to the line current. The farther the sensor with the sample, it was more difficult to detect the changes of current on the sample and the distribution intensity started to fade and broaden. Figures 4.2 to 4.11 show clear images of the magnetic distribution with different lift off.

Figures 4.2 to 4.11 show the lift off effect toward the magnetic field distribution. This simulation implied also that the skin effect to the magnetic field distribution could be related by investigating the magnetic field distribution at different lift-off, *i.e.*, the difference of depth level of the eddy current was equivalent to different level of lift-off. Moreover, the property of the magnetic field around the shapes represented by the simulated dipole current was also investigated.

#### 4.2.1 Different Depth (Z)

*Lift off, Z = 1mm*

The current line is illustrated as the black line shown in the Figure 4.2. A current dipole model was assumed as the induced eddy current, having  $x$ - and  $y$ - directions, and the accumulation of the current dipoles was equivalent to the black line in the figure. The total magnetic field of the dipole was produced by the current element of the dipole itself. The current dipole was a directed line element which generated the magnetic field in its surrounding. The Figure 4.2 shows the magnetic vector,  $\vec{B}$  produced by the current dipole where it contained  $B_x$ ,  $B_y$  and  $B_z$  components. From the distributions of  $B_x$ ,  $B_y$  and  $B_z$  as shown in Figure 4.1, it could be said measurement of the  $B_z$  component could give both  $x$ - and  $y$ - direction information of the dipole current.

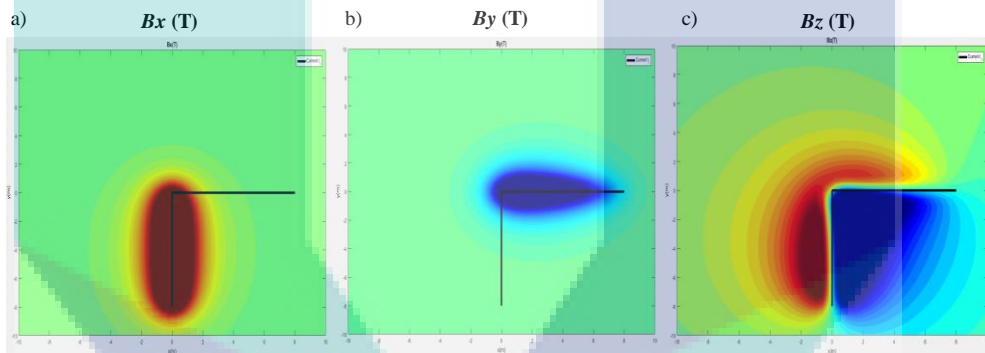


Figure 4.2 Magnetic field distributions produced by a line current in  $x$ - and  $y$ -directions with a lift off of 1 mm a)  $B_x$ , b)  $B_y$ , c)  $B_z$ .

From the derivation of equations that has been discussed in chapter 3,  $J_y$  and  $J_x$  could be estimated by using  $B_z$  where  $B_z$  contains both information on  $J_y$  and  $J_x$ . Then, using another alternate form to display the current vector, the Cohen-Hosaka transformation (equation 3.14) was used and shown by arrows in Figure 4.3 (c).

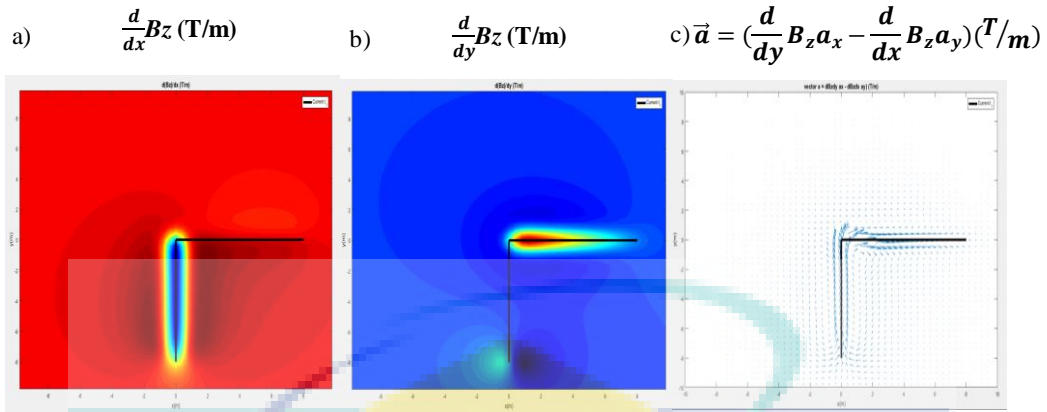


Figure 4.3 Magnetic field distributions produced by a line current in  $x$ - and  $y$ -directions with a lift off of 1 mm. a) Differential of magnetic distribution respect to position of line current in  $x$ - direction. b) Differential of magnetic distribution respect to position of line current in  $y$  – direction. c) Arrow map of the reconstructed current dipole.

From Figure 4.3 (c), it could be said that a similar information was contained in the arrow map as in the 2-D magnetic map of  $B_z$ . By using the arrow map information, the presence of the dipole combinations could be estimated. Each arrow was defined to be the vector,  $\vec{a}$ . Moreover, not only the flow of current could be estimated but the intensity of the signal with varying depth also was also observed by the size of the arrow. The lift off was 1 mm between the line current and the ECT probe in Figure 4.4 and 4.5. From Figure 4.4 and 4.5, the maps showed a strong intensity at each of the current dipole. This was caused by the fact that the nearer the sensor or detection unit towards the metallic sample, the easier the sensor could detect the changes of eddy current. Moreover, when the probe was near to the sample, the magnetic field that is produced by the eddy current was more focused in the crack area.

Lift off,  $Z = 2 \text{ mm}$

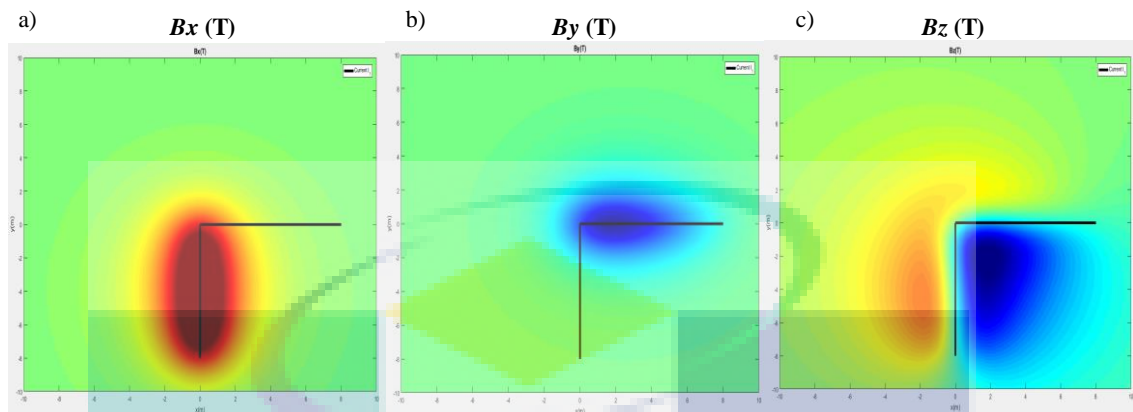


Figure 4.4 Magnetic field distributions produced by a line current in  $x$ - and  $y$ -directions with a lift off of 2 mm. a)  $B_x$ . b)  $B_y$ . c)  $B_z$ .

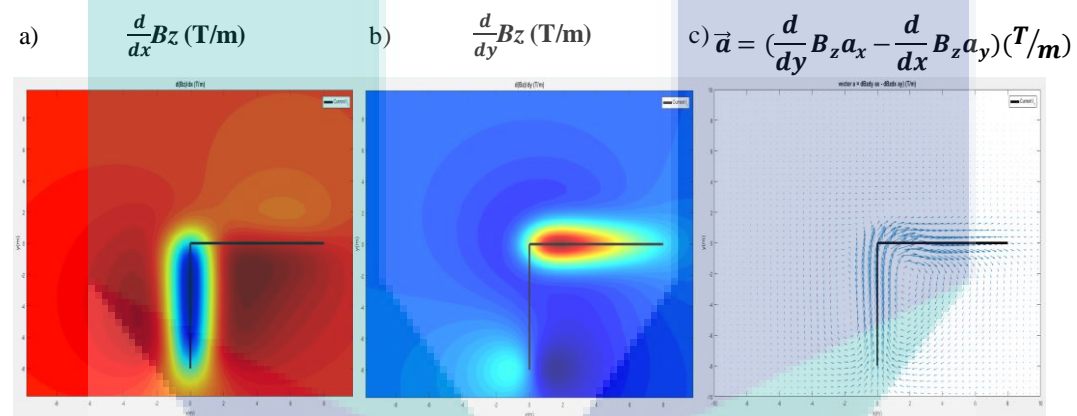


Figure 4.5 Magnetic field distributions produced by a line current in  $x$ - and  $y$ -directions with a lift off of 2 mm. a) Differential of magnetic distribution respect to position of line current in  $x$  - direction. b) Differential of magnetic distribution respect to position of line current in  $y$  - direction. c) Arrow map of the reconstructed current dipole.



Lift off,  $Z = 3 \text{ mm}$

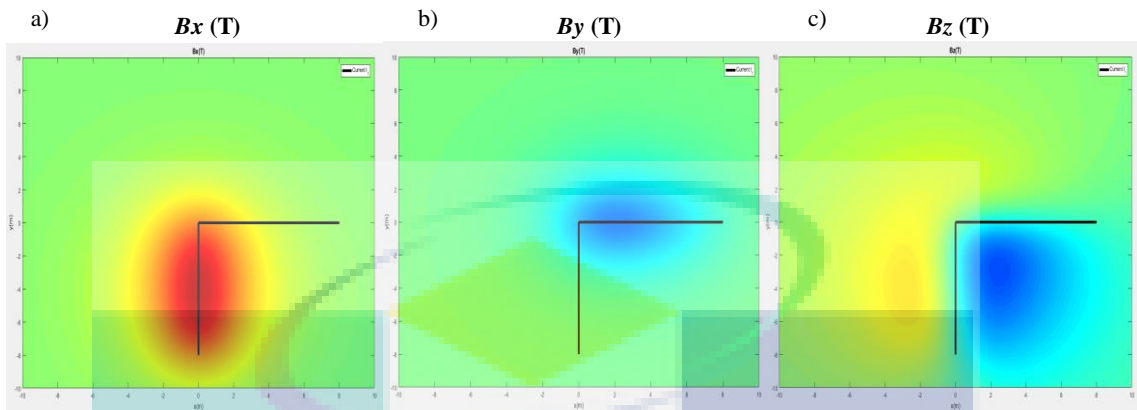


Figure 4.6 Magnetic field distributions produced by a line current in  $x$ - and  $y$ -directions with lift a off of 3 mm. a)  $B_x$ . b)  $B_y$ . c)  $B_z$ .

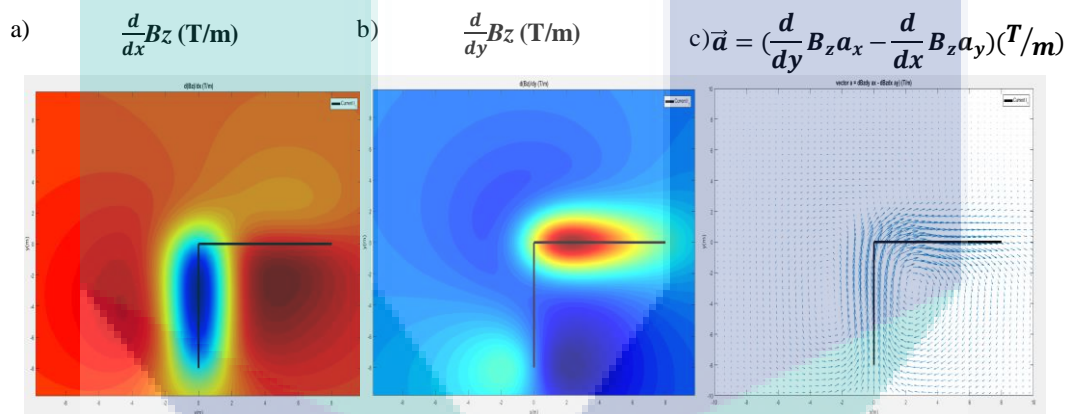


Figure 4.7 Magnetic field distributions produced by a line current in  $x$ - and  $y$ -directions with a lift off of 3 mm. a) Differential of magnetic distribution respect to position of line current in  $x$  - direction. b) Differential of magnetic distribution respect to position of line current in  $y$  - direction. c) Arrow map of the the reconstructed current dipole.

Lift off,  $Z = 4 \text{ mm}$

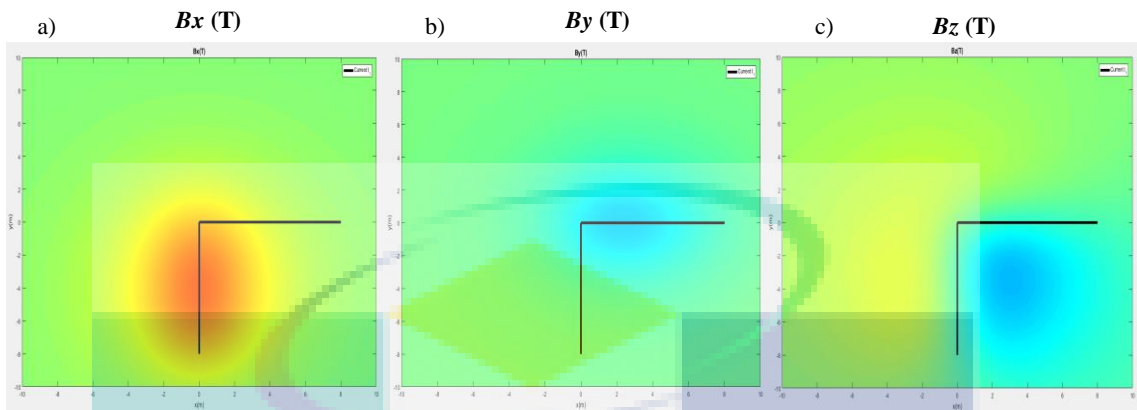


Figure 4.8 Magnetic field distributions produced by a line current in  $x$ - and  $y$ -directions with a lift off of 4 mm. a)  $B_x$ . b)  $B_y$ . c)  $B_z$ .

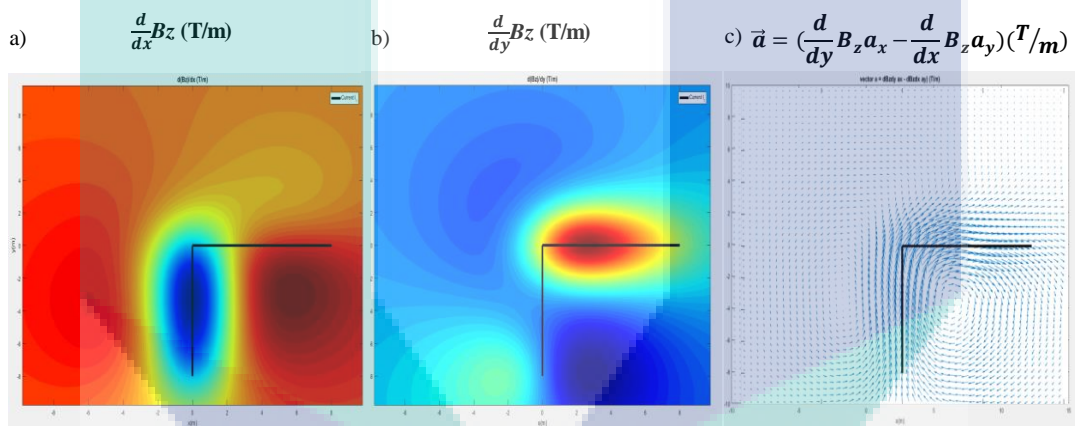


Figure 4.9 Magnetic field distributions produced by a line current in  $x$ - and  $y$ -directions with a lift off of 4 mm. a) Differential of magnetic distribution respect to position of line current in  $x$  - direction. b) Differential of magnetic distribution respect to position of line current in  $y$  - direction. c) Arrow map of the reconstructed current dipole.



Lift off,  $Z = 5 \text{ mm}$

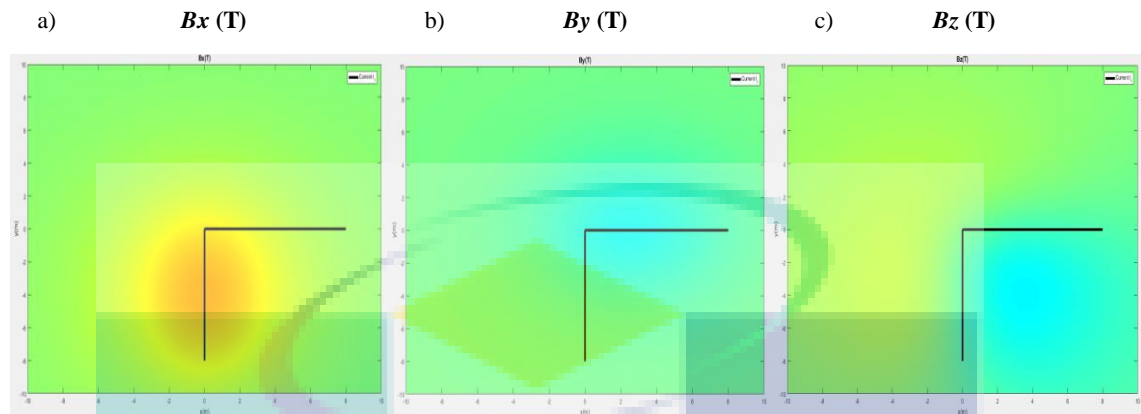


Figure 4.10 Magnetic field distributions produced by a line current in  $x$ - and  $y$ -directions with a lift off of 5 mm. a)  $B_x$ . b)  $B_y$ . c)  $B_z$ .

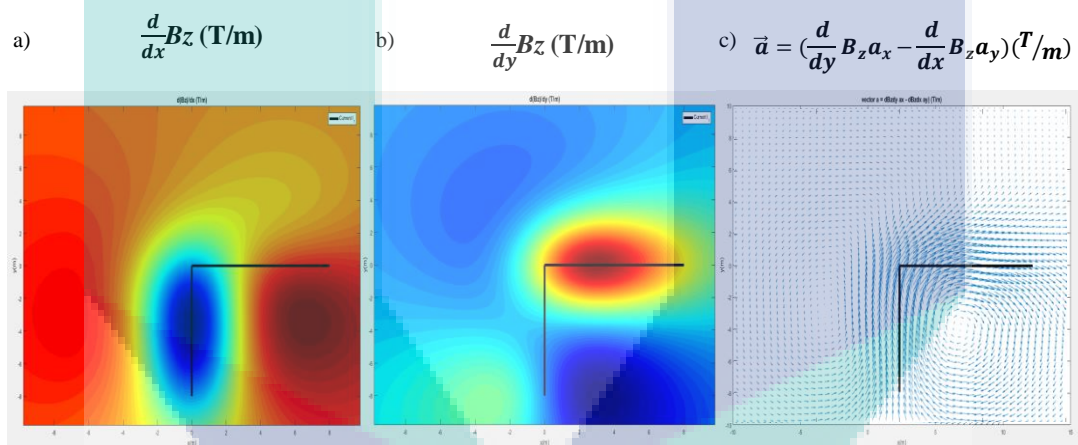


Figure 4.11 Magnetic field distributions produced by a line current in  $x$ - and  $y$ -directions with a lift off of 5 mm. a) Differential of magnetic distribution respect to position of line current in  $x$  - direction. b) Differential of magnetic distribution respect to position of line current in  $y$  - direction. c) Arrow map of the reconstructed current dipole.

The changes of intensity of the magnetic distribution when the lift off was changed are shown from Figure 4.6 to Figure 4.11. From the Figures 4.6 to 4.11, there was no drastic change when compared to Figures 4.4 and 4.5. But the difference that could be concluded was the intensity distribution of  $B_x$ ,  $B_y$  and  $B_z$  started to fade and broaden. Not only that, the magnetic field distribution progressively expanded where it was no longer focusing on the line current area. This could be concluded that the farther

the sensor to the sample, it was more difficult to detect the changes of current on the sample and reduce the estimation accuracy of the current dipole. It was important to make sure that the lift off of the sensor was minimal to the sample. The amount of lift off is strongly affected in ECT method.

### 4.3 Crack Detection Performance

#### 4.3.1 Comparison of Different Detection Technique

In this section, different detection techniques were studied to investigate the characteristic of the output signal of each technique. Since the magnetic response of the induced eddy current was detected by a phase sensitive detection using the lock-in amplifier, a reference signal was necessary to calculate the phase difference between the detected signal and the reference signal.

Figure 4.12 shows the output signal of different detection techniques. Figure 4.12 (a) shows the absolute measurement of the real and imaginary components of the magnetic field response  $B_z$  from only one AMR sensor using a constant phase of the reference signal. Although the imaginary components of the signals showed clear intensity changes at the crack area, the magnetic response due to the slits during the 90-Hz excitation was small and could not be seen clearly. Furthermore, the detected signals showed a drift characteristic of the offset signal. Similar to other frequencies, where the shallow slits were hard to be observed

To reduce the drift, a differential technique could be used. Figure 4.12 (b) shows the result of the intensity of the differential vector (sensor 1 – sensor 2)  $dB_z/d_x$  using a fix location-based phase of the reference signal when the probe was moved across the slits. The signal still showed lots of noise and the signal intensity decreased. It was hard to localize the slits if there was too much of noise in the detected signals.

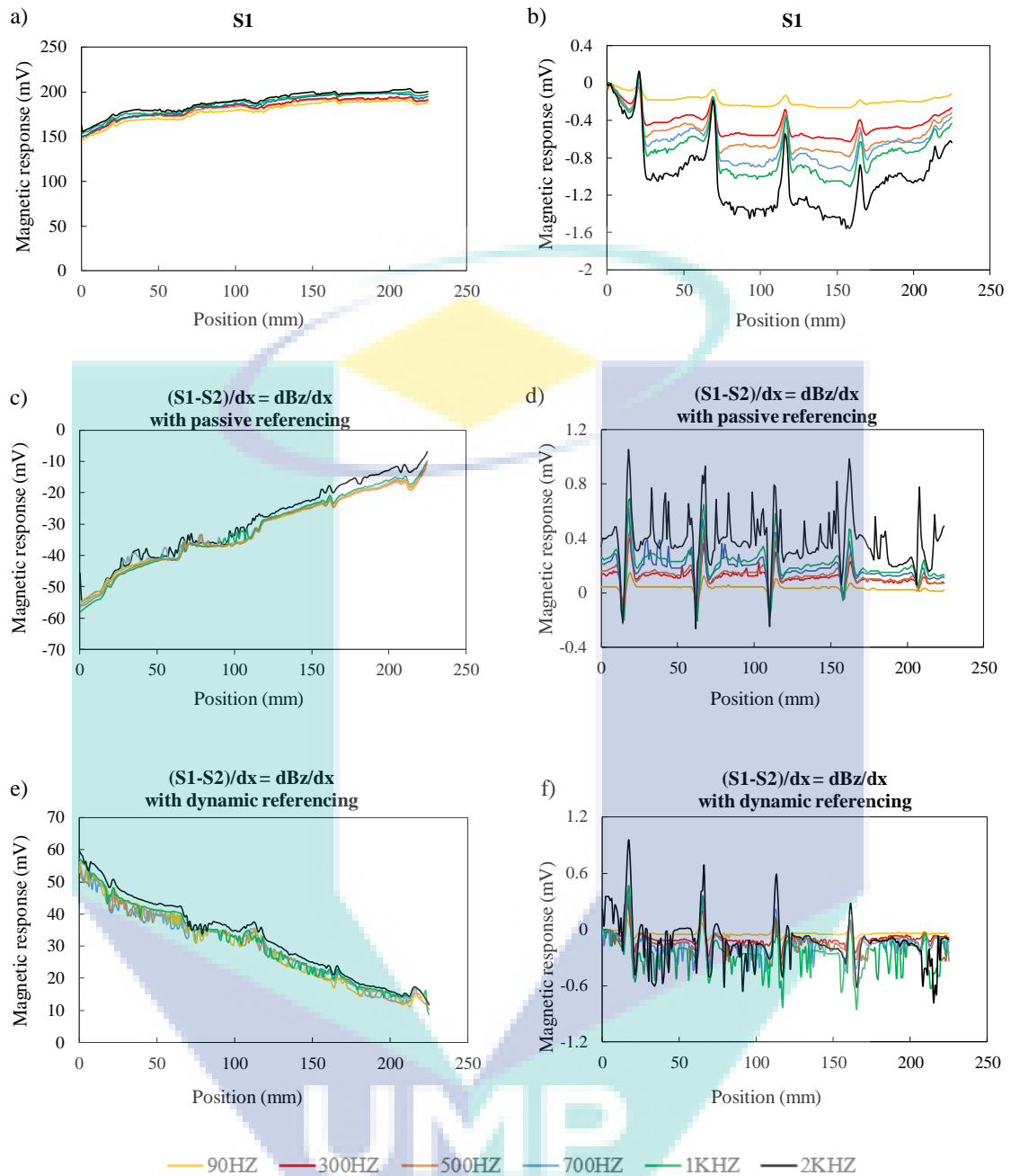


Figure 4.12 Line-scanned magnetic field intensity with differential technique. (a) The real and (b) imaginary of the absolute measurement  $B_z$  of the magnetic response with a constant phase of the reference signal. (c) The real and (d) imaginary of the differential measurement  $dB_z/dx$  of the magnetic response with a fix location-based phase referencing technique. (e) The real and (f) imaginary of the differential measurement  $dB_z/dx$  of the magnetic response with a sensor-based phase referencing technique.

Furthermore, there was still a slight drift observed at the beginning of the scanning region. This was thought due to the distributions of electrical and magnetic

properties of the sample over the scanning region. It was important to have a good reference so that the slits area could be detected clearly and easily. To reduce this effect, a new phase referencing technique was proposed where the phase of one AMR sensor was used as the reference signal.

This sensor would act as a dynamic phase referencing technique where the phase would deviate depending on the location, thus minimizing the effect of inhomogeneous magnetic properties across a finite area of the sample. The performance of this technique is shown in Figure 4.12 (c). The drift characteristic was significantly reduced and able to detect the slit-induced signal. Therefore, the differential technique was the best technique compare to the others with the condition of the required reference signal must be dynamic from one point to one point.

#### **4.3.1.1 Magnetic Response Distribution with Different Depth**

After the line scan measurement, the probe was used to map the magnetic distribution around the slits. In this section, a comparison of magnetic distribution has been made with the different detection techniques. The aim was to gain the best output signal based on the localization performance of slits. The excitation field was set to be 1-kHz and generated by a 4-mA current.

Figure 4.13 (a) shows changes of intensity around the slit area but it was difficult to expect where was the precise location of the slit since this technique did not applied differential technique. Compare to Figure 4.13 (b), the intensity changes were still visible at the presence of the slit but not as good as the next one. This due to the reference signal did not change, therefore the output signal was not as clear as the previous one. Lastly, Figure 4.13 (c) the intensity changes due to the presence of slits could clearly be seen due to the differential and a sensor-based phase referencing technique.

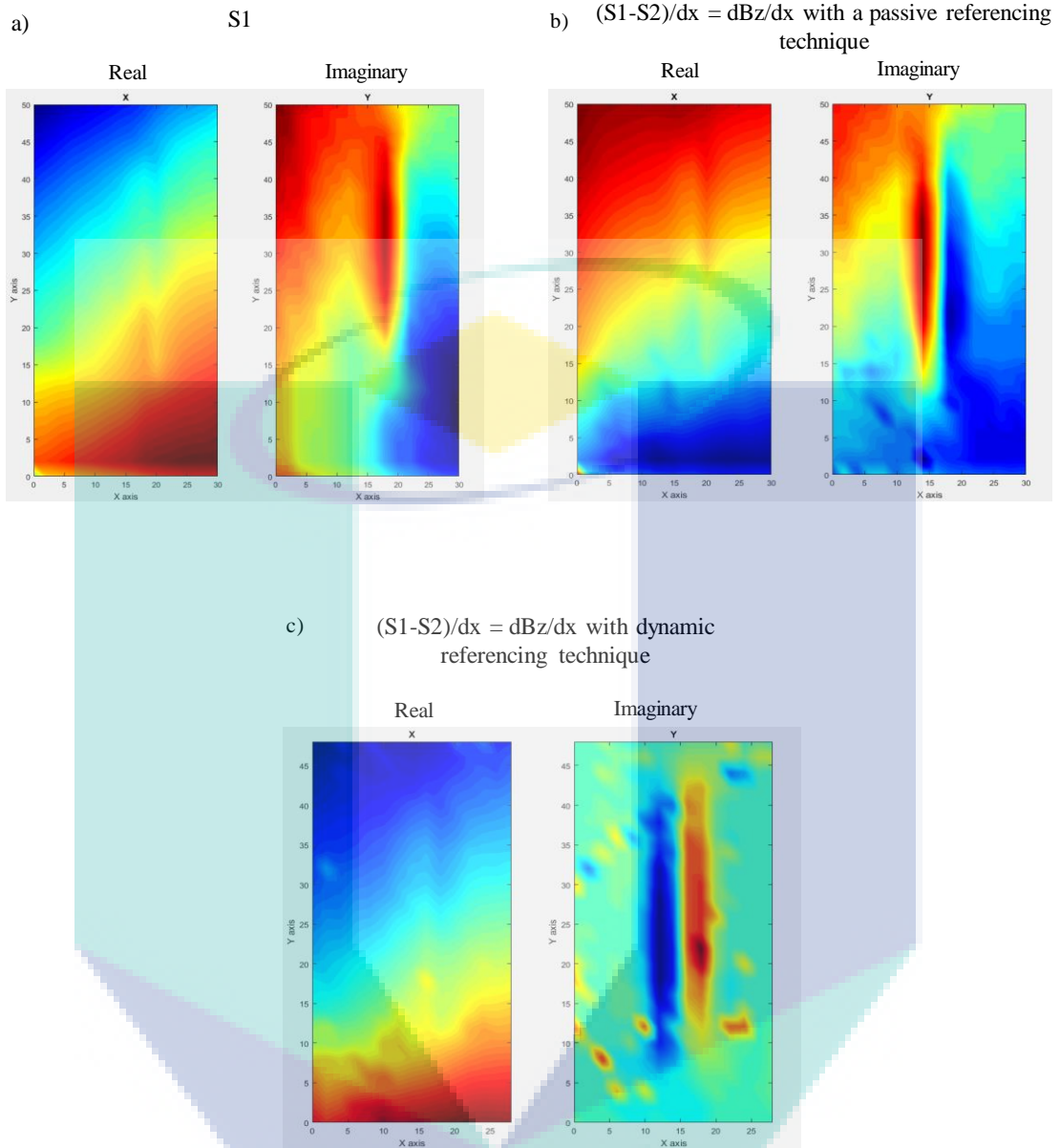


Figure 4.13 2-D magnetic map of the slit with 513- $\mu\text{m}$  depth (a) Absolute measurement  $B_z$  of the magnetic response with a constant phase of the reference signal. (b) Differential measurement  $dB_z/dx$  of the magnetic response with a fix location-based phase referencing technique. (c) Differential measurement  $dB_z/dx$  of the magnetic response with a sensor-based phase referencing technique.

## 4.3.2 Different Depth Sample

### 4.3.2.1 Frequency response characteristics

#### *Line Scanning of Slits with Different Depth*

The first experiment was conducted by using a sample with different depth of the artificial slits where the depth of the slits was from 200  $\mu\text{m}$  to 500  $\mu\text{m}$ .

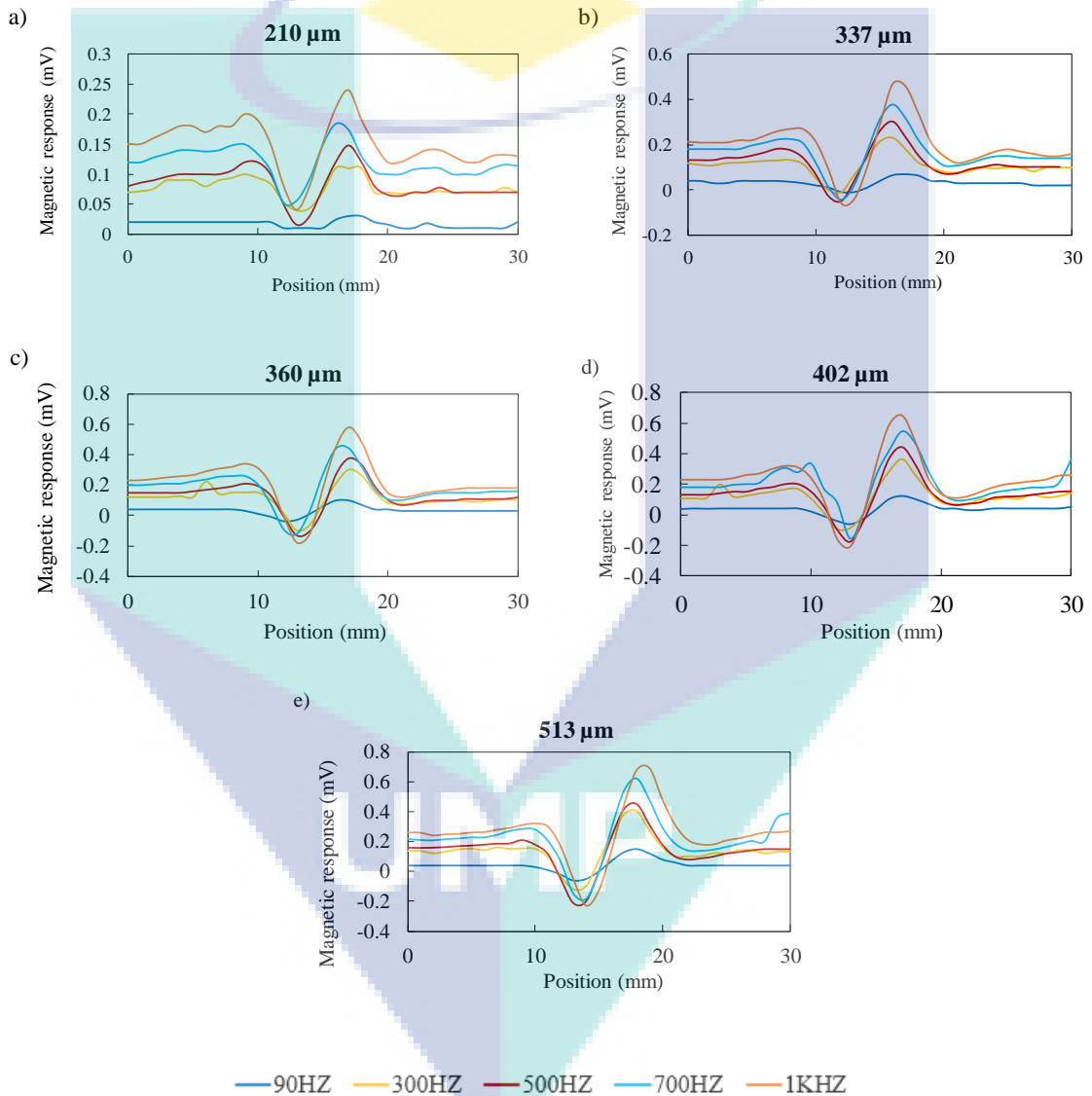


Figure 4.14 The imaginary components of the line-scanned magnetic field intensities with respect to different frequencies and slit depths. (a) 210  $\mu\text{m}$ . (b) 337  $\mu\text{m}$ . (c) 360  $\mu\text{m}$ . (d) 402  $\mu\text{m}$ . (e) 513  $\mu\text{m}$ .



This section focusses on the characteristic curves of magnetic response  $dB_z/d_x$  under different frequency conditions. Since the output signal was phase-sensitive detected using a lock-in amplifier, therefore, they had two outputs which were the real  $dB_{z,real}/d_x$  and imaginary components  $dB_{z,ima}/d_x$  as shown in Figure 4.14 below.

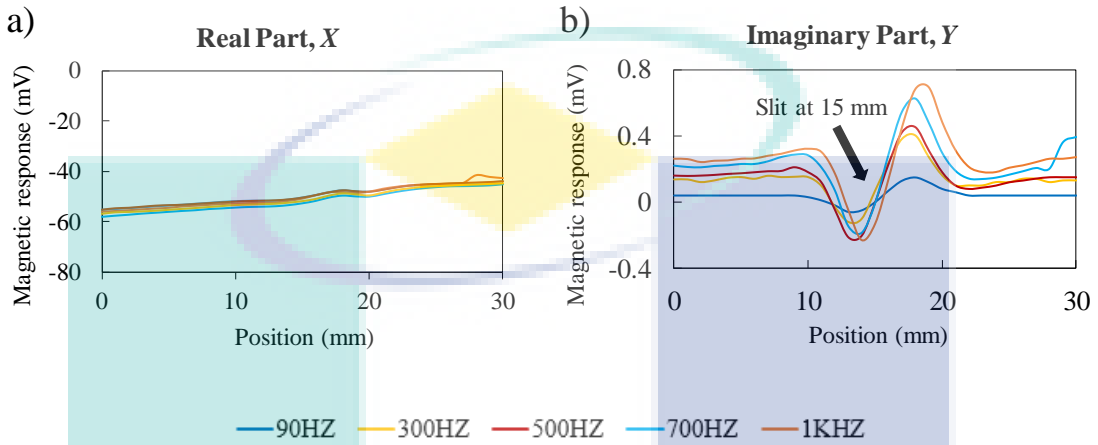


Figure 4.15 (a) The real and (b) imaginary components of the line-scanned magnetic field intensities of a slit with 513  $\mu\text{m}$  depth at different frequencies.

Although there were two output signals but only one output that would be taken into consideration throughout the experiment to detect the crack which was  $dB_{z,ima}/d_x$ .  $dB_{z,real}/d_x$  was neglected because the signal detected by the AMR sensor was a mixture of strong magnetization and small eddy current signals where the  $dB_{z,real}/d_x$  signal did not show any changes and it was difficult to identify the crack using it as shown in Figure 4.15 (a). Moreover, the imaginary output signal  $dB_{z,ima}/d_x$  showed a change of the magnetic response at the slit area compared to the real component  $dB_{z,real}/d_x$ .

Figure 4.14 shows the output signal of the imaginary component  $dB_{z,ima}/d_x$  of the magnetic response detected by the developed ECT probe. During this experiment, the frequency of the excitation magnetic field was set to be 90 Hz, 300 Hz, 500 Hz, 700 Hz, and 1 kHz. Figure 4.14 (a) shows signals of magnetic response when the ECT probe was moved horizontally across the slit where the depth was 210  $\mu\text{m}$ . The slit direction was perpendicular to the scanning direction.

From Figure 4.14, when applying the 90-Hz magnetic field, it produced the lowest signal of magnetic response, however, it still showed a slight change of magnetic response around the slit area. This output signal was related to the penetration depth equation that had been derived in chapter 2. Equation (2.47) stated that the depth of the

eddy current penetration was inversely proportional with the frequency applied. Therefore, the eddy current penetrated deeper at 90 Hz compared to other frequencies. Since the slits were on the surface only, this caused the magnetic response signal to occur slightly. But the changes of the magnetic response around the slit area increased significantly as the frequency was increased. This was due to most of the eddy currents that had been generated were accumulated to the surface and this made the magnetic sensor to detect the eddy currents easily.

The experiment was furthered with the other slits where the output signals were as shown in Figure 4.14 (b), (c), (d), and (e). Although different frequencies were applied to the slits, the patterns and the characteristics of each slit showed a same characteristic where there were changes at the slit area. In Figure 4.14 (e), the graph shows the signal of the deepest slit where the changes of the magnetic response could be clearly seen even at 90 Hz, and the magnetic response was increased compared to Figure 4.14 (a). Compared to the 90-Hz excitation field, the magnetic response signal showed a stronger intensity change with less noise and the increase of the magnetic response. The correlation between the signal intensity change and the depth of the slits will be discussed below.

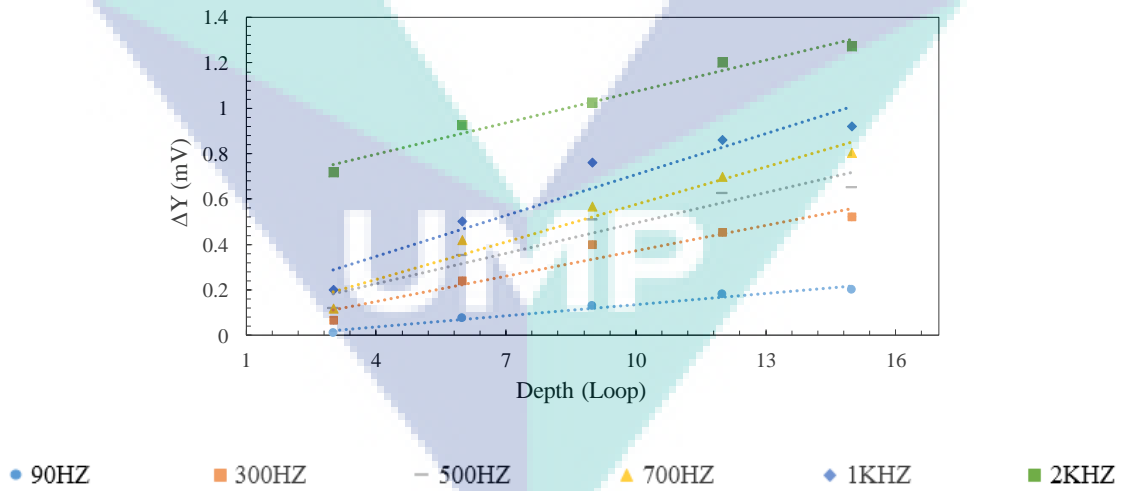


Figure 4.16 Signal difference of the different depths of slits at different frequencies.

Figure 4.16 shows the analysed waveforms of  $dB_{z, ima}/dx$  at the slit area with respect to the depth and the excitation frequency. To gain a more information, a delta value was used to represent the difference between the maximum and minimum values of the peaks and trough in the magnetic response waveforms. The delta value showed a



small value and slowly increased as the crack went deeper. This case was same to the case when the frequency was increased, the delta values would increase as well.

This graph clearly showed that when there was an increase in the excitation frequency, it could be expected that the skin depth would reduce which make the value of magnetic response increased. Since the experiment was conducted with the slits on top of the surface of the galvanized carbon steel plate, therefore, a higher selection of frequency was better where all the eddy current would linger around on the surface material. However, a low frequency could also be used since the slits still could be detected, but to facilitate the sensors to detect surface cracks, using a high frequency was recommended.

#### *Magnetic Response Distribution with Different Depth*

Figure 4.17 shows the map distribution of the gradient magnetic response  $dB_z$ ,  $ima/dx$  of the slits with different depths. The experiment was performed with three different frequencies which were 90 Hz, 500 Hz and 1 kHz where 90 Hz was assumed as a low frequency while 1 kHz as a high frequency. Since the slits had different depths, therefore, different frequencies needed to be studied as well because these two parameters were related due to the skin effect. Figure 4.17 shows the magnetic response distributions across the surface of the 1-mm slit with different depth.

Similar to the case of the line scanning, the magnetic distribution for real components was neglected in this result since the slits were not clearly observed in the map distributions. Figure 4.17 (a) shows a magnetic distribution that was performed at the 1 kHz excitation field. The result displayed a clear intensity change at the slit area, especially for the deepest slit. Moreover, the value of intensity for the deepest slit was higher compared to others and the value was decreased as the depth of slit decreased.

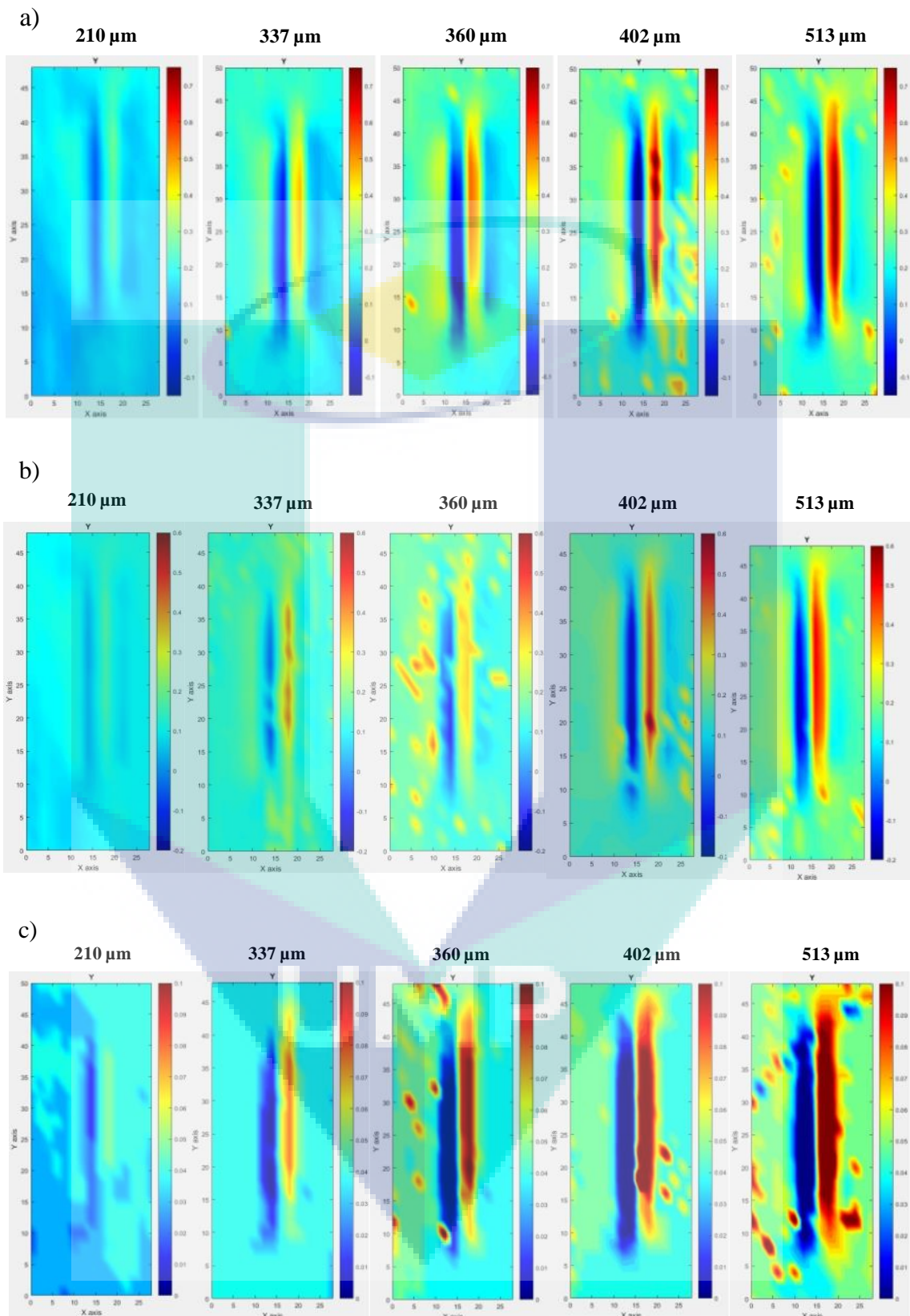


Figure 4.17 2-D magnetic map distributions of different slit depths at different frequencies. (a) 1-kHz. (b) 500-Hz. (c) 90-Hz.

However, the intensity change still could be seen even though the depth of slit was only 210  $\mu\text{m}$ . This was due to the high frequency of the excitation field where most of the eddy currents accumulated to the surface. Compare to the low excitation frequency, as shown in Figure 4.17 (c), the change of intensity was clearly seen at the deepest crack but was slowly faded as the depth of crack decreased.

The correlation between the gradient of magnetic distribution  $dB_{z,ima}/dx$  and the depth of slits could be studied through Figure 4.17. The intensity change was higher when the crack went deeper, and this could be seen through the map distributions.

#### 4.3.2.2 Amplitude

##### *Line Scanning of Slits with Different Depth*

After investigating the changes of magnetic response on the surface cracks towards different frequencies, the experiment was continued with investigating the magnetic response of all slits towards the amplitude of the excitation current. By using a similar sample as the previous one, the experiment was performed at the 90-Hz excitation field. The only difference during the experiment was the amplitude. Different amplitudes were applied to the system and the output signal  $dB_z/dx$  is shown in Figure 4.18.

Figure 4.18 (a), (b), (c), (d), (e) and (f) show different amplitudes were applied to the system from 1 mA until 10 mA. Technically, the intensity of the induced eddy current would increase when a higher current amplitude was applied. The experiment was initially started with 1 mA as shown in Figure 4.18 (a). The response that is shown in the Figure 4.18 (a) showed an intensity change at the slit area but with the presence of noise. This line scanning measurement was measured horizontally across the slits, starting with the deepest slit and ending with the lowest depth of slits. Next, the studied was continued by using 3 mA as shown in Figure 4.18 (b).

Similar to the previous graph, but this time the magnetic response showed a better result, but the noise still appeared at the end of the slits and it was difficult to identify the slit area. Then, the experiment was proceeded with 4 mA as shown in Figure 4.18 (c). The magnetic response signal showed a clear signal intensity change at each slit with lesser noise. Compared to the previous one, at this current amplitude, the results showed a better result where the lowest depth of slit could be measured as well.

Moving on to a higher value of amplitude, where it was expected that the signal would show a clear change of intensity than before.

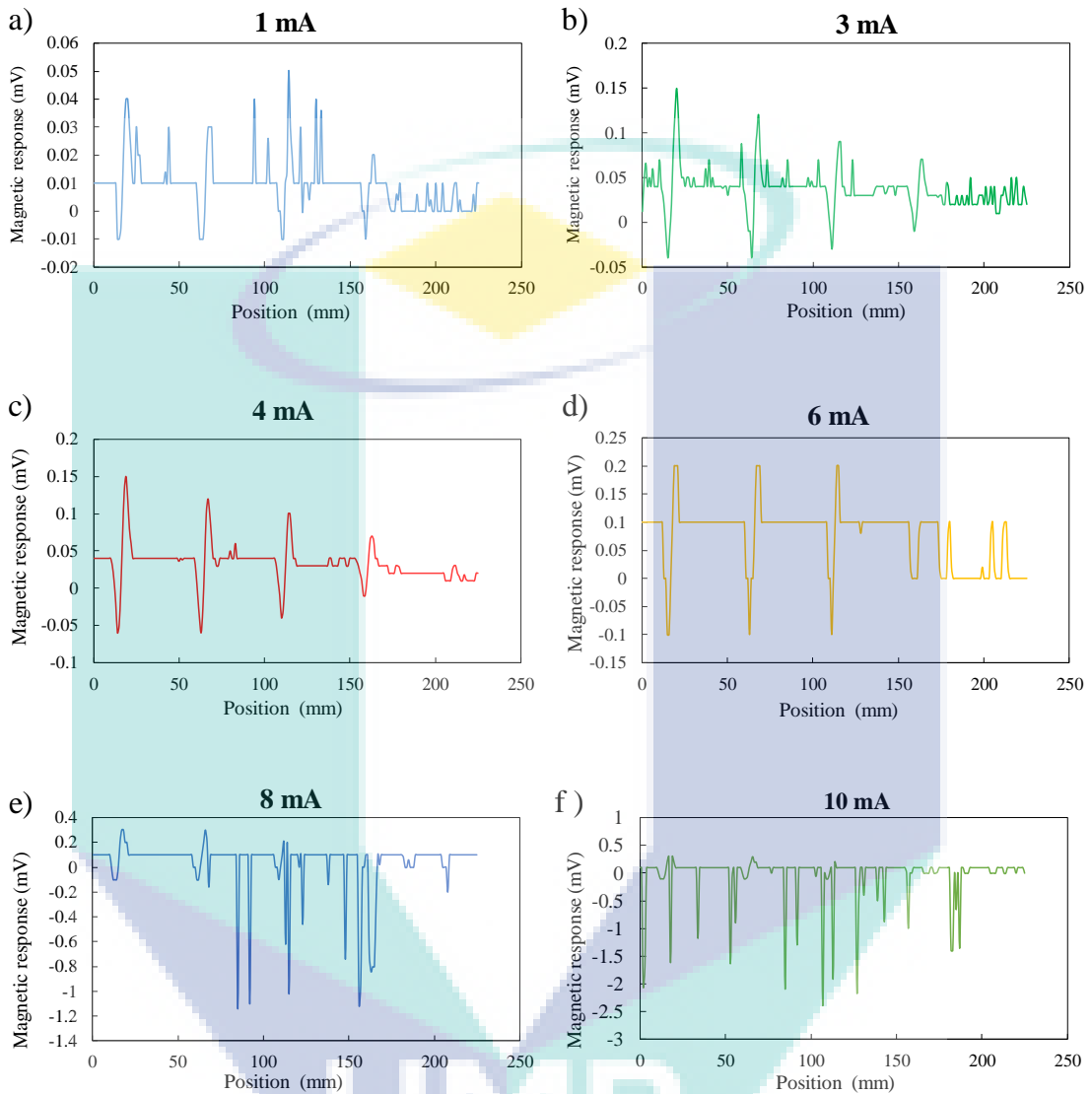


Figure 4.18 Line-scanned magnetic field intensities of different slit depths with respect to different excitation field's current. (a) 1 mA. (b) 3 mA. (c) 4 mA. (d) 6 mA. (e) 8 mA. (f) 10 mA.

However, as shown in Figure 4.18 (d), the noise started to appear back at the end of the line scan measurement. The noise was still observed in Figures 4.18 (e) and (f), where it was more noticeable when the amplitude was increased. Therefore, the most optimum amplitude was determined to be 4 mA where the signal produced a good performance and still could detect the slit that had the lowest depth.

### 4.3.3 Magnetic Distribution of Rotated Probe

As discussed in chapter 3 earlier, the position of the sensor plays an important role to succeed the differential technique process. In this section, rotation of probe was made to compare the magnetic response between different slits.

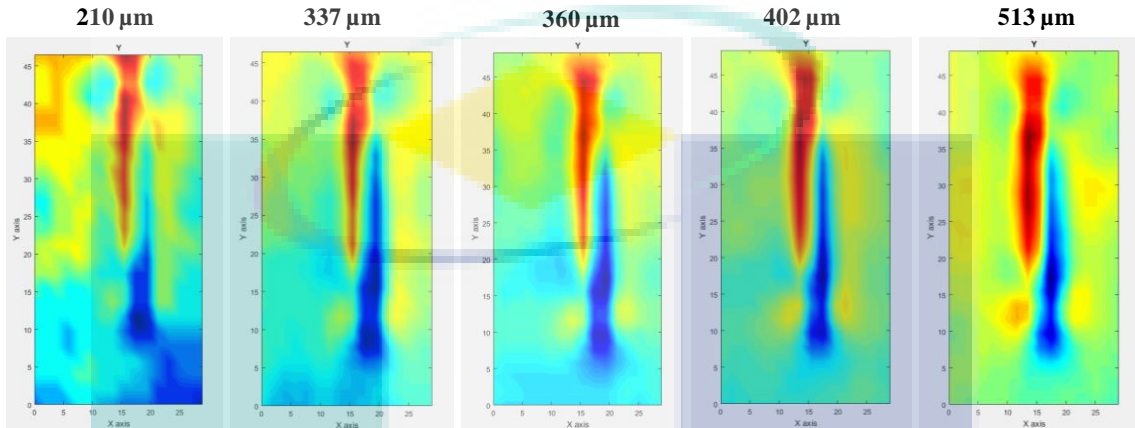


Figure 4.19 2-D magnetic map distribution after the probe has been rotated by 90 degree.

In this setup, the probe measured the magnetic response of  $dB_z/d_y$ , where in the previous setup, the probe measured the magnetic response of  $dB_z/d_x$ . The measurement of the magnetic response distribution across the slit was performed at the 1 kHz excitation field. Figure 4.19 shows an obvious magnetic response, especially around the slits. The position of the sensor was arranged as in Figure 3.16. Although the magnetic response showed changes at the slit area, compared to the previous one, this output signal required an improvement so that it could be easier to interpret the data. This showed that, the detection performance of the slits was improved when the direction of the slits (y- direction) was perpendicular to the direction of the differential signal (x- direction).

### 4.3.4 Different Width Sample

#### *Line Scanning of Slits with Different Width*

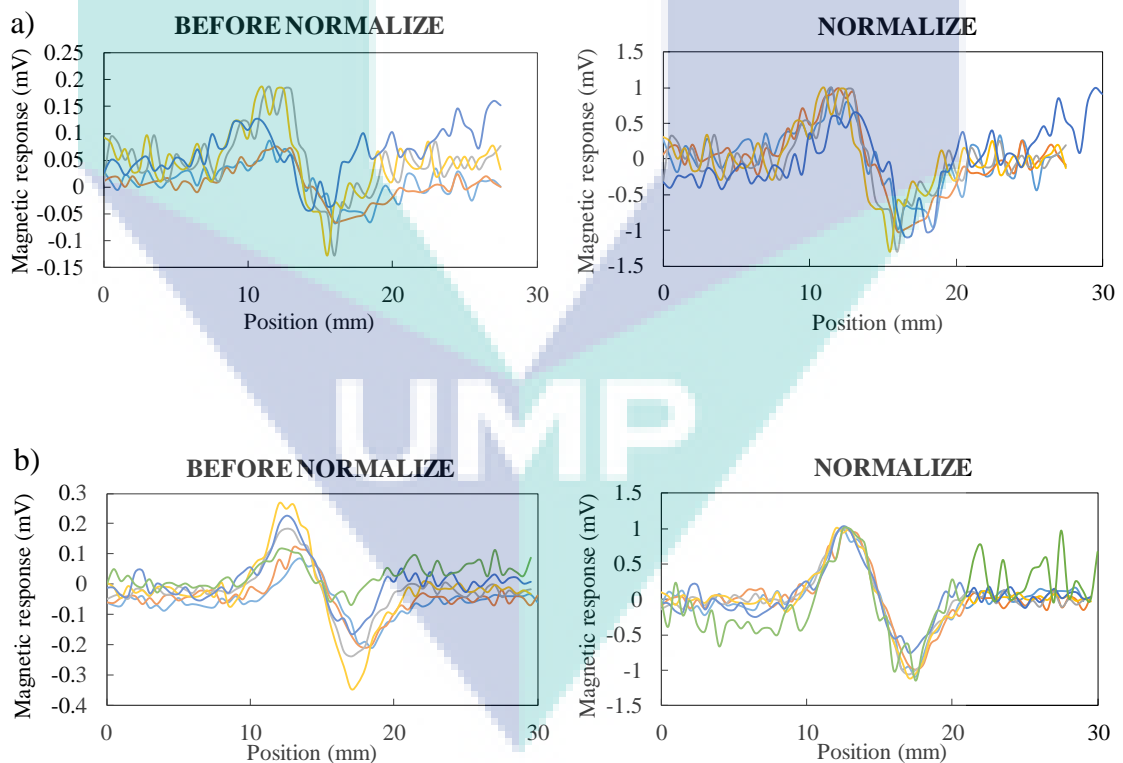
The experiment was proceeded to another sample, where different width of slits was prepared. The width of slits was from 0.05 mm to 1 mm and all slits had 30-mm length and 500- $\mu$ m deep. The experiment was carried out by changing the frequency of



the excitation magnetic field to 90 Hz, 300 Hz, 500 Hz, 700 Hz, and 1 kHz. Figure 4.20 shows the raw signal which was before normalizing the output signals and after normalizing them.

Figure 4.20 (a) revealed a change of magnetic response when applying a 90-Hz excitation field. Although the changes could be seen, lots of noise were observed since the frequency was low. The noise still could be seen when the frequency was 300 Hz, but it has decreased compared to the case of 90 Hz. Figure 4.20 (b) shows that all slits were successfully detected even the narrowest slits of 0.05 mm.

As the frequency increased, the noise was also getting invisible. Compared to the case of the 90-Hz excitation field, Figure 4.20 (e) shows a stronger intensity change with a less noise. Even though all the slits were successfully detected, the correlation between the signal intensity change and the width of slits was not clearly observed. This might be due to the larger baseline of the magnetic sensor which was 4 mm and the big dimensions between the excitation coil and the width of the slits.



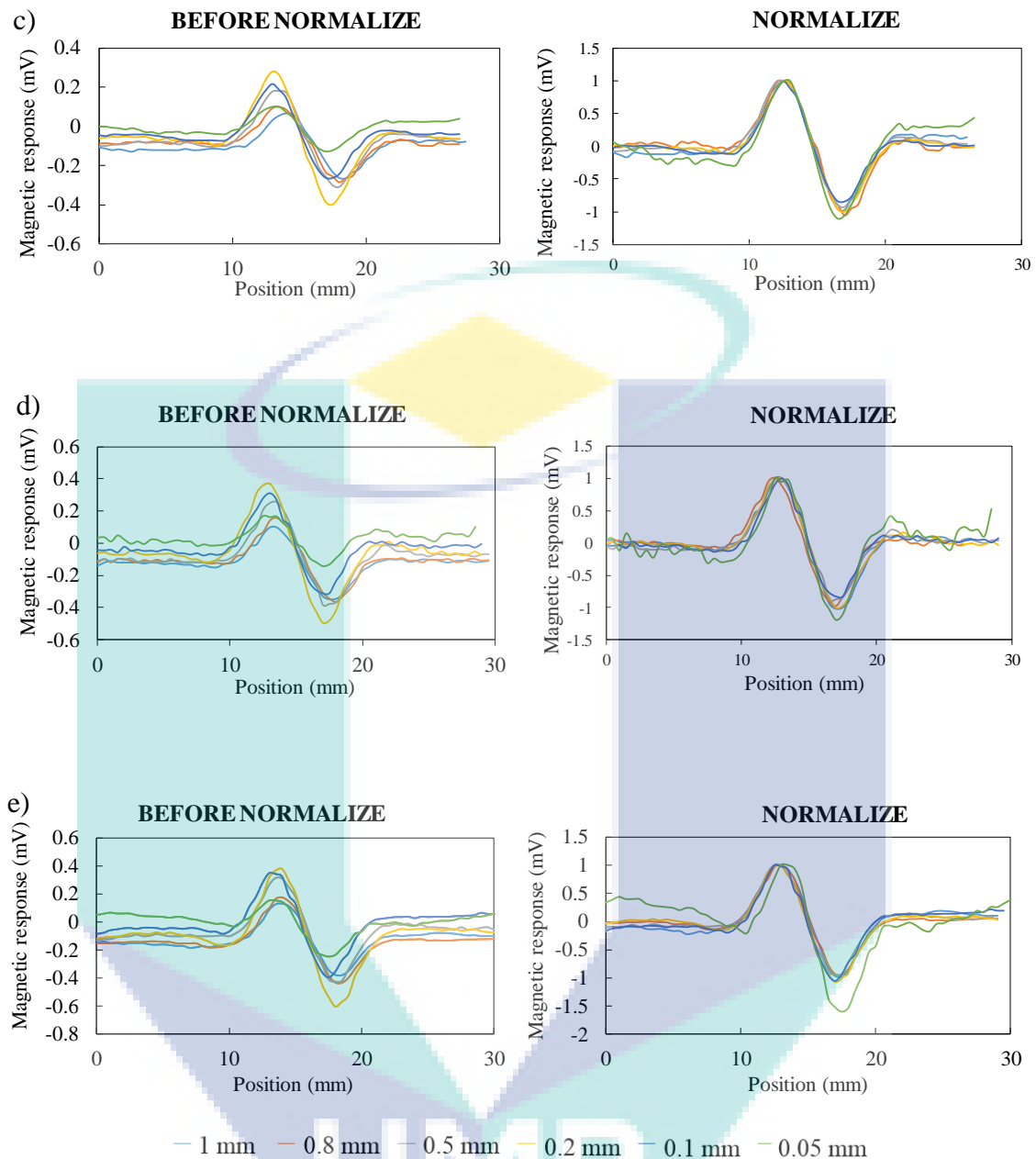


Figure 4.20 Line-scanned magnetic field intensities of different slit width at different frequencies. (a) 90-Hz. (b) 300-Hz. (c) 500-Hz. (d) 700-Hz. (e) 1-kHz.

#### *Magnetic Response Distribution with Different Width*

A 2-D scanning was implemented to evaluate the signal change corresponding to the width of the slits. Figure 4.21 depicts the 2-D scanned maps of magnetic response distributions measured at a frequency of 1 kHz. The magnetic maps reflected the slit shape. The gradient of magnetic response showed two intensity peaks where this data agreed with the line scanning data in Figure 4.21.

The shape of the slits was estimated from the magnetic map obtained through the ECT probe. From Figure 4.21, the intensity changes were almost invisible for the smallest width. This means that the current limitations of the ECT probe could be 0.05-mm width of slit where if the width of slits was less than 0.05 mm, the signal change would not probably visible. To overcome this issue, the ECT probe could be improved where this will be discussed in chapter 5.

The correlation between the gradient of magnetic distribution and the width of slits could be studied through the magnetic map in Figure 4.21. When the slit went wider, the intensity change was getting higher and obviously, this could be seen through the map distributions.

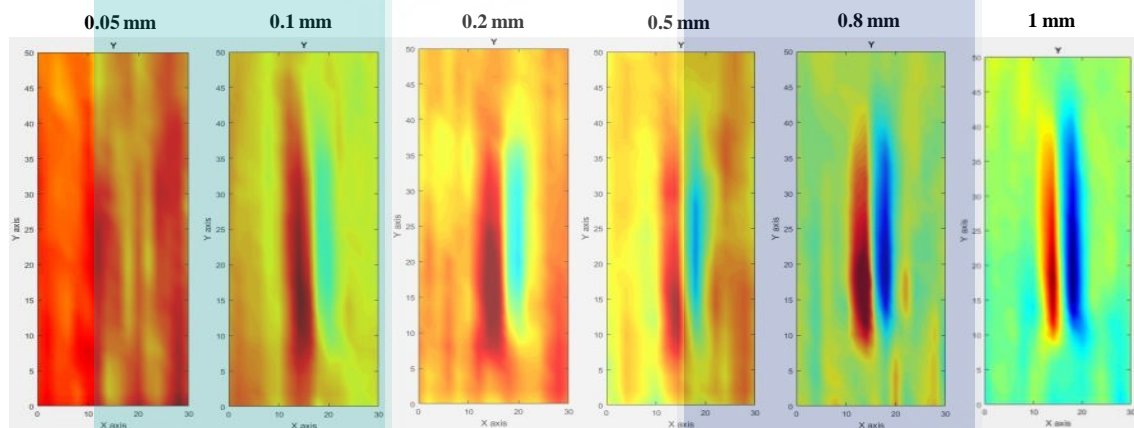


Figure 4.21 2-D magnetic map distribution of different slit widths at 1-kHz excitation field.

### 4.3.5 Different Length Sample

#### *Line Scanning of Slits with Different Length*

Three parameters could be used to describe the characteristic of the crack: crack depth, width, and length. Hence, the artificial slits were investigated with respect to each of these parameters. In this section, length of the slits will be investigated. The length dependence was evaluated using the galvanized carbon steel plates with 510- $\mu\text{m}$  deep and 1-mm wide slits at various lengths.



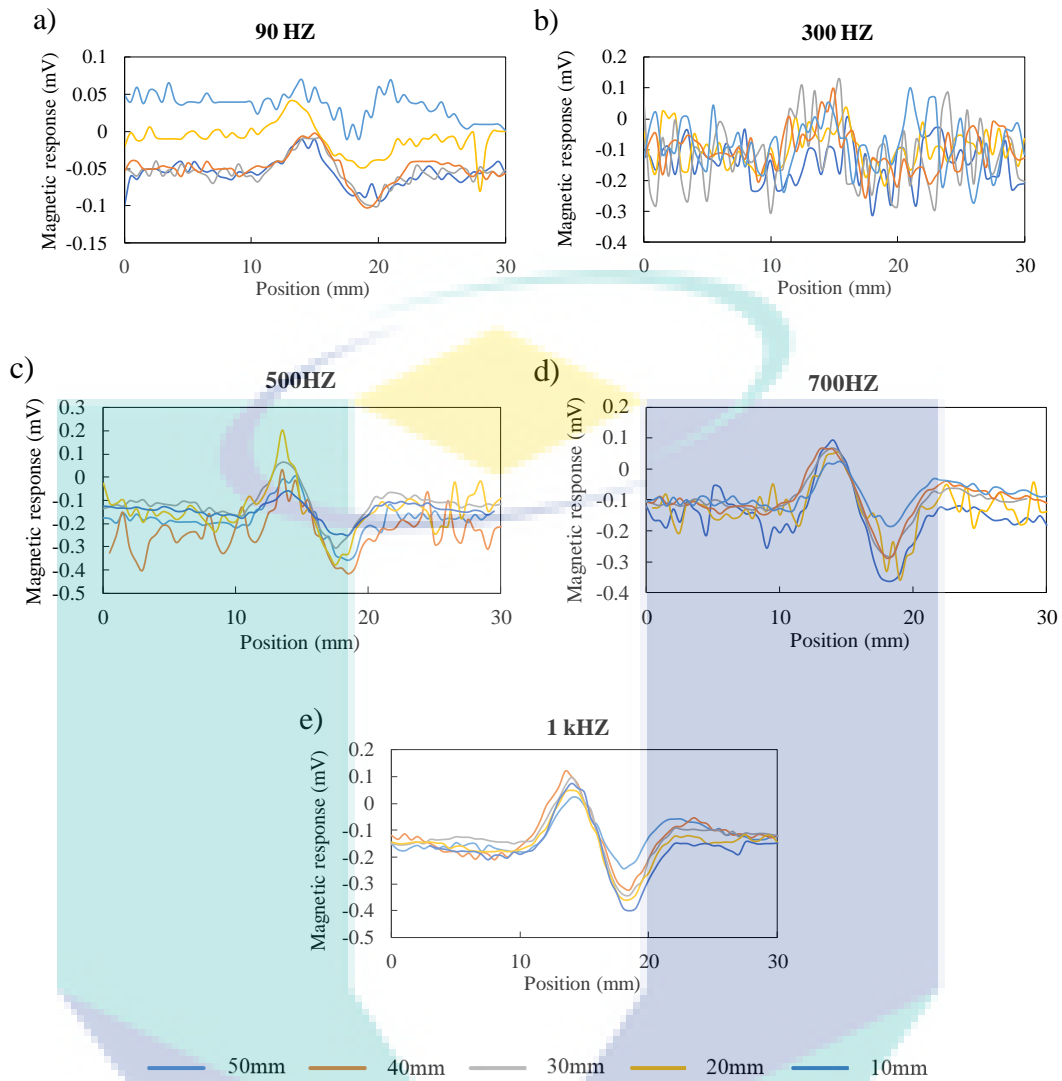


Figure 4.22 Line-scanned magnetic field intensities of different slit lengths at different frequencies. (a) 90 Hz. (b) 300 Hz. (c) 500 Hz. (d) 700 Hz. (e) 1 kHz.

Figure 4.22 shows a clear length dependence characteristic. Since the detection measurement was made for the surface slit, therefore, applying a low frequency would cause a lower signal-to-noise ratio, similar to the previous cases. However, all the slits could be detected by the probe and clearly be seen in the Figure 4.22 except for the result when the measurement was performed at the 300-Hz excitation field. A too low signal-to-noise ratio made it was difficult to investigate the slits area. The length of each slit could be clearly seen through the magnetic map distributions in Figure 4.24.

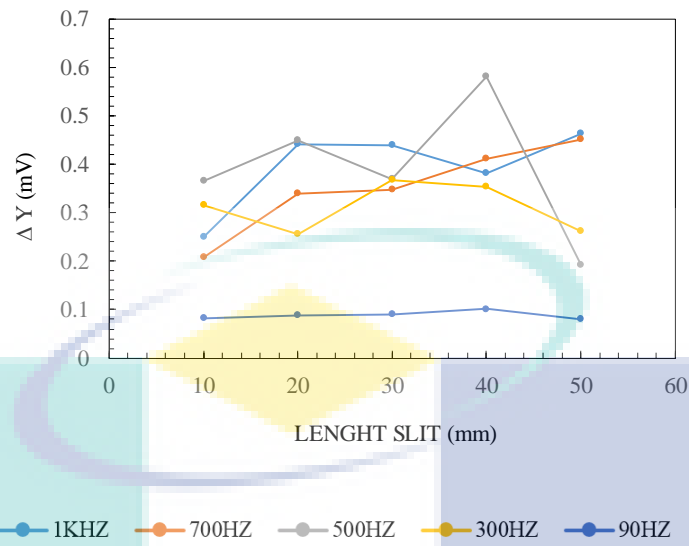


Figure 4.23 Signal difference of different slit lengths of slits at different frequencies.

The correlation between the signal intensity change and the width of the slits could be seen from Figure 4.23. This result was obtained from the raw waveforms in Figure 4.22, where the difference between the maximum and minimum values of the peaks of the waveforms was calculated. The change of intensity increased with frequency where Figure 4.23 shows frequency dependence characteristics. From the results, the detected signal was composed of the eddy current distribution change at the surface region. The surface eddy current distribution increased with length. It was shown that as the frequency as increased, the delta values increased as well.

#### *Magnetic Response Distribution with Different Length*

To evaluate the signal change corresponding to the length of the artificial slits, a 2-D scanning was implemented. The length of the slits could be obtained by mapping the magnetic response distribution.

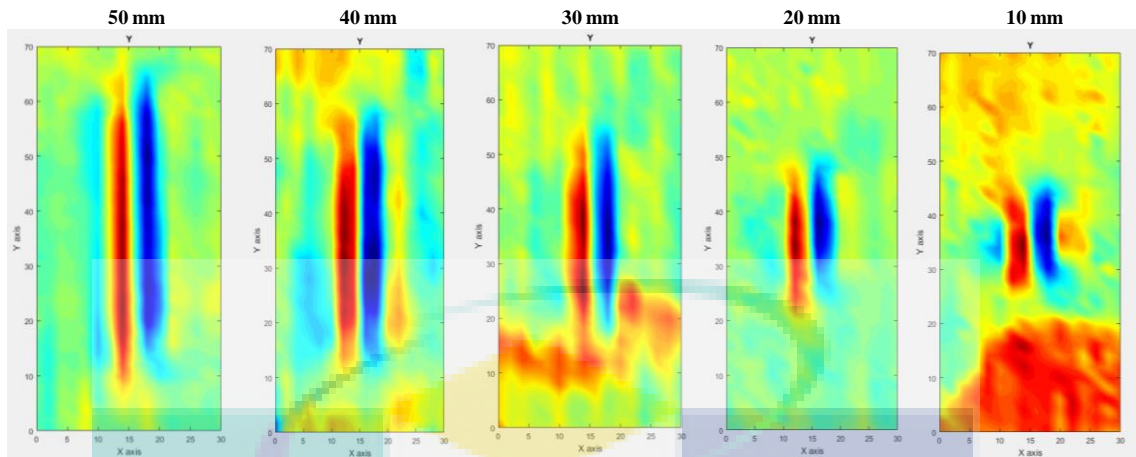


Figure 4.24 2-D magnetic map distributions of different slit length at 1-kHz excitation field.

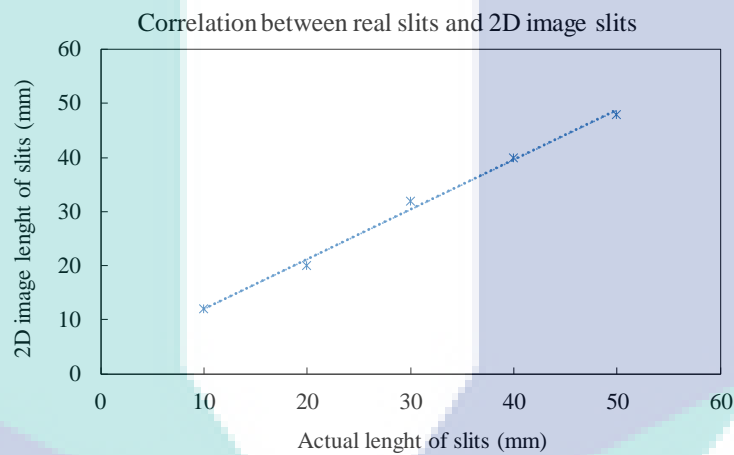


Figure 4.25 Correlation between real physical length of slits and estimated length in 2D image of magnetic field distribution.

The galvanized carbon steel plate with various lengths of slits was used. Figure 4.24 shows 2-D scanned maps of magnetic response distribution across the surface of the 1-mm slits and was performed at the 1-kHz excitation field. The magnetic distribution maps showed that the intensity change decreased as the length decreased. From the left side, the real length of the slits was 50 mm and the magnetic map showed almost similar length to the real slits. This was proven when the raw data had been analysed using the full width at half maximum technique. Figure 4.25 shows the correlation between the actual size of the slits and the length estimated from the 2D map size of slits using the full width at half maximum technique. From the figure, the linear graph shows that the magnetic map of the slits had almost accurate length with the real

length. It could be said that the length of the slit could be accurately estimated from the distribution map of the eddy current. The above results (Figure 4.24) showed that because of the existence of the slits, the eddy current could not maintain the original circular path but needed to bypass the slits. If the path of eddy current in the presence of the slits took longer time than without slits, therefore, the increase of the bypass path resulted in a delay of the phase of eddy current.

#### 4.3.6 Complex Shape Slit Sample

To test the performance of the ECT probe, a complex shape of slits was prepared where the  $x$ - and  $y$ -directed slits were combined in one sample. To produce the crack, the laser engraver was used to engrave the sample with letters ‘U’, ‘M’ and ‘P’ on the galvanized carbon steel plate with a 2-mm thickness. The artificial crack was 500- $\mu\text{m}$  deep with 1-mm width. The experiment was performed at 1 kHz since it was aimed to detect surface cracks. Figure 4.26 reveals a clear intensity change at the location of the slits. However, only the slits in the  $x$ -direction cannot be detected by the probe since the probe was set to measure the differential signal of  $dB_z/dx$ .

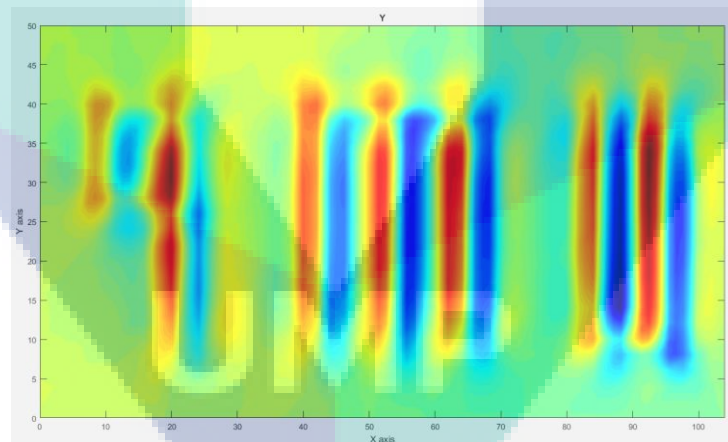


Figure 4.26 2-D magnetic map of the steel plate with ‘UMP’ slits using the ECT probe.

From the Maxwell’s equations and the Cohen-Hosaka transformation, the measure of gradient magnetic response  $dB_z/dx$  was proportional to the dipole current component of  $-J_y$  where the current density of  $J_y$  increased around the slits. This showed that the presence of the slit had directed the eddy current to be parallel with the slits, hence increasing the current density in the  $y$ -direction. From the figure above, the only

problem was the  $x$ -directed slits could not be detected causing the letters to be unclear. The detection sensitivity to perpendicular slits was much higher than that to the parallel slits.

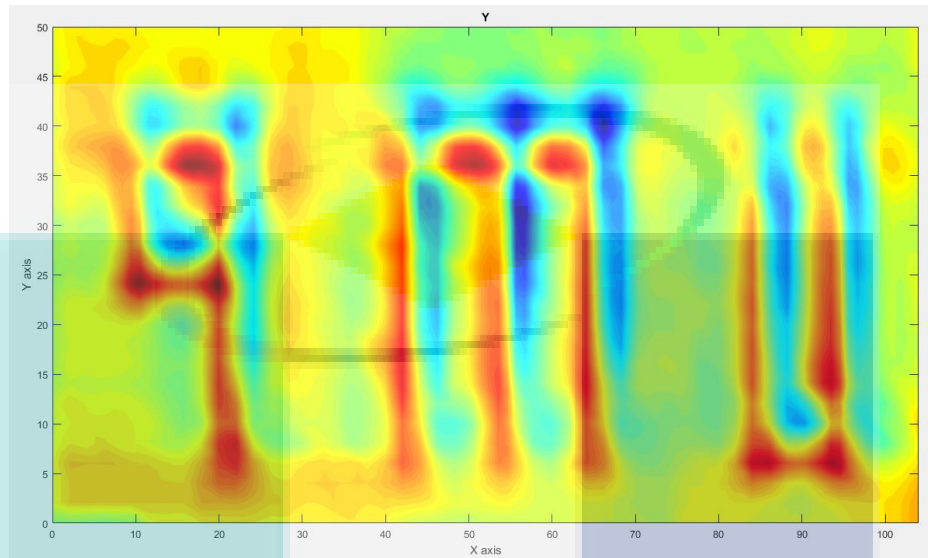


Figure 4.27 2-D magnetic map of the steel plate with ‘UMP’ slits using the ECT probe where the letter direction is perpendicular to the ECT probe.

Continuing from the previous study, the position of the steel plate was rotated 90 degree to make sure the probe was sensitive to the  $x$ -directed slits. The rotated result is shown in Figure 4.27 where a clear intensity changes at the location of slits especially where  $x$ -directed slits are located, was observed.

Similar with the previous case, according to Maxwell’s equations and the Cohen-Hosaka transformation, the measure of gradient magnetic response  $dB_{z,ima}/d_y$  was proportional to the dipole current of  $J_x$  component where the current density of  $J_x$  increased around the slits. This proved that the presence of the slits had directed the eddy current to be parallel with the slits. Even though in this case, the  $y$ -directed slits could still be seen, but the intensity change was not as clear as the previous. Improvements in the design of the ECT probe could be made to improve the detection of various types of cracks.

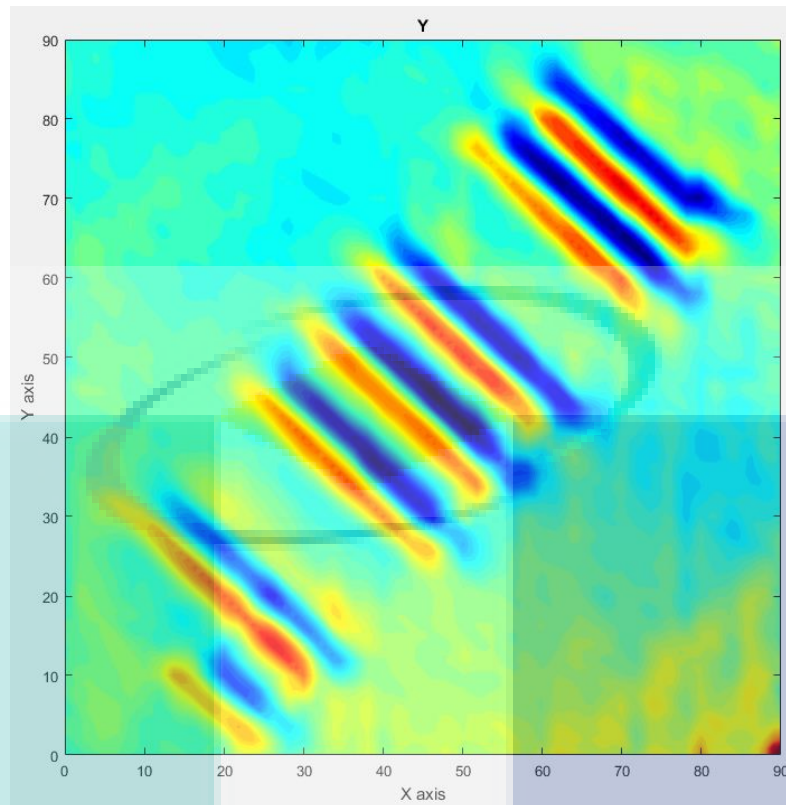


Figure 4.28 2-D magnetic map of the steel plate with ‘UMP’ slits using the ECT probe where the letter direction is rotated to 45° with respect to the ECT probe.

From the previous figures (Figure 4.26 and 4.27), the complex shape of slits shows a clear image of slits in each direction by rotating the sample plate. Therefore, to make all the direction of the slits could be evaluated, the experiment on this sample was continued where the position of the sample was rotated 45° with respect to the ECT probe  $x$ -axis. By putting the sample in this position, all the slits were not parallel to the differential axis of the probe, and the detection performance of these slits was evaluated. This position might make the ECT probe measured the slits at each direction either horizontal or vertical slits. However, even the galvanized steel plate was rotated 45° with respect to the probe, the magnetic distribution still showed no clear image of the alphabets especially the  $x$ -direction slits where the differential signal of  $dB_z/dy$  was not detected by the ECT probe. This could be resulted from the higher intensity of the  $dB_z/dx$  signals, which buried the  $dB_z/dy$  signal. Thus, to overcome this problem, improvements towards the ECT probe could be done and this has been suggested in chapter 5.



### 4.3.7 Backside Detection

To test the sensitivity of the probe for detection of backside defects, a backside detection measurement was performed with the test sample having different depth of slits from 1.0 mm to 1.8 mm.

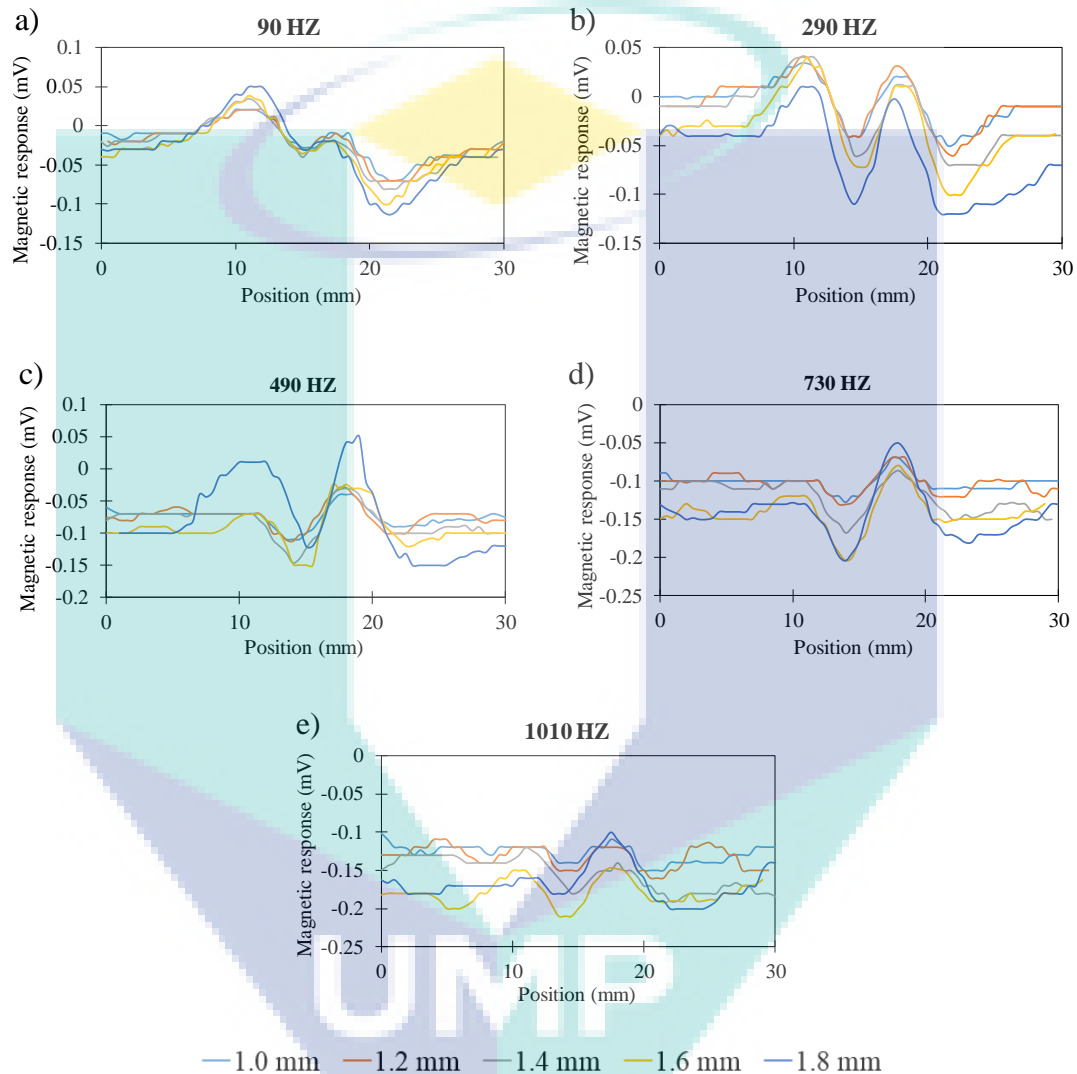


Figure 4.29 Line-scanned magnetic field intensities of different slit depths measured from the backside at different frequencies. (a) 90-Hz. (b) 300-Hz. (c) 500-Hz. (d) 700-Hz. (e) 1-kHz.

The width of the crack was constant at 1 mm. In this experiment, the slits were positioned at the back of the plate and the probe was positioned at the front surface. A line scanning was performed with different frequencies of the excitation field. Figure 4.29 shows the intensity changes in the detected signal from this slit. It was found that

the signal intensity was significantly changed at the position of the slits. Even though the signal pattern was not as good compared to the front surface scanning, but the slits could still be detected by the ECT probe. Since the line scan was performed at the 1-kHz excitation field, it could be assumed that the high frequency would result to a lower signal-to-noise ratio compared to the lower frequencies. This case was inverse with the surface scanning results where most of the eddy currents went up and made the ECT probe to detect a higher signal.

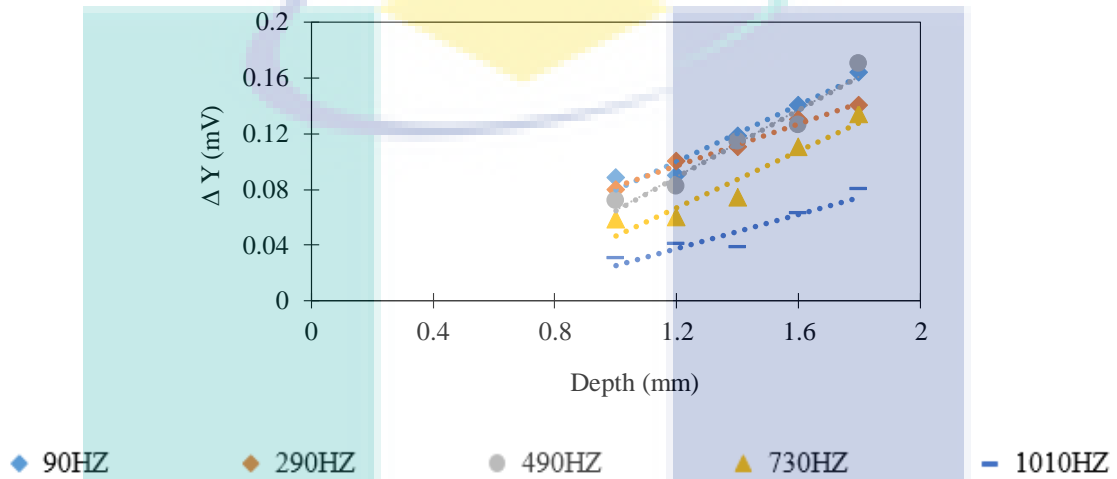


Figure 4.30 Signal difference of the different slit depths at different frequencies (backside).

The correlation between slit depth and differential signal for the case of the back-side measurement was almost same with the surface measurement and could be observed from Figure 4.30. Contradict to the surface measurement, the signal showed the lowest value when the excitation was 1 kHz compared to the other frequencies. This due to the skin depth effect where the frequency was inversely proportional to the depth of penetration hence the results were reflected in Figure 4.30. From Figure 4.30, the delta values, which were calculated from the difference between the peak and trough, increased with respect to the depth. The figure above concluded that the pattern almost linear with respect to frequency. Since the scanning measurement was performed at the back side, therefore, using a low frequency was better than a high frequency. In this case, the 90-Hz excitation field could be a sufficiently low-frequency field to have a deeper penetration depth when it comes to the back-side detection of cracks.



#### 4.4 Summary

After the probe was developed, the performance of the probe was analysed and studied with respect to different slits' parameters. The simulation of the magnetic field distribution produced by a line current was done to validate the lift off effect by manipulating the distance between the probe and line current from 1 mm to 5 mm. From the simulation, it was shown that the probe could detect the changes of eddy current more easily when it was near to the current and the resolution of the reconstructed current was improved.

When the probe was farther with the sample, the distribution intensity started to fade and broaden. Therefore, during the experiment the probe has been set to 1 mm from the sample. The first analysis of the experiment data was the comparison of different detection techniques where the probe was line-scanned above the slits' position using three different detection techniques.

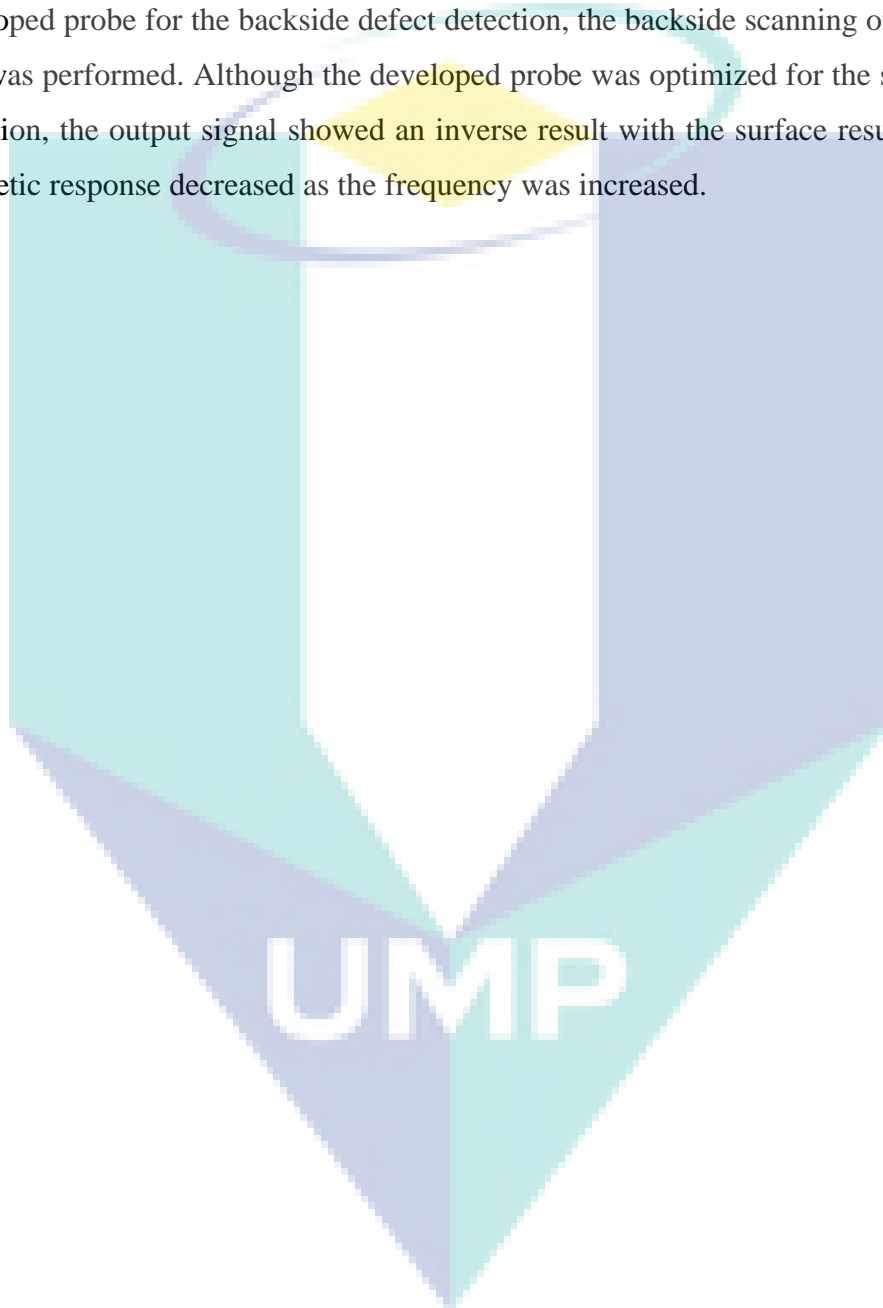
From the results, it was shown that the differential technique using the dynamic phase reference was the best technique compare to the others to reduce the drift effect and noises and able to detect slits. In this study, real component of the detected magnetic signal vector was neglected because the detected output signal contained the strong magnetization signal and did not show any changes at the slits area. The first sample with five different depths of slits was line-scanned at frequencies from 90 Hz to 1 kHz and all the slits showed increasing changes of the magnetic response at the slits area as the frequency was increased.

From the plotted data of the correlation between the depth of slits and the frequency, it was shown that the value of magnetic response was increased when the excitation frequency was increased. The 2-D scanning was implemented to evaluate the changes of magnetic response where the results showed a similar characteristic with the line-scan signal. Then, the effect of the excitation field strength was examined by applying multiple values of current amplitudes to the excitation coil. The results showed that the optimum amplitude was 4 mA to obtain a high signal-to-noise ratio of detected signal with less noises.

Next, the width dependence was evaluated using 30-mm long slits with various widths. All the slits were detected, however, the correlation between the signal intensity could not be found. Then, the length dependence was investigated using slits with a 0.2-mm width and five different length. From the 2-D map scanning, the crack length in

the magnetic map distributions was equivalent to the actual length of the slits. The next sample was the galvanized carbon steel plate with complex shapes of slits where the vertical and horizontal slits were combined.

The slit shape was estimated from the magnetic map where the output displayed a higher intensity change at the major slits. Finally, to show the possibility of the developed probe for the backside defect detection, the backside scanning of the artificial slits was performed. Although the developed probe was optimized for the surface defect detection, the output signal showed an inverse result with the surface results where the magnetic response decreased as the frequency was increased.



## CHAPTER 5

### CONCLUSION

#### 5.1 Introduction

The overall goal of this research was to develop an eddy current testing probe for small crack detection based on the differential technique that consists of the AMR sensors and home-made amplifier circuit. During the inspection of the artificial slits on the galvanized steel plates' surface, the position and characteristic of the slits could be evaluated by the ECT probes. The understanding and application of ECT technique in the NDT field were studied in this work. This chapter concludes the results and analysis of this study. Possible future works for this study are also discussed to improve for the future.

#### 5.2 Conclusion

During this study, the ECT method was applied to detect a minor surface defect and backside defect. Although the ECT method was commonly applied to non-ferromagnetic materials such as aluminium, this study aimed to apply it on ferromagnetic materials such as the galvanized steel plates. For this reason, an effective eddy current test technique has been developed for a reliable detection of the slits on the galvanized steel plates. This technique has resulted in a reliable detection of the slits using the 1-mm lift-off ECT probe. To evaluate the submillimetre crack, the probe needs to be designed properly where it should meet the requirements of the size of cracks.

The results obtained so far using the developed probe showed that defects could be detected and identified, and the efficiency of the probe was evaluated from the magnetic response measurement of the submillimetre slits. The first objective was

achieved by considering various factors such as the eddy current's direction during the development of the probe. The developed probe was then used to carry out the next objective where the magnetic response from a few samples having different depth, width, length and shapes of artificial slits was studied. Based on the results obtained and discussed in chapter 4, it was successfully shown that the developed ECT probe could detect the slits based on the magnetic response distributions induced by the eddy currents.

The second finding of this research is the validation of the system performance during defect detection with respect to the depth, width, length, and shapes of the slits. The performance of the developed ECT probe was evaluated during detection of the sub-millimetre slits on each of the ferromagnetic carbon steel plate. The results of the experiment using the artificial slits were analysed and compared to check their correlation. The first sample with different depth showed that the correlation between the depth and difference between peak and trough could be established. Then for the next sample, it was shown that the slits of different width could be detected but the correlation between the width and the difference between peak and trough could not be found. This was thought due to the baseline between the AMR sensors was bigger than the width of the slits.

Next, it was shown that the length of the current distribution each of the slits agreed well with the actual length of slits and this could be used as a confident parameter when estimating the crack length. Moreover, the results for the different shapes of slits having horizontal and vertical slits showed that the probe dependency detection depended on the slit direction. However, when horizontal and vertical slits existed together, the detection performance would be dominated by the longer slit direction. Finally, even though the developed ECT probe was optimized for the surface defect detection, it was shown that the developed probe was able to detect backside slits. Moreover, a low frequency was found to be preferable for detection of backside defects. From all the analysis that have been done, it was proven that the different parameters of the slits would give a different signal characteristic.

### 5.3 Recommendations for Future Work

This study has achieved the new ECT probe where this probe could detect a sub-millimetre slit that is valuable for the crack detection. However, there are still some conditions to study and rooms for improvements so that it can be used for real applications. The followings are some of the recommendations suggested for this research.

The developed system was able to identify artificial slits by monitoring the flow of the eddy currents in the magnetic distribution map. However, the output signal only showed if the slit was a perpendicular slit and showed a lack of performance in detecting the parallel slit as a future recommendation, a better probe needs to be developed by adding more sensors so that the defect can be detected in any direction.

Moreover, to make the probe becomes more sensitive to detect the tiny size of the defect, the area of coil needs to be reduced so that eddy current can concentrate in a small area. Future work should focus on various types of defects and develop a superior system which can be applied and be robust enough to operate in the toughest of environments.



UMP

## REFERENCES

- Abdullah, B. M., Mason, A., & Al-Shamma'A, A. (2013). Defect detection of the weld bead based on electromagnetic sensing. *Journal of Physics: Conference Series*, 450(1). <https://doi.org/10.1088/1742-6596/450/1/012039>
- Allweins, K., Kreutzbruck, M. Von, Gierelt, G., Allweins, K., Kreutzbruck, M. Von, & Gierelt, G. (2006). Defect detection in aluminum laser welds using an anisotropic magneto-resistive sensor array Defect detection in aluminum laser welds using an anisotropic magneto-resistive sensor array, *102*(2005), 1–4. <https://doi.org/10.1063/1.1852391>
- Alpsten, G. (2017). Causes of Structural Failures with Steel Structures.
- Atherton, D. L., Teitsma, A., & Atherton, D. L. (2014). Detection of anomalous stresses in gas pipelines by magnetometer survey ( invited ) Determination of acoustic speed for improving leak detection and location in gas pipelines Detection of anomalous stresses in gas pipelines by magnetometer survey ( invited ), *8130*(1982). <https://doi.org/10.1063/1.330316>
- Auld, B. A., & Moulder, J. C. (1999). Review of Advances in Quantitative Eddy Current Nondestructive Evaluation, *18*(1). <https://doi.org/10.1023/A:102189852>
- Auld, B. A., Moulder, J. C., Jefferies, S., Shull, P. J., Ayter, S., & Kenney, J. (1989). Eddy-Current Reflection Probes : Theory and Experiment, 1–11. <https://doi.org/10.1007/BF01607866>
- Biddle, C. C. (1976). Theory of Eddy Currents for Nondestructive Testing.
- Biegel, B. (2008). Metal Detection, 6–9.
- Bousack, H., & Gmbh, J. (1996). Eddy current technique with high structures, *36*(2), 83–86. [https://doi.org/10.1016/0011-2275\(96\)83807-0](https://doi.org/10.1016/0011-2275(96)83807-0)
- Chady, T., Enokizono, M., & Sikora, R. (1999). Crack Detection and Recognition Using an Eddy Current Differential Probe, *35*(3), 1849–1852. <https://doi.org/10.1109/20.767393>
- Chu, H. H., & Wang, Z. Y. (2016). A vision-based system for post-welding quality measurement and defect detection. *International Journal of Advanced Manufacturing Technology*, *86*(9–12), 3007–3014. <https://doi.org/10.1007/s00170-015-8334-1>
- Drunen, G. Van, & Cecco, V. S. (1984). Recognizing limitations in eddy · current testing, *17*(1), 9–17. [https://doi.org/10.1016/0308-9126\(84\)90108-1](https://doi.org/10.1016/0308-9126(84)90108-1)

- Dwivedi, S. N., & Sharan, A. (2003). Development of knowledge-based engineering module for diagnosis of defects in casting and interpretation of defects by nondestructive testing, *141*, 155–162. [https://doi.org/10.1016/S0924-0136\(02\)00948-2](https://doi.org/10.1016/S0924-0136(02)00948-2)
- Forrest G. West. (1960). Magneto-resistive Measurements on Domain Rotation in Nickel - Iron Alloy Films. <https://doi.org/10.1038/188129a0>
- Forster, F. (1975). Developments in the magnetography of tubes and tube welds, (December), 1975. [https://doi.org/10.1016/0029-1021\(75\)90029-8](https://doi.org/10.1016/0029-1021(75)90029-8)
- García-Martín, J., Gómez-Gil, J., & Vázquez-Sánchez, E. (2011). Non-destructive techniques based on eddy current testing. *Sensors*, *11*(3), 2525–2565. <https://doi.org/10.3390/s110302525>
- Gayer, A., Saya, A., & Shiloh, A. (1990). Automatic recognition of welding defects in real-time radiography. *NDT International*, *23*(3), 131–136. [https://doi.org/10.1016/0308-9126\(90\)90109-2](https://doi.org/10.1016/0308-9126(90)90109-2)
- Ghanei, S., Kashefi, M., & Mazinani, M. (2013). Eddy current nondestructive evaluation of dual phase steel. *Materials and Design*, *50*, 491–496. <https://doi.org/10.1016/j.matdes.2013.03.040>
- Gros, X. E. (1995). An eddy current approach to the detection of damage caused by low-energy impacts on carbon fibre reinforced materials, *16*(3), 167–173. [https://doi.org/10.1016/0261-3069\(95\)00025-9](https://doi.org/10.1016/0261-3069(95)00025-9)
- Hamia, R., Cordier, C., Saez, S., & Dolabdjian, C. (2010). Eddy-Current Nondestructive Testing Using an Improved GMR Magnetometer and a Single Wire as Inducer : A FEM Performance Analysis, *46*(10), 3731–3737.
- He, D. (2017). AMR Sensor and its Application on Nondestructive Evaluation. *Magnetic Sensors - Development Trends and Applications*. <https://doi.org/10.5772/intechopen.70334>
- Holt, C., Thompson, E., Yarnamoto, T., Matsuo, Y., Ohya, Y., Milone, A. F., ... Bozorth, R. M. (1983). Stress Induced Magnetization Changes of Steel Pipes-La boratory Tests, *M*(4), 1564–1568. <https://doi.org/10.1109/TMAG.1984.1063572>
- Hutchins, D. A. (1999). Air-coupled ultrasonic testing of metals using broadband pulses in through-transmission, *37*, 19–22. [https://doi.org/10.1016/S0041-624X\(98\)00034-1](https://doi.org/10.1016/S0041-624X(98)00034-1)
- Jander, A., Smith, C., & Schneider, R. (2005). Magneto-resistive sensors for nondestructive evaluation. *Proceedings of SPIE*, 1–13. <https://doi.org/10.1117/12.601826>
- Janousek, L., Capova, K., Yusa, N., & Miya, K. (2008). Multiprobe Inspection for Enhancing



Sizing Ability in Eddy Current Nondestructive Testing, *44*(6), 1618–1621.  
<https://doi.org/10.1109/TMAG.2008.916547>

Jiles, D. C. (1990). Review of magnetic methods for non destructive evaluation-part 2. *NDT International*, *23*(2), 83–92. [https://doi.org/10.1016/0308-9126\(90\)91892-W](https://doi.org/10.1016/0308-9126(90)91892-W)

K. Kuijk ; W. van Gestel ; F. Gorter. (1975). The Barber Pole, A Linear Magnetoresistive Head, *M*(5), 1215–1217. <https://doi.org/10.1109/TMAG.1975.1058886>

Kasai, N., Fujiwara, Y., Sekine, K., & Sakamoto, T. (2008). ARTICLE IN PRESS NDT & E International Evaluation of back-side flaws of the bottom plates of an oil-storage tank by the RFECT, *41*, 525–529. <https://doi.org/10.1016/j.ndteint.2008.05.002>

Kreutzbruck, M., & Allweins, K. (2002). High field resolution for nondestructive testing using sensitive magnetometers, *101*, 85–91. [https://doi.org/10.1016/S0924-4247\(02\)00186-3](https://doi.org/10.1016/S0924-4247(02)00186-3)

Lee, J. Y., Lee, S. J., Jiles, D. C., Garton, M., Lopez, R., & Brasche, L. (2003). Sensitivity Analysis of Simulations for Magnetic Particle Inspection Using the Finite-Element Method, *39*(6), 3604–3606. <https://doi.org/10.1109/TMAG.2003.816152>

Marazani, T., Madyira, D. M., & Akinlabi, E. T. (2017). Repair of cracks in metals : A review. *Procedia Manufacturing*, *8*(October 2016), 673–679.  
<https://doi.org/10.1016/j.promfg.2017.02.086>

Massa, G. M. (2000). Finding the optimum conditions for weld testing by magnetic particles, (February 1976), 16–26. [https://doi.org/10.1016/0029-1021\(76\)90029-3](https://doi.org/10.1016/0029-1021(76)90029-3)

Mercier, D. Ã., Lesage, J., Decoopman, X., & Chicot, D. (2006). Eddy currents and hardness testing for evaluation of steel decarburizing, *39*, 652–660.  
<https://doi.org/10.1016/j.ndteint.2006.04.005>

Morimoto, K., Araki, Y., Satake, K., & Shimizu, N. (1992). Numerical and experimental analysis of eddy current testing for a tube with cracks, *28*(March), 1469–1472.  
<https://doi.org/10.1109/20.123973>

Morozov, M., Rubinacci, G., Tamburrino, A., & Ventre, S. (2006). Numerical Models of Volumetric Insulating Cracks in Eddy-Current Testing With Experimental Validation, *42*(5), 1568–1576. <https://doi.org/10.1109/TMAG.2006.870025>

Mottl, Z. (1990). The quantitative relations between true and standard depth of penetration for air-cored probe coils in eddy current testing, *23*(1), 11–18. [https://doi.org/10.1016/0308-9126\(90\)91444-X](https://doi.org/10.1016/0308-9126(90)91444-X)

Nesvijski, E. G. (2000). Some aspects of ultrasonic testing of composites, *0263*, 151–155.

[https://doi.org/10.1016/S0263-8223\(99\)00088-4](https://doi.org/10.1016/S0263-8223(99)00088-4)

- Saari, M. M., Ishihara, Y., Tsukamoto, Y., Kusaka, T., Morita, K., Sakai, K., ... Tsukada, K. (2014). Optimization of an AC/DC High-Tc SQUID Magnetometer Detection Unit for Evaluation of Magnetic Nanoparticles in Solution. *IEEE Transactions on Applied Superconductivity*, 2014(October), 1–1. <https://doi.org/10.1109/TASC.2014.2363633>
- Saari, M. M., Nadzri, N. A., Halil, A. M., Ishak, M., Sakai, K., Kiwa<sup>3</sup>, T., & Tsukada<sup>3</sup>, K. (2019). Design of Eddy Current Testing Probe for Surface Defect Evaluation. *International Journal of Automotive and Mechanical Engineering*, 16(1), 1–11. <https://doi.org/10.15282/ijame.16.1.2019.19.0481>
- Saari, M. M., Sakai, K., Kiwa, T., Sasayama, T., Yoshida, T., & Tsukada, K. (2015). Characterization of the magnetic moment distribution in low-concentration solutions of iron oxide nanoparticles by a high- T c superconducting quantum interference device magnetometer, 321, 1–5. <https://doi.org/10.1063/1.4919043>
- Sasayama, T., Ishida, T., Matsuo, M., & Enpuku, K. (2016). Thickness Measurement of an Iron Plate Using Low-Frequency Eddy Current Testing, 26(5), 1–5. <https://doi.org/10.1109/TASC.2016.2535366>
- Schabowicz, K. (2010). State-of-the-art non-destructive methods for diagnostic testing of building structures – anticipated development trends, X(3), 8–9. [https://doi.org/10.1016/S1644-9665\(12\)60133-2](https://doi.org/10.1016/S1644-9665(12)60133-2)
- Sen, T., Anoop, C. S., & Sen, S. (2017). Study and Analysis of Two GMR-Based Eddy- Current Probes for Defect-Detection. *2017 IEEE International Instrumentation and Measurement Technology Conference (I2MTC)*, 1–6. <https://doi.org/10.1109/I2MTC.2017.7969874>
- Shu, L., Songling, H., & Wei, Z. (2007). Development of differential probes in pulsed eddy current testing for noise suppression, 135, 675–679. <https://doi.org/10.1016/j.sna.2006.10.013>
- Slawomir, T. (2007). Induction coil sensors — a review, 31. <https://doi.org/10.1088/0957-0233/18/3/R01>
- Soni, A. (2018). Advances and Researches on Non Destructive Testing : A Review ScienceDirect Advances and Researches on Non Destructive Testing : A Review, (March). <https://doi.org/10.1016/j.matpr.2017.11.620>
- Stumm, W., & Rotomat, T. (1974). Tube testing by electromagnetic ndt methods--1, (October), 251–256. [https://doi.org/10.1016/0029-1021\(74\)90171-6](https://doi.org/10.1016/0029-1021(74)90171-6)
- Stutzke, N. A., Russek, S. E., Pappas, D. P., Tondra, M., Stutzke, N. A., Russek, S. E., ... Tondra, M. (2014). Low-frequency noise measurements on commercial magnetoresistive

magnetic field sensors Low-frequency noise measurements on commercial magnetoresistive magnetic field sensors, *107*(2005), 2003–2006.  
<https://doi.org/10.1063/1.1861375>

Taylor, P., Pedersen, L. B., Magnusson, K., & Zhengsheng, Y. (2014). Research in Nondestructive Evaluation Eddy Current Testing of Thin Layers Using Co-planar Coils, (December), 37–41. <https://doi.org/10.1080/09349840009409649>

Thien, N. D., Chi, C. Le, & Ngoc, H. N. (2017). An Approach to the Automatic Detection of Weld Defects in Radiography Films Using Digital Image Processing.  
<https://doi.org/10.1109/ICSSE.2017.8030899>

Tondo, F. A., Porto, R. W., Villalobos, L. F. S. S. M., Brusamarello, V. J., & Campestrini, L. (2017). Eddy Current Probe Identification and Analysis. *IEEE Transactions on Instrumentation and Measurement*, *66*(8), 2166–2173.  
<https://doi.org/10.1109/TIM.2017.2684858>

Tsukada, K., Hayashi, M., Nakamura, Y., Sakai, K., & Kiwa, T. (2018). Small Eddy Current Testing Sensor Probe Using a Tunneling Magnetoresistance Sensor to Detect Cracks in Steel Structures. *IEEE Transactions on Magnetics*, *PP*, 1–5.  
<https://doi.org/10.1109/TMAG.2018.2845864>

Tsukada, K., Kiwa, T., Kawata, T., & Ishihara, Y. (2006). Low-Frequency Eddy Current Imaging Using MR Sensor Detecting Tangential Magnetic Field Components for Nondestructive Evaluation, *42*(10), 3315–3317.  
<https://doi.org/10.1109/TMAG.2006.879754>

Tsukada, K., Yoshioka, M., Kawasaki, Y., & Kiwa, T. (2010). Detection of back-side pit on a ferrous plate by magnetic flux leakage method with analyzing magnetic field vector. *NDT and E International*, *43*(4), 323–328. <https://doi.org/10.1016/j.ndteint.2010.01.004>

Vértesy, G., & Kim, D. L. K. (2013). Detection of the Subsurface Cracks in a Stainless Steel Plate Using Pulsed Eddy Current. <https://doi.org/10.1007/s10921-013-0188-6>

## PUBLICATIONS

Nadzri, N. A., Hoe, C. K., & Saari, M. M. (2018). Vehicle Detection System Using Tunnel Magnetoresistance Sensor, 547–555. [https://doi.org/10.1007/978-981-10-8788-2\\_49](https://doi.org/10.1007/978-981-10-8788-2_49)

Nadzri, N. A., Ishak, M., Saari, M. M., & Halil, A. M. (n.d.). Development of Eddy Current Testing System for Welding Inspection, (1), 1–5.

Nadzri, N. A., Saari, M. M., & Razali, S. (2018). Detection of Metallic Contaminant in Aluminium Soda Can Using TMR Sensor, 527–535. [https://doi.org/10.1007/978-981-10-8788-2\\_47](https://doi.org/10.1007/978-981-10-8788-2_47)

Saari, M. M., Nadzri, N. A., Halil, A. M., Ishak, M., Sakai, K., Kiwa<sup>3</sup>, T., & Tsukada<sup>3</sup>, K. (2019). Design of Eddy Current Testing Probe for Surface Defect Evaluation. *International Journal of Automotive and Mechanical Engineering*, 16(1), 1–11. <https://doi.org/10.15282/ijame.16.1.2019.19.0481>

The logo of UMPA (Universiti Malaysia Perlis) is a large, stylized shield shape. It is divided into four quadrants by a white vertical line and a white horizontal line that meet at the center. The top-left quadrant is light blue, the top-right is light purple, the bottom-left is light green, and the bottom-right is light blue. The letters 'UMPA' are written in white, bold, sans-serif font across the bottom of the shield.

UMPA

## APPENDIX A

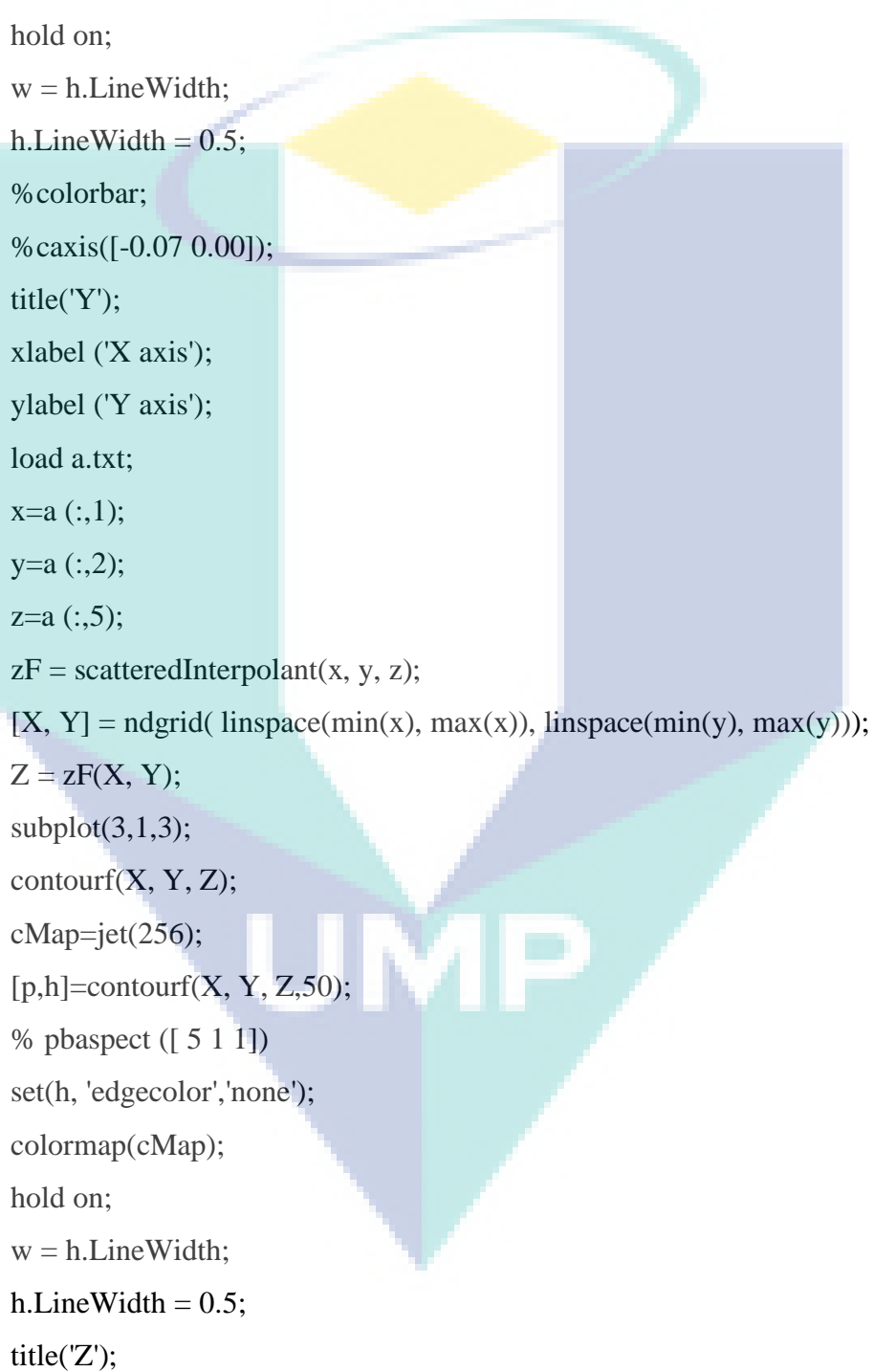
### *Codes for 2D Mapping Via Mat lab*

```
load a.txt;
x=a(:,1);
y=a(:,2);
z=a(:,3);
zF = scatteredInterpolant(x, y, z);
[X, Y] = ndgrid( linspace(min(x), max(x)), linspace(min(y), max(y)));
Z = zF(X, Y);
subplot(3,1,1);
contourf(X, Y, Z);
cMap=jet(256);
[p,h]=contourf(X, Y, Z,50);
% pbaspect ([ 5 1 1])
set(h, 'edgecolor','none');
colormap(cMap);
hold on;
w = h.LineWidth;
h.LineWidth = 0.5;
% yaxis([-25 25])
title('X');
xlabel ('X axis');
ylabel ('Y axis');
load a.txt;
x=a(:,1);
y=a(:,2);
z=a(:,4);
zF = scatteredInterpolant(x, y, z);
[X, Y] = ndgrid( linspace(min(x), max(x)), linspace(min(y), max(y)));
Z = zF(X, Y);
subplot(3,1,2);
contourf(X, Y, Z);
```

```

cMap=jet(256);
[p,h]=contourf(X, Y, Z,50);
% pbaspect ([ 5 1 1])
set(h, 'edgecolor','none');
colormap(cMap);
hold on;
w = h.LineWidth;
h.LineWidth = 0.5;
%colorbar;
%caxis([-0.07 0.00]);
title('Y');
xlabel ('X axis');
ylabel ('Y axis');
load a.txt;
x=a (:,1);
y=a (:,2);
z=a (:,5);
zF = scatteredInterpolant(x, y, z);
[X, Y] = ndgrid( linspace(min(x), max(x)), linspace(min(y), max(y)));
Z = zF(X, Y);
subplot(3,1,3);
contourf(X, Y, Z);
cMap=jet(256);
[p,h]=contourf(X, Y, Z,50);
% pbaspect ([ 5 1 1])
set(h, 'edgecolor','none');
colormap(cMap);
hold on;
w = h.LineWidth;
h.LineWidth = 0.5;
title('Z');

```



## APPENDIX B

### *Codes for Current Flow Simulation Via Mat Lab*

```
clc; %clear the command window
clear; %clear all variables
close all; % to close all opened Figure
% to set lowest and highest point on line along the directions for both I1
% and I2
ymin1= -8;
ymax1= 0;
xmin2 = 0;
xmax2 =8;
zheight = 5;
% information of the line current
I1 = 1*10^-3; % magnitude of current I1
I2 = 1*10^-3; % magnitude of current I2
% to set number of segments for each line current distribution
NumberOfI1Divisions = 50;
NumberOfI2Divisions = 50;
% to compute step size in both x and y directions
dy1=(ymax1-ymin1)/NumberOfI1Divisions;
dx2=(xmax2-xmin2)/NumberOfI2Divisions;
dl1 = [0,dy1,0]; % differential line vector-1 in z-direction
dl2 = [dx2,0,0]; % differential line vector-2 in (-z)-direction
mu0 = 4*pi*1e-7; % permeability of the free space
% to set number of plotting points along x & y axes
NumberOfXPlottingPoints = 50;
NumberOfYPlottingPoints = 50;
% to set the minimum and maximum plotting points on the plane
PlotXmin=-10;
PlotXmax=10;
PlotYmin=-10;
PlotYmax=10;
```



```

%to compute step size in x,y and z direction
PlotStepX= (PlotXmax-PlotXmin)/(NumberOfXPlottingPoints-1);
PlotStepY= (PlotYmax-PlotYmin)/(NumberOfYPlottingPoints-1);
%to build arrays of plot plane
[XData,YData]=meshgrid(PlotXmin:PlotStepX:PlotXmax,
PlotYmin:PlotStepY:PlotYmax);
% to initialize the zero array to fill in the flux density vectors
B1x=zeros(NumberOfXPlottingPoints,NumberOfYPlottingPoints);
B1y=zeros(NumberOfXPlottingPoints,NumberOfYPlottingPoints);
B1z=zeros(NumberOfXPlottingPoints,NumberOfYPlottingPoints);
B2x=zeros(NumberOfXPlottingPoints,NumberOfYPlottingPoints);
B2y=zeros(NumberOfXPlottingPoints,NumberOfYPlottingPoints);
B2z=zeros(NumberOfXPlottingPoints,NumberOfYPlottingPoints);
Btx=zeros(NumberOfXPlottingPoints,NumberOfYPlottingPoints);
Bty=zeros(NumberOfXPlottingPoints,NumberOfYPlottingPoints);
Btz=zeros(NumberOfXPlottingPoints,NumberOfYPlottingPoints);
for ii=1:NumberOfXPlottingPoints
for jj=1:NumberOfYPlottingPoints
PlotX = XData(ii,jj);
PlotY = YData(ii,jj);
Rp=[PlotX PlotY zheight]; %position vector of observation point
% Magnetic flux density due to current I1
for m=1:NumberOfI1Divisions
X1LineCenter = 0; % x-coordinate of line current 1
Y1LineCenter = ymin1+(m-1)*dy1+0.5*dy1; % y-coordinate of line current
1
Z1LineCenter = 0; % ; z-coordinate of line current 1
Rc1 = [X1LineCenter Y1LineCenter Z1LineCenter]; %position vector of the
center of the line segment
R1 = Rp-Rc1; %directional vector pointing from current line segment to the
current observation point
norm_R1=norm(R1); %to get the magnitude of the vector R
R1_Hat=R1/norm_R1; %the unit vector in the direction of R

```

```

dH1=(1/(4*pi*norm_R1*norm_R1))*cross(I1*dI1,R1_Hat); %this is the
contribution from current element
B1x(ii,jj)=B1x(ii,jj)+ mu0*dH1(1,1);
B1y(ii,jj)=B1y(ii,jj)+ mu0*dH1(1,2);
B1z(ii,jj)=B1z(ii,jj)+ mu0*dH1(1,3);
end % end of loop m
% Magnetic flux density due to current I2
for n=1:NumberOfI2Divisions
    X2LineCenter = xmin2+(n-1)*dx2+0.5*dx2; % x-coordinate of line current 2
    Y2LineCenter = 0; % y-coordinate of line current 2
    Z2LineCenter = 0; % ; z-coordinate of line current 2
    Rc2=[X2LineCenter Y2LineCenter Z2LineCenter]; %position vector of center
of current subsection
    R2=Rp-Rc2; %directional vector pointing from current subsection to the current
observation point
    norm_R2=norm(R2); %to get the magnitude of the vector R
    R2_Hat=R2/norm_R2; %the unit vector in the direction of R
    dH2=(1/(4*pi*norm_R2*norm_R2))*cross(I2*dI2,R2_Hat); %this is the
contribution from current element
    B2x(ii,jj)=B2x(ii,jj)+ mu0*dH2(1,1);
    B2y(ii,jj)=B2y(ii,jj)+ mu0*dH2(1,2);
    B2z(ii,jj)=B2z(ii,jj)+ mu0*dH2(1,3);
    Btx(ii,jj)=Btx(ii,jj)+B1x(ii,jj)+B2x(ii,jj);
    Bty(ii,jj)=Bty(ii,jj)+B1y(ii,jj)+B2y(ii,jj);
    Btz(ii,jj)=Btz(ii,jj)+B1z(ii,jj)+B2z(ii,jj);
end % end of loop n
end % end of loop jj
end % end of loop ii
zaxismax= 3*10^-9;
Figure(1)
cMap=jet(256);
[p,h]=contourf(XData,YData,Btx,50);
set(h, 'edgecolor','none');
colormap(cMap);

```

```

hold on
h3 = plot([X1LineCenter,X1LineCenter],[ymin1,ymax1]); % plot line current 1
h4 = plot([xmin2,xmax2],[Y2LineCenter,Y2LineCenter]); % plot line current 2
set([h3,h4],'color','black', 'LineWidth',4); % to set the color and thickness of the

```

line current

```

caxis([-zaxismax zaxismax]);
title('Bx(T)');
xlabel('x(m)');%label x axis
ylabel('y(m)');%label y axis
legend([h3], 'Current I_1');
Figure(2)
cMap=jet(256);
[p,h]=contourf(XData,YData,Bty,50);
set(h, 'edgecolor','none');
caxis([-zaxismax zaxismax]);
colormap(cMap);
hold on
h3 = plot([X1LineCenter,X1LineCenter],[ymin1,ymax1]); % plot line current 1
h4 = plot([xmin2,xmax2],[Y2LineCenter,Y2LineCenter]); % plot line current 2
set([h3,h4],'color','black', 'LineWidth',4); % to set the color and thickness of the

```

line current

```

title('By(T)');
xlabel('x(m)');%label x axis
ylabel('y(m)');%label y axis
legend([h3], 'Current I_1');
Figure(3)
cMap=jet(256);
[p,h]=contourf(XData,YData,Btz,50);
set(h, 'edgecolor','none');
caxis([-zaxismax zaxismax]);
colormap(cMap);
hold on
h3 = plot([X1LineCenter,X1LineCenter],[ymin1,ymax1]); % plot line current 1
h4 = plot([xmin2,xmax2],[Y2LineCenter,Y2LineCenter]); % plot line current 2

```

```

set([h3,h4],'color','black', 'LineWidth',4); % to set the color and thickness of the
line current
title('Bz(T)');
xlabel('x(m));%label x axis
ylabel('y(m));%label y axis
legend([h3], 'Current I_1');
% axis(1.5*[PlotXmin,PlotXmax,PlotYmin,PlotYmax]); %re-scale the axes to
the appropriate range
dBzdx=zeros(NumberOfXPlottingPoints-1,NumberOfYPlottingPoints-1);
dBzdy=zeros(NumberOfXPlottingPoints-1,NumberOfYPlottingPoints-1);
[XData1,YData1]=meshgrid(PlotXmin+PlotStepX/2:PlotStepX:PlotXmax-
PlotStepX/2, PlotYmin+PlotStepY/2:PlotStepY:PlotYmax-PlotStepY/2);
for ii=1:NumberOfXPlottingPoints-1 %column aka x
    for jj=1:NumberOfYPlottingPoints-1 %row aka y
        dBzdx(jj,ii)=(Btz(jj,ii+1)-Btz(jj,ii))/PlotStepX;
        dBzdy(jj,ii)=(Btz(jj+1,ii)-Btz(jj,ii))/PlotStepX;
    end
end
end
Figure(4)
% surf(XData1,YData1,dBzdx), hold on
%h3 = plot3([X1LineCenter,X1LineCenter],[ymin1,ymax1],[-1*10^-10,-1*10^-
10]); % plot line current 1
%h4 = plot3([xmin2,xmax2],[Y2LineCenter,Y2LineCenter],[-1*10^-10,-1*10^-
10]); % plot line current 2
cMap=jet(256);
[p,h]=contourf(XData1,YData1,dBzdx,50);
set(h, 'edgecolor','none');
colormap(cMap);
hold on
h3 = plot([X1LineCenter,X1LineCenter],[ymin1,ymax1]); % plot line current 1
h4 = plot([xmin2,xmax2],[Y2LineCenter,Y2LineCenter]); % plot line current 2
set([h3,h4],'color','black', 'LineWidth',4); % to set the color and thickness of the
line current
xlabel('x(m));%label x axis

```

```

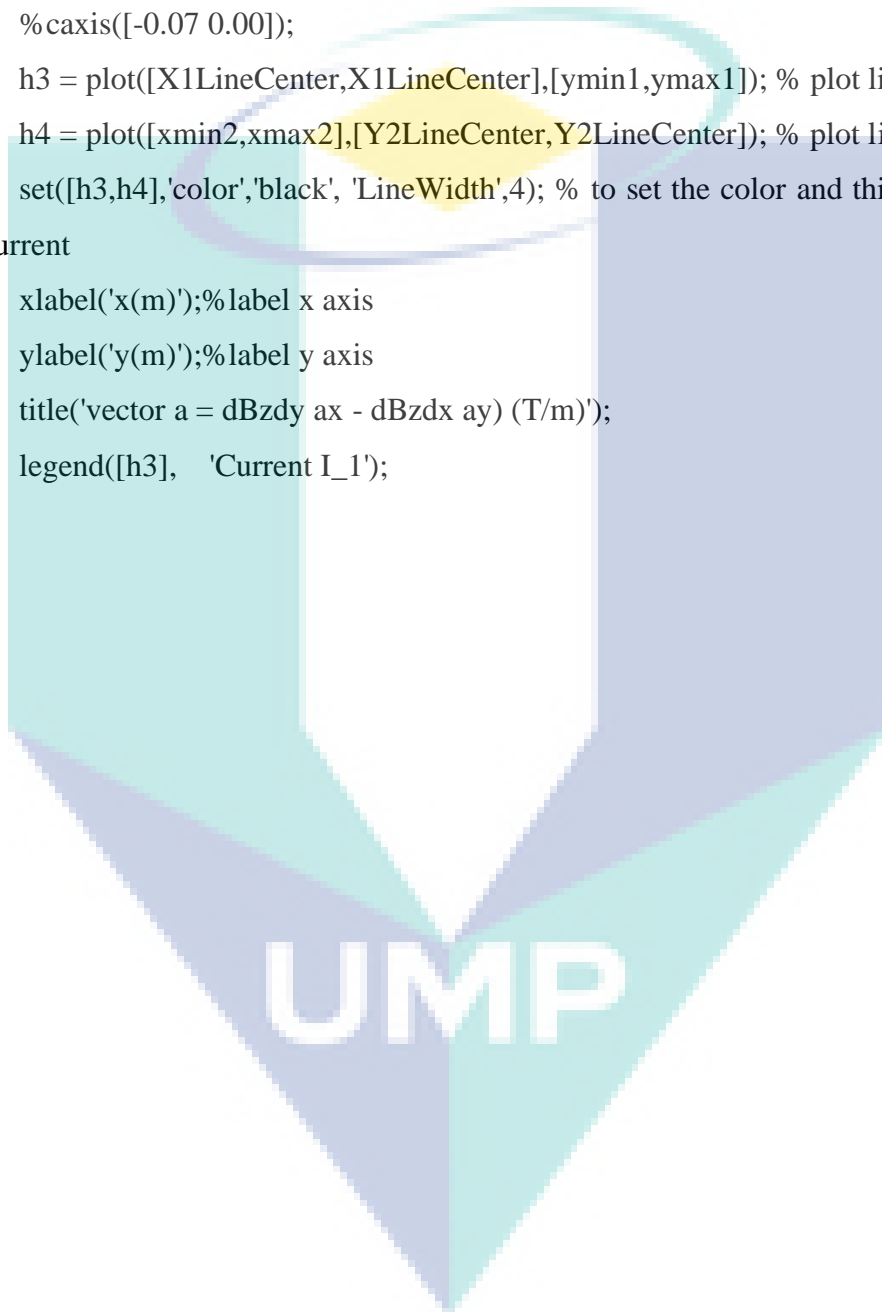
ylabel('y(m)');% label y axis
title('d(Bz)/dx (T/m)');
legend([h3], 'Current I_1');
Figure(5)
% surf(XData1,YData1,dBzdy), hold on
%h3 = plot3([X1LineCenter,X1LineCenter],[ymin1,ymax1],[-1*10^-10,-1*10^-
10]); % plot line current 1
%h4 = plot3([xmin2,xmax2],[Y2LineCenter,Y2LineCenter],[-1*10^-10,-1*10^-
10]); % plot line current 2
cMap=jet(256);
[p,h]=contourf(XData1,YData1,dBzdy,50);
set(h, 'edgecolor','none');
colormap(cMap);
hold on
%colorbar;
%caxis([-0.07 0.00]);
h3 = plot([X1LineCenter,X1LineCenter],[ymin1,ymax1]); % plot line current 1
h4 = plot([xmin2,xmax2],[Y2LineCenter,Y2LineCenter]); % plot line current 2
set([h3,h4],'color','black', 'LineWidth',4); % to set the color and thickness of the
line current
xlabel('x(m)');% label x axis
ylabel('y(m)');% label y axis
title('d(Bz)/dy (T/m)');
legend([h3], 'Current I_1');
Figure(6)%arrow vector recreation
% surf(XData1,YData1,dBzdy), hold on
%h3 = plot3([X1LineCenter,X1LineCenter],[ymin1,ymax1],[-1*10^-10,-1*10^-
10]); % plot line current 1
%h4 = plot3([xmin2,xmax2],[Y2LineCenter,Y2LineCenter],[-1*10^-10,-1*10^-
10]); % plot line current 2
%cMap=jet(256);
%[p,h]=contourf(XData1,YData1,sqrt(dBzdy^2+dBzdx^2),50);
%set(h, 'edgecolor','none');
%colormap(cMap);

```

```

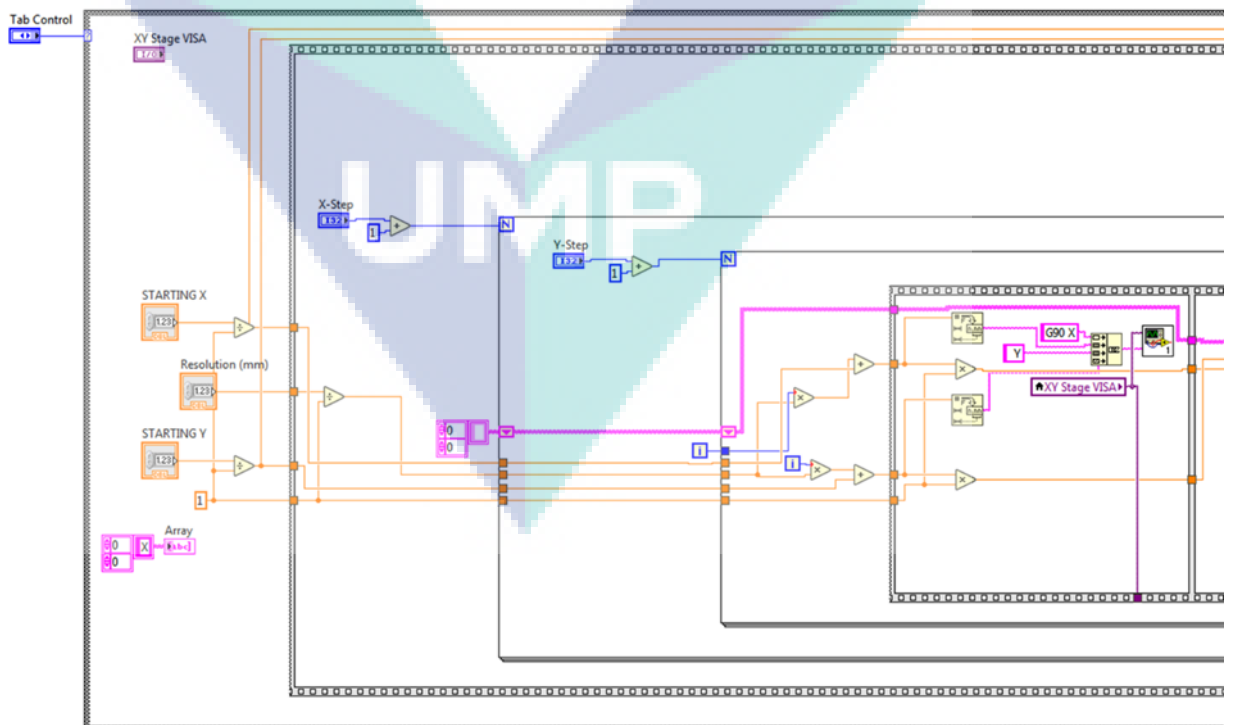
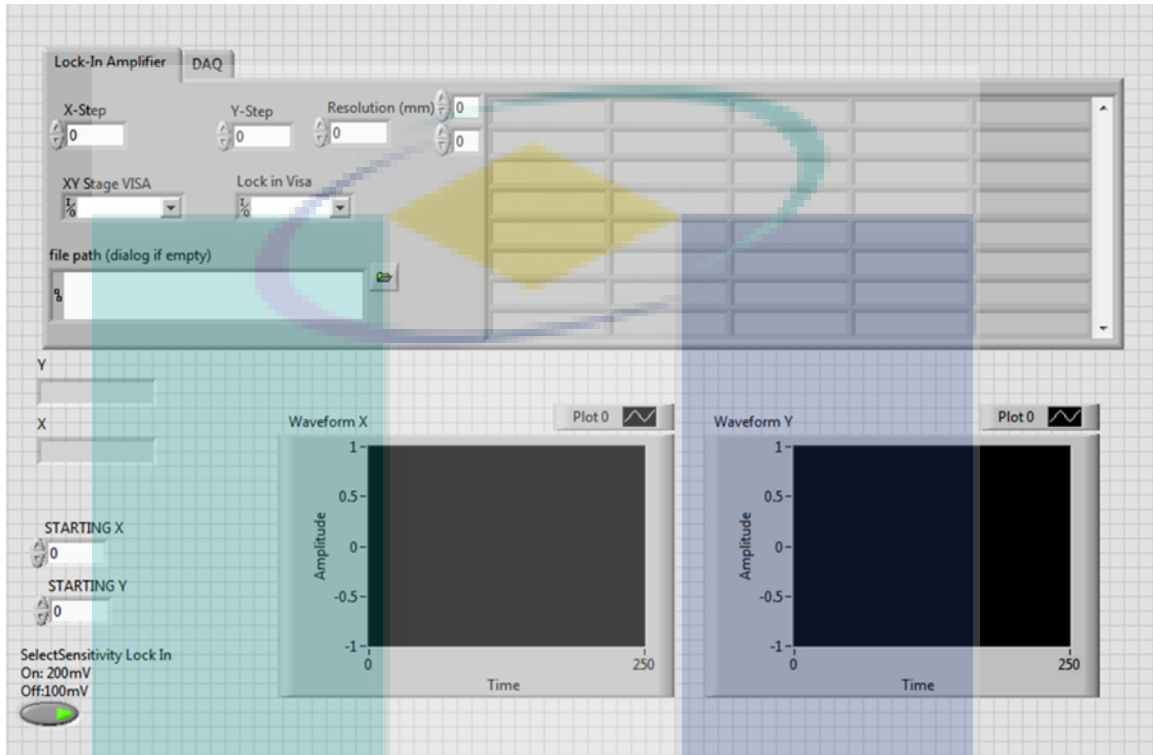
%hold on
h1=quiver(XData1,YData1,dBzdy,-dBzdx),
set(h1,'AutoScale','on', 'AutoScaleFactor', 3)
hold on
%colorbar;
%caxis([-0.07 0.00]);
h3 = plot([X1LineCenter,X1LineCenter],[ymin1,ymax1]); % plot line current 1
h4 = plot([xmin2,xmax2],[Y2LineCenter,Y2LineCenter]); % plot line current 2
set([h3,h4],'color','black', 'LineWidth',4); % to set the color and thickness of the
line current
xlabel('x(m)');% label x axis
ylabel('y(m)');% label y axis
title('vector a = dBzdy ax - dBzdx ay) (T/m)');
legend([h3], 'Current I_1');

```

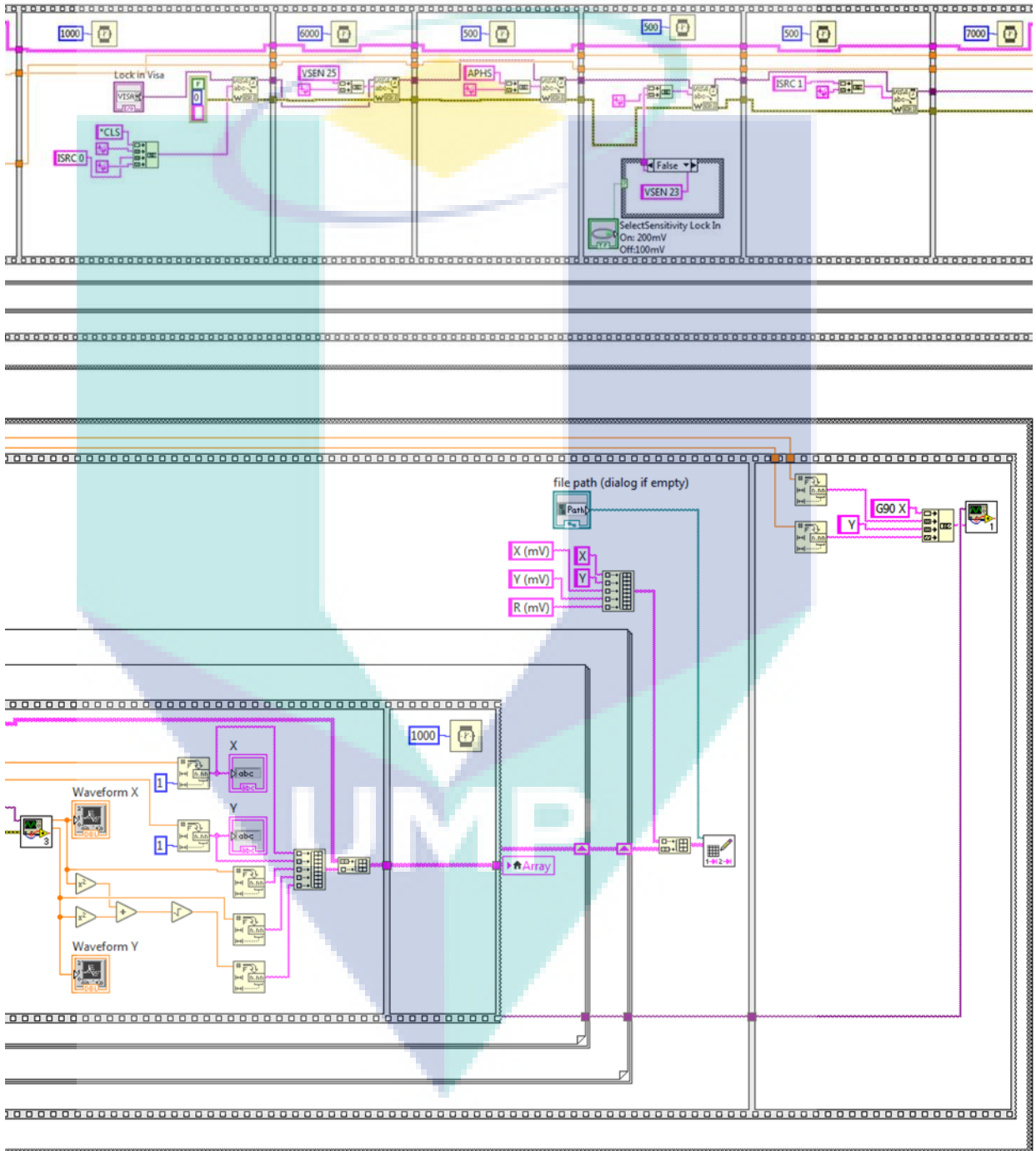


## APPENDIX C

Front panel (GUI) and block diagram of the measurement system via Lab view VI







# An MFL Probe using Shiftable Magnetization Angle for Front and Back Side Crack Evaluation

Mohd Aufa Hadi Putera Zaini  
Faculty of Electrical and Electronics  
Engineering  
Universiti Malaysia Pahang  
26600 Pekan, Malaysia  
mek18006@stdmail.ump.edu.my

Aiman Mohd Halil  
Faculty of Mechanical Engineering  
Universiti Malaysia Pahang  
26600 Pekan, Malaysia  
aimanmh@ump.edu.my

Mohd Mawardi Saari  
Faculty of Electrical and Electronics  
Engineering  
Universiti Malaysia Pahang  
26600 Pekan, Malaysia  
mmawardi@ump.edu.my

Keiji Tsukada  
Graduate School of Interdisciplinary  
Science and Engineering in Health  
Systems  
Okayama University,  
Okayama 700-8530, Japan  
tsukada@cc.okayama-u.ac.jp

Nurul A'in Nadzri  
Faculty of Electrical and Electronics  
Engineering  
Universiti Malaysia Pahang,  
26600 Pekan, Malaysia  
mel17005@stdmail.ump.edu.my

**Abstract**—Magnetic Flux Leakage (MFL) is one of the common methods in Non-destructive Tests employing magnetic technique. It can be used to detect flaws such as cracks in metallic materials such as steel, whereas, steel is widely known as a base material used for constructions. Therefore, early detection of these flaws is very crucial in order to prevent any accident that could cost lives. Conventionally, MFL method utilizes a strong magnetic field to saturate samples and detects the magnetic flux leakage. However, in this study, a sensitive magnetic probe has been developed to remove the need of using a strong magnetic field to saturate samples. The MFL probe is fabricated with 2 AMR sensors, a home-made amplifier circuit, a set/reset circuit and a flexible yoke. Furthermore, the flexible yoke is proposed in order to apply the magnetic field to the sample at different magnetization angles. Using the developed probe, we measure the magnetic responses at front and back side surfaces of a 2-mm galvanized steel plate at different frequencies. The sample itself is embedded with artificial slits with different depth, ranging from 1.0 mm to 1.6 mm. Moreover, the effect of different magnetization angle of 60° and 90° from the surface is also discussed. From the results, it can be said that the 60° magnetization angle from the surface is proved to provide a considerable improvement for the surface slit detection, while, having close to no effect compared to the 90° magnetization angle on the back side slit detection.

**Keywords**—NDT, magnetic flux leakage, crack in steel, magnetization angle

## I. INTRODUCTION

Nowadays, steel structures are commonly used in various infrastructures such as buildings and transportations. The steel itself is considered as a versatile and basic material for constructions which can exist in a myriad of forms such as plates, cables as well as in reinforcement and fabricated structures, such as buildings [1]. Thus, the safety and workability of the steel structures should always be monitored to prevent fatal accidents. Early detection of defects such as cracks in steel structures is very important either for the front side crack or the back side crack. There are several ways at which cracking can occur such as due to fatigue, which is caused by the exposure of continues stress and strain on a uniform metallic material [2], [3].

This is where Non-destructive Test (NDT) comes into play, which is quite essential in terms of the defect detection

such as cracks in a material. NDT, which is composed of a wide-ranging group of analysis techniques, offers an inspection method that can conserve both money and time since the serviceability of the subject that are being evaluated is not harmed or permanently altered or changed. For steel components, the NDT techniques can be divided into a few methods such as visual inspection, ultrasonic inspection, radiography, and magnetic methods [1], [4]–[8]. The visual inspection method can be immediately ruled out as this method struggles in tackling flaws that are quite impossible to be seen with naked eyes such as back side cracks and sub-millimeter cracks.

Therefore, the magnetic method can be regarded as a favorable technique especially in the inspection of metallic materials such as steel due to the fact that the material is conductive and possesses strong magnetic properties. Furthermore, the reason why magnetic method is quite popular is due to its characteristics which is safe, fast and non-contact. The magnetic methods of NDT can be categorized into two principles of measurement, which is the eddy current and flux leakage measurements [9].

The eddy current approach depends on the analysis of the characteristics of eddy current which is generated in a conductive compound after a magnetic field is applied to it. There are few methods that are based on this approach such as the Eddy Current Testing (ECT), Pulse Eddy Current (PEC) and Remote Field Testing (RFT) [10]–[12]. For conventional ECT, it basically utilizes two types of coils: a detection coil and an excitation coil. Usually, an AC current is supplied to the excitation coil which will emit primary magnetic field to the conductive compound. Then, the induced secondary magnetic field of the eddy current is then picked up by the detection coil [13]. In the detection of crack, the eddy current circulation in the compound will be disrupted whenever there are flaws. However, an improve version of ECT probe that utilizes a compact magnetic sensor has been reported to replace the use of the inductive detection coil where it can provide a distinct signal of crack detection based on frequency response characteristic and localized detection performance [14].

The other principle of measurement in the magnetic methods is the flux leakage measurement. While the setup is almost the same as the eddy current measurement, this approach differs on the detection principle. Basically, this

approach relies on the disruption of magnetic flux at the surface of a metallic material which is located at the location of a defect in the metallic material. In this approach, there are two methods available which are the Magnetic Particle Inspection (MPI) and the Magnetic Flux Leakage (MFL). Compared to MPI which utilizes substances like iron fillings, MFL method uses a device, or simply a magnetometer to capture those flux leakages [8]. Furthermore, an improvement of using a sensitive magnetic sensor such as the Anisotropic Magnetoresistive (AMR) sensor has been implemented which successfully reduce the need for the magnetic saturation of the metallic material [9]. The design and analysis of the MFL systems however, do require a complex understanding of interactions among the leakage flux, excitation field and the flaws in the compound [15].

In this research, a compact and small-sized non-saturated MFL probe with flexible yoke is developed. The probe is fabricated from 2 AMR sensors (HMC1001, Honeywell) to form a differential probe. This probe is designed to evaluate front and back side cracks which is difficult to be seen via naked eyes. Artificial slits of different depths ranging from 1 mm to 1.6 mm are fabricated on a galvanized steel plate with a thickness of 2 mm and they are evaluated using the developed system. Then, the performance of the developed MFL probe is assessed by analyzing the magnetic response resulted from the artificial slits.

## II. EXPERIMENTAL SETUP

### A. Development of Yoke

Compared to the conventional MFL system where the core of the yoke is made up in solid state, this research is focusing on developing a rather flexible yoke to make the yoke more versatile and can be shaped to compensate with the housing of the MFL probe. Instead of using a rigid material such as soft iron core, the core is replaced by a mixture of slime and iron powder to make the yoke becomes flexible. The slime itself is actually a mixture of PVA glue and saline solution. Therefore, an optimum mixture of iron powder, PVA glue and saline solution with a ratio of 1:0.24:0.04 is used to fabricate the yoke's core. Then, the mixture is filled in the yoke housing. The yoke is divided into 3 part, which is a connector and two identical yoke ends. The connector is fabricated from Thermoplastic Polyurethane (TPU) which is a rubber-like material and also referred to as the bridge between rubbers and plastics. This by any means, allows the connector to be extremely flexible, durable and smooth to the touch. Finally, all three parts of the yoke is assembled. Then, each end of the yoke is wound by excitation coils with 100 turns of a 0.65-mm magnet wire. The developed yoke can be bent, thus, allowing the sample to be magnetized at shiftable magnetization angles below than  $90^\circ$  from the surface as in Fig. 1.

### B. MFL Probe

The MFL probe is fabricated with two AMR sensors, a home-made amplifier circuit, a set/reset circuit and a flexible yoke with excitation coils wound at the both ends of the yoke. In this research, a sensitive sensor is used in order to enable the non-saturation technique of MFL. Comparing with other sensors, SQUID is considered as the most sensitive sensor as it possesses the lowest noise [16].

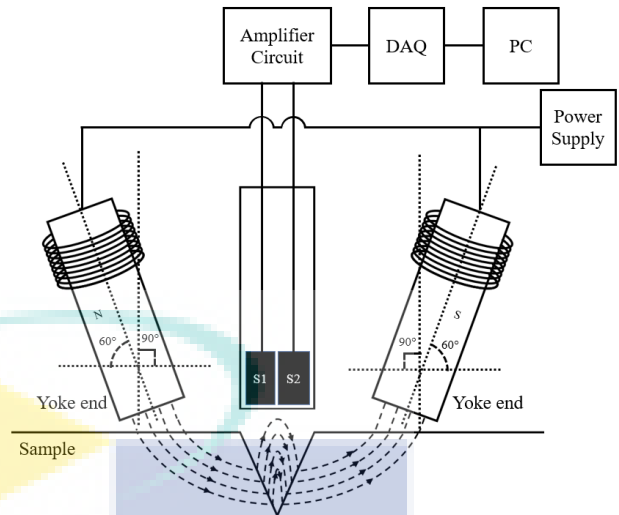


Fig. 1. Schematic diagram of the MFL system

However, due to the fact that it needs liquid nitrogen or helium for cooling, the SQUID sensor requires a complex heat insulation structure where it may not be easily compacted [17], [18]. On the other hand, AMR sensors offer a sensitive detection and is small in size. The AMR sensor used in this research consists of 4 resistive MR elements wound with a set/reset strap in a Wheatstone bridge connection as shown in Fig. 2. These AMR elements can easily lose its sensitivity whenever it is exposed with a strong magnetic field. Thus, by using the set/reset strap, the sensitivity of the AMR sensor can be recovered by flowing high-pulse current through it [19]. Therefore, a set/reset circuit is developed to provide those high-pulse current which can be controlled manually and automatically.

Also, it is worth noting that, two AMR sensor will be used in the probe. Basically, an AMR sensor will output absolute values. Thus, any magnetic response obtained via one AMR sensor is not a pure signal coming from the flux leakage as it will contain a lot of magnetic noises including the environmental noise. Therefore, two AMR sensor is proposed to form a differential sensor and the response from one sensor will be referenced with the other sensor. This will eliminate background noises and improve the MFL probe sensitivity. The distance between the two sensor or the baseline is set to be 4 mm. Then, to make the output of the sensor to be readable by a data acquisition (DAQ) card (NI-USB 6212, National Instruments), an amplifier circuit is fabricated. The amplifier circuit basically consists of two instrumentation amplifiers (INA), each with a gain of 40 dB.

### C. Measurement System

The measurement system consists of the developed MFL probe, power supply, DAQ card, and PC as shown in Fig. 1. The excitation coils are provided with signals of variable frequencies. Then, the pre-amplified signal of the two AMR sensors is connected to the DAQ card. The MFL probe is then attached to an XY-stage with a dimension of 55 cm  $\times$  45 cm. An XY-stage controller is developed via a virtual instrument (LabVIEW, National Instruments). Meanwhile, the excitation coils at both yoke ends are connected with a power supply.



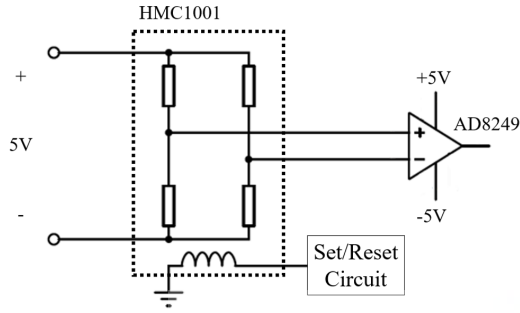


Fig. 2. Schematic diagram of one HMC1001 AMR sensor connected to an AD8249 Instrumentation Amplifier and a Set/Reset circuit.

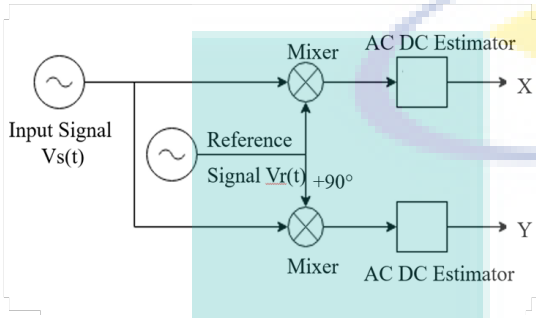


Fig. 3. Block diagram of the digital lock-in amplifier that has been developed via LabVIEW.

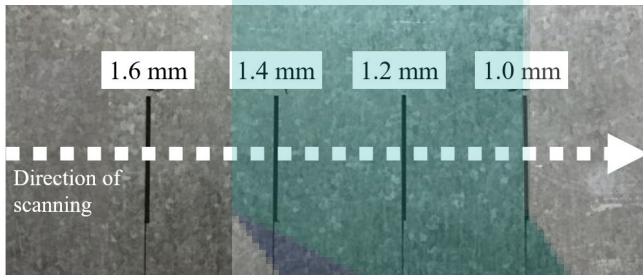


Fig. 4. Scanning procedure on the galvanized steel sample with artificial slits with depths of ranging from 1.0 mm to 1.6 mm.

A lock-in amplifier (LIA) is very crucial in this research as it helps extracting signal amplitudes and phases in extremely noisy environments. However, instead of using a hardware-type LIA, which is huge in size, a digital LIA is developed via LabVIEW as shown in Fig. 3 by obtaining the data streamed by the DAQ card. The experiment setup is hugely simplified by eliminating the huge LIA by replacing it with a DAQ card. Finally, an integration of the XY-stage controller and the DAQ system is developed via LabVIEW.

The sample used is made up of galvanized steel with a thickness of 2 mm with artificial slits with depths of 1 mm, 1.2 mm, 1.4 mm and 1.6 mm. For every measurement, a line scan is conducted as indicated in Fig. 4. The resolution of the line scanning is set to be 1 mm.

The measurement is conducted for two different magnetization angles which are at  $60^\circ$  and  $90^\circ$  from the surface of the sample. Then, for each angle, the frequency of at 0.3 A. the signal supplied into the excitation coils is varied to be 10 Hz, 40 Hz, 130 Hz and 490 Hz, while the amplitude is fixed.

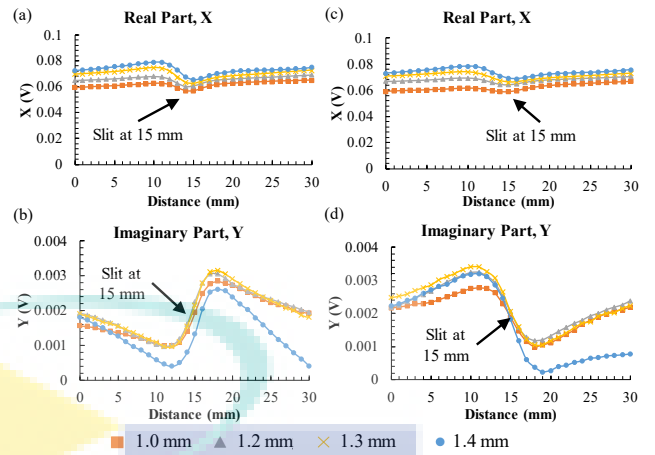


Fig. 5. Raw waveforms from measurements of front side and back side slits at a frequency of 40 Hz and an amplitude of 0.3 A. (a) Real and (b) imaginary parts of the front side measurements. (c) Real and (d) imaginary parts of the back side measurements.

### III. RESULTS AND DISCUSSION

#### A. Raw Waveform

From the line scan measurement at the excitation frequency of 40 Hz and amplitude of 0.3 A as shown in Fig. 5, the real and imaginary parts did differ with each other. For the real part, the magnetic response reached a minimum value at the position of slits, while for the imaginary part, the slit position can be identified in between the peak and trough of the magnetic response. Also, the real part of the signal can be regarded as the MFL signal. Meanwhile, the imaginary signal could represent the eddy current signal, which is lagging  $90^\circ$  in nature compared to the excitation magnetic field. The results for the front side measurement can be seen in Fig 5 (a) and (b), while, Fig. 5 (c) and (d) are the results of the back side measurement. By comparing those two, from the real part perspective, it could be seen that the signals were almost identical between front and back side measurements. However, from the imaginary part point of view, the signals could be said to be inverse to each other. In the front side measurement, it can be seen that the intensity change was from minimum to maximum, while, the intensity change for the back side measurement was from maximum to minimum. The difference could be caused by eddy current dependency that dominated the front surface.

#### B. Measurement of two different magnetization angles.

From Fig. 6, the result of the  $90^\circ$  magnetization angle for front side and back side can be seen. In this result, delta values of real and imaginary parts were used where they represented the difference between the maximum value and the minimum value of the peaks and troughs in the magnetic response waveforms. For the front side, it can be seen that whenever there was an increase in frequency, the delta values increased as well, be it in the real part or the imaginary part. From the real part for the front side measurement, it can be seen that, as the depth of slits went deeper, the delta values were also incremented. However, as the depth increased, the increase of delta value would start to decrease at some point and saturated as shown in Fig. 6 (a). This showed that that the flux leakage was reaching

saturation as the depth increased. The same phenomenon could be said for the imaginary part with the only difference was the increment of delta values with regards of depth was much less as in Fig. 6 (b). However, by increasing the frequency, the delta values were increased as well but, by a huge margin compared to the real part.

The case seemed to be quite different for the back side measurement in terms of the increase of delta values with respect to frequency. The overall delta values for the real part of the backside measurement (Fig. 6 (c)) was smaller compared to the delta values of the front side measurement but with an increasing characteristic as the frequency increased. However, the increase margin was quite small compared to front side measurement. However, for the case of the 490-Hz frequency, the delta value seemed to be constant without showing any effect with regard of depth. This might be caused by the eddy current dependency which blocked the penetration of the magnetic field at a high frequency. However, the imaginary part of the back side measurement indicated that the delta values were also increased when the depth as well as frequency increased as shown in Fig. 6 (d). However, the effect of the frequency was insignificant compared to the delta of imaginary part of the front side as shown in Fig. 6 (b).

Fig. 7 shows the signal difference extracted from line scan measurements at the 60° magnetization angle. The aim for this measurement was to compare the effect of 90° and 60° magnetization angles towards the delta values of both front side and back side measurements. From Fig. 7 (a), it can be seen that the delta values of the real part for the front side measurement at the 60° magnetization angle showed an increase compared to the delta of the real part for the front side measurement at the 90° magnetization angle as shown in Fig. 6 (a). However, as the depth increased more than 1.4 mm for the 60° magnetization angle, the delta values started to decrease, showing that it reached saturation faster compared to the 90° magnetization angle measurement. Next, by observing the delta of the imaginary part for the front side measurement at the 60° magnetization angle, it can be seen that the increase was greater compared to the delta of the imaginary part of the front side measurement at the 90° magnetization angle. But both imaginary data showed an increase of delta values with respect to the depth as well as the frequency.

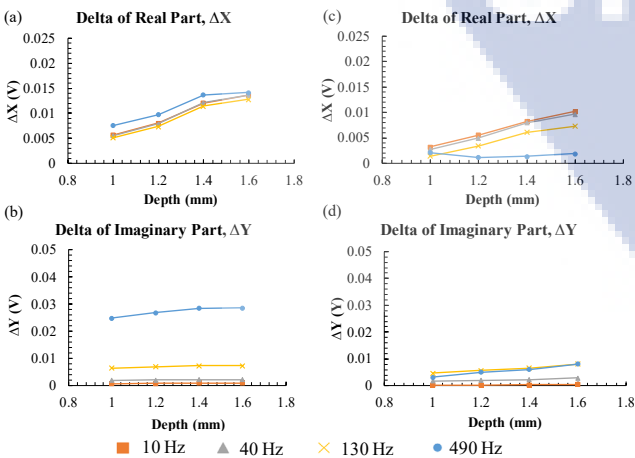


Fig. 6. Signal differences at the 90° magnetization angle. Delta values of (a) real and (b) imaginary parts of the front side measurements. Delta values of (c) real and (d) imaginary parts of the back side measurements.

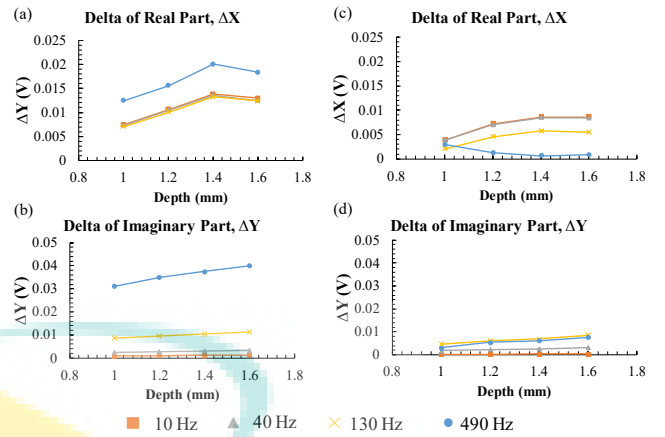


Fig. 7. Signal differences at the 60° magnetization angle. Delta values of (a) real and (b) imaginary parts of the front side measurements. Delta values of (c) real and (d) imaginary parts of the back side measurements.

The case for the back side measurement at 60° magnetization angle was almost identical to the back side measurement at magnetization angle of 90°. Especially when it was observed in terms of the delta values of the imaginary parts of both measurements as shown in Fig. 6 (d) and Fig. 7 (d). But, for the delta values of the real parts, there was a slight difference. From Fig. 6 (c), it can be seen that the delta values were increased with respect to the depth except for frequency of 490 Hz. The pattern could be said to be almost linear with respect to the frequency. However, from Fig. 7 (c), when at the 60° magnetization angle, the increase of the delta values was not linear with respect to the depth. However, for depth less than 1.2 mm, the rate of the increase was superior compared to the case of the 90° magnetization angle (Fig. 6 (c)).

From these measurements at the 90° and 60° magnetization angles, it could be concluded that the angle of the magnetization has a non-negligible effect for the surface defect detection while less or no effect to the backside defect detection.

#### IV. CONCLUSION

In this research, we developed a non-saturated MFL probe using shiftable magnetization angle for front and back side defect detection. The performance of the developed probe was demonstrated in evaluation of the front and back side slits at different excitation frequency and magnetization angle. The raw waveforms of the real and imaginary parts showed that the slit position can be identified based on peaks and troughs. The signal differences between peaks and troughs showed that the depth of the slits could be estimated for the front and back side slits. It could be said that, the front side measurement did produce an overall higher delta values compared to the back side measurement. Then, the effect of different magnetization angle has also been reviewed. The obtained data showed that, the 60° magnetization angle showed a promising characteristic for the surface slit detection as it provided a higher slope of delta values compared to the case of the 90° magnetization angle. However, this was not the case for the back side measurement. The results of the tilted angle simply showed that the delta values of either real or imaginary component achieve saturation at a faster rate compared the normal angle.

## ACKNOWLEDGMENT

The authors would like to thank to the Ministry of Higher Education of Malaysia (grant no. RDU160115) and the Universiti Malaysia Pahang (grant no. RDU170377) for laboratory facilities and financial assistance.

## REFERENCES

- [1] A. Mccrea, D. Chamberlain, and R. Navon, "Automated inspection and restoration of steel bridges — a critical review of methods and enabling technologies," vol. 11, pp. 351–373, 2002.
- [2] R. Ghoni, M. Dollah, A. Sulaiman, and F. Mamat Ibrahim, "Defect Characterization Based on Eddy Current Technique: Technical Review," *Adv. Mech. Eng.*, vol. 2014, 2014.
- [3] M. I. Ahmad, A. Arifin, and S. Abdullah, "Evaluation of magnetic flux leakage signals on fatigue crack growth of mild steel," no. January, 2016.
- [4] L. Goglio and M. Rossetto, "Ultrasonic testing of adhesive bonds of thin metal sheets," *NDT E Int.*, vol. 32, no. 6, pp. 323–331, 1999.
- [5] Jingpin Jiao, Junjun Sun, Nan Li, Guorong Song, Bin Wu, and Cunfu He, "Micro-crack detection using a collinear wave mixing technique," *NDT E Int.*, vol. 62, pp. 122–129, Mar. 2014.
- [6] G.-R. Tillack, C. Nockemann, and C. Bellon, "X-ray modeling for industrial applications," *NDT E Int.*, vol. 33, no. 7, pp. 481–488, Oct. 2000.
- [7] D. C. Jiles, "Review of magnetic methods for nondestructive evaluation," *NDT&E Int.*, vol. 21, no. 5, pp. 311–319, Apr. 1988.
- [8] D. C. Jiles, "Review of magnetic methods for nondestructive evaluation (Part 2) D.C.," vol. 23, pp. 83–92, 1990.
- [9] K. Tsukada, M. Yoshioka, Y. Kawasaki, and T. Kiwa, "Detection of back-side pit on a ferrous plate by magnetic flux leakage method with analyzing magnetic field vector," *NDT E Int.*, vol. 43, no. 4, pp. 323–328, Jun. 2010.
- [10] B. A. Auld and J. C. Moulder, "Review of advances in quantitative eddy current nondestructive evaluation," *J Nondestruct Eval*, vol. 18, pp. 3–36, 1999.
- [11] N. Kasai, Y. Fujiwara, K. Sekine, and T. Sakamoto, "Evaluation of back-side flaws of the bottom plates of an oil-storage tank by the RFECT," *NDT E Int.*, vol. 41, no. 7, pp. 525–529, 2008.
- [12] B. J.-C. Lebrun Bruno, Jayet Yves, "Pulsed Eddy Current Signal Analysis: Application To The Experimental Detection and Characterization of Deep Flaws in Highly Conductive Materials," vol. 30, pp. 163–70, 1997.
- [13] R. Pohl, A. Erhard, H. Montag, H. Thomas, and H. Wu, "NDT techniques for railroad wheel and gauge corner inspection," vol. 37, pp. 89–94, 2004.
- [14] K. Tsukada, M. Hayashi, Y. Nakamura, K. Sakai, and T. Kiwa, "Small Eddy Current Testing Sensor Probe Using a Tunneling Magnetoresistance Sensor to Detect Cracks in Steel Structures," *IEEE Trans. Magn.*, vol. PP, pp. 1–5, 2018.
- [15] Z. D. Wang, Y. Gu, and Y. S. Wang, "A review of three magnetic NDT technologies," *J. Magn. Magn. Mater.*, vol. 324, no. 4, pp. 382–388, 2012.
- [16] S. Tumanski, "Induction coil sensors - A review," *Meas. Sci. Technol.*, vol. 18, no. 3, 2007.
- [17] M. M. Saari, K. Sakai, T. Kiwa, T. Sasayama, T. Yoshida, and K. Tsukada, "Characterization of the magnetic moment distribution in low-concentration solutions of iron oxide nanoparticles by a high- T c superconducting quantum interference device magnetometer," *J. Appl. Phys.*, vol. 117, no. 17, p. 17B321, May 2015.
- [18] M. M. Saari *et al.*, "Optimization of an AC/DC High-Tc SQUID Magnetometer Detection Unit for Evaluation of Magnetic Nanoparticles in Solution," *IEEE Trans. Appl. Supercond.*, vol. 25, no. 3, pp. 1–4, Jun. 2015.
- [19] D. He, "AMR Sensor and its Application on Nondestructive Evaluation," in *Magnetic Sensors - Development Trends and Applications*, InTech, 2017.

## Design of Eddy Current Testing Probe for Surface Defect Evaluation

M. M. Saari<sup>1\*</sup>, N. A. Nadzri<sup>1</sup>, A. M. Halil<sup>2</sup>, M. Ishak<sup>2</sup>, K. Sakai<sup>2</sup>, T. Kiwa<sup>3</sup>, and K. Tsukada<sup>3</sup>

<sup>1</sup>Faculty of Electrical & Electronics Engineering, Universiti Malaysia Pahang,  
26600 Pekan, Pahang, Malaysia,

\*Email: mmawardi@ump.edu.my

Phone: +6094246119; Fax: +6094246111

<sup>2</sup>Faculty of Mechanical Engineering, University Malaysia Pahang,  
Pekan Campus, 26600 Pekan, Pahang, Malaysia,

<sup>3</sup>Graduate School of Interdisciplinary Science and Engineering in Health Systems,  
Okayama University,  
Okayama 700-8530, JAPAN

### ABSTRACT

Early detection of defects in metallic components used in infrastructure is crucial to ensure their safety and reliability. This paper presents a development of a small eddy current testing (ECT) probe for evaluation of sub-millimeter surface defects. The ECT probe is developed in a planar differential using sensitive anisotropy magnetoresistance sensors and the signal amplification is achieved by a home-made instrumentation amplifier. The developed ECT probe is evaluated by performing phase sensitive measurement of the magnetic responses of sub-millimeter surface slits at the excitation field of 200 Hz and 10 kHz. Compared to the real component of the magnetic response, the imaginary component can be used to identify the existence and position of the slits based on the signal intensity change caused by the induced eddy current. The spatial distribution of the magnetic response measured by the ECT probe can be used to estimate the dimension of the slit. It is expected that the developed ECT probe can be utilized for assessment of sub-millimeter surface defect.

Keywords: Eddy current testing (ECT); crack detection; gradiometer; ferromagnetic material; Anisotropic Magnetoresistance (AMR) sensor.

### INTRODUCTION

Nondestructive testing (NDT) serves as a crucial process to ensure safety and reliability in metallic materials that are being used in important applications such as infrastructure. Crack in metallic parts is one of the defects that can lead to fatal accidents where early detection of it is crucial to prevent accidents. Cracking can arise in a uniform metallic material due the fatigue caused by the exposure of continues stress and strain on it [1,2], and in weld areas where metallic parts are joined together by the welding processes [3,4]. Furthermore, it is reported that welding defects are the main cause of the catastrophic failure of the metallic structures such as in the gas pipeline system [5] and obtaining the optimized parameters for each welding process is one of the crucial steps to prevent defects [6–8]. It is worth to note that, cracking in the welding area can occur during and after the welding process due to hot and cold cracking, formation of cavities, impurities inclusions such as oxides and non-metallic slag, lack of fusion, incomplete



penetration and undercut [4]. Moreover, arise of fatigue cracks is also possible in a welded component when it is exposed to fatigue loads.

To detect defects such as crack, a variety of NDT techniques have been developed and used in industries for inspection of the surface, internal and back side defects such as magnetic testing, visual inspection, radiographic (X-ray) testing, and ultrasonic testing [2,5,9]. Each method has its advantages such as the visual inspection is simple, quick and relatively inexpensive; however, this method is limited to surface defects and requires experienced inspectors [2]. In the case of X-ray and ultrasonic testing, sub-surface defects can be assessed owing to the penetration of high energy electromagnetic and sound waves, respectively. Compared to the X-ray method, ultrasonic testing is not harmful and the testing equipment is more compact, making it easier to be applied at the field test. However, ultrasonic testing requires trained operators for a precise assessment of defects [10]. Since metallic materials are conductive and possess strong magnetic properties, the defect inspection using the magnetic method is one of the promising techniques owing to its safe, fast and non-contact nature. Furthermore, its measurement system is also simple and can be compacted easily [11]. The common measurement technique using the magnetic method includes measurement of induced eddy current in the metallic parts by AC magnetic field, namely, eddy current testing (ECT) [2,12,13], pulse eddy current (PEC) testing [14–16] and measurement of magnetic flux leakage from the metallic parts during application of external magnetic fields, namely, magnetic flux leakage (MFL) testing [1,17].

In a typical ECT system, an excitation coil is used to induced eddy current while magnetic sensors such as detection coils, Hall [18], Tunnelling Magnetoresistance (TMR) [9,19] and Anisotropy Magnetoresistance (AMR) sensors [20,21] and Superconducting Quantum Interference Devices (SQUID) [22,23] are utilized. In this method, the utilization of the electromagnetic waves penetration depth governed by the so-called skin effect enables the detection of the buried defects. When an excitation magnetic field  $B_0 e^{j2\pi ft}$  is applied perpendicularly to a conductive material that lies in the  $xy$  plane, based on Maxwell's equations, the induced eddy current components are given by

$$\begin{aligned} J_x &= J_{x0} e^{-(\pi f \mu \sigma)^{1/2} z} e^{j(2\pi ft + \alpha_0 - (\pi f \mu \sigma)^{1/2} z)} \\ J_y &= J_{y0} e^{-(\pi f \mu \sigma)^{1/2} z} e^{j(2\pi ft + \alpha_0 - (\pi f \mu \sigma)^{1/2} z)}, \end{aligned} \quad (1)$$

where  $\mu$ ,  $\sigma$ ,  $J_{x0}$ ,  $J_{y0}$  and  $\alpha_0$  are permeability, conductivity of the sample,  $x$ - and  $y$ -components of the induced current, and phase lag at the surface, respectively. The first exponential term in Equation (1) shows the decay of the induced current as a function of depth  $z$  within the material, *i.e.*, the skin depth, and the depth  $\delta$  of the skin effect is expressed when it decays to  $J_{x0}/e$  as

$$\delta = z = \sqrt{\frac{1}{\pi f \mu \sigma}}. \quad (2)$$

The second exponential term in Equation (1) shows the phase angle delay of the induced eddy current with respect to  $z$ . Moreover, it is also obvious that when the frequency  $f$  is increased,  $\delta$  decreases while the phase angle delay increases. The induced eddy current then can be determined by measuring the secondary magnetic field produced by the induced eddy current based of Maxwell's equation of  $\text{rot } \mathbf{H} = \mathbf{J}$ . Since the magnetic

field measurement is carried out outside the material where the eddy current is governed by the skin depth effect, this reflects that the ECT is a non-volumetric current measurement. Moreover, by manipulating the frequency of the excitation magnetic field, the penetration depth of the magnetic field can be controlled, hence different depth level of the eddy current can be investigated. To shorten the measurement time, a simultaneous measurement of multiple frequency components can be used to obtain a richer information of eddy current distribution at different depth and this method has been shown in the PEC and multi-frequency techniques [15]. Compared to the conventional single frequency excitation of the ECT method, a pulse of magnetic field which contains harmonics of the frequency components is applied to the conductive sample. This will induce a response of a pulse magnetic field generated from the eddy current where it contains the magnitude and delay information and commonly can be analysed in time and frequency domains [24]. However, it should be noted that the magnetic response contains also the effect of magnetization properties of the material where commonly a reference signal is required in order to subtract this effect and isolate only the eddy current information in the PEC technique. For these reasons, ECT technique is commonly applied for coating thickness measurement, conductivity, magnetic permeability, plate thickness measurement, surface and near-surface crack evaluation [9,23,25–28]. On the other hand, PEC technique has been applied for subsurface evaluation of thick samples such as tubular structures, thickness measurements and corrosion evaluations [15,26,29]. It is worth to mention that utilization of highly sensitive magnetic sensors from the DC region such as SQUIDs has enabled the low-frequency ECT technique to be used in the characterization of subsurface and deep defects [20,23,27,30].

The MFL system works by detecting the magnetic flux leakage introduced by a flaw. Commonly, to reduce the influence of magnetization fluctuations which is problematic in the case of ECT technique, a strong magnetic field is applied by using an electromagnetic yoke to a ferromagnetic sample in order to saturate its magnetization. Anomalies such as cracks in the path of the magnetic flux will produce a leakage and this leakage can be detected by magnetic sensors. The MFL technique has shown a better detection performance not limited to surface cracks [31]. However, the use of the electromagnet yoke and high current to saturate the sample magnetization results to a size increase of the MFL system.

On the other hand, the ECT system offers a compact system for the surface crack detection in a small and nonplanar shape of sample. The effect of the magnetization fluctuation can be minimized by using a planar differential detection unit such that offset fluctuations can be reduced by subtracting the detection output with a reference detection unit. Moreover, it has also been shown that the reduction the detection area under the ECT probe results to the increase of signal ratio between crack induced eddy current and the magnetization signal from a sample [9]. The use of small magnetic sensors and excitation coils can improve the localization performance of the crack detection. In this work, based on above considerations, we report on a development of a small eddy current probe for detection of cracks in welded parts. Moreover, since cracks can develop as low as sub-millimeter in size (micro-crack) at the surface and as a form of internal cracks, which may not clearly observe by visual inspection, it is important to achieve a sensitive detection with a sub-millimeter resolution. Furthermore, since cracks can develop from the level of microstructure, the capability to have early detection of them is important so that an early assessment can be made before they progress to a severe condition and causing accidents. For this

reason, a first-order planar differential ECT probe fabricated from high sensitivity AMR sensors (HMC1001, Honeywell) is developed with a home-made instrumentation amplifier. As a preliminary step for the detection of cracks in welded parts, artificial slits on a carbon steel plate is used as a representation of crack defect for the detection purpose. The width of the artificial slits was set not larger than 1 mm. Then, the performance of the developed ECT probe is evaluated by measuring magnetic response resulted from the artificial slits.

## METHODS AND MATERIALS

### ECT Probe

The schematic circuit of the developed ECT probe is shown in Figure 1. The AMR sensor is mainly composed of a resistive Wheatstone bridge of 4 AMR elements and a set/reset strap, which is wound around the AMR elements. **The sensitive axis of the AMR sensor is positioned to detect the normal component of magnetic field with respect to the sample, i.e., the  $B_z$ -component.** The set/reset strap is used to recover the sensitivity of the AMR sensor by re-aligning the magnetization direction of the AMR elements towards their anisotropy axes. For this reason, re-magnetization of the AMR elements by flowing high pulse currents through the set/reset strap are periodically required in order to preserve the sensitivity of the sensor. When a magnetic field is applied to the direction of the AMR sensitive axis, its resistance will change and resulting to unbalanced voltage between the mid-points of the bridge branches. The voltage difference between these two points can be measured accurately by an instrumentation amplifier (INA) where the loading effect is reduced. Ensuring the low noise characteristic of the INA is considerably important so that a high sensitivity detection unit can be achieved. For this reason, a home-made INA is fabricated from ultra-low noise operation amplifiers of AD797 in the conventional topology of 3 operational amplifiers. A gain of 99 is chosen to achieve sufficient amplification output between  $-5$  V and  $5$  V and to preserve a wide dynamic range of the INA frequency response. A set/reset circuit is developed to apply a high-current pulse into the set/reset strap and can be physically controlled by a mechanical switch. The INAs are powered by a voltage rail-splitter of TLE2426 and the AMR sensors are biased at  $5$  V using a linear voltage regulator. The outputs of the INAs are connected to a lock-in amplifier for a phase sensitive detection in a differential mode. The excitation coil is fabricated by a  $0.1$ -mm diameter Cu wire and forms a  $60$ -turn square coil. The excitation coil has a dimension of  $11$  mm  $\times$   $11$  mm and its current is fed from the reference signal of the lock-in amplifier. The two AMR sensors are separated by a  $4$ -mm baseline and inserted inside the excitation coil. The position of the ECT probe is determined by an  $XY$  stage and a sample can be scanned with a maximum dimension of  $45$  cm  $\times$   $60$  cm.

When an AC magnetic field is applied to a ferromagnetic sample, a magnetic response  $S_I$  is produced and consists of a large magnetization signal  $S_{mag,1}$  due its magnetization curve  $M-H$  characteristic [11,32] and a small eddy current induced signal  $S_{eddy,1}$ . This can be illustrated by Figure 2. When a defect is present in the sample, a phase delay in  $S_{eddy,1}$  is introduced where the induced eddy current takes a longer path to enclose its loop. By taking  $S_I$  as the reference signal for the phase detection of the differential signal  $S_I - S_2$ , the phase delay of the small eddy current can be detected since the large fluctuation of  $S_{mag,1}$  is minimized by means of difference between two sensors. However, it should be noted that the baseline and the size of the excitation coil have a great effect to  $S_{mag,1}$  since the distribution of magnetic property may exist

between a finite distance on the sample, resulting to a poor cancellation of  $S_{mag,1}$ . Since the differential signal  $S_1 - S_2$  is measured at a baseline of  $\Delta x = 4$  mm, the differential signal of the  $B_z$ -component is equivalent to a gradient of  $\Delta B_z / \Delta x \approx \partial B_z / \partial x$ .

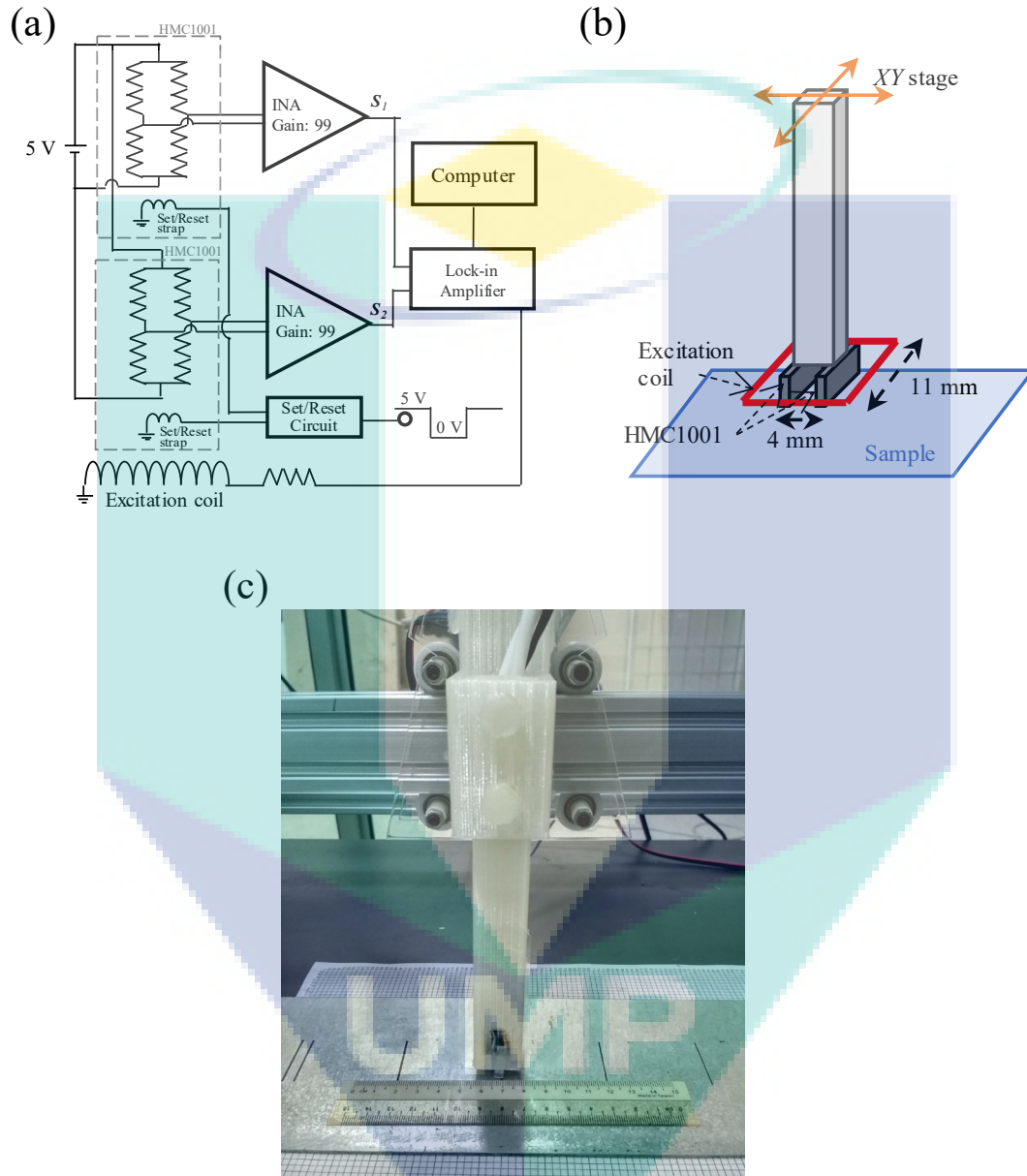


Figure 1. (a) The schematic diagram of the developed ECT probe's circuit. (b) The spatial arrangement of the AMR sensors and the excitation coil. (c) Photograph of the fabricated ECT probe.



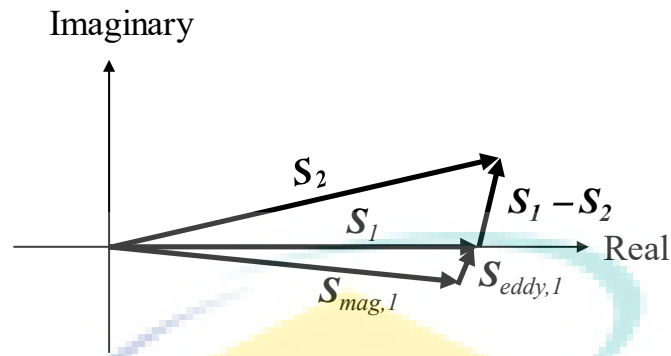


Figure 2. Differential vector of the measured magnetic signals.

### Carbon Steel Plate with Laser-Engraved Slits

To test the performance of the developed ECT probe, artificial slits were laser-engraved on a 3-mm carbon steel plate. In order to realize the detection of sub-millimeter cracks which are hardly visible with the naked eyes [33], the width of the slits was set to be not larger than 1 mm. The slits have a depth and length of 0.3 mm and 30 mm with different widths from 0.2 mm to 1.0 mm. The slits are shown in Figure 3, where they are separated by an interval of 50 mm. It was noted that the carbon steel plate showed a non-negligible magnetic remanence, in which may affect the measurement of the eddy current component.

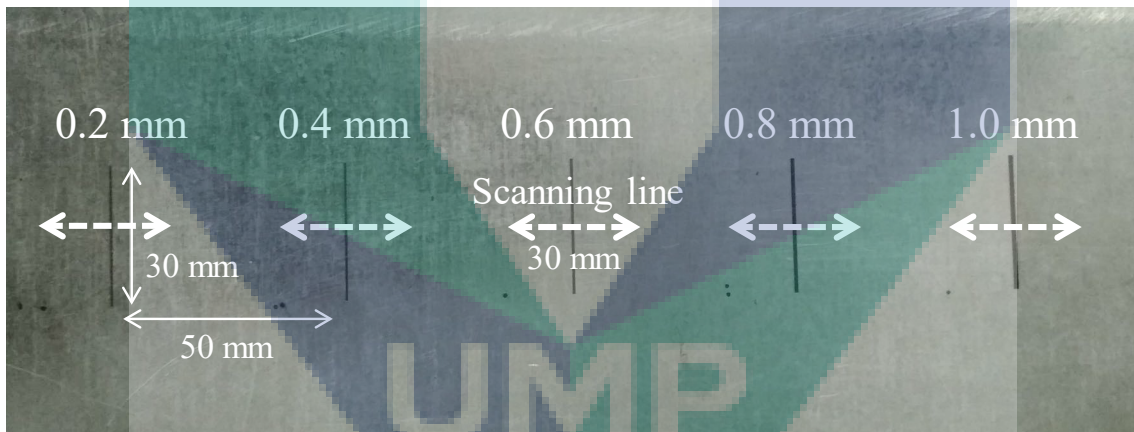
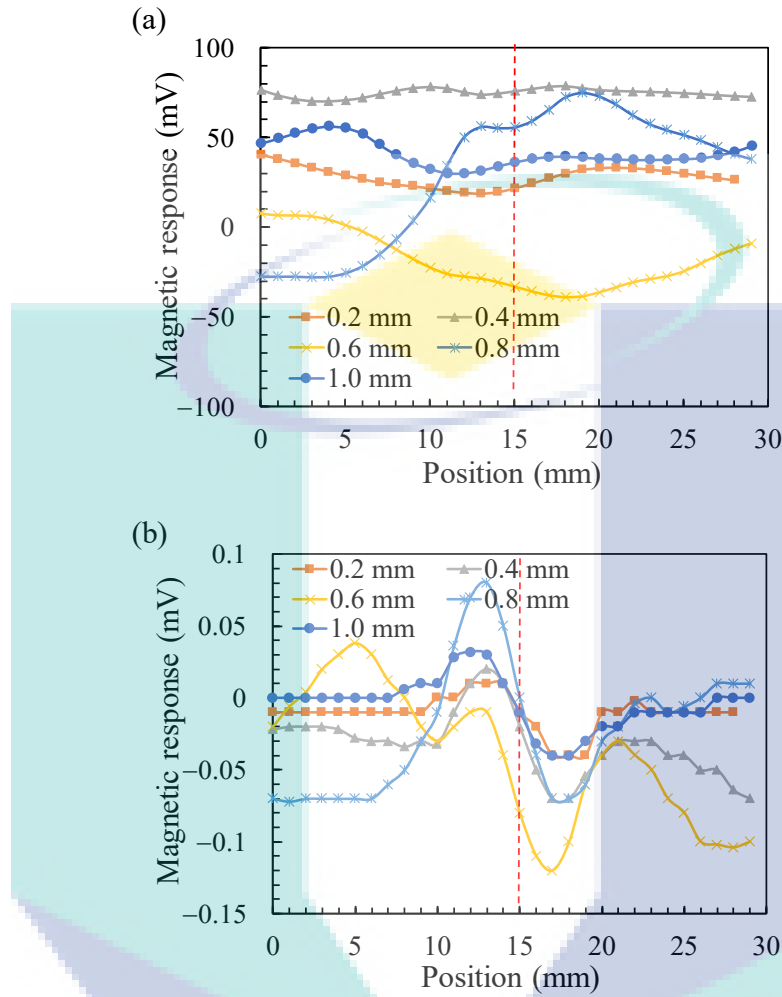


Figure 3. Artificial slits (defect) of width from 0.2 mm to 1 mm on a carbon steel plate. The white horizontal dashed line shows the line scanning direction of the ECT probe.

## RESULTS AND DISCUSSION



**Figure 4.** (a) The real and (b) imaginary components of the gradient magnetic response  $\partial B_z / \partial x$  with respect to the position of the slits during the line scanning at 200 Hz. The scanning direction was at the centre and perpendicular to the direction of the slits. The position of the slits was set to be located at 15 mm (the red vertical lines).

### Line Scanning of Slits using ECT Probe

Using the prepared carbon steel plate, we first measured the magnetic response from each slit by means of line scanning measurements. Figure 4 shows the real and imaginary components of the differential magnetic response when the ECT probe was moved horizontally across the slits, following the white dashed line shown in Figure 3. The ECT probe was displaced in the range of 30 mm with a 1-mm interval and the positions of the slits were set to be located at 15 mm. The excitation magnetic field was set to be 200 Hz and generated by a 4-mA<sub>pp</sub> current. The real component (Figure 4 (a)) showed a slight change of magnetic response around the slit position of 15 mm. Moreover, the imaginary component (Figure 4 (b)) revealed an apparent change of the magnetic response at the slit position compared to the real component. However, it should be noted that the intensity of the real component was higher compared to the imaginary component and this could be thought to be resulted from the strong magnetization signal of the carbon steel plate. Although the differential signal method was applied in the detection, the magnetic response of both components showed a non-

constant drift characteristic. This drift characteristic might be resulted from the distribution of the magnetic properties across the surface of the carbon steel metal and the slight variation of the lift off between the surface and the magnetic sensors. The magnetic response change of the real component at the slit position could be interpreted as the magnetic flux leakage component, i.e., the real component is in-phase with the excitation field. The imaginary component represented the out-of-phase magnetic response and the fluctuations of this imaginary component at the slit position could be considered as the delay and intensity change of the eddy current [11]. As shown in Figure 4 (b), the existence of the slit had resulted to the delay of the eddy current, which could be detected from the imaginary components of the measured differential magnetic responses.

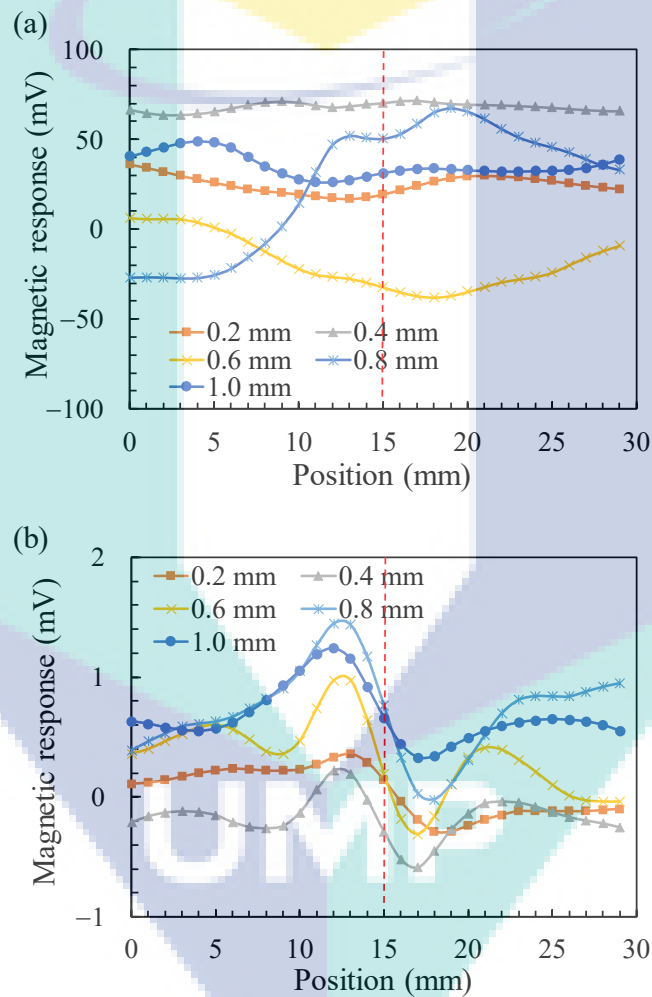


**Figure 5.** (a) The real and (b) imaginary components of the gradient magnetic response  $\partial B_z / \partial x$  with respect to the position of the slits during the line scanning at 10 kHz. The scanning direction was at the centre and perpendicular to the direction of the slits. The position of the slits was set to be located at 15 mm, indicated by the red vertical lines.

In Figure 5, the line scanning measurement was performed at the excitation field of 10 kHz where a higher intensity of the eddy current generation was expected at the surface of the carbon steel plate. The magnitude and characteristic of the real component was almost similar to the case of the 200-Hz excitation field. Although a slight change in the real component was observed at the slit position, the imaginary component showed a clearer intensity change at the slit position. Compared to the case



of the 200-Hz excitation field, the imaginary component of the 0.2-mm slit showed a stronger intensity change with less noise. Since the excitation frequency was increased by 50 times, it could be expected that the skin depth will reduce to around 7 times. This might increase the eddy current density near the surface by approximately 7 times, which was in reasonable agreement with the increase of the magnetic response. The distance between the peak and trough around the slit position revealed the distance of the 4-mm baseline between the magnetic sensors, which was smaller compared to the width of the slits. Moreover, the correlation between the signal intensity change and the width of the slits was not clearly observed. This could be thought due to the larger baseline of the magnetic sensors and the dimension of the excitation coil compared to the width of the slits.

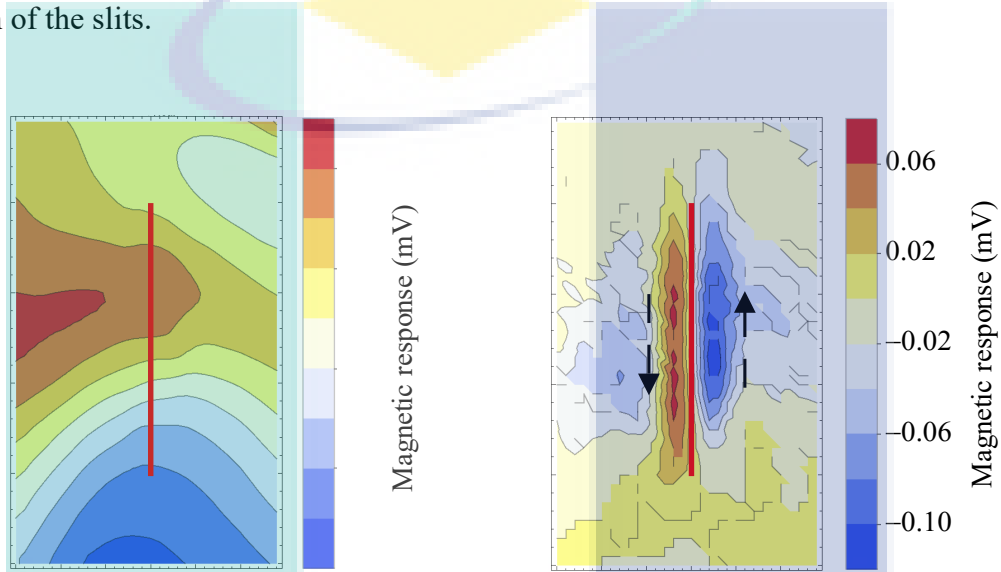


Figure 6. (a) The distributions of real and (b) imaginary component of the gradient magnetic response  $\partial B_z / \partial x$  for the 0.2-mm slit. The excitation magnetic field was 200 Hz.

### Magnetic Response Distribution of 0.2-mm Slit

A measurement of the gradient magnetic response distribution across the surface of the 0.2 mm slit was performed at the 200-Hz excitation field. Figure 6 shows the spatial distributions of the real and imaginary components in the region of 30 mm  $\times$  50 mm. The gradient magnetic response was measured in the interval of 1 mm and the slit was positioned at  $x = 15$  mm and in the  $y$ -direction. The intensity change due to the presence of the slit was not clearly observed in the real component distribution. The resulted real component distribution was thought due to the distribution of magnetic properties across the plate. Although the imaginary component showed a slightly noisy response in the line scanning measurement (Figure 4 (b)), the imaginary component distribution revealed a clear intensity change at the location of the slit. This intensity change reflected the delay and density change of the eddy current caused by the slit. From the Maxwell's equation  $\text{rot } \mathbf{H} = \mathbf{J}$  and the Cohen-Hosaka transformation [34], the measured  $\partial B_z / \partial x$  was proportional to the dipole current component of  $-J_y$ , where the current density of  $J_y$  increased around the slit. This showed that the existence of the slit had directed the eddy current to be parallel with the slit. Moreover, the length in the  $y$ -direction of the region where the intensity change occurred was almost similar to the

length of the slit. This proves that the imaginary component distribution can be used to estimate the dimension of the defect. This result proved that the developed ECT probe was able to identify the defect based on the current dipole vector, even though in the case of the smallest slit. The capability of the ECT technique to resolve sub-millimeter defects is also shown in reference [9] where a gradient Tunnelling Magnetoresistance sensor was developed and able to detect a crack width as low as 0.3 mm. Improvements in the design of the excitation coil can also be expected to improve the detection of sub-millimeter defects.

## CONCLUSIONS

In this study, a small ECT probe for the surface defect evaluation in welded parts was developed. To assure a sensitive detection of the magnetic response from cracks, a planar differential probe consisted of sensitive AMR sensors and a home-made instrumentation amplifier was designed and fabricated. The performance of the developed ECT probe was evaluated by the magnetic response measurement of the sub-millimeter slits on the ferromagnetic carbon steel plate. Compared to the real component, the imaginary component of the measured differential signal could identify the presence of the slits at the excitation frequency of 200 Hz and 10 kHz. The distribution map of the magnetic response revealed that the signal intensity was changed around the location of the slit and could be used to estimate the dimension of the surface defect. In the future, the study is expected to be extended in detection of cracks in welded parts and serve as a powerful tool in providing early assessment of defects in metallic parts.

## ACKNOWLEDGEMENTS

The authors would like to thank to the Ministry of Higher Education of Malaysia (grant no. RDU160115) and the Universiti Malaysia Pahang (grant no. RDU170377) for laboratory facilities and financial assistance.

## REFERENCES

- [1] Ahmad MI., Arifin A, Abdullah S. Evaluation of magnetic flux leakage signals on fatigue crack growth of mild steel. *Journal of Mechanical Engineering and Sciences* 2015; 9: 1727-1733
- [2] Ghoni R, Dollah M, Sulaiman A, Mamat Ibrahim F. Defect Characterization Based on Eddy Current Technique: Technical Review. *Advances in Mechanical Engineering* 2014; 2014
- [3] Tsukada K, Majima Y, Nakamura Y, Hayashi M. Nondestructive evaluation of defects in welded sections of rails via unsaturated AC magnetic flux leakage measurements with a gradiometer. : 1-8
- [4] Petcher PA, Dixon S. Weld defect detection using PPM EMAT generated shear horizontal ultrasound. *NDT and E International* 2015; 74: 58-65
- [5] Yusof MFM, Kamaruzaman MA, Zubair M, Ishak M. Detection of defects on weld bead through the wavelet analysis of the acquired arc sound signal. *Journal of Mechanical Engineering and Sciences* 2016; 10: 2031-2042
- [6] Yaakob KI, Ishak M, Idris SRA. The effect of pulse welding parameters on weld geometry of boron steel using low power fibre laser. *JOURNAL OF MECHANICAL ENGINEERING AND SCIENCES* 2017; 11: 2895-2905

- [7] Shah LH, Mohamad UK, Yaakob KI, Razali AR, Ishak M. Lap joint dissimilar welding of aluminum AA6061 and galvanized iron using TIG. *Journal of Mechanical Engineering and Sciences (JMES)* 2016; 10: 1817-1826
- [8] Hussin MH, Che Lah NA. Effects of temperature on the surface and subsurface of Al-Mg-Si welded joints. *JOURNAL OF MECHANICAL ENGINEERING AND SCIENCES* 2017; 11: 2743-2754
- [9] Tsukada K, Hayashi M, Nakamura Y, Sakai K, Kiwa T. Small Eddy Current Testing Sensor Probe Using a Tunneling Magnetoresistance Sensor to Detect Cracks in Steel Structures. *IEEE Transactions on Magnetics* 2018; PP: 1-5
- [10] Dobie G, Summan R, Pierce SG, Galbraith W, Hayward G. A noncontact ultrasonic platform for structural inspection. *IEEE Sensors Journal* 2011; 11: 2458-2468
- [11] Tsukada K, Majima Y, Nakamura Y, Yasugi T, Sakai K, Kiwa T. Detection of inner cracks in thick steel plates using non-saturated AC magnetic flux leakage testing with a magnetic resistance gradiometer. *2017 IEEE International Magnetics Conference (INTERMAG) 2017*; 9464: 1-2
- [12] Hamia R, Cordier C, Dolabdjian C. Eddy-current non-destructive testing system for the determination of crack orientation. *NDT & E International* 2014; 61: 24-28
- [13] Horan P, Underhill PR, Krause TW. Pulsed eddy current detection of cracks in F/A-18 inner wing spar without wing skin removal using Modified Principal Component Analysis. *NDT & E International* 2013; 55: 21-27
- [14] Nafiah F, Sophian A. Pulsed eddy current imaging of inclined surface cracks. *Indonesian Journal of Electrical Engineering and Informatics* 2017; 5: 309-316
- [15] Sophian A, Tian G, Fan M. Pulsed Eddy Current Non-destructive Testing and Evaluation: A Review. *Chinese Journal of Mechanical Engineering (English Edition)* 2017; 30: 500-514
- [16] Kiwa T, Hayashi T, Kawasaki Y, Yamada H, Tsukada K. Magnetic thickness gauge using a Fourier transformed eddy current technique. *NDT and E International* 2009; 42: 606-609
- [17] Tsukada K, Yoshioka M, Kiwa T, Hirano Y. A magnetic flux leakage method using a magnetoresistive sensor for nondestructive evaluation of spot welds. *NDT and E International* 2011; 44: 101-105
- [18] Azaman KN, Sophian A, Nafiah F. Effects of Coil Diameter in Thickness Measurement Using Pulsed Eddy Current Non-destructive Testing. *IOP Conference Series: Materials Science and Engineering* 2017; 260
- [19] Tsukada K, Yasugi T, Majima Y, Sakai K, Kiwa T. Absolute-magnetic-field measurement using nanogranular in-gap magnetic sensor with second-harmonic and liquid-nitrogen-temperature operation. *AIP Advances* 2017; 7: 056670
- [20] Tsukada K, Kiwa T, Kawata T, Ishihara Y. Low-Frequency Eddy Current Imaging Using MR Sensor Detecting Tangential Magnetic Field Components for Nondestructive Evaluation. *IEEE Transactions on Magnetics* 2006; 42: 3315-3317
- [21] He D. AMR Sensor and its Application on Nondestructive Evaluation. In *Magnetic Sensors - Development Trends and Applications*. InTech, 2017.
- [22] Hatsukade Y, Shinyama Y, Yoshida K, Kage T, Takai Y, Aly-Hassan M, Nakai A, Hamada H, Tanaka S. SQUID NDE on braided carbon fiber reinforced polymers with middle-end fibers under step-by-step tensile loading. *IEEE Transactions on Applied Superconductivity* 2013; 23: 0-4

- [23] Hatsukade Y, Tanaka S. Mobile NDE System Utilizing Robust HTS-SQUID Magnetometer for Use in Unshielded Environments. *IEEE Transactions on Applied Superconductivity* 2016; 26
- [24] Kiwa T, Kawata T, Yamada H, Tsukada K. Fourier-transformed eddy current technique to visualize cross-sections of conductive materials. *NDT and E International* 2007; 40: 363-367
- [25] Coil HTS, Sasayama T, Ishida T, Matsuo M, Enpuku K. Thickness Measurement of an Iron Plate Using Low-Frequency Eddy Current Testing. 2016; 26: 1-5
- [26] García-Martín J, Gómez-Gil J, Vázquez-Sánchez E. Non-destructive techniques based on eddy current testing. *Sensors* 2011; 11: 2525-2565
- [27] He DF, Tachiki M, Itozaki H. Highly sensitive anisotropic magnetoresistance magnetometer for Eddy-current nondestructive evaluation. *Review of Scientific Instruments* 2009; 80: 1-3
- [28] Chen X, Lei Y. Electrical conductivity measurement of ferromagnetic metallic materials using pulsed eddy current method. *NDT & E International* 2015; 75: 33-38
- [29] Xu X, Liu M, Zhang Z, Jia Y. A Novel High Sensitivity Sensor for Remote Field Eddy Current Non-Destructive Testing Based on Orthogonal Magnetic Field. *Sensors* 2014; 14: 24098-24115
- [30] Kiwa T, Tahara H, Miyake E, Yamada H, Tsukada K, Eddy A. Non-Contact Thickness Gauge for Conductive Materials Using HTS SQUID System. 2009; 19: 801-803
- [31] Tsukada K, Yoshioka M, Kawasaki Y, Kiwa T. Detection of back-side pit on a ferrous plate by magnetic flux leakage method with analyzing magnetic field vector. *NDT and E International* 2010; 43: 323-328
- [32] Saari MM, Sakai K, Kiwa T, Sasayama T, Yoshida T, Tsukada K. Characterization of the magnetic moment distribution in low-concentration solutions of iron oxide nanoparticles by a high-  $T_c$  superconducting quantum interference device magnetometer. *Journal of Applied Physics* 2015; 117: 17B321
- [33] Verma J, Taiwade RV. Effect of welding processes and conditions on the microstructure, mechanical properties and corrosion resistance of duplex stainless steel weldments—A review. *Journal of Manufacturing Processes* 2017; 25: 134-152
- [34] Cohen D, Hosaka H. Part II: magnetic field produced by a current dipole. *Journal of electrocardiology* 1976; 9: 409-417



# Influence of Viscosity on Dynamic Magnetization of Thermally Blocked Iron Oxide Nanoparticles Characterized by a Sensitive AC Magnetometer

Mohd Mawardi Saari<sup>1</sup> · Nazatul Shareena Suhaimi<sup>1</sup> · Mohd Herwan Sulaiman<sup>1</sup> · Nurul Akmal Che Lah<sup>2</sup> · Kenji Sakai<sup>3</sup> · Toshihiko Kiwa<sup>3</sup> · Keiji Tsukada<sup>3</sup>

Received: 8 May 2018 / Accepted: 16 January 2019  
© Springer Science+Business Media, LLC, part of Springer Nature 2019

## Abstract

In this work, we show that the viscosity of carrier liquid affects the dynamic magnetization of thermally blocked multi-core iron oxide nanoparticles. The core size of the nanoparticles was determined from the magnetization curve measured by a specially developed high- $T_c$  SQUID magnetometer and calculated to be 11.7 nm. Using an AC magnetometer developed based on induction coils, the dynamic magnetization of the multi-core iron oxide nanoparticle solution was measured from 3 Hz to 10.48 kHz. Later, we reconstructed of the hydrodynamic size distribution of the particles by assuming a log-normal distribution of particle size in an AC susceptibility model by Shliomis and Stepanov, which accounts for anisotropic directions of the easy axes of magnetic nanoparticles with respect to the excitation field direction. The reconstructed hydrodynamic sizes showed an average diameter of 130 nm and agreed with the size determined by dynamic light scattering method. In the case of increasing viscosity of the carrier liquids from 0.89 to 8.11 mPa s, the dynamic magnetization peaks of the imaginary component have shifted to a lower frequency region. We showed that the harmonics ratio and phase delay upon the magnetic field excitation at 30 Hz could also be used to determine the viscosity of carrier liquid independently.

**Keywords** Brownian relaxation · Dynamic magnetization · Iron oxide nanoparticles · Magnetometer

## 1 Introduction

Magnetic nanoparticles (MNPs) have received significant interest recently, mainly owing to their size of being able to interact with their environment at the nanometer scale, and their high signal-to-noise ratio of detection using the magnetic method. MNPs have been utilized in the *in vivo* imaging as a contrast agent in magnetic resonance imaging (MRI) technique [1] and recently, as a tracer in an emerging tomographic imaging modality called magnetic particle imaging (MPI)

technique [2–7]. Since their non-linear magnetic signal is one type of transparent to biological tissues, MPI shows a promising clinical application owing to its high temporal and spatial resolutions compared to other imaging techniques. In fact, MNPs' intrinsic magnetic characteristics and their environmental interaction are commonly utilized in biomedical applications such as exploiting their heat generation at a high frequency in magnetic hyperthermia [8, 9] and magnetic relaxation in magnetic immunoassays [10]. Moreover, it was also reported that MNPs enable a sensitive viscosity determination of their suspension liquid [11]. On the whole, MNPs are preferable and have been employed in a wide range of applications through the exploitation of their dynamics magnetization which is strongly depended by the effects of the particle size, morphology, intrinsic magnetic properties, and environmental interaction (e.g., viscosity and hydrodynamic size). Therefore, clarification on these factors is essential so that MNPs can be tailored for intended applications [12].

The magnetic characterization of the MNPs can be achieved from the DC and AC susceptibility [13] methods apart from magnetic relaxation [14] and remanence methods. The AC susceptibility measurement can provide the information of size

✉ Mohd Mawardi Saari  
mmawardi@ump.edu.my

<sup>1</sup> Faculty of Electrical & Electronic Engineering, Universiti Malaysia Pahang, Pekan Campus, 26600 Pekan, Pahang, Malaysia

<sup>2</sup> Innovative Manufacturing, Mechatronics and Sports Lab (iMAMs), Faculty of Manufacturing Engineering, Universiti Malaysia Pahang, Pekan Campus, 26600 Pekan, Pahang, Malaysia

<sup>3</sup> Graduate School of Interdisciplinary Science and Engineering in Health Systems, Okayama University, Okayama 700 8530, Japan



distribution, harmonics, and magnetic anisotropy with a fast response to the measurement by observing Neel and Brownian relaxations [15]. The DC susceptibility could also provide the size distribution of the MNP's core [16, 17]. To evaluate and serve as one of the methods for the standardization of MNPs, we have reported specially designed DC and AC magnetometers [18, 19]. In this work, using the developed magnetometers, the investigation on the dynamics of a commercial ferromagnetic multi-core iron oxide nanoparticles at a different viscosity of carrier liquids is performed. Later, the distribution of magnetic moment is constructed based on the measured magnetization curve. The hydrodynamic size of the particles is determined from the AC susceptibility model proposed by Shliomis and Stepanov [20], which includes an inter-potential- and intra-potential-well contribution to the magnetic response. The measurements on the harmonic profile of MNPs at the different intensity of AC magnetic fields are presented. Also, the viscosity of carrier liquids that is estimated from the imaginary part of the dynamic magnetization, ratio, and lagging phase of the odd harmonics even at the different intensity of the AC excitation fields are also demonstrated.

## 2 Methodology

### 2.1 AC Magnetometer

The AC magnetometer used in this work has been specially developed for characterization of MNPs [19]. Briefly, the AC magnetometer is mainly composed of the excitation and detection units. In the excitation unit, an excitation coil is resonated by a capacitor network to reduce the impedance of the excitation coil at the high-frequency region. The capacitor network is fabricated to resonate the excitation coil at discrete frequencies on a logarithmic scale. The 300-turn excitation coil is fabricated from a Litz wire and designed to achieve a high homogeneity and efficiency of the excitation field [21]. In the detection unit, a first-order axial differential coil is used as the detection sensor. The first-order differential coil is composed of two identical 1000-turn coils, whose inner diameter and baseline are 15 mm and 23 mm, respectively. The attenuation of the direct feedthrough is achieved by manually tuning the position of the detection coil relative to the excitation coil. The signal from the detection coil is lock-in detected using a lock-in amplifier (LI5640, NF Corporation) for a phase-sensitive detection.

### 2.2 AC Susceptibility Model

Shliomis and Stepanov proposed that for an ensemble of MNPs with randomly distributed easy axes, the complex AC susceptibility in response to the applied AC magnetic field is given by [20, 22, 23]:

$$\chi = \frac{1}{3} \left( \frac{\chi_{\parallel}}{1 + i\omega\tau_{\parallel}} + 2\chi_{\perp} \right). \tag{1}$$

Here,  $\omega = 2\pi f$ ,  $\chi_{\parallel}$ ,  $\chi_{\perp}$ , and  $\tau_{\parallel}$  are the angular frequency, the susceptibilities for particles with easy axes parallel and perpendicular to the applied AC field, and the parallel component of relaxation time. The parallel and perpendicular components of susceptibilities are expressed by  $\chi_{\parallel} = \frac{\mu_0 M_s^2 V_c}{k_B T} \frac{R'}{R}$  and  $\chi_{\perp} = \frac{\mu_0 M_s^2 V_c}{k_B T} \frac{R - R'}{2R}$  with  $R(\sigma) = \int_0^1 e^{\sigma x^2} dx$  and  $R'(\sigma) = \int_0^1 x^2 e^{\sigma x^2} dx$ . Here,  $\mu_0$  is the vacuum permeability,  $M_s$  is the saturation magnetization of MNP,  $V_c$  is the core volume of MNP, and  $\sigma = KV_c/k_B T$  is the dimensionless ratio between the anisotropy energy  $KV_c$  and thermal energy  $k_B T$ . In the large barrier range where the magnetic moment is thermally blocked,  $\sigma \gg 1$ ,  $\chi_{\perp}$  reaches the independent temperature value  $\mu_0 M_s^2 / 2K$  whereas  $\chi_{\parallel} \approx \mu_0 M_s^2 V_c / k_B T - \mu_0 M_s^2 / K$  [22]. In this large barrier, Eq. (1) can be rewritten by,

$$\chi = \chi_0 \left( \frac{\sigma - 1}{\sigma} \frac{1}{1 + i\omega\tau_{\parallel}} + \frac{1}{\sigma} \right), \tag{2}$$

where static susceptibility  $\chi_0 = \mu_0 M_s^2 V_c / 3k_B T$ . It should be noted that the expression given in Eq. (2) is similar to equation in the reference [24] where the second term in the right-hand side stands for the intra-potential-well contribution, which is in contrast to the standard Debye model given by  $\chi = \chi_0 / (1 + i\omega\tau)$ .

Furthermore,  $\tau_{\parallel}^{-1} = \tau_l^{-1} + \tau_B^{-1}$  represents the effective relaxation time of longitudinal Neel and Brownian relaxation times, where they are given by  $\tau_l = \tau_0 \sqrt{\pi} e^{\sigma} / 2\sigma^{3/2}$  ( $\sigma \geq 2$ ) and  $\tau_B = 3V_H \eta / k_B T$ , respectively. Here,  $\tau_0$  is the intrinsic relaxation time related to intra-potential-well dynamics (typically of the order  $10^{-9}$  s [24]),  $V_H$  is the hydrodynamic volume of MNPs, and  $\eta$  is the viscosity of carrier liquid. In the case where  $\tau_B \ll \tau_l$ , i.e., thermally blocked MNPs, and the hydrodynamic diameter  $D_H$  described by a log-normal distribution  $f(D_H) = \exp\left(-(\ln(D_H/D_0))^2 / 2\delta_D^2\right) / \sqrt{2\pi} D_H \delta_D$ , the dynamic susceptibility of multi-core MNPs can be expressed by,

$$\chi = \chi_0 \left( \frac{\sigma - 1}{\sigma} \int_0^{\infty} \frac{f(D_H) dD_H}{1 + i\omega\tau_B} + \frac{1}{\sigma} \right), \tag{3}$$

where  $D_0$  and  $\delta_D$  are the median and dimensionless parameter related to the standard deviation. The average diameter and standard deviation of  $D_H$  are given by  $D_0 \exp(\delta_D^2 / 2)$  and  $D_0 \exp(\delta_D^2 / 2) \sqrt{\exp(\delta_D^2) - 1}$ . In this work, we assume that  $\sigma$  and  $\chi_0$  can be approximated by the average ratio of anisotropy and thermal energies  $\langle \sigma \rangle$ , and average static susceptibility  $\langle \chi_0 \rangle$  for multi-core particles [15]. Then, the real  $\chi'$  and imaginary parts  $\chi''$  of the susceptibility can be expressed by,

$$\chi' = \langle \chi_0 \rangle \left( \frac{\langle \sigma \rangle - 1}{\langle \sigma \rangle} \int_0^\infty \frac{f(D_H) dD_H}{1 + (\omega\tau_B)^2} + \frac{1}{\langle \sigma \rangle} \right), \tag{4}$$

$$\chi'' = \langle \chi_0 \rangle \left( \frac{\langle \sigma \rangle - 1}{\langle \sigma \rangle} \int_0^\infty \frac{\omega\tau_B f(D_H) dD_H}{1 + (\omega\tau_B)^2} \right). \tag{5}$$

It should be noted that Eqs. (4) and (5) are almost similar to equations derived in references [24, 25]; however,  $\langle \sigma \rangle$  and  $\langle \chi_0 \rangle$  were used instead of individual values of particles and the high frequency susceptibility  $\chi_\infty$  in reference [25] could be estimated using the relation between the first and second terms of Eq. (4) even in a narrowband frequency measurement range.

### 2.3 Sample Preparation

The commercial multi-core iron oxide nanoparticle used in this study was nanomag®-D (Micromod Partikeltechnologie GmbH) with a typical diameter of 130 nm. The five sets of the different carrier liquid viscosity were prepared by varying the weight of glycerol mixed in a constant volume of purified water from 0 to 80 wt/V %. Then, 200  $\mu$ l of stock suspension of the particles was diluted in 1 ml of the prepared carrier liquids. The dynamic magnetization with respect to excitation frequency was measured using the developed AC magnetometer [19] from 3 Hz to 10.48 kHz at a constant amplitude of 2.6 mT. The response characteristic at different amplitudes of the excitation field was measured at 30 Hz from 1.3 to 7.8 mT.

## 3 Result and Discussion

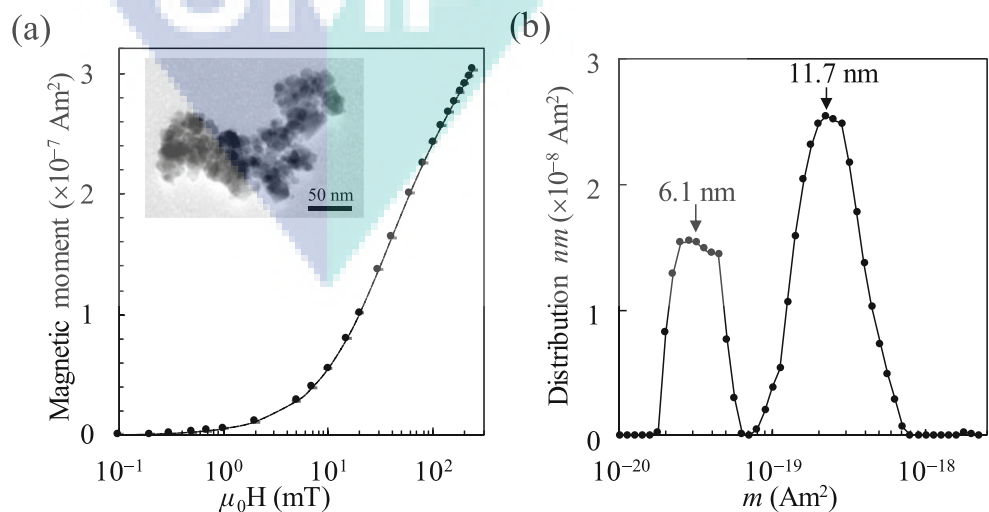
### 3.1 The Distribution of Core and Hydrodynamic Sizes

Fig. 1 a shows the initial magnetization curve measured by the high- $T_c$  SQUID magnetometer from 0.1 to 240 mT. From the

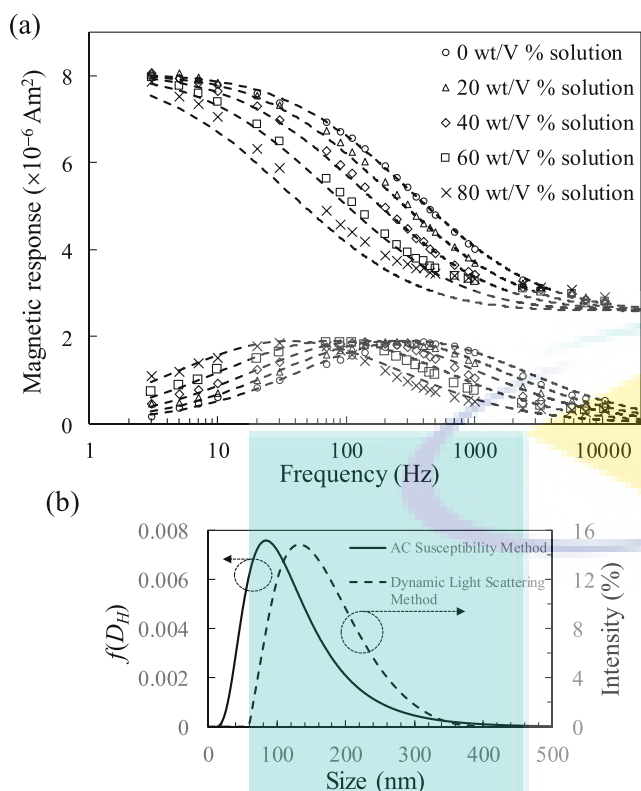
magnetization curve, the distribution of magnetic moment is constructed as shown in Fig. 1 b. Details on the distribution construction can be found in references [18, 26]. The highest peak corresponding to a core size of 11.7 nm, was in good agreement with the size determined from transmission electron microscopy image (see the superimposed image in Fig. 1a). The saturation magnetization of  $M_s = 295$  kA/m was determined from the measured magnetization curve to calculate the core size and reasonably agreed to the value reported in reference [7] for a 12-nm iron oxide particle. Compared to the  $M_s$  of bulk magnetite (from 470 to 515 kA/m), the determined  $M_s$  was smaller and could be thought due to the existence of mixed phase of magnetite and maghemite. The existence of the second peak corresponded to a particle size of 6.1 nm was assumed to occur due to the substantial inter-core interaction effect that was not accounted in the static magnetization model.

Figure 2 a depicts the dynamic magnetizations of the iron oxide nanoparticles in the carrier liquids having different wt/V % of glycerol. The peaks of the imaginary part of the dynamic magnetization reflected the Brownian relaxation process of the thermally blocked iron oxide nanoparticle where their positions shifted to a lower frequency as the wt/V % of the glycerol increased in the carrier liquids. The thermally blocked particle could be resulted from the presence of the hysteresis in the magnetization [18] where it was also reported in [7] for a 12-nm iron oxide particle. The response showed that the viscosity of the carrier liquid was increased due to the Brownian relaxation mechanism. The peak position of the imaginary part around 400 Hz agreed with the result reported in reference [27]. Using 0.89 mPa s as the viscosity of the purified water (0 wt/V % solution) at 25 °C, the distribution of  $D_H$  was determined based on the nonlinear curve fitting of Eq. (4) in the least-squares sense. The solid line shows the constructed hydrodynamic size distribution in Fig. 2 b, where an average diameter of 130 nm, the standard deviation of

**Fig. 1** a The static magnetization of the multi-core iron oxide nanoparticles. b The constructed distribution of magnetic moment







**Fig. 2** **a** The real and imaginary parts of dynamic magnetization in different viscosity of carrier liquids. **b** The constructed distributions of hydrodynamic diameter from AC susceptibility and DLS methods

76 nm, and  $\langle \sigma \rangle$  of 3.1 were obtained. The comparison between hydrodynamic diameter obtained from the dynamic magnetization and intensity weighted distribution measured using the dynamic light scattering (DLS) method (Zetasizer Nano S90, Malvern Instruments, Worcestershire, UK) is shown as the solid and dashed lines as indicated in Fig. 2 b. The DLS measurement had resulted in a Z-average of 128.7 nm; however, it should be noted that the intensity weighted distribution may overestimate the size due to domination of a few large particles, i.e., the intensity is proportional to  $D_H^6$  [15].

### 3.2 The Effect of Viscosity on the Dynamics of Particles

The dashed lines in Fig. 2 a show the real and imaginary parts derived from the hydrodynamic diameter distribution. The response indicates a good agreement with the measured data. Since the viscosity of the carrier liquid reflects the peak position of the imaginary part, we estimated the viscosity of the 20 to 80 wt/V % solutions by fitting their imaginary parts with Eq. (5). Here, the previously determined hydrodynamic diameter distribution of the 0 wt/V % solution was used in the nonlinear curve fitting. The dashed lines in Fig. 2 a show the derived for both real and imaginary parts with their corresponding viscosities are plotted in Fig. 3.

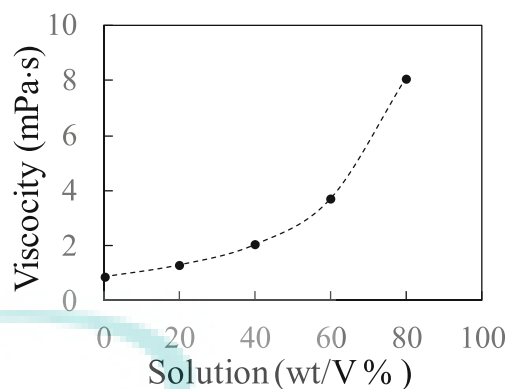


**Fig. 3** Estimated viscosity of the carrier liquids with respect to wt/V % of glycerol in the carrier liquids

The derivation results obtained from imaginary parts are in good agreement with the measured data while a slight deviation of the real parts was observed, particularly for the 80 wt/V % solution. This deviation was thought due to the existence of the  $\sigma$  distribution and further clarification on the effect should be investigated.

In practice, measurements that requiring sweeping of a wide range of frequency region result to increment of measuring time. The results indicated that for the change of the real and imaginary parts, a single-frequency measurement could be used to obtain the concentration of MNPs and environmental factors that affected the dynamic magnetization of MNP such as the viscosity of the carrier liquid [28]. The selection of the measurement frequency is crucial, depending on the types of relaxation mechanism. In this work, we selected a frequency of 30 Hz since a lower frequency can capture the information of the Brownian relaxation process occurred at a higher frequency owing to the distribution of the particle size. Figure 4 shows the intensity profile of the first, third, and fifth harmonics of the iron oxide nanoparticle with respect to the viscosity at different intensities of the AC excitation field. Generally, the intensity of the harmonics decreased with the increase of viscosity, which was consistent with the results indicated in Fig. 2 a. Moreover, the intensity of the harmonics increased with the magnitude of the excitation field. However, it should be noted that the increment in the harmonic intensity profile is correlated with the increase in the MNPs concentration, i.e., a slight difference in concentrations of MNPs may result to a negligible difference in harmonic intensity, resulting to an estimation error of the viscosity. This can be shown by the first harmonic during the excitation field of 7.8 mT. On the other hand, the phase angle of the harmonics reflects the phase change of the Brownian relaxation process. In this case, Fig. 5 shows the phase angle change of the harmonics referenced at the phase angle of 0 wt/V % solution (viscosity of 0.89 mPa.s). The phase delay of the harmonics is increased with the increase of the viscosity, which was consistent with the increasing magnitude of the imaginary part in Fig. 2 a.

**Fig. 4** **a** The intensity of the first  $f_1$ , **b** third  $f_3$ , and **c** fifth  $f_5$  harmonics concerning viscosity and excitation field

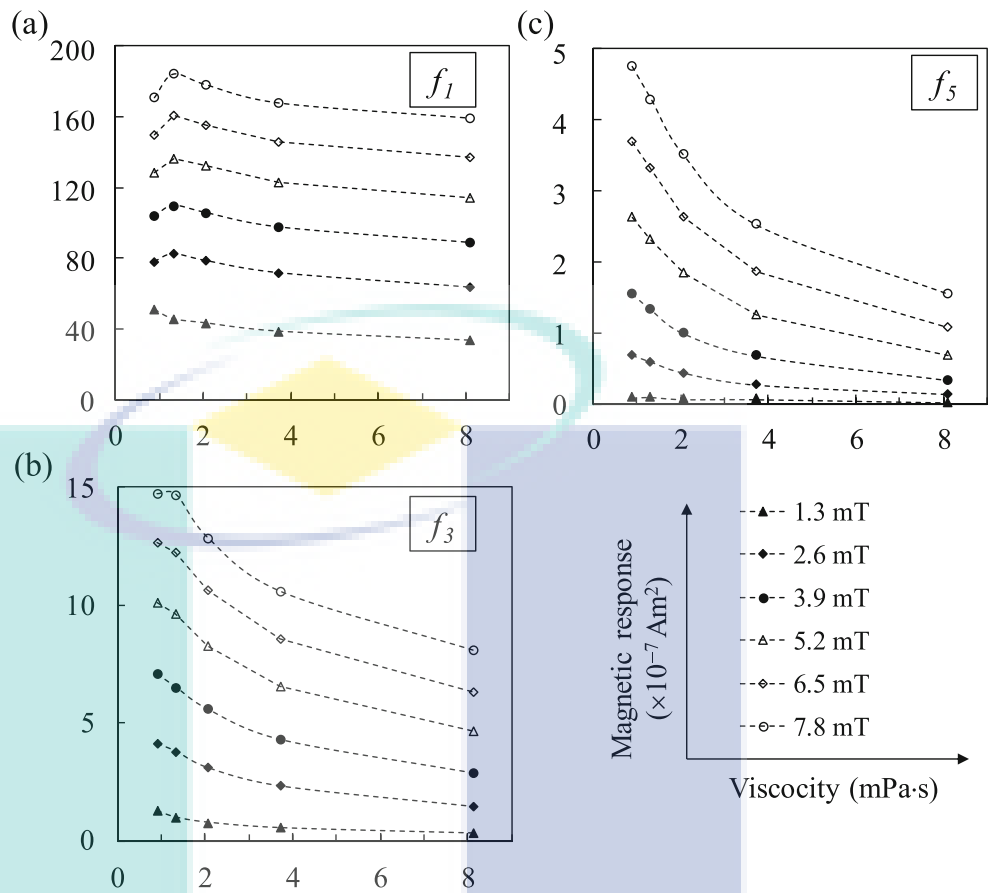


**Fig. 5** **a** The phase angle of the first  $f_1$ , **b** third  $f_3$ , and **c** fifth  $f_5$  harmonics concerning viscosity and excitation field

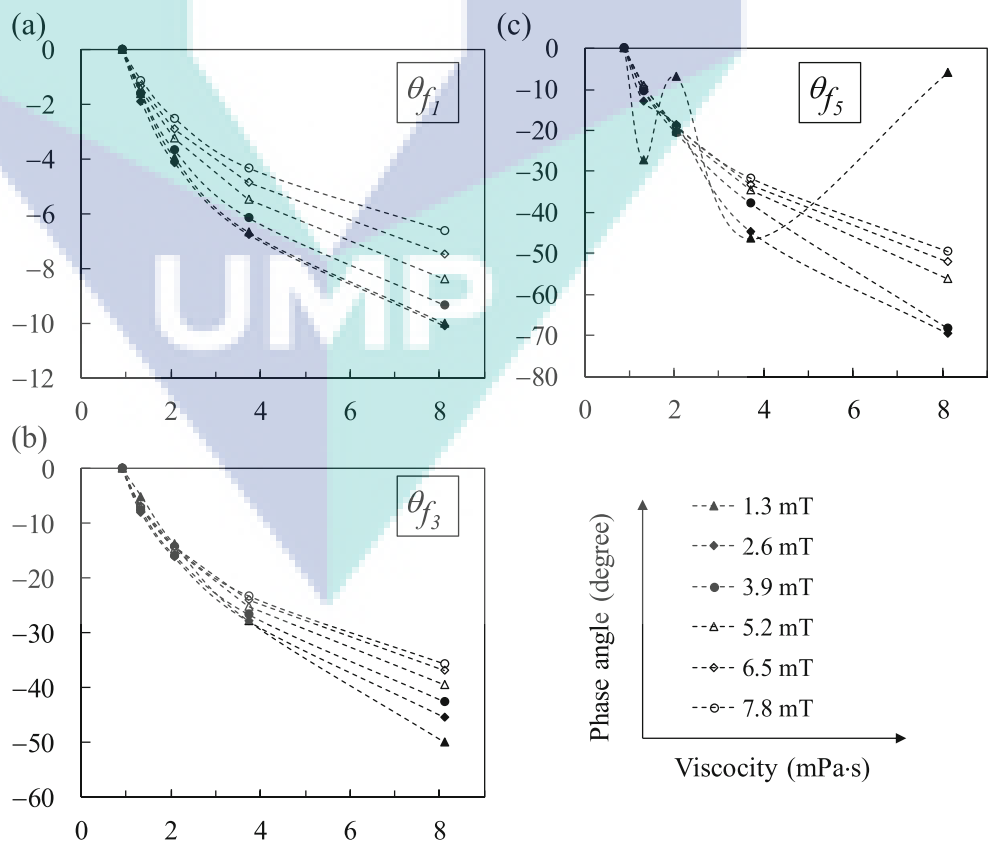
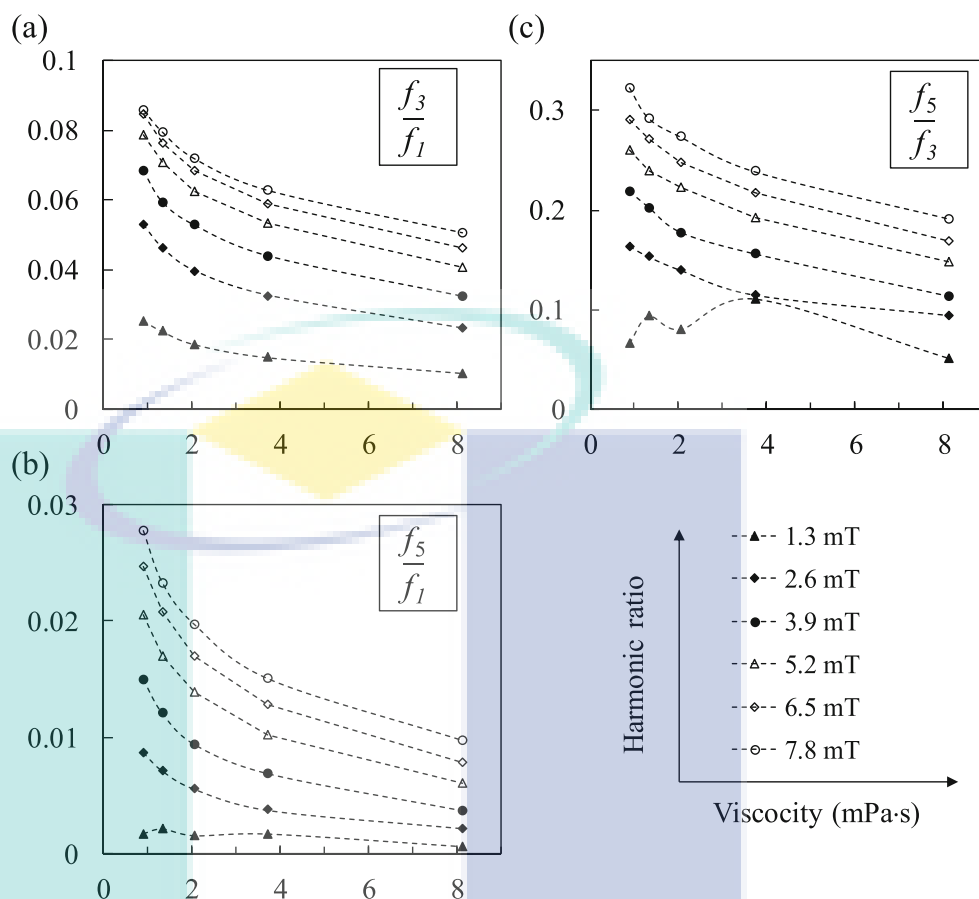


**Fig. 6** **a** The harmonics ratio of the  $f_3/f_1$ , **b**  $f_5/f_1$ , and **c**  $f_5/f_3$  with respect to viscosity and excitation field



However, the phase delay was reduced at a higher magnitude of the excitation field. The phenomenon can be interpreted as the higher intensity of magnetic field has increased the magnetic torque of the thermally blocked particles where it reduces the relaxation time, thus resulting in the reduced phase delay. At this point, the viscosity of liquid carrier could be determined quantitatively based on the MNP solution phase angle profile using a known distribution of the hydrodynamic diameter. However, it must be noted that the phase delay is sensitive to the noise when the harmonics intensity is relatively small and comparable to the noise. The condition is shown by the phase angle of the fifth harmonic at the excitation field of 1.3 mT<sub>pp</sub> in Fig. 5 c. It is known that the intensity of the harmonics is proportional to the concentration of MNPs. By taking a ratio between harmonics, the effect of concentration can be normalized, thus providing a rather simple determination of viscosity using harmonics ratio compared to determination of phase delay. Figure 6 shows the third-to-first, fifth-to-first, and fifth-to-third ratios as a function of the viscosity. The harmonics ratio decreased with the increase of the viscosity. Since high magnetic field will produce a higher harmonics intensity, the harmonics ratio will also increase when the intensity of the excitation field is increased. However, it shall be noted that the phase delay and harmonic

ratio were not linear and depended on the strength of the AC magnetic field. Therefore, it can be proved that harmonics ratio can be used as a concentration-independent parameter in the determination of the MNP's dynamics.

#### 4 Conclusion

The static and dynamic magnetizations of the multi-core iron oxide nanoparticles have been characterized by the developed systems. The core size of 11.7 nm and its hydrodynamic diameter profile with an average diameter of 130 nm derived from their static and dynamic magnetizations were consistent with the results achieved by TEM analysis and DLS measurement. It is indicated that the environmental factors such as viscosity could affect the dynamic behavior of MNPs where the peaks of the imaginary components shifted to a lower frequency region when the solution viscosity was increased from 0.89 to 8.11 mPa s. Also, it was shown that the harmonic ratio decreased and the phase angle delay increased when the viscosity was increased. The harmonics ratio and phase angle delay could be used as the concentration-independent parameter to estimate the viscosity of the

liquid carrier where it can be implemented in certain applications such as in the magnetic immunoassay and magnetic particle imaging (MPI) technique.

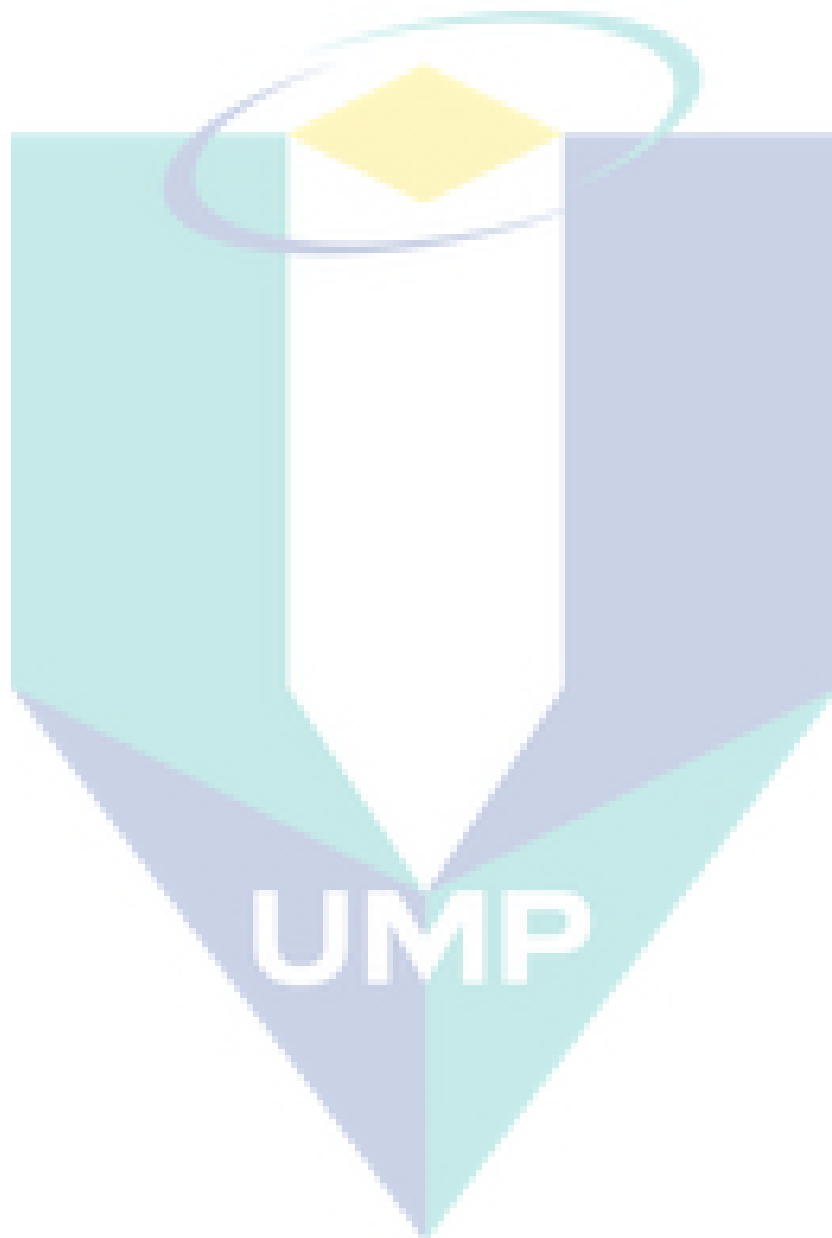
**Funding Information** This work was supported by the Ministry of Higher Education of Malaysia under grant number of RDU 160115, Research Management Center of Universiti Malaysia Pahang under grant number of RDU 170377, and the “Strategic Promotion of Innovative R&D” of the Japan Science and Technology Agency (JST).

**Publisher's Note** Springer Nature remains neutral with regard to jurisdictional claims in published maps and institutional affiliations.

## References

- Saritas, E.U., Goodwill, P.W., Croft, L.R., Konkle, J.J., Lu, K., Zheng, B., Conolly, S.M.: Magnetic particle imaging (MPI) for NMR and MRI researchers. *J. Magn. Reson.* **229**, 116–126 (2013). <https://doi.org/10.1016/j.jmr.2012.11.029>
- Gleich, B., Weizenecker, J.: Tomographic imaging using the non-linear response of magnetic particles. *Nature.* **435**, 1214–1217 (2005). <https://doi.org/10.1038/nature03808>
- Goodwill, P.W., Scott, G.C., Stang, P.P., Conolly, S.M.: Narrowband magnetic particle imaging. *IEEE Trans. Med. Imaging.* **28**, 1231–1237 (2009). <https://doi.org/10.1109/TMI.2009.2013849>
- Bai, S., Hirokawa, A., Tanabe, K., Sasayama, T., Yoshida, T., Enpuku, K.: Narrowband magnetic particle imaging utilizing electric scanning of field free point. *IEEE Trans. Magn.* **51**, 1–4 (2015). <https://doi.org/10.1109/TMAG.2015.2438029>
- Vogel, P., Rückert, M.A., Klauer, P., Kullmann, W.H., Jakob, P.M., Behr, V.C.: First in vivo traveling wave magnetic particle imaging of a beating mouse heart. *Phys. Med. Biol.* **61**, 6620–6634 (2016). <https://doi.org/10.1088/0031-9155/61/18/6620>
- Graeser, M., Knopp, T., Swargulski, P., Friedrich, T., von Gladiss, A., Kaul, M., Krishnan, K.M., Ittrich, H., Adam, G., Buzug, T.M.: Towards picogram detection of superparamagnetic Iron-oxide particles using a gradiometric receive coil. *Sci. Rep.* **7**, 6872 (2017). <https://doi.org/10.1038/s41598-017-06992-5>
- Ozel, F., Kockar, H., Karaagac, O.: Growth of iron oxide nanoparticles by hydrothermal process: effect of reaction parameters on the nanoparticle size. *J. Supercond. Nov. Magn.* **28**, 823–829 (2015). <https://doi.org/10.1007/s10948-014-2707-9>
- Connord, V., Mehdaoui, B., Tan, R.P., Carrey, J., Respaud, M.: An air-cooled Litz wire coil for measuring the high frequency hysteresis loops of magnetic samples - a useful setup for magnetic hyperthermia applications. *Rev. Sci. Instrum.* **85**, 093904 (2014). <https://doi.org/10.1063/1.4895656>
- Mamiya, H., Jeyadevan, B.: Hyperthermic effects of dissipative structures of magnetic nanoparticles in large alternating magnetic fields. *Sci. Rep.* **1**, 157 (2011). <https://doi.org/10.1038/srep00157>
- Enpuku, K., Tanaka, T., Matsuda, T., Dang, F., Enomoto, N., Hojo, J., Yoshinaga, K., Ludwig, F., Ghaffari, F., Heim, E., Schilling, M.: Properties of magnetic nanoparticles in the Brownian relaxation range for liquid phase immunoassays. *J. Appl. Phys.* **102**, 054901 (2007). <https://doi.org/10.1063/1.2775882>
- Calero-DdelC, V.L., Santiago-Quifonez, D.I., Rinaldi, C.: Quantitative nanoscale viscosity measurements using magnetic nanoparticles and SQUID AC susceptibility measurements. *Soft Matter.* **7**, 4497 (2011). <https://doi.org/10.1039/c0sm00902d>
- Karaagac, O., Kockar, H.: A simple way to obtain high saturation magnetization for superparamagnetic iron oxide nanoparticles synthesized in air atmosphere: optimization by experimental design. *J. Magn. Magn. Mater.* **409**, 116–123 (2016). <https://doi.org/10.1016/j.jmmm.2016.02.076>
- Ludwig, F., Balceris, C., Jonasson, C., Johansson, C.: Analysis of ac susceptibility spectra for the characterization of magnetic nanoparticles. **9464** (2017). <https://doi.org/10.1109/TMAG.2017.2693420>
- Ludwig, F., Heim, E., Schilling, M.: Characterization of superparamagnetic nanoparticles by analyzing the magnetization and relaxation dynamics using fluxgate magnetometers. *J. Appl. Phys.* **101**, 113909 (2007). <https://doi.org/10.1063/1.2738416>
- Bogren, S., Fornara, A., Ludwig, F., del Puerto Morales, M., Steinhoff, U., Hansen, M., Kazakova, O., Johansson, C.: Classification of magnetic nanoparticle systems—synthesis, standardization and analysis methods in the nanomag project. *Int. J. Mol. Sci.* **16**, 20308–20325 (2015). <https://doi.org/10.3390/ijms160920308>
- Sasayama, T., Yoshida, T., Saari, M.M.M., Enpuku, K.: Comparison of volume distribution of magnetic nanoparticles obtained from M-H curve with a mixture of log-normal distributions. *J. Appl. Phys.* **117**, 17D155 (2015). <https://doi.org/10.1063/1.4919268>
- Berkov, D.V., Görmert, P., Buske, N., Gansau, C., Mueller, J., Giersig, M., Neumann, W., Su, D.: New method for the determination of the particle magnetic moment distribution in a ferrofluid. *J. Phys. D: Appl. Phys.* **33**, 331–337 (2000). <https://doi.org/10.1088/0022-3727/33/4/303>
- Saari, M.M., Sakai, K., Kiwa, T., Sasayama, T., Yoshida, T., Tsukada, K.: Characterization of the magnetic moment distribution in low-concentration solutions of iron oxide nanoparticles by a high- $T_c$  superconducting quantum interference device magnetometer. *J. Appl. Phys.* **117**, 17B321 (2015). <https://doi.org/10.1063/1.4919043>
- Suhaimi, N.S., Saari, M.M., Mohamed, A.I., et al.: Development of a compact and sensitive AC magnetometer for evaluation of magnetic nanoparticles solution. In: 2017 IEEE 8th Control and System Graduate Research Colloquium (ICSGRC). IEEE, pp 221–224 (2017)
- Shliomis, M.I., Stepanov, V.I.: Frequency dependence and long time relaxation of the susceptibility of the magnetic fluids. *J. Magn. Magn. Mater.* **122**, 176–181 (1993). [https://doi.org/10.1016/0304-8853\(93\)91067-H](https://doi.org/10.1016/0304-8853(93)91067-H)
- Saari, M.M., Suhaimi, N.S., Razali, S., et al.: Development of a resonant excitation coil of AC magnetometer for evaluation of magnetic fluid. *J. Telecommun Electron Comput Eng.* **10**, 127–130 (2018)
- Svedlindh, P., Jonsson, T., García-Palacios, J.L.: Intra-potential-well contribution to the AC susceptibility of a noninteracting nano-sized magnetic particle system. *J. Magn. Magn. Mater.* **169**, 323–334 (1997). [https://doi.org/10.1016/S0304-8853\(96\)00756-1](https://doi.org/10.1016/S0304-8853(96)00756-1)
- Ludwig, F., Balceris, C., Johansson, C.: The anisotropy of the AC susceptibility of immobilized magnetic nanoparticles—the influence of intra-potential-well contribution on the AC susceptibility spectrum. *IEEE Trans. Magn.* **53**, 1–4 (2017). <https://doi.org/10.1109/TMAG.2017.2692038>
- Enpuku, K., Sasayama, T., Yoshida, T.: Estimation of magnetic moment and anisotropy energy of magnetic markers for biosensing application. *J. Appl. Phys.* **119**, 184902 (2016). <https://doi.org/10.1063/1.4948951>
- Prieto Astalan, A., Jonasson, C., Petersson, K., Blomgren, J., Ilver, D., Krozer, A., Johansson, C.: Magnetic response of thermally blocked nanoparticles in a pulsed magnetic field. *J. Magn. Magn. Mater.* **311**, 166–170 (2007). <https://doi.org/10.1016/j.jmmm.2006.10.1182>

26. van Rijssel, J., Kuipers, B.W.M., Erné, B.H.: Non-regularized inversion method from light scattering applied to ferrofluid magnetization curves for magnetic size distribution analysis. *J. Magn. Mater.* **353**, 110–115 (2014). <https://doi.org/10.1016/j.jmmm.2013.10.025>
27. Ahrentorp, F., Astalan, A.P., Jonasson, C., et al.: Sensitive high frequency AC susceptometry in magnetic nanoparticle applications. *AIP Conf Proc.* **1311**, 213–223 (2010). <https://doi.org/10.1063/1.3530015>
28. Rauwerdink, A.M., Weaver, J.B.: Harmonic phase angle as a concentration-independent measure of nanoparticle dynamics. *Med. Phys.* **37**, 2587–2592 (2010). <https://doi.org/10.1118/1.3426294>



# Detection of Metallic Contaminant in Aluminium Soda Can Using TMR Sensor



Nurul A'in Nadzri, Mohd Mawardi Saari, Saifuddin Razali, Mohd Rusllim Mohamed and Hamzah Ahmad

**Abstract** The contaminant is one of the big concerns in food processing industry and metallic objects can be one of the contaminant factors since most of the food processing equipment and tools are composed of metallic parts. Metal detector is used because these contaminant objects might cause injury to the consumers. Moreover, even the smallest particle of metals can lead to machinery failure. In this study, we have developed an inspection system for detecting the magnetic remanence of the contaminants. The system utilizes a Tunnel Magnetoresistance (TMR) Mag3110 magnetometer. An Arduino operating software was developed for data acquisition of Mag3110, and identification of the presence of the contaminant. In order to optimize the position of the magnetometer so that detection sensitivity can be enhanced, we performed a simulation based on magnetic moment dipole. The system performance was evaluated using stainless steel balls. The developed system could detect a stainless steel ball having diameter as small as 0.1 cm. The detected signal is sent to the control panel to analyze the presence of a metal object. The magnetic response with respect to position of the sensor, different size of metal objects and magnetization effect, is studied as well.

**Keywords** Metal detector · Magnetometer · Magnetic remanence

## 1 Introduction

Canned foods are one of the processed foods that popular in this age. Due to this, to ensure the safety of the consumers, finding a detector that can detect any foreign bodies in canned products before they are being distributed to market is important [1, 2]. A mixture of metallic contaminants to food is a serious problem not only for

---

N. A. Nadzri · M. M. Saari (✉) · S. Razali · M. R. Mohamed · H. Ahmad  
Faculty of Electrical & Electronic Engineering, Universiti Malaysia Pahang,  
26600 Pekan, Pahang, Malaysia  
e-mail: mmawardi@ump.edu.my

© Springer Nature Singapore Pte Ltd. 2018  
M. H. A. Hassan (ed.), *Intelligent Manufacturing & Mechatronics*,  
Lecture Notes in Mechanical Engineering,  
[https://doi.org/10.1007/978-981-10-8788-2\\_47](https://doi.org/10.1007/978-981-10-8788-2_47)

527



the consumers; it also can affect the mechanism and operation of machines in food processing lines which can cause a high cost to repair the machine.

Metal detection is the most popular metallic detection system method that has been used in food industries [3, 4]. This method can identify large metallic objects and works well in bulk containers of raw materials. Kwan et al. [5] proposed a detection method of foreign object by using an x-ray technique for a dry food manufacturing line. This method is widely used because it is easy to operate and can work efficiently in high production lines. However, detection resolution of this method may not be sufficient for detection of small size or low density foreign objects. Moreover, to generate an x-ray, a high voltage power supply is required and the system is high cost.

According to Tanaka et al. [6–8], they proposed a method using Superconducting Quantum Interference Device (SQUID) system for the detection of small magnetic contaminants. This method has been proposed because the high-sensitivity of the SQUID can overcome the problem where the X-ray system has low detection resolution for thin materials. The SQUID system has a good ability detection for small magnetic materials. This system has already been installed in food industry plant. Moreover, Krause et al. [9] discussed about a detection system of magnetic contaminations in industrial products using High Temperature Superconductor (HTS) SQUIDs. They mentioned that the key requirement of industrial quality control resides in the inspection at the end of the production lines, in which the products need to go through inspection after they are wrapped. The use of SQUID magnetometers allows the realization of excellent sensitivity.

In this paper, a magnetometer of Mag3110 (Freescale) is used to detect metal contaminants in aluminum canned foods. This sensor is selected because it is small, low-power, low-cost and having digital 3-axis detection capability. This sensor is based on Tunnel Magnetoresistance (TMR) and it can detect magnetic field strength as low as 0.1  $\mu$ T. An Arduino Uno is used as a core platform that featured in the developed system.

## 2 Methodology

We first study magnetic dipole moment by using a simulation method. Based on the simulation result, we measure signal from steel balls at different conditions.

In the experiment, the sensor was fixed below the conveyer belt to increase detection sensitivity, assuming that metal contaminants are located at the bottom of a can. By using the Mag3110 sensor, a testing technique based on the remanent magnetic field of metallic contaminants is developed. The size of contaminants has also been considered. The magnetic responses are experimentally determined using steel balls with different diameters to test the sensitivity of the developed system.

An analogue-to-digital conversion of the Mag3110 sensor has been achieved by using the Arduino board. The software of the Arduino board is developed to suit the



developed system. All the collected data will be sent to a computer and the result will be displayed on the computer.

### 2.1 Theoretical Calculation

We first simulate the pattern of magnetic fields produced by a steel ball. From the distribution characteristic of magnetic fields, the optimum configuration for the magnetic sensor can be determined. Using the magnetic dipole law, the response of magnetic field from a magnetic moment dipole  $m$  can be expressed as

$$B = \frac{\mu_0}{4\pi} \left( \frac{3\mathbf{m} \cdot \mathbf{r}}{r^5} \mathbf{r} - \frac{\mathbf{m}}{r^3} \right). \tag{1}$$

Using Eq. (1), it is possible to simulate the magnetic field of  $x$ -,  $y$ - and  $z$ -oriented dipoles. Here,  $\mu_0$ ,  $\mathbf{m}$ , and  $\mathbf{r}$  are vacuum permeability, magnetic moment vector and distance vector from magnetic moment dipole to observation point. The simulated theoretical data can also be used in order to satisfy the visualization requirements in industrial applications. According to Eq. (1), ferromagnetic objects such as iron that are moving through the detection space, will cause temporary but detectable changes due to the magnetization induced by the Earth’s ambient magnetic field.

From the magnetic dipole law, Eq. (1) can be simplified to find the axial magnetic field  $B_z$  with different value of distance,  $r$ , and it is given by

$$B_z = \frac{\mu m z}{2\pi r^3} = \frac{\mu D^3 M}{12r^3}. \tag{2}$$

Here,  $M$ ,  $D$ , and  $\mu$  are the magnetization, diameter and magnetic permeability of the steel ball.

Furthermore, the movement of the contaminants will produce an inertia force where they may roll during detection. Due to this reason, we have included in the simulation where the magnetic moment dipole is tilted to different values of angles. Moreover, since the rolling of contaminants will affect the magnetic signal, this requires us to determine the best detection direction of the magnetic field. To study this effect, the inclination of a magnetic moment of the steel ball is simulated from 0 to 90° in  $x$ - $y$ , plane. Since metal components have magnetic remanence characteristic that can be represented by magnetic moments, we assume that the magnetic moment is pointing towards  $z$ -axis when the tilting angle is 0° from the  $z$ -axis. When the sensor senses the magnetic field of the contaminant and it will produce values of magnetic field vectors which are composed of  $x$ -,  $y$ -, and  $z$ -components of magnetic fields,  $B_x$ ,  $B_y$  and  $B_z$ , respectively.

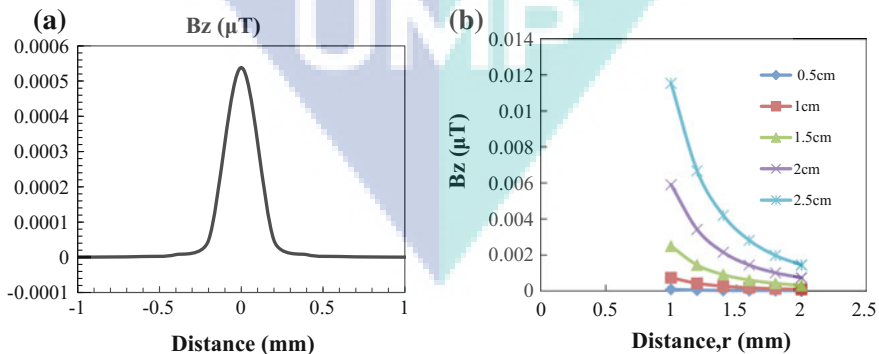
### 3 Result and Discussion

#### 3.1 Simulation of Magnetic Moment Dipole

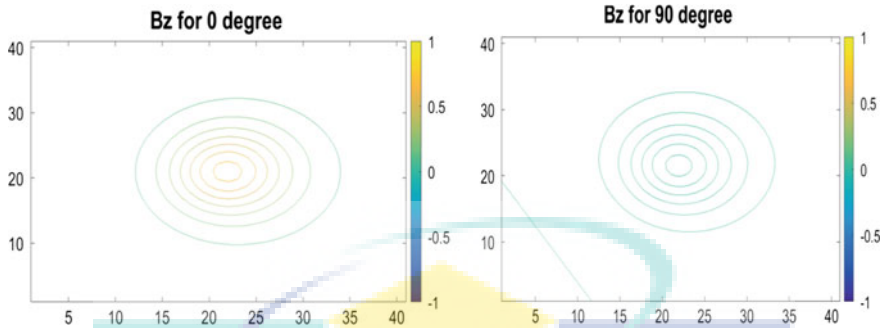
The results of the calculated signal traces using Eq. (1) are displayed in Fig. 1a and b. Here, we assumed the value of  $M = 6000$  A/m, and the diameter  $D$  of the steel ball is 0.01 m. From the Fig. 1, we could conclude that if the steel ball is located close to the sensor, the reading of the magnetic field will be high. The distance of the sensor to the contaminants needs to be considered so that the contaminants can be detected efficiently. A particle is detectable if the peak-to-peak signal detected by the sensor is greater than the noise of the environmental and the sensor. From Fig. 1b where we set the diameter from 0.5 cm until 2.5 cm, it was found that the intensity of the magnetic field increased as the size of the steel ball was increased. As we can see from Fig. 1b, the smallest diameter of steel balls gave the intensity of magnetic field near to zero, in which the presence of metal contaminant could be difficult to be determined. In this case, the sensitivity of the sensor is very crucial where a sensitive sensor is capable to detect the presence of small metallic contaminants.

Figure 2 shows the simulation results of the  $B_z$  component using Matlab (MathWorks, USA) when the ball is pointing towards  $z$ -axis with the angles of  $0^\circ$  and  $90^\circ$ .

From Fig. 2, it was concluded that, the detection response using  $B_z$  component showed a higher value when the ball was pointing towards  $z$ -axis with the angle of  $0^\circ$ . The magnetic field was strong at  $z$ -axis when the angle was  $0^\circ$  but the field intensity gradually became weaker when the magnetic moment of the ball rolled towards  $90^\circ$ . The intensity was higher when the ball was pointing at  $0^\circ$  since the sensor sensed the magnetic field in the  $z$ -axis.



**Fig. 1** a Signal of metal particle (diameter 0.01 m), passing the sensor plane at a distance about 10 cm. The solid line shows the trace simulated with the particle alone. b Signal of metal particle with different diameters of the stainless steel balls



**Fig. 2** Graph of  $B_z$  magnetic response of a magnetic dipole pointing at 0 and  $90^\circ$  from  $z$ -axis, respectively

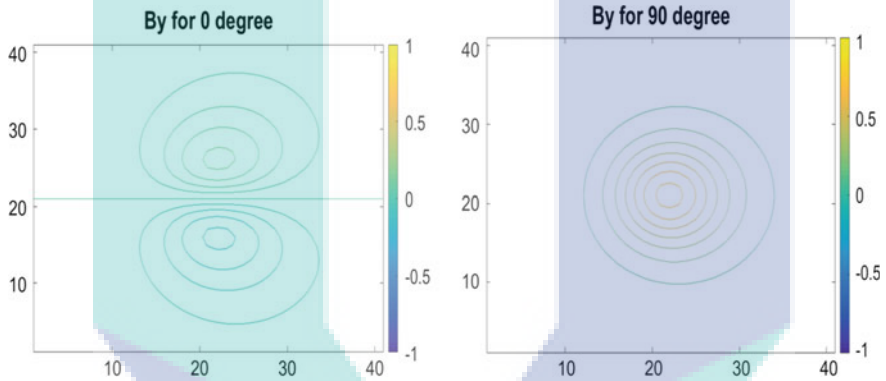


**Fig. 3** Graph of  $B_y$  magnetic response of a magnetic dipole pointing at 0 and  $90^\circ$  pointing towards  $z$ -axis, respectively

Figure 3 shows the results for the  $B_y$  component when the ball was pointing towards  $z$ -axis with the angles of 0 and  $90^\circ$ . For the magnetic field response in the  $y$ -component, it was different with the  $z$ -component, where we could see that the magnetic field was weak when the ball was pointing at  $0^\circ$ . However, the strength of magnetic field gradually increased when the value of the angle was increased.

Figure 4 shows the results for  $x$ -component of the magnetic field  $B_x$ , when the ball was pointing at the angles of 0 and  $90^\circ$ . The results were almost the same with  $B_y$ ; however, the position of the contours was changed. When the ball was pointing at  $0^\circ$ , the strength of the magnetic field was weak but it gradually increased when the value of the angle was increased. Furthermore, from the distribution profiles of  $B_x$ ,  $B_y$  and  $B_z$ , the magnetic responses were high when the steel ball was near to the sensor, i.e., a sensor with a capability of measuring  $x$ -,  $y$ -, and  $z$ -components of magnetic fields can be placed at the center of production lines such as carrier conveyer belts, to enhance the detection sensitivity.

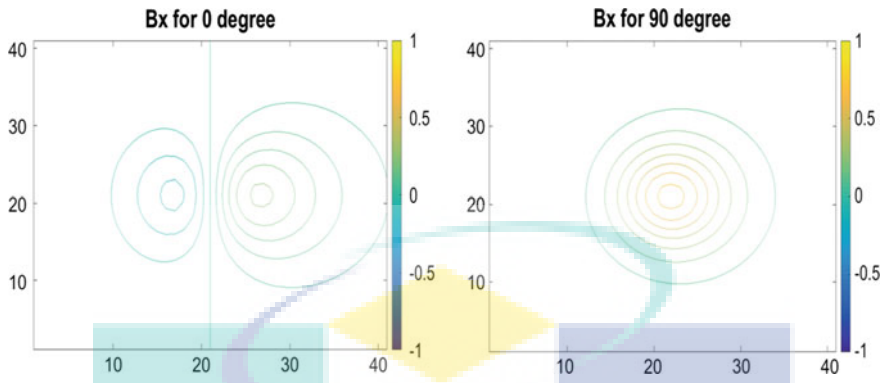


**Fig. 4** Graph of  $B_x$  magnetic response of a magnetic dipole pointing at 0 and 90° from z-axis, respectively

### 3.2 Measurement of Steel Balls

In Fig. 5a, the vertical axis shows the signal intensity of an aluminium can and a white steel nail with length of 3 cm, and Fig. 5b shows the signal intensity when the nail was placed inside the aluminium can. By fixing the sensor at a fixed position, we moved the aluminium can and nail separately. From the measured signal, it shows that the signal reached a maximum when the sample was on top of the sensor. For the aluminium can signal, spurious signals were observed. This was thought that the aluminium can might contain other magnetized metal particles and was not made of pure aluminium. For Fig. 5b, it shows that the signal intensity was almost similar to the signal intensity of the nail. The sensor could sense the remanent magnetic field of the nail despite it was placed inside the aluminium can.

Figure 6a shows the results of magnetic field vectors that responded to x-, y- and z-directions of remanent fields from a 0.5 cm steel ball. The intensity of  $B_x$  was

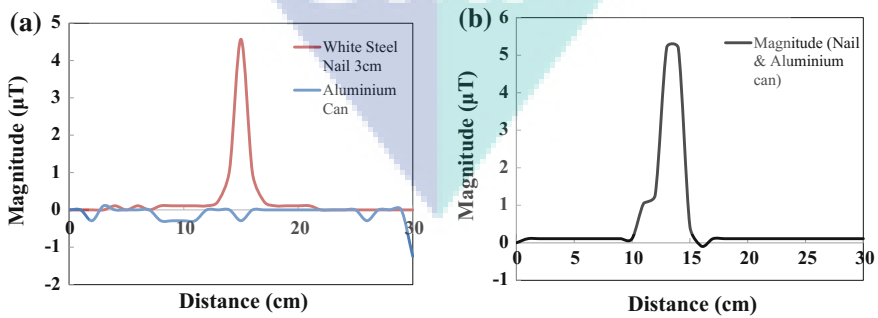


**Fig. 5 a** Magnitude signal of a nail and aluminium can. **b** Magnitude signal of the nail placed inside the aluminium can

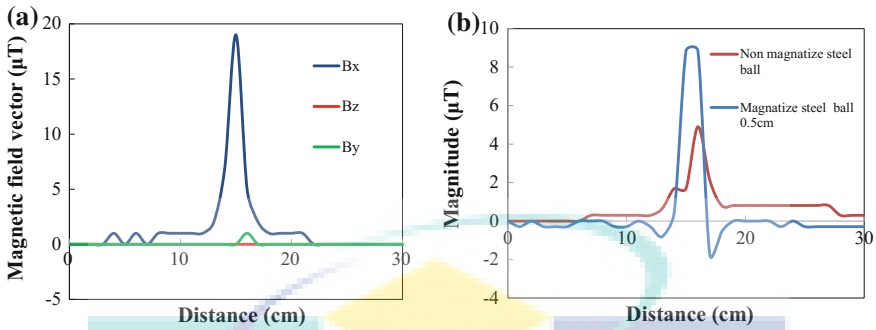


**Fig. 6** **a** Magnetic field vector signals that responded to  $B_x$ ,  $B_y$  and  $B_z$ , respectively, of a 0.5 cm steel ball. **b** Magnitude signal of the 0.5 cm steel ball before and after magnetization

higher compare to  $B_y$  and  $B_z$ . This was thought that the magnetic moments in the metal were pointing towards  $x$ -axis. Figure 6b shows results of the magnetized and non-magnetize steel balls of 0.5 cm diameter. After the steel ball was magnetized, the magnitude was increased compare to the non-magnetize steel ball. Since this method is based of magnetic remanence measurement, the magnetic remanence in a metal object can be improved temporarily by magnetizing it with external magnetic field such as by using a magnet.

Figure 7a shows the magnitudes of the detected magnetic fields at different positions of the steel ball in an aluminium can. From the differences in the position of magnetic responses, the position of the steel ball could be determined based on the response characteristics. Figure 7b shows the intensity of magnetic response of different sizes of steel balls. In this experiment steel balls with diameter of 0.5, 0.3 and 0.1 cm were used. The peak intensity was not correlated with the size of steel balls. This was thought due to the magnetic properties of the steel balls, which is reflected by the magnetic permeability  $\mu$  and magnetization  $M$  as shown in Eq. (2) [10]. However, the width of the signal reflected the size of the steel balls where the

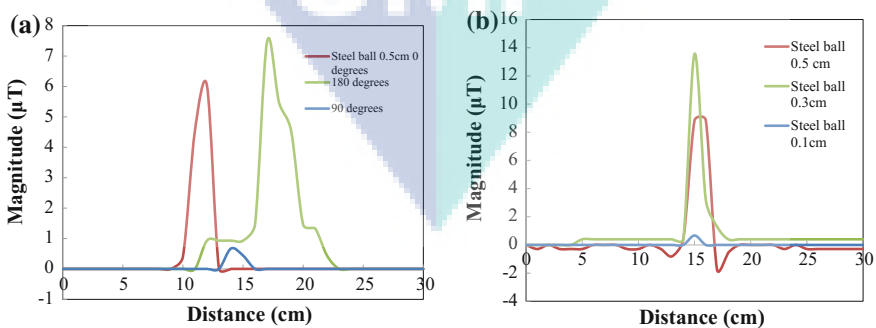


**Fig. 7** **a** Magnitude signal of steel ball (0.5 cm) at different location. **b** Magnitude signal of steel ball with different size of steel balls

steel ball of 0.5 cm diameter has a bigger width of signal compared to others. From here, the signal width could be used to estimate the size of the metallic contaminants. The developed system was able to detect the magnetic response from the steel balls as small as 0.1 cm by using the Mag3110 sensor. Although further improvement in detection sensitivity can be expected by using a superior magnetic sensor such as SQUIDs for detection size smaller than 0.1 mm [8], a compact and low-cost system with sufficient sensitivity was shown by the developed system.

## 4 Conclusion

The fundamental studies on metal detector system have led to the finding of factors that affect the magnetic signal intensity from metallic parts. Based on the theoretical result, a detection system of metallic contaminants was developed based on detection of the remanent magnetic field using the Mag3110 magnetic sensor. The position of the sensor has been optimized to increase the performance of the system on the basis of simulation results. The effectiveness of the metal detection system was experimentally conducted using steel balls with different diameters. A good qualitative agreement with theoretically predicted characteristics was found. The system could detect a steel ball having a diameter as small as 0.1 cm diameter. Thus, the developed metal detection system can be expected to be used for the inspection of wrapped aluminium products.

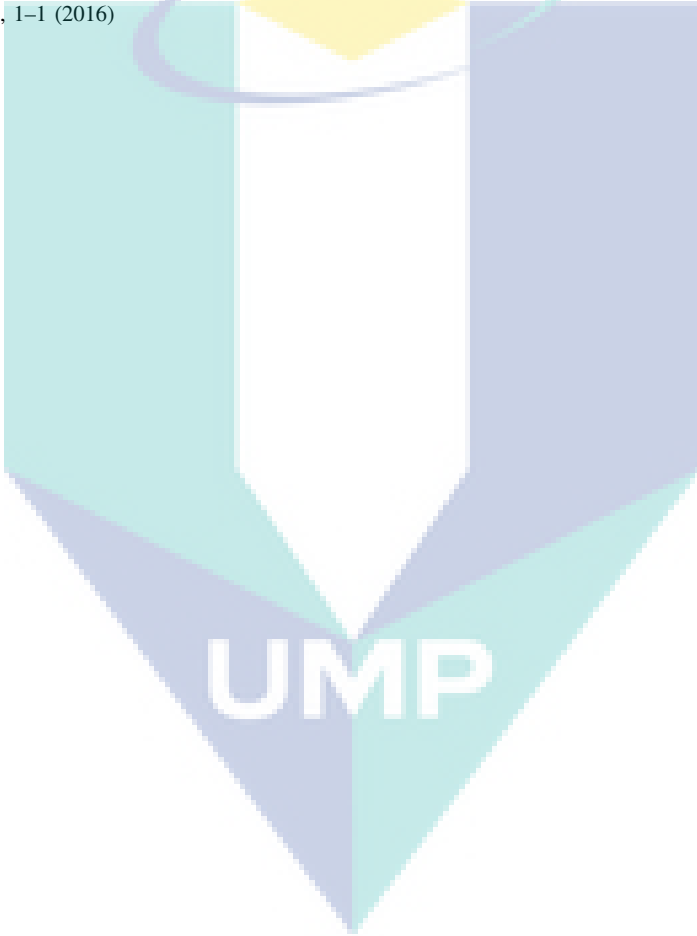
**Acknowledgements** This work was supported by Ministry of Higher Education of Malaysia under grant number of RDU160115 and Research Management Center of Universiti Malaysia Pahang under grant number of RDU170377.

## References

1. Miyakawa, T., Honjo, K.: Development of instrument detecting nonmetal foreign body in food material. In: 1993 IEEE Instrumentation and Measurement Technology Conference, pp. 519–533. IEEE (1993)
2. Patel, D., Hannah, I., Davies, E.R.: Automatic detection of foreign objects in food products. In: 4th International Conference on Advanced Factory Automation (Factory 2000), pp 517–522. IEE (1994)
3. Zhao, Y., Yin, W., Ktistis, C., et al.: On the low-frequency electromagnetic responses of in-line metal detectors to metal contaminants. *IEEE Trans. Instrum. Meas.* **63**, 3181–3189 (2014)
4. Tanaka, S., Akai, T., Hatsukade, Y., Suzuki, S.: High Tc SQUID detector for magnetic metallic particles in products. *IEICE Trans. Electron.* **E92–C**, 323–326 (2009)
5. Kwon, J.S., Lee, J.M., Kim, W.Y.: Real-time detection of foreign objects using X-ray imaging for dry food manufacturing line. In: Proceedings of the International Symposium on Consumer Electronics ISCE, pp. 1–4 (2008)



6. Nagaishi, T., Kamitani, F., Ota, H., et al.: First practical high Tc SQUID system for the detection of magnetic contaminants in commercial products. *IEEE Trans. Appl. Supercond.* **17**, 800–803 (2007)
7. Tanaka, S., Kitamura, Y., Uchida, Y., et al: Development of metallic contaminant detection system using eight-channel high-Tc SQUIDs. *IEEE Trans. Appl. Supercond.* **23**, 1600404–1600404 (2013)
8. Tanaka, S., Kitamura, Y., Hatsukade, Y., et al.: Metallic contaminant detection system using multi-channel high Tc SQUIDs. *J. Magn. Magn. Mater.* **324**, 3487–3490 (2012)
9. Krause, H.J., Panaitov, G.I., Wolters, N., et al.: Detection of magnetic contaminations in industrial products using HTS SQUIDs. *IEEE Trans. Appl. Supercond.* **15**, 729–732 (2005)
10. Tsukada, K., Haga, Y., Morita, K., et al.: Detection of inner corrosion of steel construction using magnetic resistance sensor and magnetic spectroscopy analysis. *IEEE Trans. Magn.* **9464**, 1–1 (2016)



# Vehicle Detection System Using Tunnel Magnetoresistance Sensor



Nurul A'in Nadzri, Chai Kar Hoe, Mohd Mawardi Saari, Saifuddin Razali, Mohd Razali Daud and Hamzah Ahmad

**Abstract** Vehicle detectors are useful to provide essential information such as parking occupancy and traffic flow. To create one robust vehicle detector which works not only in controlled environment (i.e. indoor), but it should also work in outdoor environment, a vehicle detection using magnetic approach is proposed. The magnetic signal of a vehicle will be measured based on magnetic remanence technique where it will be processed to a cloud database. To achieve a low-cost and sensitive system, a Tunnel Magnetoresistance (TMR) sensor is employed. With the combinations of software filter and state machine's algorithm, the occupancy of the car park can be identified with high accuracy. After a few series of real field testing, it is shown that a vehicle in a parking lot can be detected by measuring the surrounding magnetic field that is disrupted by the presence of vehicles. The proposed system is tested for forward and reverse parking, and it shows a high accuracy detection for a B-segment sedan car. It can be expected that by using the proposed technique, detection of vehicles using a low-cost system with capability of online monitoring can be realized.

**Keywords** Tunnel magnetoresistance • Magnetic sensors • Vehicle detectors

## 1 Introduction

Intelligent transport [1], smart cities [2, 3] and Internet of Things [4] are terms that surround us all the time in this century. With growing population, mobility of people using vehicles will increase rapidly and this will result to severe issues such as parking problem of vehicles. Hence, intelligent and centralized solutions to lessen these problems are highly desired, where specifically in the case of vehicle parking problem, gathering and online monitoring data about traffic flow and

---

N. A. Nadzri · C. K. Hoe · M. M. Saari (✉) · S. Razali · M. R. Daud · H. Ahmad  
Faculty of Electrical & Electronic Engineering, Universiti Malaysia Pahang,  
26600 Pekan, Pahang, Malaysia  
e-mail: mmawardi@ump.edu.my

© Springer Nature Singapore Pte Ltd. 2018  
M. H. A. Hassan (ed.), *Intelligent Manufacturing & Mechatronics*,  
Lecture Notes in Mechanical Engineering,  
[https://doi.org/10.1007/978-981-10-8788-2\\_49](https://doi.org/10.1007/978-981-10-8788-2_49)

547

absentees of vehicle in a parking slot are important. Based on the real-time data, traffic congestion and the required time to find a vehicle parking slot can be mitigated by efficiently controlling the flow of vehicles.

In conventional ways of vehicle detection, ultra-sonic sensor is used to obtain the information of parking spot due to its low cost, easy installation, and high accuracy. The vehicle detection using the ultrasonic sensor works by emitting radio waves and detecting the reflected radio waves. This method works efficiently in a controlled environment such as inside indoor; however, it is sensitive to the fluctuations of temperature and extreme air turbulence such as in stormy weather, causing unstable measurement with the loss of signal. Besides that, using the ultra-sonic sensor is not preferable for on-street parking where interference of the surrounding traffics may affect the detection of vehicles [5, 6].

Detection of vehicles using laser sensor is one of the popular methods its low cost and easy installation [7, 8]. However, the light of the laser is easily being distorted by weather and light conditions, making it not suitable for all-weather and outdoor vehicle detection usage [9]. In the case of detection using induction loop, this method requires magnetic fields to be generated and the magnetic responses from the metallic body of vehicles, i.e., effect of Eddy's current, are measured. However, this method consumes a higher electricity power to generate the magnetic fields and the system is not compact due to the size of induction loops [10].

In this paper, a magnetic remanence based detection technique is proposed using a low-cost and sensitive magnetometer with combination of an Arduino board and a Motorola M-WICOM platform of Beagle Bone Black (ARM microprocessor). The used platform has sufficient computing power and its functions can be extended for connectivity with cloud database and online monitoring. The magnetometer MAG3110 (Freescale) is used because it is small, low-power, and has digital 3-axis of detection fields. This sensor utilized next generation magnetic tunnel junction (MTJ) technology which enable itself to have high sensitivity under a very low magnetic field strength condition. MAG3110 is capable of detecting small changes in magnetic field with the sensitivity of  $0.10 \mu\text{T}$ . Furthermore, the size of Mag3110 is small, enabling a compact system, while having immunity to environment noises such as temperature, wind and rain water.

## 2 Methodology

### 2.1 Hardware Setup

As for hardware setup, it can be separated into two parts namely a wireless sensor node and a control terminal.

On the wireless sensor node side, the magnetometer MAG3110 is connected to the Arduino board and the  $x$ -,  $y$ -, and  $z$ -axis magnetic field data will be transferred over the air via a 2.4 Ghz RF module.

On the control terminal side, another RF module is connected directly with M-Wicom Platform of Beagle Bone Black for data logging, data processing and decision-making purposes via UART serial protocol. As for the positions of the wireless sensor node, it is placed in the middle of a parking space, having a 5 m length and 2.5 m width.

## 2.2 Parking Occupancy Detection Algorithm

The occupancy of a parking space can be categorized under binary recognition problem, which possess two states; vacant and occupied conditions.

During parking process of a vehicle, it will undergo entering- and parking-stop stages. Initially, the parking space is vacant. During this vacant condition, the sensor will obtain the background magnetic field of  $x$ -,  $y$ -, and  $z$ -components for background references. For the next phase, when the vehicle is entering the car park regardless of forward or reverse position, it will create a disturbance and causing the surrounding magnetic fields to fluctuate. Next, the parking space is now occupied, and the vehicle will create a stable disturbance on the background magnetic fields. The magnetic fields would also have fluctuated when the vehicle is leaving the parking space. Finally, the parking space is vacant when the vehicle left and the sensor will obtain the background magnetic field again.

As for vehicle detection, it is preferable to use magnitude instead of individual magnetic components. The vehicle detection algorithm based on vector magnitude will be more accurate compared individual  $x$ -,  $y$ -, and  $z$ -axis magnetic fields. The intensity of the magnetic field vectors would be

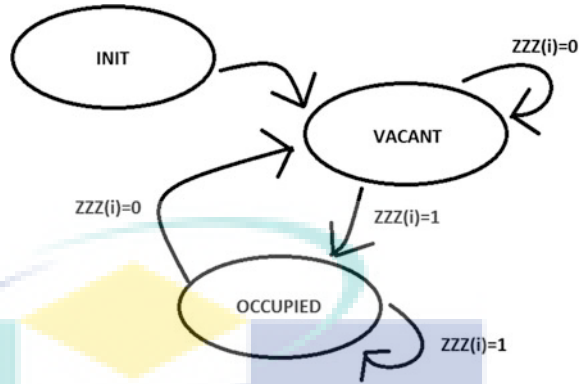
$$G(i) = \sqrt{X_i^2 + Y_i^2 + Z_i^2}, \tag{1}$$

where  $X_i$ ,  $Y_i$  and  $Z_i$  is the magnetic fields of  $x$ -,  $y$ - and  $z$ -axis, respectively.

All signals obtained via sensor will include noises. Hence, moving average filter is introduced to reduce the effect due to random variation. The equation of moving average is given by

$$A(i) = \begin{cases} \frac{G(i) + G(i - 1) + \dots + G(1)}{i} & \text{for } i < Z \\ \frac{G(i) + G(i - 1) + \dots + G(i - Z + 1)}{Z} & \text{for } i \geq Z \end{cases} \tag{2}$$

**Fig. 1** Algorithm's state machine



$G(i)$  is the magnetic vector magnitude obtained earlier and  $Z$  is the averaging filter buffer size. Note that the higher the buffer size, the smoother the graph will be.

Based on all above criteria, the proposed algorithm for the detection system state is shown in Fig. 1. The system state will consist of State: {INIT, VACANT, OCCUPIED}, Input: [ZZZ(i)]: {0, 1}, and Output: [DD(i)]: {0, 1}. The objective of this system state is to detect the occupancy of parking space, whenever there is a vacancy in the spot, the output would yield  $DD(i) = 0$ , which indicates no car. Otherwise  $DD(i) = 1$  indicates it is occupied.

For initialization state  $S1$ : {INIT}, before the program begins, the parking lot must be ensured vacant as this is the pre-requisite for the detection algorithm to work. When the initialization finishes, the sensor will obtain the surrounding magnetic field data and calculate the desired threshold. When the initializing time passes a pre-defined value, it will jump to state  $S2$ : {VACANT} where it starts to detect changes in magnetic fields. When the obtained magnetic field data has exceeded certain the pre-determined threshold (i.e., obtained data exceed of  $G$  from calibrated value) for a certain count (i.e. parameter  $H$ ), it will go for the next state. Otherwise, if it stays between the predefined value, it will yield  $ZZZ(i) = 0$  and continue to monitor for major changes in magnetic fields. During the state  $S2$ : {VACANT}, the system will output  $DD(i) = 0$  to indicate there is no car in the parking space. A reset count system (i.e. parameter  $I$ ) has been added to act as a failsafe mechanism in the case of variable  $H$  is being triggered by false alert. When the parking space is occupied by a vehicle, the system state will turn to  $S3$ : {OCCUPIED}. The sensor will continue to obtain changes in magnetic fields. During this state, the system will yield  $DD(i) = 1$  to indicate that the parking space is being occupied. Occupancy of parking space is determined by the flow chart as shown in Fig. 2.

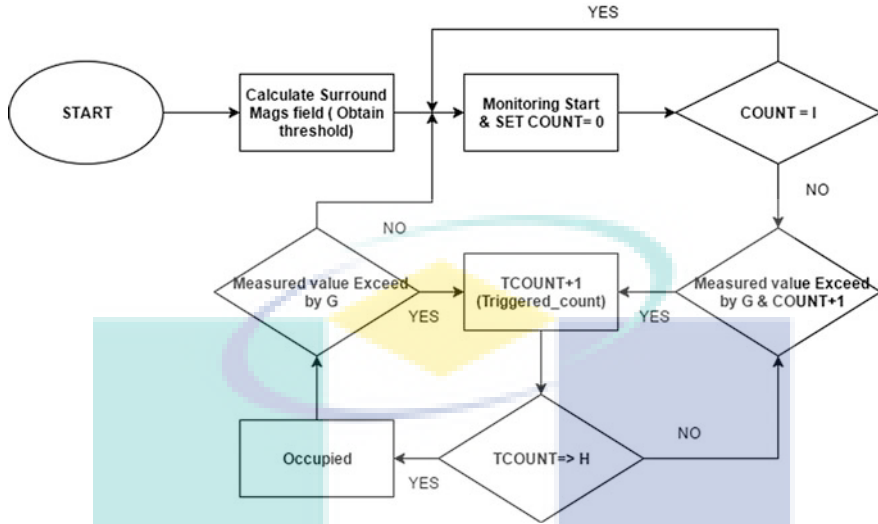


Fig. 2 Flow chart of the proposed algorithm

### 3 Results and Discussion

#### 3.1 Initial Field Testing Magnetic Response

In this preliminary study, the size of car was fixed as a constant variable since the difference in size of car will yield different waveform. Figure 3a shows the magnetic responses for a B-segment sedan car parked on a parking space using forward parking method, i.e., the front part of the car including its engine will first pass through the magnetic sensor located in the middle of the parking space. Note that the sampling rate of data obtained was fixed at 15 Hz or 1 sample every 0.067 s.

From Fig. 3a, that magnetic signals fluctuated when the car was entering or leaving the sensor. When the car completely stopped, or left, the signal became stable.

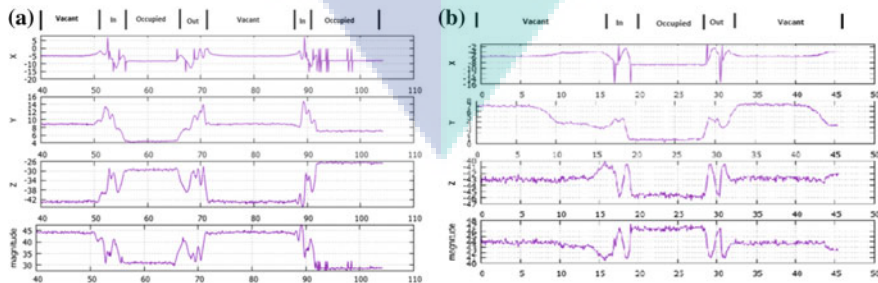
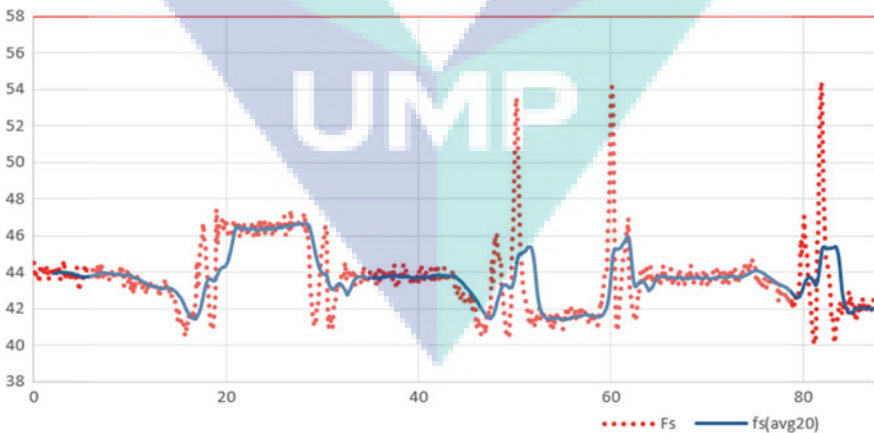


Fig. 3 a Magnetic response for forward parking. b Magnetic response for reverse parking

However, when the vehicle was in the parking slot and completely stopped, the signal fluctuation of the  $x$ -axis magnetic field was observed. This was due to the magnetization and demagnetization of the car air conditional compressor's clutch. Furthermore, loose metallic parts under vehicles will vibrate and this can contribute to the spikes in the detected magnetic signal. Nevertheless, the spikes can be eliminated by using a filter and this enhances the precision in car detection. The disturbance of environmental magnetic field can be verified by comparing the magnitude between a vacant and an occupied parking slot. When the parking space was occupied, the sensor detected a significantly lower magnitude as the car acted as a magnetic shield between the sensor and earth's magnetic field. Based on the measured magnetic responses, the magnitude of the magnetic field was reduced when the car entered the parking space. Moreover, the magnitude of the detected magnetic field showed a positive gradient when the car was leaving the parking space.

Figure 3b shows the magnetic response for a vehicle parking using reverse parking method, i.e., the boot of the car will first pass the magnetic sensor. The magnitude of an occupied parking space using reverse parking method showed a higher value compared to the magnitude when the parking space was vacant. The difference in the signal characteristics between occupied states of forward and reverse parking methods was thought to be due to the different metallic parts of the car detected by the sensor. Nevertheless, the disturbance of magnetic signal can be used as an indicator for the presence of vehicles.

To increase detection sensitivity and eliminating the noises in the measured data, a digital moving average filter was used. In Fig. 4, the dotted line is the initially obtained data containing noises. While the solid line represents the filtered data with buffer size of  $Z = 20$ , where the output was smoothed.



**Fig. 4** Unfiltered versus filtered data



### 3.2 Real-Field Testing with Working Detection Algorithm

The coefficients of the proposed algorithm were set as follows:  $G = 1$ ,  $H = 30$  (where if  $H$  has been triggered for more than 30 times, it will determine that a vehicle is exist in the parking space) and  $I = 450$  (where the counter of  $H$  will be reset after a half minute as the system gathers 15 data in one second, i.e., 15 Hz).

The Parameter  $G = 1$  is chosen based on initial field testing magnetic response, whenever the instantaneous magnetic field are larger or smaller by  $1 \mu T$ , it will increase counter  $H$  by 1. On the initial field testing, whenever the vehicle is parked using forward parking, the magnitude of magnetic field would be lower by  $10 \mu T$  compared to initial value when there exists no vehicle. As for reverse parking, the magnitude of occupied car park is higher by 1.5 times compared to vacant car park. Thus, this made  $G = 1$  is a very good threshold value for vehicle detection purposes.

The parameter  $H$  is introduced to prevent false detection and acts as a failsafe system. In real world scenario, the magnetometer will also pick up noisy spikes from surrounding environment, hence the parameter  $H = 30$  was introduced. Whenever the system pick-up changes in the magnetic field compared to initial value for 30 times, it will classify as a vehicle is present in the parking space. In the proposed algorithm, every second the magnetometer will read 15 sampling data, thus continuous changes in magnetic field for two consecutive seconds, it will indicate a vehicle exists.

Parameter  $I$  was introduced to complement the existence of parameter  $H$ . The purpose of parameter  $I$  was to reset  $H$  counter every 30 s in the case counter  $H$  had been increased previously due to false alert. In the proposed algorithm, the data sampling rate was fixed at 15 Hz, thus parameter  $I$  was set to 450 for reset process in every half minute.

Using above parameters, the experiment result is shown in Table 1. From the tabulated results in Table 1, the vehicle detection rate was 95% for the current system and its detection algorithm. In the 20 times of parking attempts, 10 of the samples were using B-segment sedan cars and another 10 of samples were using A-segment mini cars.

In the 10 attempts of B-segment sedan and A-segment mini cars, respectively, 5 attempts were reverse parking and another 5 were forward parking. The proposed remanence magnetic based detection system with the threshold algorithm could identify all the presence of the B-segment sedan cars in the parking space. On the other hand, in the case of A-segment mini cars, only 5 attempts of forward parking and 4 attempts of reverse parking could be detected by the proposed system. One of the reverse parking was not detected due to less soft and hard metallic parts appear

**Table 1** Result of real field testing using proposed algorithm

Number of parking attempts	Number of vehicle detected in the car park	Accuracy of the threshold-based algorithm
20	19	0.95

in the bonnet area of the vehicle bodies, resulting in a false detection by the algorithm. Fundamentally, different shape and size of vehicles will produce different magnetic responses; however, the disturbance of environmental magnetic field due to the vehicle can be accurately detected by using a sensitive sensor and a superior algorithm. Further improvement of detection rate could be expected by optimizing the algorithm and the position of the magnetic sensor.

## 4 Conclusion

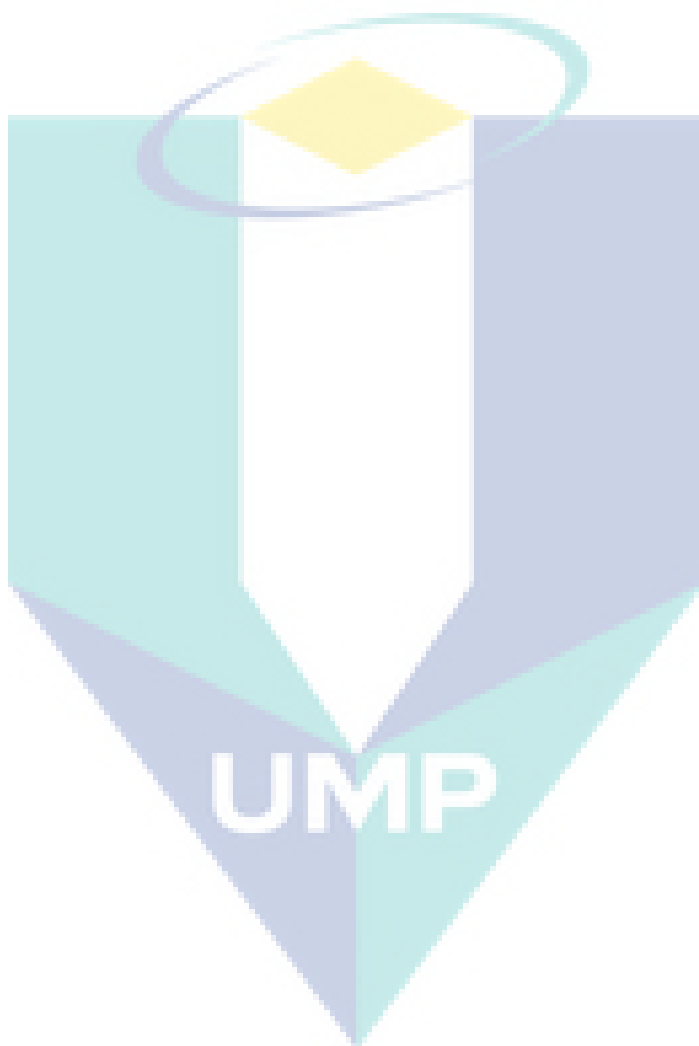
In this paper, vehicle detection in parking space using magnetic remanence technique for real-time monitoring system is presented. The disturbance of surrounding magnetic fields caused by the hard and soft metallic parts of vehicle bodies could be detected by using a Tunnel Magnetoresistance sensor. The detected signals were transmitted to the M-Wicom Platform of Beagle Bone Black using the RF modules. Based on the analysis, the proposed threshold-based vehicle detection algorithm showed a high detection accuracy of 95%. For future works, the experiment can be extended with more sample of vehicle including C-, D-, and E-segment cars as well as the optimization of the detection algorithm. This vehicle parking detection system can be extended to support certain additional features such as the direction of vehicle entering the car park, and the size of vehicle.

**Acknowledgements** This work was supported by Ministry of Higher Education of Malaysia under grant number of RDU 160115 and Research Management Center of Universiti Malaysia Pahang under grant number of RDU 170377.

## References

1. Schulz, W., Geis, I.: Future role of cost-benefit analysis in intelligent transport system-research. *IET Intell. Transp. Syst.* **9**, 626–632 (2015)
2. Mone, G.: The new smart cities. *Commun. ACM.* **58**, 20–21 (2015)
3. Glasmeier, A., Christopherson, S.: Thinking about smart cities. *Camb. J. Reg. Econ. Soc.* **8**, 3–12 (2015)
4. Lee, I., Lee, K.: The internet of things (IoT): applications, investments, and challenges for enterprises. *Bus. Horiz.* **58**, 431–440 (2015)
5. Mimbela, L.E.Y., Klein, L.A.: A summary of vehicle detection and surveillance technologies used in intelligent transportation systems. <http://www.nmsu.edu/~traffic/> (November, 2000)
6. Gorden, R.L., Reiss, R.A., Haenel, H., Case, E.R., French, R.L., Mohaddes, A., Wolcott, R.: Traffic control systems handbook, FHWA-SA-95-032, Washington, D.C., Federal Highway Administration, U.S. Department of Transportation, February, 1996A
7. Texas Transportation Institute. Alternative vehicle detection technologies for traffic signal systems. Technical Report. Austin. 2008.A
8. US Department of Transportation, Federal Highway Administration: A new look at sensors. *Public Roads.* **71**(3), 32–39 (2007)

9. Abdelbaki, H.M., Hussain, K., Gelenbe, E.: A laser intensity image based automatic vehicle classification system. In: 2001 Proceedings of the IEEE Conference on Intelligent Transportation Systems, pp. 460–465
10. Mishra, D.P., Asutkar, G.M.: Vehicle detection and classification using wireless sensor network. *IJAREEIE* 2(10) (2013)



# A Resonant Type AC Magnetometer for Evaluation of Magnetic Nanoparticles



Nazatul Sharreena Suhaimi, Mohd Mawardi Saari, Hamzah Ahmad, Mohd Rusllim Mohamed and Nurul Akmal Che Lah

**Abstract** Characterization of magnetic nanoparticles is crucial in order to optimize them for different applications requiring specific characteristics. In this article, we report a characterization system using AC susceptibility method. An AC magnetometer system which is composed of the induction coil and resonant capacitors is developed to evaluate the performance of the magnetic nanoparticles. The induction coil consists of excitation and detection coil. The excitation coil is designed with solenoid coils and fabricated with a Litz wire which is composed of 60 strands of copper wire with 0.1 mm diameter to reduce the increase of AC resistance at high frequency. The detection coil is designed to be a first-order differential coil which is used to reduce the environmental noise and cancel the excitation magnetic field. The detection coil is fabricated with a copper wire and it is placed at the center of the excitation coil. The excitation coil is connected to the resonant capacitors to cancel the reactant component and to permit the high magnetic field in the high-frequency region. The resonant capacitors are fabricated with multiple values of capacitors. When the developed system is in the resonant mode, the current flow is constant up to the frequency of 32.5 kHz. The developed system can evaluate the magnetic nanoparticles at different frequency responses. Using the developed system, it is shown that the Neel particles exist inside the solution of magnetic nanoparticles used in this study.

**Keywords** AC magnetometer • Magnetic nanoparticles • Coil

---

N. S. Suhaimi · M. M. Saari (✉) · H. Ahmad · M. R. Mohamed  
Faculty of Electrical & Electronic Engineering, Universiti Malaysia Pahang,  
Pekan Campus, 26600 Pekan, Pahang, Malaysia  
e-mail: mmawardi@ump.edu.my

N. A. Che Lah  
Innovative Manufacturing, Mechatronics and Sports Lab (iMAMS),  
Faculty of Manufacturing Engineering, Universiti Malaysia Pahang,  
Pekan Campus, 26600 Pekan, Pahang, Malaysia

© Springer Nature Singapore Pte Ltd. 2018  
M. H. A. Hassan (ed.), *Intelligent Manufacturing & Mechatronics*,  
Lecture Notes in Mechanical Engineering,  
[https://doi.org/10.1007/978-981-10-8788-2\\_9](https://doi.org/10.1007/978-981-10-8788-2_9)

93

## 1 Introduction

Magnetic nanoparticles are mostly applied in the biomedical areas such as *in vivo* imaging [1], magnetic hyperthermia [2], and magnetic immunoassay. There are different applications of magnetic nanoparticles requiring different characteristics of the magnetic nanoparticles. Therefore, the characterization of the magnetic nanoparticles is important. The characterization of the magnetic nanoparticles can be done by AC susceptibility [3], magnetic relaxation [4], and remanence measurement. In this paper, the AC susceptibility is used to characterize the magnetic properties of the magnetic nanoparticles. The AC susceptibility measurement can provide the information of size distribution, harmonics and magnetic anisotropy with a fast response to the measurement. Moreover, the use of a phase sensitive detector can permit a higher sensitivity. In this method, the excitation coil will apply an AC field to a sample and the detection coil will detect the AC response that produced by the sample [5]. During this process, magnetic relaxations such as Neel and Brownian relaxations can be observed. Neel relaxation occurs when the rotation of magnetic moment occurs within the nanocrystals while Brownian relaxation occurs when the particles are physically rotated and the magnetic moment is blocked at a certain direction [6].

For that purpose, an AC magnetometer system is developed to evaluate the performance of the magnetic nanoparticles. There are a few systems, that have been developed such Imego AC susceptometry using an ordinary induction coil technique [7]. This system is possible to measure the dynamic magnetic properties from 1 Hz until 10 MHz at a low excitation field of  $H = 24$  A/m. There is also another system was reported that measure hysteresis loop in a high frequency region using an air-cooled Litz wire coil [8]. Since the magnetic nanoparticles are applied in different frequencies and excitation fields, an AC magnetometer that is able to characterize them in a wide region of frequency and excitation field is highly desired. This AC magnetometer can also serve as a standardization technique for magnetic nanoparticles.

In this article, to fulfill the aforementioned system, we have developed an AC magnetometer system using an induction coil technique for the characterization of the magnetic nanoparticles [9]. The induction coil is composed of an excitation and detection coils. The excitation coil is designed as a Helmholtz coil which has two solenoid coils aligned to be co-axial in a series configuration, separated with a 4 mm gap. The radius of the excitation coil is 15 mm. The detection coil is designed as a first-order differential coil. In order to achieve high homogeneity and sufficient amplitude of the excitation magnetic field, the excitation coil with resonant capacitors is developed [10]. The resonant capacitor is developed with the multiple values of the capacitors in order to achieve a resonant frequency up to 82.32 kHz. The capacitors are constructed in the series and/or parallel configuration. For this study, film capacitors such as polypropylene capacitors are used where they are capable to withstand high current and voltage.

## 2 Methodology

### 2.1 System Configuration

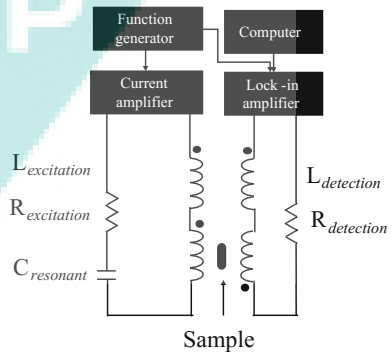
Figure 1 shows the system configuration of AC magnetometer with the resonant capacitor. The detection coil is inserted into the center of the excitation coil. The excitation coil is connected to a current amplifier (TS 250, Accel Instruments). The current amplifier will provide a high current to the excitation coil. The high current from the current amplifier is based on the reference signal that is supplied by the function generator of the lock-in amplifier (LI 5640, NF Corporation). The lock-in amplifier is used as a Phase Sensitive Detection (PSD) to detect the signal. When the high current flows through the excitation coil, the sample is magnetized. The magnetization of the sample can cause the sample to produce a magnetic field. The magnetic field of the sample is detected by the detection coil. The detection coil will send the signal to the lock-in amplifier and lock-in amplifier will send the signal to a computer.

### 2.2 The Design of Excitation Coil

The excitation coil is designed based on the Helmholtz coil configuration with two solenoid coils. The design of the excitation coil is referred to the Biot-Savart's law based on a multi-layer surface current model and can be expressed as;

$$\mathbf{B}(\mathbf{r}') = \frac{\mu_0}{4\pi} \sum_{n=1}^N \sum_{i=1}^S \frac{\mathbf{J}_n S_{i,n} \times (\mathbf{r}' - \mathbf{r}_n)}{|\mathbf{r}' - \mathbf{r}_n|^3}, \tag{1}$$

**Fig. 1** The schematic diagram of the developed AC magnetometer system with resonant capacitors



where  $\mu_0$  is referred to the vacuum magnetic permeability,  $\mathbf{J}_n$  is the surface current density vector at  $n$  layer,  $s_{i,n}$  is the surface unit area,  $\mathbf{r}_n$  is the position of the surface current and  $\mathbf{r}'$  is the position of the point observation. From the Eq. (1), it shows that the strength of the magnetic field can be high if the distance between the current element to the observation point is reduced and this is equal to the radius minimization of the excitation coil. The radius of the excitation coil should not be designed too big or small because it will give an effect to the reduction of the magnetic field uniformity area. However, the radius of the excitation coil must fit the diameter of the detection coil.

The excitation coil was fabricated of two solenoid coils which are connected in series and both solenoid coils are separated by a 4 mm gap. The excitation coil is fabricated from a Litz wire which is composed of 60 strands of the copper wire. The number of turn for each side of the coil is 150 turns. The length and radius of the coil are 26 mm and 15 mm. The resistance and inductance of the excitation coil were measured to be 1.3516  $\Omega$  and 1.5176 mH at 1 V and 1 kHz by a LCR meter (GW INSTEK LCR-816).

Then, the excitation coil will be connected to the resonant capacitor in a series connection and it will form an RLC circuit. The resonant capacitor is designed with the multiple values of capacitors. In the resonance mode, the capacitance can be calculated as;

$$C = \frac{1}{(2\pi f)^2 \times L}, \quad (2)$$

where  $f$  is the frequency and  $L$  is the inductance of excitation coil. From the RLC circuit, the resonant frequency can be calculated by manually selecting the values of capacitors. The range of the resonant frequency was set from 581 Hz to 82.32 kHz.

### 2.3 The Design of Detection Coil

The detection coil is designed as a first-order differential coil. The first-order differential coil is chosen because it can minimize the environmental magnetic noise and external magnetic field. The detection coil is composed of a copper wire with the diameter of 0.25 mm. The length and the radius of the detection coil are 19 mm and 7 mm. The number of turn for each side of the coil is 1000 turns and the detection coil was wound in the opposite direction for both sides of the coil [9]. The resistance and inductance of the detection coil were measured to be 41.456  $\Omega$  and 16.755 mH.



## 2.4 The Preparation of the Iron Oxide Nanoparticles as a Sample

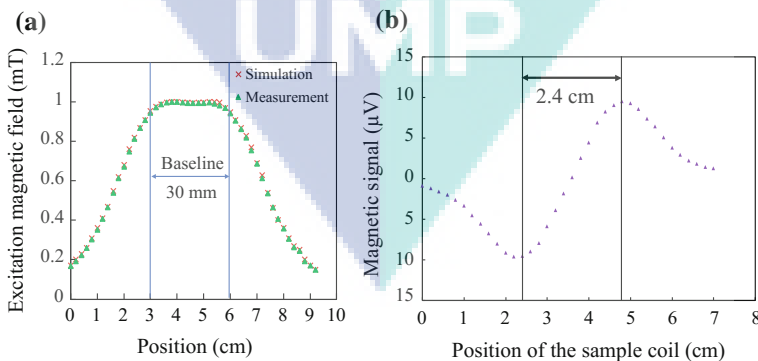
The iron oxide nanoparticles (Nanomag-D102, Micromod Partikeltechnologie GmbH) with a median diameter 100 nm was used in the experiment. The iron oxide nanoparticles of D102 were prepared in two different environments such as liquid and dry states to evaluate their frequency response. The solution was filled inside a tube whose diameter is 7 mm and it will be placed at the center of one detection coil. For this experiment, the sample of D102 was prepared in 200  $\mu$ l.

## 3 Result and Discussion

### 3.1 The Characteristic of the Excitation Coil

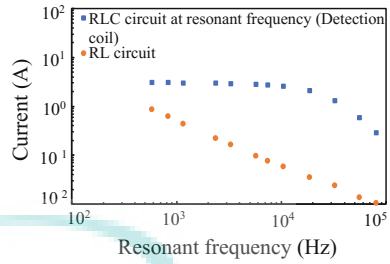
The distribution of magnetic field was determined by using a teslameter. The rod of the teslameter was moved through the excitation coil from 0 mm to 92 mm with the interval of 2 mm. Figure 2a shows the distribution line of the excitation magnetic field at the excitation coil with respect to the different positions of the teslameter. The magnetic field was uniform from the region of 30 mm to 60 mm which was from the center of one coil to the center of another coil and the magnetic field produced at the center was 5.22 mT/A. The result of measurement was compared to the result of the simulation. The simulation result showed the same value with the measurement result. The inhomogeneity in this region has been calculated to be 7%.

The small sample coil with 30 turns was fabricated to detect the magnetic signal at the detection coil. The small sample coil was moved along the detection coil from 0 mm to 72 mm with 2 mm interval. Figure 2b shows the magnetic signal of the



**Fig. 2** a The distribution line of excitation magnetic field at the excitation coil with respect to the position of rod teslameter. b The magnetic signal of the detection coil with respect to the position of the small sample coil

**Fig. 3** The intensity of current flow through the excitation coil with respect to the frequency



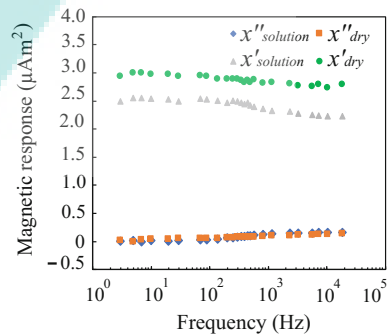
detection coil by moving the small sample coil along the detection coil. The highest magnetic signal was produced from the center of each coil. The distance between the first peak to the second peak was 24 mm which was the distance between the centers of each coil. The negative and positive magnetic signal produced by the detection coil was referred to the turn direction of each coil.

Figure 3 shows the result of the intensity of current flow through the excitation coil at different resonant frequencies. Before the resonant capacitor was connected to the excitation coil, the current flow through the excitation coil was decreased when the frequency was increased. Then, when the resonant capacitor was connected to the excitation coil, the current flow through the excitation was constant at 3 A until 32.5 kHz.

### 3.2 The Frequency Response of the Magnetic Nanoparticles in Dry and Solution State

Figure 4 shows the magnetic response produced by the D102 at different frequencies. In this experiment, two components such as  $\chi'$  (in-phase magnetization) and  $\chi''$  (out-of-phase magnetization) were measured. For  $\chi'$ , the magnetic response of the D102 in the solution state showed a same characteristic of the magnetic response that produced in the dry state, which it was constant over the frequency

**Fig. 4** The magnetic response of the D102 with respect to the frequency



region. This was because the sample of D102 did not being affected by Brownian relaxation. For the  $\chi''$ , the magnetic response of the D102 is started to increase when the frequency is increased. This could be thought that D102 has undergone Neel relaxation.

## 4 Conclusion

In this work, an AC magnetometer system with resonant capacitors is developed. The AC magnetometer system is able to measure the magnetic response of the magnetic nanoparticles in the range of 3 Hz–32.5 kHz with the amplitude magnetic field per unit current at the center of 5.2 mT/A. The resonant capacitor with the multiple values of capacitance was developed to maintain the flow of current through the resonant circuit until the frequency reached 32.5 kHz. The developed AC magnetometer system was capable to evaluate the magnetic response of the magnetic nanoparticles based on the frequency response. The mechanism of Neel relaxation was observed for D102.

**Acknowledgements** This work was supported by Ministry of Higher Education of Malaysia under grant number of RDU 160115 and Research Management Center of Universiti Malaysia Pahang under grant number of RDU 170377.

## References

1. Enpuku, K., et al.: Magnetic nanoparticle imaging using cooled pickup coil and harmonic signal detection. *Jpn. J. Appl. Phys.* **52**, 87001 (2013)
2. Sadiq, A.A., Othman, N.B., Jamil, M.M.A.: Magnetic Particle Imaging System For Cancer Diagnosis : An Overview, vol. 10, no. 19, pp. 8556–8561 (2015)
3. Ludwig, F., Balceris, C., Jonasson, C., Johansson, C.: Analysis of ac susceptibility spectra for the characterization of magnetic nanoparticles, vol. 9464, no. 3 (2017)
4. Ludwig, F., Heim, E., Schilling, M.: Characterization of superparamagnetic nanoparticles by analyzing the magnetization and relaxation dynamics using fluxgate magnetometers. *J. Appl. Phys.* **101**(11), 113909 (2007)
5. Youssif, M.I., Bahgat, A.A., Ali, I.A.: AC Magnetic Susceptibility Technique for the Characterization of High Temperature Superconductors, vol. 23, pp. 231–250 (2000)
6. Bogren, S., et al.: Classification of magnetic nanoparticle systems—synthesis, standardization and analysis methods in the nanomag project. *Int. J. Mol. Sci.* **16**(9), 20308–20325 (2015)
7. Ahrentorp, F., et al.: Sensitive high frequency AC susceptometry in magnetic nanoparticle applications. *AIP Conf. Proc.* **1311**, 213–223 (2010)
8. Connord, V., Mehdaoui, B., Tan, R.P., Carrey, J., Respaud, M.: An air-cooled Litz wire coil for measuring the high frequency hysteresis loops of magnetic samples—a useful setup for magnetic hyperthermia applications. *Rev. Sci. Instrum.* **85**(9) (2014)
9. Tumanski, S.: Induction coil sensors—a review. *Meas. Sci. Technol.* **18**(3), R31–R46 (2007)
10. Yang, T.Q., Enpuku, K.: SQUID magnetometer utilizing normal pickup coil and resonant-type coupling circuit. *Phys. C Supercond.* **392–396**, 1396–1400 (2003)



## Research articles

# Harmonics distribution of iron oxide nanoparticles solutions under diamagnetic background



Mohd Mawardi Saari<sup>a,\*</sup>, Nurul Akmal Che Lah<sup>b</sup>, Kenji Sakai<sup>c</sup>, Toshihiko Kiwa<sup>c</sup>, Keiji Tsukada<sup>c</sup>

<sup>a</sup> Faculty of Electrical and Electronic Engineering, Universiti Malaysia Pahang, Pekan Campus, Pekan 26600, Pahang, Malaysia

<sup>b</sup> Innovative Manufacturing, Mechatronics and Sports Lab (iMAMS), Faculty of Manufacturing Engineering, Universiti Malaysia Pahang, Pekan Campus, Pekan 26600, Pahang, Malaysia

<sup>c</sup> Graduate School of Natural Science and Technology, Okayama University, 3-1-1 Tsushima Naka, Kita Ku, Okayama 700-8530, Japan

## ARTICLE INFO

## Article history:

Received 25 October 2017

Received in revised form 1 December 2017

Accepted 15 December 2017

Available online 16 December 2017

## Keywords:

Magnetic nanoparticles

Diamagnetism

Water

Harmonics generation

SQUID magnetometer

## ABSTRACT

The static and dynamic magnetizations of low concentrated multi-core iron oxide nanoparticles solutions were investigated by a specially developed high- $T_c$  Superconducting Quantum Interference Device (SQUID) magnetometer. The size distribution of iron oxide cores was determined from static magnetization curves concerning different concentrations. The simulated harmonics distribution was compared to the experimental results. Effect of the diamagnetic background from carrier liquid to harmonics distribution was investigated with respect to different intensity and position of peaks in the magnetic moment distribution using a numerical simulation. It was found that the diamagnetic background from carrier liquid of iron oxide nanoparticles affected the harmonics distribution as their concentration decreased and depending on their magnetic moment distribution. The first harmonic component was susceptible to the diamagnetic contribution of carrier liquid when the concentration was lower than 24  $\mu\text{g/ml}$ . The second and third harmonics were affected when the peak position of magnetic moment distribution was smaller than  $m = 10^{-19} \text{ Am}^2$  and the concentration was 10  $\text{ng/ml}$ . A highly sensitive detection up to sub-nanogram of iron oxide nanoparticles in solutions can be achieved by utilizing second and third harmonic components.

© 2017 Elsevier B.V. All rights reserved.

## 1. Introduction

Magnetic nanoparticles (MNPs) have attracted many interests, particularly in bio-medical applications owing to their promising characteristics and detection techniques [1–11]. Detection of MNPs for *in vivo* and *ex-vivo* applications can be performed by utilizing their magnetic properties such as magnetic susceptibility [2–4], relaxation [5–7] and remanence [8,9]. Compared to the latter magnetic properties, magnetic susceptibility is measured in the presence of an excitation magnetic field where the feedthrough generated from the excitation field can reduce the detection sensitivity of MNPs. A cancellation circuit of the excitation magnetic field [12,13] and a band-stop filter [14] can be used to reduce this interference. Furthermore, the nonlinear magnetization characteristic of MNP is commonly utilized in dynamic (AC) magnetization measurements to isolate the frequency component of excitation magnetic fields [15–17]. Since the magnetic response is measured in the presence of excitation magnetic field, this magnetic response contains the induced signal from the environment of MNPs, *i.e.*,

diamagnetic carrier liquid [18]. The magnetic response from the diamagnetic carrier liquid such as water can be comparable to the magnetic response of MNPs in the case of high intensity of excitation magnetic field and highly diluted MNP solutions which are used in the most bio-medical applications. Although the magnetization characteristic of the diamagnetic carrier liquid is known to be linear, this diamagnetic background deforms the observed static magnetization curve of MNPs suspended in the diamagnetic carrier liquid. When an AC magnetic field is applied to MNPs, the induced magnetic response reflects the derivatives of the static magnetization curve where it contains harmonic components. Therefore, the effect of the diamagnetic contribution to the induced harmonics must be clarified so that MNPs can be optimized for a highly sensitive detection of MNPs in the suspension of diamagnetic liquid.

In this study, we investigated the magnetization curves and harmonics distribution of commercial multi-core iron oxide nanoparticles in low concentration solutions using our specially developed AC–DC magnetometer. The magnetometer mainly consists of a high-critical-temperature superconducting quantum interference device (high- $T_c$  SQUID) coupled with an optimized flux transformer. We performed reconstructions of magnetization

\* Corresponding author.

E-mail address: [mmawardi@ump.edu.my](mailto:mmawardi@ump.edu.my) (M.M. Saari).

curves to analyze the size distribution of iron oxide cores using a non-negative non-regularized inversion method. We compared the measured and simulated harmonics on the basis of particle size distribution. We simulated the ratio of harmonics with respect to different concentrations and magnetic moment distributions to evaluate the effect of the diamagnetic contribution of water as a carrier liquid. The static magnetization curves indicate the deformation due to diamagnetism of water is a function of concentration. The first harmonic component is significantly affected by the diamagnetic background of water and depended on the concentration. Compared to other components, second and third harmonics offer a high signal-to-noise detection of MNPs in low concentration solutions as they are resilient to the diamagnetic background in a wide distribution of magnetic moment and low concentration solutions. Optimization of the magnetic moment of particles will permit a highly sensitive detection on MNPs in the intended applications.

## 2. Material and measurement system

### 2.1. Magnetic nanoparticles

We investigated static and dynamic magnetic responses from commercial magnetic nanoparticles: nanomag<sup>®</sup>-D-spio (Micromod Partikeltechnologie GmbH). These particles are iron oxide multi-core particles where clusters of single-domain iron oxide nanoparticles are coated in dextran. The size of the iron oxide cores and the typical diameter of these multi-core particles are 12 nm and 100 nm, respectively. The composition of iron oxide in these multi-core particles is 35 wt%. These multi-core particles are suspended in water to form a stock solution with a particle concentration of  $7.5 \times 10^{12}$  particles per ml and iron concentration of 2.4 mg/ml. We prepared four sets of low-concentration magnetic fluids by diluting the stock solution in purified water with dilution factors from 25 to 100. The iron concentrations of the diluted solutions were 24 µg/ml, 48 µg/ml, 72 µg/ml, and 96 µg/ml. These solutions were encased in acrylic cases of 20 mm in length, 15 mm in width, and 9 mm in height, which were constructed from 1 mm acrylic plates.

### 2.2. High- $T_c$ SQUID magnetometer

We have developed a highly sensitive magnetometer utilizing a high- $T_c$  SQUID with a flux transformer for magnetic property evaluation of MNPs in solutions. The developed magnetometer consisted primarily of a high- $T_c$  SQUID with a flux-transformer, a vibrating-sample stage, a computer-controlled electromagnet, and a data acquisition system. The magnetization signal of a sample at room temperature was sensed by a planar differential coil, which was fixed between the poles of the electromagnet. This detection coil was fabricated from 2 elliptical Cu coils with a small compensation coil and was optimized geometrically for detection of static and dynamic magnetizations [12,19]. The magnetization signal was transferred to the high- $T_c$  SQUID via a superconducting flip-chip coil. We measured the static magnetization upon excitation of any given DC magnetic field by modulating the position of the sample along the baseline of the differential coil at a vibration frequency of 2.8 Hz. On the other hand, the dynamic magnetization of a stationary sample upon application of AC and DC magnetic fields was measured by utilizing the gradient characteristic of the differential coil. The DC magnetization output of the developed system was calibrated with a magnetic property measurement system (MPMS3, Quantum Design) by measuring the magnetization of a same paramagnetic MnF<sub>2</sub> sample. The developed system showed a sensitivity of  $3 \times 10^{-10}$  Am<sup>2</sup> at the vibration

frequency of 2.8 Hz, which was better in comparison to conventional magnetometers using induction coils and conventional amplifiers. A detailed explanation of the developed system has been reported previously [19,20].

## 3. Theoretical model

### 3.1. Static magnetization curve

The magnetization of MNPs can be expressed by the Langevin function for particles with no magnetic interparticle interactions and have isotropic spin governed by thermal fluctuations and the magnetization field [21–24]. For a physical sample, magnetic moments  $m = M_s V$  are distributed to some extents due to size distribution. Here,  $M_s$  is the intrinsic saturation magnetization and  $V$  is the core volume. The magnetization  $M$  of MNPs measured at an applied magnetic field  $\mu_0 H_j$  can be expressed as

$$M(\mu_0 H_j) = \sum_{i=1}^N \rho_i(m) m_i L(m_i \mu_0 H_j / k_B T) \Delta m_i \quad (1)$$

where  $\rho_i(m) \Delta m_i = n_i$  represents the number of particles with a magnetic moment between  $m_i$  and  $m_i + \Delta m_i$ ,  $k_B$  is the Boltzmann constant,  $T$  is the absolute temperature,  $\mu_0$  is the vacuum permeability, and  $L(m_i \mu_0 H_j / k_B T) = \text{Coth}(m_i \mu_0 H_j / k_B T) - 1 / (m_i \mu_0 H_j / k_B T)$  is the Langevin function. When the magnetic response of MNPs is measured in a carrier liquid, the magnetization observed by the measurement system can be expressed as

$$M_{\text{observed}}(\mu_0 H_j) = \sum_{i=1}^N \rho_i(m) m_i L(m_i \mu_0 H_j / k_B T) \Delta m_i - C \mu_0 H_j \quad (2)$$

where  $C$  is the diamagnetic parameter of the carrier liquid. The diamagnetic parameter  $C$  can be determined by measuring the magnetization curve of the carrier liquid.

### 3.2. Distribution of magnetic moment

To properly construct the distribution of magnetic moment, a correction to the measured magnetization curves due to the diamagnetic background was performed by subtracting the magnetization curves of the solutions with the water. The distribution of magnetic moment can be constructed by fitting Eq. (1) with the measured data after correction of diamagnetic background. Eq. (1) can be rewritten in a vector form as  $\mathbf{M}_{\text{exp}} = \mathbf{L} \mathbf{w}$  for data measured at  $J$  points of the magnetic field. The components of  $\mathbf{M}_{\text{exp}}$  and  $\mathbf{w}$  vectors can be expressed by  $M_{\text{exp}} \equiv M(\mu_0 H_j)$  ( $j = 1, \dots, J$ ) and  $w_i \equiv n_i(m) m_i \Delta m_i$  ( $i = 1, \dots, N$ ), and  $\mathbf{L}$  is a  $J \times N$  matrix with the elements of  $L_{ji} = L(m_i \mu_0 H_j / k_B T)$ . Here,  $w_i$  represents the magnetic weight of the corresponding magnetic moment  $m$  in the distribution. By performing minimization of the mean squares deviation  $\xi^2 = \|\mathbf{M}_{\text{exp}} - \mathbf{L} \mathbf{w}\|^2$  between the measured and calculated magnetization values, the distribution of the magnetic weight  $w_i$  with respect to  $m$  can be determined. We used a non-regularized non-negative inversion method to minimize the deviation in which this method requires no prior information on the shape of the distribution and enforces positive constraints of the solution. The minimization program was coded in Mathematica (Wolfram Research, USA). A detailed explanation of this method can be found in Ref. [24,25].

### 3.3. Harmonics distribution

To investigate the effect of the diamagnetic background to the harmonics distribution, we consider a low-frequency region where the harmonics are not affected by Neel and Brownian relaxations.



An excitation frequency of 5 Hz was selected in the experiment and simulation. In the case of MNP systems that satisfy Eq. (1) and where effects such as Neel and Brownian relaxations can be ignored, the magnetic response upon the excitation AC and DC magnetic fields can be assumed to follow the magnetization curve of MNP systems. The magnetic response contains a distribution of harmonic components since it reflects the shape of the magnetization curve in the regions covered by the excitation magnetic fields. Magnetization  $M(t)$  of MNPs upon the excitation of magnetic field  $B_{excitation}(t) = B_{amp}\sin(\omega t) + B_{DC}$  can be expressed as

$$M(t) = M_{observed}(B_{excitation}(t)) = M_0 + M_1 \cos(\omega t + \theta_1) + M_2 \cos(2\omega t + \theta_2) + \dots + M_n \times \cos(n\omega t + \theta_n) \quad (3)$$

where  $M_n$  is the amplitude coefficient and  $\theta_n$  is the phase angle at angular frequency  $n\omega$ . In the case a conductive detection coil is used to detect the magnetic response, the detected signal is proportional to the time derivative of  $M(t)$ . In the experiment, we measured the first, second, and third harmonics since their signal-to-noise ratio are higher compared to the other harmonics. Furthermore, these harmonics are commonly used in applications that require a high sensitivity of MNPs' detection. In addition, we performed numerical simulation of the harmonics response on the basis of the obtained magnetic moment distribution. Then, Fast Fourier Transform (FFT) analysis was used to extract harmonic components. The effect of diamagnetic contribution to the harmonics distribution was investigated with respect to concentration and position of magnetic moment distribution.

#### 4. Magnetization curve and magnetic moment distribution

Fig. 1 shows the measured magnetization curves of the iron oxide nanoparticles at different concentrations. The magnetization curves were measured in the region from  $-240$  mT to  $240$  mT in a closed loop measurement starting from initial magnetization curve. As a reference for background signal subtraction, magnetization curves of water and sample case are also shown in Fig. 1. A superparamagnetic characteristic with  $H_s$  of approximately  $\mu_0 H = 40$  mT was observed for all concentration with negligible hysteresis. A deformation of magnetization curve due to the diamagnetic background at the region above  $150$  mT was observed, particularly in the case of the lowest concentration solution.

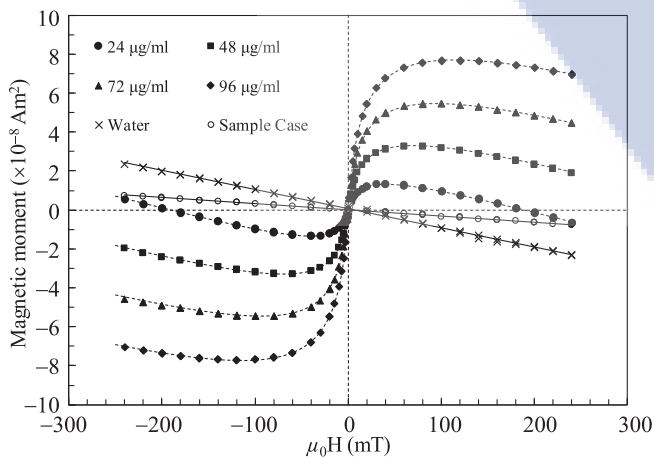


Fig. 1. Magnetization curves of the highly diluted iron oxide nanoparticle solutions of different concentrations. Magnetization curves of water and sample case were measured to account the diamagnetic background.

The reconstructed distribution of magnetic weight with respect to  $m$  is shown in Fig. 2. All of the prepared solutions showed a similar distribution shape and peak. The magnetization curves derived from the reconstructed distributions with consideration of diamagnetic background are indicated by the dashed lines in Fig. 1. A good quality fit of the measured magnetization curves was obtained as the norm of residuals  $\sigma = \sqrt{\sum(M_{exp} - M_{cal})^2}$  between the measured and calculated magnetization showed values  $< 2.8 \times 10^{-9}$  Am<sup>2</sup>. Here,  $M_{cal}$  is the calculated magnetization from the constructed distribution using Eq. (2). Although the shape of the distributions remains similar, their peaks which reflect to the most magnetically contributed particles will reduce proportionally with the concentration. Assuming the shape of the iron oxide cores is spherical where  $m = (\pi/6)d^3M_s$ , the peaks at  $m = 4 \times 10^{-19}$  Am<sup>2</sup> can be calculated to correspond to a core size of  $d = 13.19$  nm. Here, the intrinsic saturation magnetization  $M_s = 333$  kA/m was calculated from the magnetization value at  $240$  mT and the specific density of  $5150$  kg/m<sup>3</sup> was used. This calculated core size reasonably agreed with the size estimated from the Transmission Electron Microscopy (TEM) image (see the superimposed image in Fig. 2).

The magnetization slope of the solutions approached the slope value of water in the region above  $150$  mT as the concentration decreased. This can be explained by the decreasing number of particles having  $m$  smaller than  $4 \times 10^{-19}$  Am<sup>2</sup> since the magnetization of particles larger than  $m = 4 \times 10^{-19}$  Am<sup>2</sup> starts to saturate in the region higher than  $50$  mT [26]. The diamagnetic deformation of magnetization curve was not apparently observed in high concentration solutions since the linear magnetization of small particles having  $m_i \mu_0 H_j / k_B T < 2$  cancels out the diamagnetic contribution of water.

The shape deformation of magnetization curve can be explained by the magnetization ratio between iron oxide nanoparticles and water. The saturation of magnetization of iron oxide nanoparticles and the strong magnetization of water has resulted in a shape deformation of magnetization curve in a high magnetic field region. The shape deformation can shift to the low-magnetic field region as the concentration of iron-oxide nanoparticles, i.e., magnetization intensity decreases. The magnetization curve of a highly diluted solution can be substantially deformed by the diamagnetic

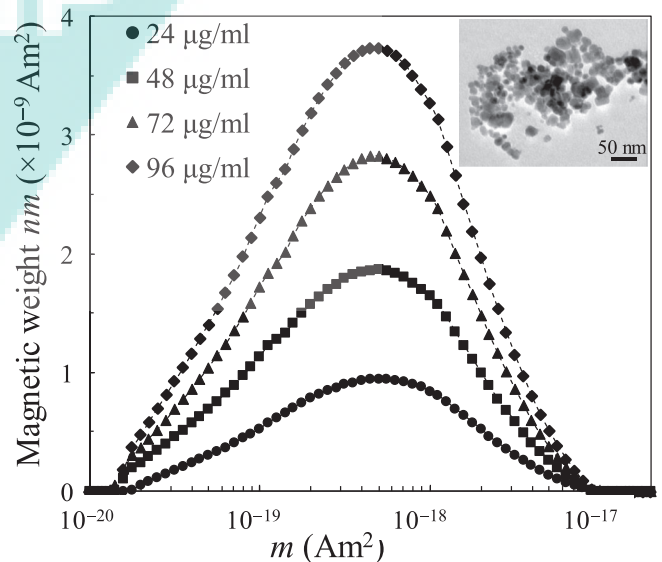


Fig. 2. Reconstructed distributions of magnetic moment in all concentrations. The superimposed picture shows TEM image of iron oxide cores.

effect, and this may result in an estimation error of MNPs' concentration in applications requiring highly sensitive detection.

AC susceptibility measurement method is commonly utilized to measure the magnetic response from MNPs in broad applications since it enables a fast and sensitive evaluation. Fundamentally, magnetic responses of MNPs during exposure of AC and DC magnetic fields are the reflection of their non-linear magnetization curve, composed of harmonic spectrums in the frequency domain. Therefore, deformation of magnetization curves has direct effect to the induced harmonics, and this may hinder accurate quantitative evaluation of MNPs in applications requiring high detection sensitivity such as Magnetic Particle Imaging (MPI) technique and magnetic immunoassay.

### 5. Harmonics in diluted multi-core iron oxide nanoparticle solutions

Rapid progress has been made in understanding factors that affect the dynamic magnetization of MNPs in solutions due to Brownian and Neel relaxations [27,28]. However, to simplify the investigation on the effect of diamagnetic background to harmonics, we investigate the dynamic magnetization in a low-frequency region where Neel and Brownian relaxations can be ignored. Furthermore, the diamagnetic background, *i.e.*, the negative susceptibility of water, was assumed to be constant. We considered only the first three harmonics since the intensity of higher harmonics rapidly decrease. Fig. 3 shows the signal intensities of the first  $f_1$ , second  $f_2$  and third  $f_3$  harmonic components of 96  $\mu\text{g/ml}$  solution during exposure of AC magnetic field of 30 mT<sub>pp</sub> and 5 Hz and DC magnetic field from 0 to 80 mT. The closed markers are the measured harmonics using the high- $T_c$  SQUID magnetometer while the solid lines are calculated harmonics derived from the reconstructed moment distributions and the diamagnetic background of water. The calculated harmonics agreed well with the measured harmonics, reflecting the shape of magnetization curve of the solution. The  $f_1$  component is the first field-derivative of magnetization curve, *i.e.*, slope, where it decreased with increasing DC magnetic field. The  $f_2$  component is the derivative of the  $f_1$  component, having a maximum at  $B_{DC} = 10$  mT. The  $f_3$  component had 2 peaks at  $B_{DC} = 0$  mT and 13 mT. It is noteworthy that the detection SNR of MNPs can be improved by selecting a proper bias of the DC magnetic field where harmonics have maximum responses.

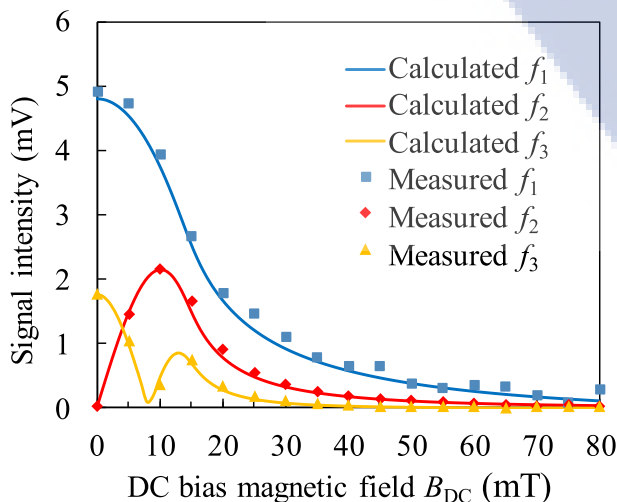


Fig. 3. Measured and calculated distributions of first  $f_1$ , second  $f_2$ , and third  $f_3$  harmonics over DC magnetic field.

From the reconstructed magnetic moment, the concentration of the iron-oxide nanoparticles is proportional to the sum of magnetic weight  $w_i$  in the distribution where the concentration proportions to the peak value if the shape distribution is similar. Closed circles in Fig. 4 show the peaks value of the reconstructed moment distributions with respect to the concentration. To investigate the deformation of magnetization curve in lower concentrations, we simulated the harmonics of the iron oxide nanoparticles solutions having peak values showed by the open circles in Fig. 4. The range of concentration was set at 10 ng/ml to 96  $\mu\text{g/ml}$ . Fig. 5 shows the intensity of the  $f_1$ ,  $f_2$  and  $f_3$  harmonic components with respect to concentration during excitation of the AC magnetic field of 30 mT<sub>pp</sub> and 5 Hz. The harmonics derived from the moment distributions are shown by the solid lines where measured harmonics are represented by the closed markers. The derived  $f_1$  components agreed well with the measured harmonic in the region is above 24  $\mu\text{g/ml}$ , which confirmed the reduction of diamagnetic contribution as observed from the first harmonic component results. The observed first harmonic component  $f_1 = \frac{d}{dt}M_{1,observ}$  by an induction coil can be expressed as

$$\frac{d}{dt}M_{1,observ} = \frac{dM_{MNP}}{dH} \cdot \frac{dH}{dt} + \frac{dM_{water}}{dH} \cdot \frac{dH}{dt} = (\chi_{MNP} + \chi_{water}) \cdot \frac{dH}{dt} \quad (4)$$

where  $M_{MNP}$ ,  $M_{water}$ ,  $\chi_{MNP}$  and  $\chi_{water}$  are magnetization and susceptibility of magnetic nanoparticles and water, respectively. Since  $\chi_{water}$  is small and having a constant negative value, it has a negligible effect on  $\chi_{MNP}$  at high concentration. When  $\chi_{MNP}$  is lower than  $\chi_{water}$ , the  $f_1$  component is dominated by  $\chi_{water}$ . The phase differences  $\Delta\theta_k = \theta_{f_k,diamagnetic} - \theta_{f_k}$  of harmonics between iron oxide nanoparticles with and without diamagnetic contribution,  $f_{k,diamagnetic}$  and  $f_k$ , respectively, are shown by the dashed lines. The phase difference of the observed  $f_1$  component turned to 180 degrees in the concentration region smaller than 3  $\mu\text{g/ml}$ , indicating that the observed signal intensity was dominated by negative susceptibility of water. Compared to the  $f_1$  component,  $f_2$  and  $f_3$  harmonics responded linearly with decreasing concentration. Their phase differences showed no difference, confirming that they are not affected by the diamagnetic background. The characteristic of harmonics with respect to concentration was consistent with the result reported in Ref. [29] where a highly sensitive system with excellent attenuation of the feedthrough interference of the excita-

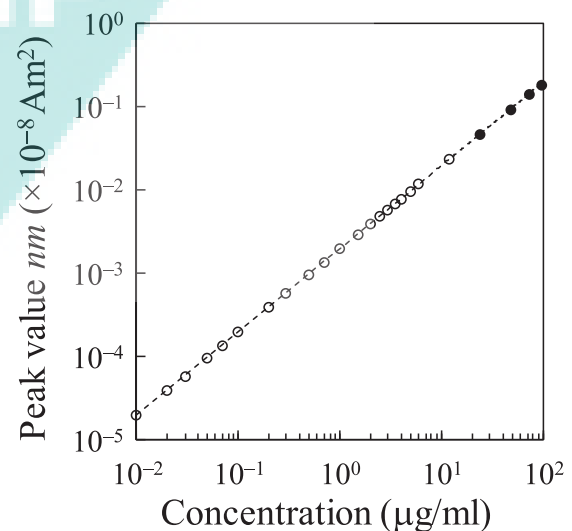


Fig. 4. Peak values of reconstructed distributions of magnetic moment (closed circles). Peak values for simulation in lower concentration are shown by the open circles.



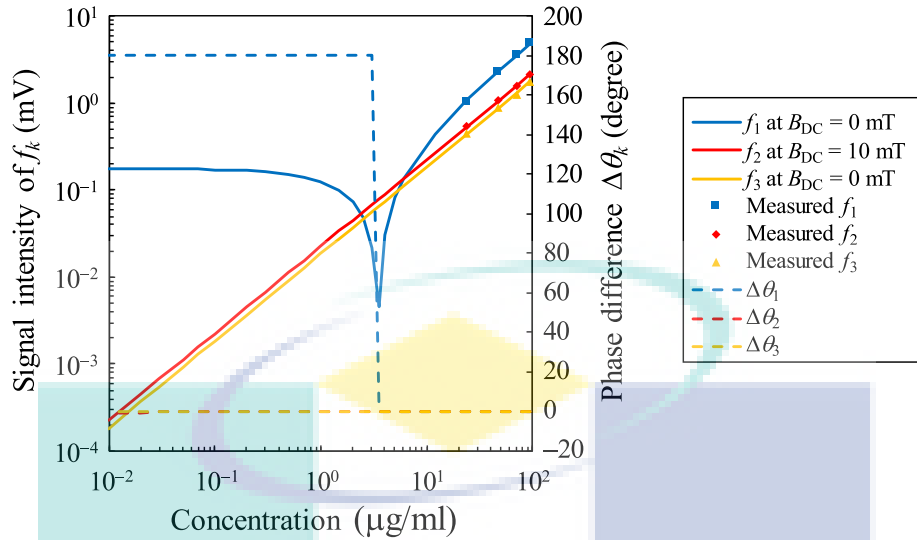


Fig. 5. Simulated (solid lines) and measured (closed markers) signal intensities of first  $f_1$ , second  $f_2$ , and third  $f_3$  harmonics with respect to the concentration. The phase difference between MNPs with and without the diamagnetic background is shown by the dashed lines.

tion magnetic field, can measure the diamagnetic background of water. In our developed system, there were still non-negligible interferences due the excitation magnetic field and the hysteresis of the core of the electromagnet.

It should be noted that harmonics of MNPs also depend on magnetic moment distribution besides AC and DC magnetic fields and concentration. The relation between diamagnetic effect and magnetic moment distribution must be clarified so that harmonics detection technique can be optimized to enable highly sensitive detection of MNPs in solutions.

### 6. Harmonics dependency on magnetic moment distribution of iron oxide nanoparticle solutions

For physical particles that follow Eq. (1), the shape of the magnetization curve depends on their magnetic weight  $w$  and their distribution ratio of Zeeman and thermal energies;  $m_i \mu_0 H_j / k_B T$ . Since harmonics reflect of the shape of magnetization curve, they are significantly related to the magnetic moment distribution. We investigate the relation between the diamagnetic effect and magnetic moment distribution by simulating harmonics under diamagnetic background. We assume a set of unimodal distributions, having a same total magnetic weight, i.e., concentration, but with different peak positions with respect to  $m$ . Although it is convenient to assume a shape of a log-normal distribution, we set the shape and spread of distributions to be identical to the reconstructed distribution in a logarithmic scale of  $m$ , as shown in Fig. 6. The peak positions relative to  $m$  were set from  $1.4 \times 10^{-21} \text{ Am}^2$  to  $8.9 \times 10^{-16} \text{ Am}^2$ . Then, the harmonics were simulated from magnetization curves reconstructed from the prepared distributions, respectively.

We first analyzed the intensity of harmonics without diamagnetic contribution during exposure of 30-mT<sub>pp</sub> AC magnetic field and DC magnetic field from 0 mT to 80 mT. The DC bias magnetic fields where the highest peaks of the  $f_1$ ,  $f_2$  and  $f_3$  components were observed, are shown in Fig. 7. The highest response of the  $f_1$  and  $f_3$  components can be obtained when  $B_{DC} = 0 \text{ mT}$ . Since the  $f_2$  component is related to the even-number function [30], the saturation point of magnetization is shifted to a higher DC magnetic field when the peak position of distribution is smaller than  $3.6 \times 10^{-19} \text{ Am}^2$ . Interestingly, the DC magnetic field of the  $f_2$  peak becomes almost constant in the case of the peak position of distri-

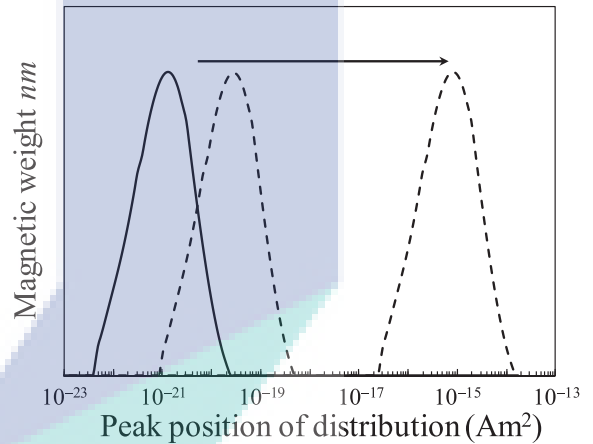


Fig. 6. Peak position of distributions for harmonic simulation.

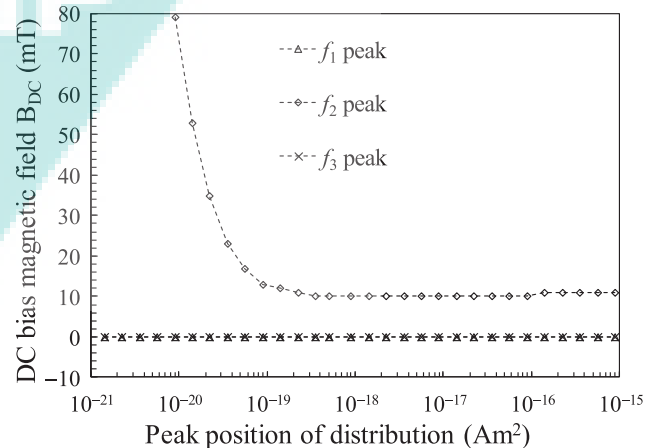


Fig. 7. Bias of the DC magnetic field corresponding to the highest peak of the first  $f_1$ , second  $f_2$ , and third  $f_3$  harmonics for different distributions of magnetic moment.

bution is greater than  $5 \times 10^{-19} \text{ Am}^2$ . This can be beneficial in applications using the  $f_2$  component where a constant  $B_{DC}$  can be used to analyzed MNPs' distribution across this region. It must

be noted that the DC magnetic field of  $f_2$  peak varies depending on the distribution shape of  $m$  and the AC magnetic field.

To examine the effect of diamagnetic contribution, we calculated the intensity ratio  $S_k = f_{k,diamagnetic}/f_k$  and phase difference  $\Delta\theta_k = \theta_{f_{k,diamagnetic}} - \theta_{f_k}$  of harmonics with and without diamagnetic background for different distributions of  $m$ . Here,  $f_{k,diamagnetic}$ ,  $f_k$ ,  $\theta_{f_{k,diamagnetic}}$  and  $\theta_{f_k}$  are the signal intensities and phases of  $k$ -th harmonics with and without diamagnetic background, respectively. Furthermore, as shown in Fig. 5, the effect due to concentration is also needed to be considered. Fig. 8 shows the signal ratio  $S_k$  and phase difference  $\Delta\theta_k$  of the first, second and third harmonics. To illustrate the effect of concentration, we calculated the harmonic signal ratio  $S_k$  at 3 conditions: high concentration of 96  $\mu\text{g/ml}$ , intermediate concentration of 3  $\mu\text{g/ml}$  and low concentration of 10  $\text{ng/ml}$ .

In the first harmonic, the signal ratio  $S_1$  of the 96- $\mu\text{g/ml}$  solution was approximately 1 when the peak position of distribution was in the region  $m \geq 10^{-19} \text{ Am}^2$ , showing that the diamagnetic contribution had the negligible effect on the signal intensity. In the region  $m < 10^{-19} \text{ Am}^2$ , the diamagnetic contribution decreased the signal intensity of  $f_{1,diamagnetic}$ , i.e., the magnetization from diamagnetic background reduced the magnetization of MNPs. The signal intensity of  $f_{1,diamagnetic}$  was dominated by the diamagnetic background in the region  $m < 10^{-20} \text{ Am}^2$  as shown by the change of the phase difference  $\Delta\theta$ .  $S_1$  showed a value greater than 1 due to a rapid decrease in the signal intensity of  $f_1$ , i.e., the magnetization of MNPs reduced significantly with decreasing of  $m$ . In the case of the 3- $\mu\text{g/ml}$  solution, transition point of  $m$  where  $\Delta\theta$  started to deviate from 0 degree was shifted to a higher region compared to the 96- $\mu\text{g/ml}$  solution, showing the effect of concentration to the observed magnetization. In the region  $m > 5 \times 10^{-19} \text{ Am}^2$ , although the magnetization of MNPs was dominant,  $S_1$  was smaller than 1 due to the nonnegligible effect of the diamagnetic background which had reduced the signal intensity of  $f_{1,diamagnetic}$ . In the case of the

10- $\text{ng/ml}$  solution, the signal intensity was entirely dominated by diamagnetic background as shown by  $\Delta\theta$ .

$S_2$  for the second harmonic was calculated for peak positions of  $m \geq 8.9 \times 10^{-21} \text{ Am}^2$  because the peak of  $f_2$  distribution over the DC magnetic field for  $m < 8.9 \times 10^{-21} \text{ Am}^2$  was located at  $B_{DC}$  higher than 80 mT. The values of  $S_2$  of the 96- $\mu\text{g/ml}$  and 3- $\mu\text{g/ml}$  solutions were 1 and constant over the calculated  $m$  region. The diamagnetic contribution had the negligible effect to the observed second harmonic as concluded from  $\Delta\theta_2$ . However, in the case of the 10- $\text{ng/ml}$  solution, the diamagnetic effect was observed in the region  $m < 10^{-19} \text{ Am}^2$ .

$S_3$  for the third harmonic showed a similar characteristic to  $S_1$  where the transition point of  $m$  was shifted to a higher region when the concentration was decreased. However, compared to  $S_1$  of the 10- $\text{ng/ml}$  solution,  $S_3$  was not affected by the diamagnetic contribution in the region of  $m \geq 8.9 \times 10^{-20} \text{ Am}^2$ . For other higher harmonics, a similar characteristic to  $S_3$  was obtained where the transition points were approximately located at  $m = 10^{-19} \text{ Am}^2$  (data not shown) for the 10- $\text{ng/ml}$  solution. The simulated results showed a good agreement with the first and third harmonics reported in Ref. [29], in which Resovist (Fujifilm RI Pharma Co., Ltd.) had the highest peak at  $m = 2.82 \times 10^{-18} \text{ Am}^2$  [31]. The third harmonic showed a good linearity with respect to concentration while the linearity of the first harmonic was deformed in the region lower than 6  $\mu\text{g/ml}$ . This proved that the first harmonic was susceptible to the diamagnetic background compared to the third harmonic in this region of  $m$ .

From this simulation result, we could conclude that the  $f_1$  harmonic was susceptible to the diamagnetic background and depended on the concentration. However, the  $f_2$  and  $f_3$  harmonics for the particles that have peaked at  $m$  more significant than  $10^{-19} \text{ Am}^2$  were 'transparent' to the diamagnetic contribution even at the concentration of 10  $\text{ng/ml}$ . This is equivalent to an iron oxide core size larger than 8.3 nm if the aforementioned intrinsic saturation magnetization and specific density were used. It should be

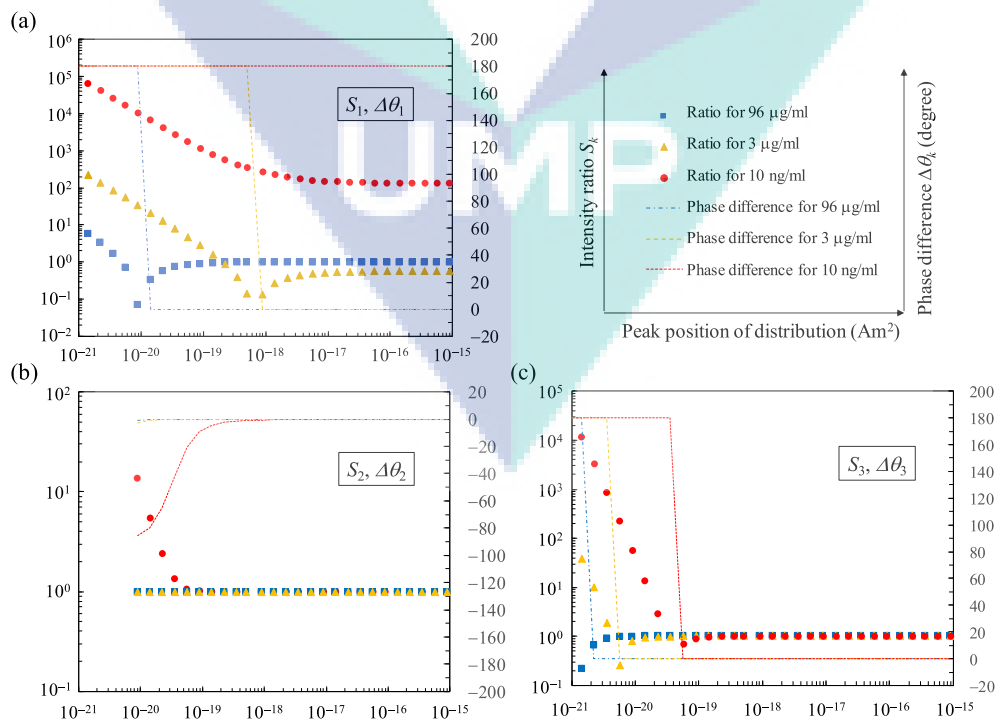


**Fig. 8.** Simulated signal ratio  $S_k$  of (a) first, (b) second, and (c) third harmonics, plotted as a function of the peak position of magnetic moment distribution for 96- $\mu\text{g/ml}$  solution (closed boxes), 3- $\mu\text{g/ml}$  solution (closed triangles) and 10- $\text{ng/ml}$  solution (closed circles). The dashed lines shown the phase difference between MNPs with and without the diamagnetic background.

noted that external noises were not accounted in this study in such as the feedthrough interference of the excitation magnetic field can limit the sensitivity of the  $f_1$  measurement by reducing the field resolution of a magnetic sensor. To reduce the feedthrough efficiently so that a sensitive measurement can be achieved, it will require a cancellation rate  $B_{\text{detect}}/B_{\text{excite}}$  to be smaller than  $10^{-5}$  [12]. Here,  $B_{\text{excite}}$  and  $B_{\text{detect}}$  are excitation magnetic field and magnetic field detected by the sensor. It was also reported that the  $f_1$  harmonic could be reconstructed from higher harmonic components [32,33]. On the other hand, the  $f_2$  and  $f_3$  harmonics can be used to realize a highly sensitive detection up to sub nanogram of MNPs such in MPI and magnetic immunoassay applications. Assuming a MNPs solution of  $100 \mu\text{l}$  [34], the detection of sub nanogram of MNPs in solution can be expected for particles that have peak distribution of magnetic moment  $m$  more significant than  $10^{-19} \text{ Am}^2$  by using a highly sensitive magnetic sensor such as SQUID. Other factors such as Neel and Brownian relaxations, and distribution shape of  $m$  should be considered so that an accurate response of MNPs under the diamagnetic background can be unravelled to achieve higher detection sensitivity.

## 7. Conclusion

Environmental factors surrounding MNPs such as the viscosity of carrier liquid influences the observed magnetization. In this study, we investigated the effect of the diamagnetic background to harmonics of multi-core iron oxide nanoparticles solutions. Deformation of magnetization curves of low concentration solutions was observed by the specially developed magnetometer. Using the reconstructed distribution of magnetic moment, the simulated harmonics agreed well with the measured harmonics, showing that the first component is susceptible and harmonics were not completely 'transparent' to the diamagnetic background. The effect of the diamagnetic background was found to be depended on the concentration of MNPs and the distribution of magnetic moment. The realization for sub-nanogram detection of MNPs under the diamagnetic background can be achieved by selecting particles that have peak distribution of magnetic moment  $m$  more significant than  $10^{-19} \text{ Am}^2$ .

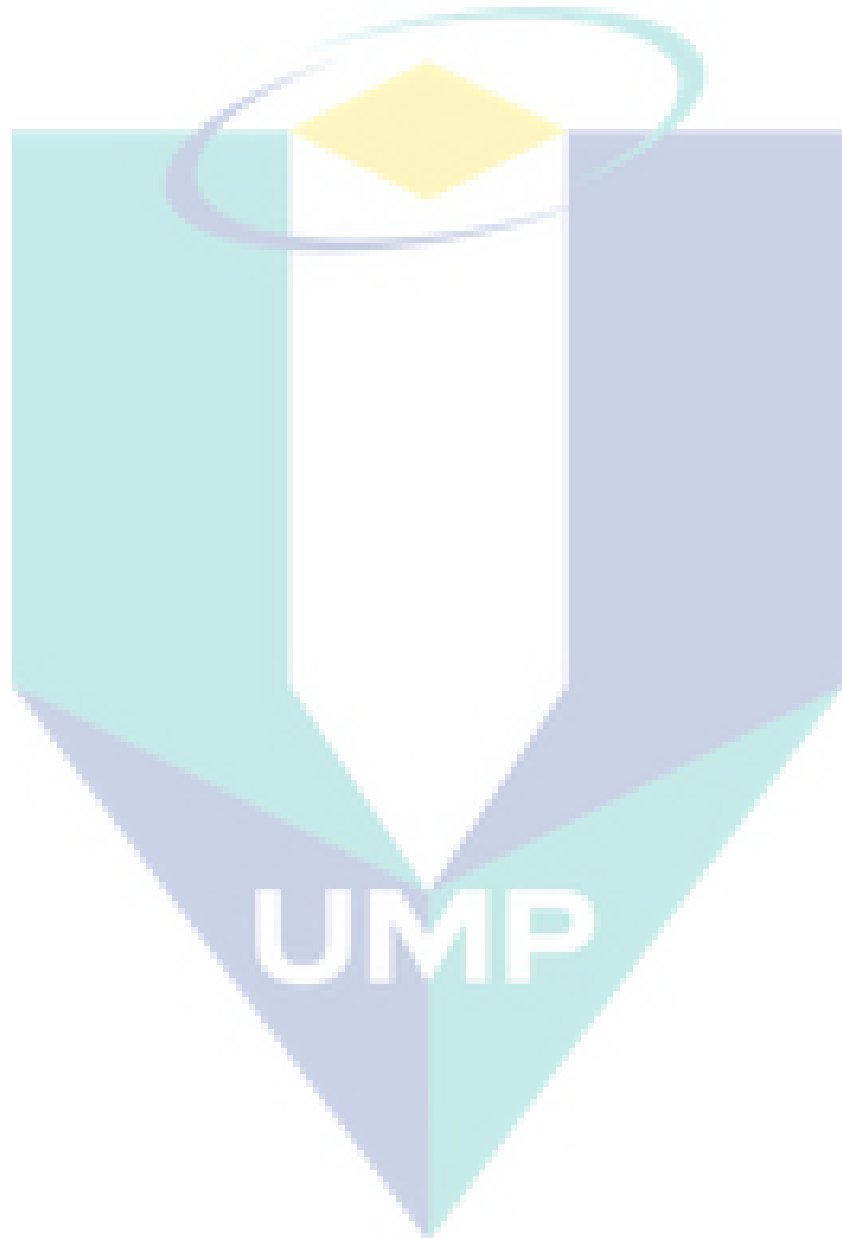
## Acknowledgements

This work was supported by Ministry of Higher Education of Malaysia under grant number of RDU 160115, Research Management Center of Universiti Malaysia Pahang under grant number of RDU 170377 and the "Strategic Promotion of Innovative R&D" of the Japan Science and Technology Agency (JST).

## References

- [1] L. Trahms, Colloidal Magnetic Fluids, Springer Berlin Heidelberg, Berlin, Heidelberg, 2009, pp. 327–358, <https://doi.org/10.1007/978-3-540-85387-9>.
- [2] C.-Y. Hong, C.C. Wu, Y.C. Chiu, S.Y. Yang, H.E. Horng, H.C. Yang, Magnetic susceptibility reduction method for magnetically labeled immunoassay, Appl. Phys. Lett. 88 (2006) 212512, <https://doi.org/10.1063/1.2206557>.
- [3] K. Enpuku, T. Tanaka, Y. Tamai, M. Matsuo, AC susceptibility of magnetic markers in suspension for liquid phase immunoassay, J. Magn. Mater. 321 (2009) 1621–1624, <https://doi.org/10.1016/j.jmmm.2009.02.099>.
- [4] S.-H. Chung, A. Hoffmann, K. Guslienko, S.D. Bader, C. Liu, B. Kay, L. Makowski, L. Chen, Biological sensing with magnetic nanoparticles using Brownian relaxation (invited), J. Appl. Phys. 97 (2005) 10R101, <https://doi.org/10.1063/1.1853694>.
- [5] K. Enpuku, T. Tanaka, T. Matsuda, F. Dang, N. Enomoto, J. Hojo, K. Yoshinaga, F. Ludwig, F. Ghaffari, E. Heim, M. Schilling, Properties of magnetic nanoparticles in the Brownian relaxation range for liquid phase immunoassays, J. Appl. Phys. 102 (2007) 54901, <https://doi.org/10.1063/1.2775882>.
- [6] D. Eberbeck, C. Bergemann, S. Hartwig, U. Steinhoff, L. Trahms, Binding kinetics of magnetic nanoparticles on latex beads and yeast cells studied by magnetorelaxometry, J. Magn. Mater. 289 (2005) 435–438, <https://doi.org/10.1016/j.jmmm.2004.11.122>.
- [7] N.L. Adolphi, D.L. Huber, J.E. Jaetao, H.C. Bryant, D.M. Lovato, D.L. Fegan, E.L. Venturini, T.C. Monson, T.E. Tessier, H.J. Hathaway, C. Bergemann, R.S. Larson, E.R. Flynn, Characterization of magnetite nanoparticles for SQUID-relaxometry and magnetic needle biopsy, J. Magn. Mater. 321 (2009) 1459–1464, <https://doi.org/10.1016/j.jmmm.2009.02.067>.
- [8] A. Tsukamoto, K. Saitoh, D. Suzuki, N. Sugita, Y. Seki, A. Kandori, K. Tsukada, Y. Sugiura, S. Hamaoka, H. Kuma, N. Hamasaki, K. Enpuku, Development of multisample biological immunoassay system using HTS SQUID and magnetic nanoparticles, IEEE Trans. Appl. Supercond. 15 (2005) 656–659, <https://doi.org/10.1109/TASC.2005.849988>.
- [9] K. Enpuku, K. Soejima, T. Nishimoto, H. Tokumitsu, H. Kuma, N. Hamasaki, K. Yoshinaga, Liquid phase immunoassay utilizing magnetic marker and high T [sub c] superconducting quantum interference device, J. Appl. Phys. 100 (2006) 54701, <https://doi.org/10.1063/1.2337384>.
- [10] F. Ludwig, E. Heim, S. Mauselein, D. Eberbeck, M. Schilling, Magnetorelaxometry of magnetic nanoparticles with fluxgate magnetometers for the analysis of biological targets, J. Magn. Mater. 293 (2005) 690–695, <https://doi.org/10.1016/j.jmmm.2005.02.045>.
- [11] A. Tsukamoto, K. Saitoh, N. Sugita, H. Kuma, Y. Sugiura, S. Hamaoka, N. Hamasaki, K. Enpuku, Improvement of sensitivity of multisample biological immunoassay system using HTS SQUID and magnetic nanoparticles, Phys. C Supercond. 445–448 (2006) 975–978, <https://doi.org/10.1016/j.physc.2006.06.019>.
- [12] M.M. Saari, Y. Ishihara, Y. Tsukamoto, T. Kusaka, K. Morita, K. Sakai, T. Kiwa, K. Tsukada, Optimization of an AC/DC high-Tc SQUID magnetometer detection unit for evaluation of magnetic nanoparticles in solution, IEEE Trans. Appl. Supercond. 25 (2015) 1–4, <https://doi.org/10.1109/TASC.2014.2363633>.
- [13] M. Graeser, T. Knopp, P. Szwargulski, T. Friedrich, A. von Gladiss, M. Kaul, K.M. Krishnan, H. Itrich, G. Adam, T.M. Buzug, Towards picogram detection of superparamagnetic iron-oxide particles using a gradiometric receive coil, Sci. Rep. 7 (2017) 6872, <https://doi.org/10.1038/s41598-017-06992-5>.
- [14] M. Graeser, T. Knopp, M. Grüttnner, T.F. Sattel, T.M. Buzug, Analog receive signal processing for magnetic particle imaging, Med. Phys. 40 (2013) 42303, <https://doi.org/10.1118/1.4794482>.
- [15] A.D. Hibbs, R.E. Sager, S. Kumar, J.E. McArthur, A.L. Singaas, K.G. Jensen, M.A. Steindorf, T.A. Aukerman, H.M. Schneider, A SQUID-based AC susceptometer, Rev. Sci. Instrum. 65 (1994) 2644, <https://doi.org/10.1063/1.1144664>.
- [16] K. Tsukada, T. Kiwa, H. Tahara, E. Miyake, H. Yamada, A. Tsukamoto, A. Kandori, Highly sensitive measurement of moisture content using HTS-SQUID, IEEE Trans. Appl. Supercond. 19 (2009) 878–881, <https://doi.org/10.1109/TASC.2009.2019659>.
- [17] K. Enpuku, S. Nabekura, Y. Tsuji, S. Okada, M. Matsuo, A. Tsukamoto, T. Mizoguchi, A. Kandori, Detection of magnetic nanoparticles utilizing cooled normal pickup coil and high Tc SQUID, Phys. C Supercond. 469 (2009) 1634–1637, <https://doi.org/10.1016/j.physc.2009.05.072>.
- [18] M.M. Saari, Y. Tsukamoto, T. Kusaka, Y. Ishihara, K. Sakai, T. Kiwa, K. Tsukada, Effect of diamagnetic contribution of water on harmonics distribution in a dilute solution of iron oxide nanoparticles measured using high-Tc SQUID magnetometer, J. Magn. Mater. 394 (2015) 260–265, <https://doi.org/10.1016/j.jmmm.2015.06.090>.
- [19] M.M. Saari, K. Sakai, T. Kiwa, K. Tsukada, Optimization of the detection technique for a vibrating-sample magnetometer using high-Tc SQUID, IEEE Trans. Appl. Supercond. 23 (2013) 1600204, <https://doi.org/10.1109/TASC.2012.2227919>.
- [20] M.M. Saari, K. Sakai, T. Kiwa, A. Tsukamoto, S. Adachi, K. Tanabe, A. Kandori, K. Tsukada, Development of a compact moving-sample magnetometer using High-Tc superconducting quantum interference device, Jpn. J. Appl. Phys. 51 (2012) 46601, <https://doi.org/10.1143/JJAP.51.046601>.
- [21] S. Behrens, Colloidal Magnetic Fluids, Springer Berlin Heidelberg, Berlin, Heidelberg, 2009, pp. 1–82, <https://doi.org/10.1007/978-3-540-85387-9>.
- [22] J.B. Weaver, A.M. Rauwerdink, C.R. Sullivan, I. Baker, Frequency distribution of the nanoparticle magnetization in the presence of a static as well as a harmonic magnetic field, Med. Phys. 35 (2008) 1988, <https://doi.org/10.1118/1.2903449>.
- [23] Y. Higuchi, S. Uchida, A.K. Bhuiya, T. Yoshida, K. Enpuku, Characterization of magnetic markers for liquid-phase detection of biological targets, IEEE Trans. Magn. 49 (2013) 3456–3459, <https://doi.org/10.1109/TMAG.2013.2242852>.
- [24] J. van Rijssel, B.W.M. Kuipers, B.H. Erné, Non-regularized inversion method from light scattering applied to ferrofluid magnetization curves for magnetic size distribution analysis, J. Magn. Mater. 353 (2014) 110–115, <https://doi.org/10.1016/j.jmmm.2013.10.025>.
- [25] M.D. Woodhams, M.D. Hendy, Reconstructing phylogeny by quadratically approximated maximum likelihood, Bioinformatics 20 (Suppl 1) (2004) i348–54, <https://doi.org/10.1093/bioinformatics/bth926>.
- [26] K. Enpuku, T. Morishige, T. Mihaya, T. Miyazai, M. Matsuo, S. Haku, T. Yoshida, Magnetic nanoparticle imaging using cooled pickup coil and harmonic signal detection, Jpn. J. Appl. Phys. 52 (2013) 87001, <https://doi.org/10.7567/JJAP.52.087001>.
- [27] S.A. Shah, D.B. Reeves, R.M. Ferguson, J.B. Weaver, K.M. Krishnan, Mixed Brownian alignment and Neel rotations in superparamagnetic iron oxide nanoparticle suspensions driven by an ac field, Phys. Rev. B - Condens. Matter Mater. Phys. 92 (2015) 1–11, <https://doi.org/10.1103/PhysRevB.92.094438>.
- [28] D.B. Reeves, J.B. Weaver, Magnetic nanoparticle sensing: decoupling the magnetization from the excitation field, J. Phys. D Appl. Phys. 47 (2014) 45002, <https://doi.org/10.1088/0022-3727/47/4/045002>.

- [29] T. Mizoguchi, A. Kandori, R. Kawabata, K. Ogata, T. Hato, A. Tsukamoto, S. Adachi, K. Tanabe, S. Tanaka, K. Tsukada, K. Enpuku, Highly sensitive third harmonic detection method of magnetic nanoparticles using AC susceptibility measurement system for liquid phase assay 1 1 IEEE Trans. Appl. Supercond. 8223 (2016), <https://doi.org/10.1109/TASC.2016.2581703>.
- [30] K. Tsukada, T. Yasugi, Y. Majima, K. Sakai, T. Kiwa, Absolute-magnetic-field measurement using nanogranular in-gap magnetic sensor with second-harmonic and liquid-nitrogen-temperature operation, AIP Adv. 7 (2017) 56670, <https://doi.org/10.1063/1.4978217>.
- [31] K. Enpuku, T. Sasayama, T. Yoshida, Estimation of magnetic moment and anisotropy energy of magnetic markers for biosensing application, J. Appl. Phys. 119 (2016) 184902, <https://doi.org/10.1063/1.4948951>.
- [32] Z.W. Tay, P.W. Goodwill, D.W. Hensley, L.A. Taylor, B. Zheng, S.M. Conolly, A. High-Throughput, Arbitrary-waveform, MPI spectrometer and relaxometer for comprehensive magnetic particle optimization and characterization, Sci. Rep. 6 (2016) 34180, <https://doi.org/10.1038/srep34180>.
- [33] K. Lu, P.W. Goodwill, E.U. Saritas, B. Zheng, S.M. Conolly, Linearity and shift invariance for quantitative magnetic particle imaging, IEEE Trans. Med. Imaging. 32 (2013) 1565–1575, <https://doi.org/10.1109/TMI.2013.2257177>.
- [34] B. Zheng, P.W. Goodwill, N. Dixit, D. Xiao, W. Zhang, B. Gunel, K. Lu, G.C. Scott, S.M. Conolly, Optimal broadband noise matching to inductive sensors: application to magnetic particle imaging, IEEE Trans. Biomed. Circuits Syst. 11 (2017) 1041–1052, <https://doi.org/10.1109/TBCAS.2017.2712566>.





# Development of A Resonant Excitation Coil of AC Magnetometer for Evaluation of Magnetic Fluid

Mohd Mawardi Saari<sup>1</sup>, Nazatul Sharreena Suhaimi<sup>1</sup>, Saifudin Razali<sup>1</sup>, Nurul Akmal Che Lah<sup>2</sup>,

Kenji Sakai<sup>3</sup>, Toshihiko Kiwa<sup>3</sup> and Keiji Tsukada<sup>3</sup>

<sup>1</sup>Faculty of Electrical & Electronic Engineering, Universiti Malaysia Pahang, 26600 Pekan, Pahang, Malaysia

<sup>2</sup>Innovative Manufacturing, Mechatronics and Sports Lab (iMAMS), Faculty of Manufacturing Engineering, Universiti Malaysia Pahang, 26600 Pekan, Pahang, Malaysia

<sup>3</sup>Graduate School of Natural Science and Technology, Okayama University, 3-1-1 Tsushima Naka, 700-8350 Okayama, Japan

mmawardi@ump.edu.my

**Abstract**—A high-homogeneity excitation coil with a resonant circuit for AC magnetometer is developed. A solenoid coil is designed to produce a high-homogeneity and strong excitation field using a resonant frequency method. The solenoid coil is fabricated with a Litz wire to suppress the increase of AC resistance due to the skin and proximity effects in the high-frequency region. The Litz wire is composed of 60 strands of copper wires with 0.1-mm diameter. The resonant frequency method is applied to cancel the reactance component by connecting the excitation coil with a capacitor in a series configuration. To enable excitation of the magnetic field at multiple frequencies, a resonant circuit consists of multiple values of resonant capacitors is constructed. The fabricated excitation coil showed a high homogeneity of the magnetic field and was able to maintain a constant resonant current up to 32.5 kHz.

**Index Terms**—Coil; Impedance; Magnetometer; Resonant Circuit.

## I. INTRODUCTION

Magnetic nanoparticles (MNPs) are commonly applied in biomedical such as *in vivo*-imaging, magnetic hyperthermia and magnetic immunoassay [1], [2]. Their characteristics of magnetic properties are being utilized in different applications of magnetic nanoparticles where these applications require distinct features of MNPs. Due to this reason, the characterization of the magnetic nanoparticles is important so that they can be optimized for the intended applications. The magnetic properties of the magnetic nanoparticles can be characterized using magnetic susceptibility [3], [4], relaxation [5]–[7] and remanence measurements [8], [9]. AC susceptibility method is commonly utilized because it can provide information on size distribution, harmonics, magnetic anisotropy, relaxation etc. with a fast response to the measurement [10]. However, there are some technical issues need to be solved in this method such as sensitivity reduction due to the interference of excitation magnetic field, inhomogeneity of excitation magnetic field, the limited magnitude of excitation magnetic field at high frequencies and so on [11], [12].

In order to achieve high homogeneity and sufficient magnitude of excitation magnetic field in high-frequency regions, an excitation coil with a resonant circuit is developed in this work. The excitation coil is constructed from two solenoid coils which are connected in series and separated by 4 mm of distance. The excitation coil is designed so that a

strong and uniform magnetic field can be generated at its axis while maintaining a compact size. Furthermore, the distribution of magnetic field is simulated during optimization of the radius and length of the excitation coil.

The excitation magnetic field is generated based on Biot-Savart's law where a current is supplied to the excitation coil by a power supply. For evaluation of AC susceptibility value of MNPs, an AC excitation magnetic field is applied to MNPs, and their AC response is measured. However, in the case of operating the excitation coil at a high frequency, the coil's impedance will increase significantly due to its inductance as well as the AC resistance. The utilization of Litz wire in the construction of the excitation coil can reduce the AC resistance [13], [14], however, reduction of coil's inductance will decrease the strength of the excitation magnetic field as it relates to the number of turns. Although using a superior power supply can overcome this issue, it is an expensive solution. On the other hand, the reactance of the excitation coil can be simply reduced by using capacitors to form a resonant RCL circuit with the expense of a narrow-band excitation frequency [15], [16]. To achieve a broad resonant frequency of up to 82.32 kHz, a resonant circuit consists of multiple resonant capacitors is developed in this work.

## II. METHODOLOGY

### A. System Configuration

Figure 1 shows a schematic diagram of the developed AC magnetometer system. The developed system consists of inductive excitation and detection coils. The excitation coil is connected to a current amplifier (TS 250, Accel Instruments). A lock-in amplifier (LI 5640, NF Corporation) is used for the signal detection of the inductive detection coil. Based on the reference signal from the lock-in amplifier, it will act as a function generator and provide a sine wave signal to the current amplifier. The current amplifier converts the signal to a high current signal and supplies it to the excitation coil. The excitation field will magnetize a sample that is placed inside the excitation coil. Subsequently, the magnetization of the sample produces a magnetic field where the detection coil will detect this magnetic field. The lock-in detected signal of the detection coil is sent to a computer for signal analysis.

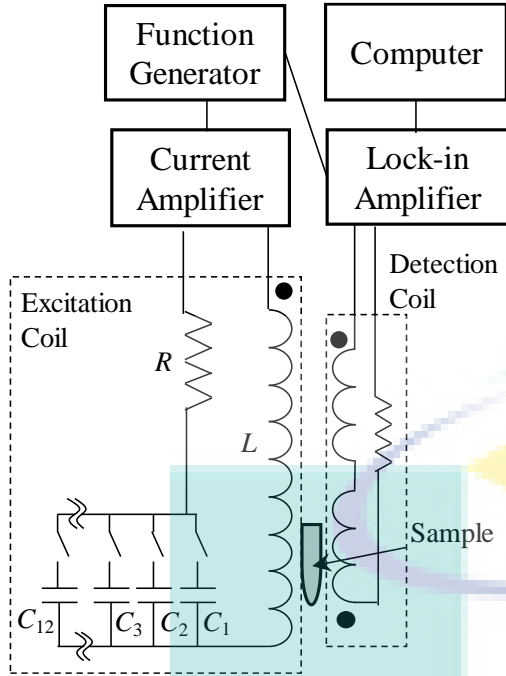


Figure 1: Schematic diagram of the developed system.

### B. Development of The Excitation Coil

The design of the excitation coil is optimized by analyzing the internal distribution of the magnetic field. In this work, the Biot-Savart's equation based on a multi-layer surface current model was used in the simulation of the magnetic field distribution. The magnetic field  $\mathbf{B}(\mathbf{r}')$  at observation point  $\mathbf{r}'$  resulted from multi-layer surface current can be expressed as:

$$\mathbf{B}(\mathbf{r}') = \frac{\mu_0}{4\pi} \sum_{n=1}^N \sum_{i=1}^S \frac{\mathbf{J}_n s_{i,n} \times (\mathbf{r}' - \mathbf{r}_n)}{|\mathbf{r}' - \mathbf{r}_n|^3}, \quad (1)$$

where  $\mu_0$  is the vacuum magnetic permeability,  $\mathbf{J}_n$  is the surface current density vector at  $n$  layer,  $s_{i,n}$  is the unit area of the surface  $S$  and  $\mathbf{r}_n$  is the position of the surface current. From Equation (1), it is evident that reducing the distance between current element  $\mathbf{r}_n$  and point observation  $\mathbf{r}'$  can result to increase in the magnetic field. This is equal to the reduction in the radius of the excitation coil. However, if the radius is too small, this will reduce the uniform area of the magnetic field; therefore, an optimum radius must be selected where the size of the sample and detection coil are also being considered. It should be noted that the intensity of the magnetic field can be increased by increasing the number of layer  $n$ . However, this will result to increase in resistance and inductance. Furthermore, impedance increase due to proximity effect and core losses can be expected when  $n$  is too high. Therefore, a moderate value of a number of  $n$  must be considered. From the numerical simulations of the magnetic field distribution, the excitation coil was fabricated of two identical solenoid coils which were connected in series. A 4-mm gap was placed between the solenoid coils for cooling purpose. The number of turn for one solenoid coil was 150 turns and was fabricated with the Litz wire. The Litz wire was composed of 60 strands of copper wires with 0.1-mm diameter. The radius and length of one solenoid coil were 15 mm and 26 mm. The resistance and inductance of the excitation coil were measured to be 1.3516  $\Omega$  and 1.5176 mH at 1 V and 1 kHz.

### C. Resonant Circuit

When the excitation coil is connected to the power supply, the electrical circuit is equal to an  $RL$  circuit where self-capacitance of the excitation coil is small and can be ignored [17]. The impedance of the  $RL$  circuit can be expressed as:

$$Z(\omega) = R_{DC} + R_{AC}(\omega) + j\omega L, \quad (2)$$

where  $\omega = 2\pi f$  is angular frequency,  $R_{DC}$  is the DC resistance,  $R_{AC}$  is AC resistance, and  $L$  is the inductance of the excitation coil. Here,  $R_{DC}$  is constant while  $R_{AC}$  is a function of  $\omega$ . From Equation (2), the impedance increases with respect to the frequency where a  $10^3$ -fold increase in frequency will result in a  $10^3$ -fold increase in the impedance. This means that to maintain a constant flow of current, the supply voltage must be increased by  $10^3$  times. When a capacitor  $C$  is connected to the excitation coil, the equivalent electrical circuit can be expressed as:

$$Z(\omega) = R_{DC} + R_{AC}(\omega) + j(\omega L - 1/\omega C). \quad (3)$$

When the circuit turns into a resonant mode where the imaginary part of the impedance becomes zero, the resonant frequency  $f_R$  can be expressed as:

$$f_R = \frac{1}{2\pi\sqrt{LC}}. \quad (4)$$

In this mode, the flowing current is limited by the resistance of the circuit only and a clean sine wave current can be obtained as the circuit acts as a band-pass filter. Moreover, the resonant frequency can be selected by using different values of  $C$ .

Based on these designs, a resonant circuit composed of multiple values of polypropylene film capacitors was designed and fabricated. The range of the resonant frequency was set from 581 Hz to 82.32 kHz. To achieve the desired resonant frequencies, capacitor networks consist of combinations of parallel and/or series connections were fabricated. The calculated and measured resonant frequencies were compared as well to the impedance.

## III. EXPERIMENTAL RESULT

The normalized distribution of the simulated excitation magnetic field  $B_y$  and  $B_z$  is shown in Figure 2. The axis of the excitation coil was set to  $z = 1.7$  cm. The distributions were calculated at 2-mm interval in the region of  $0 \text{ mm} \leq y \leq 90 \text{ mm}$  and  $-15 \text{ mm} \leq z \leq 15 \text{ mm}$ . The contours were divided by 5%-interval. From the distributions of  $B_y$  and  $B_z$ , a homogeneity of 95% could be obtained when the sample was placed at a  $y$ -position of 35 mm to 55 mm. Figure 3 shows the calculated and measured distribution of excitation magnetic field  $B_y$  along the axis of the excitation coil. The distribution of magnetic field along the axis of the excitation coil was measured using a Teslometer. The strength of the excitation magnetic field per unit current at the centre was measured to be 5.2 mT/A. The simulation agreed well with the measured distribution. From the result, the magnetic field showed a high uniformity in the region of 30 mm to 60 mm and sufficient for a cylindrical sample of 10-mm diameter and



10-mm length. In this region, the inhomogeneity was calculated to be 6%.

Figure 4 shows the calculated impedance of the excitation coil when it is connected to different values of capacitors. Here, the resistance was assumed as constant over frequency. As a comparison, the impedance of the *RL* circuit is also shown. The impedance of the *RL* circuit increases rapidly

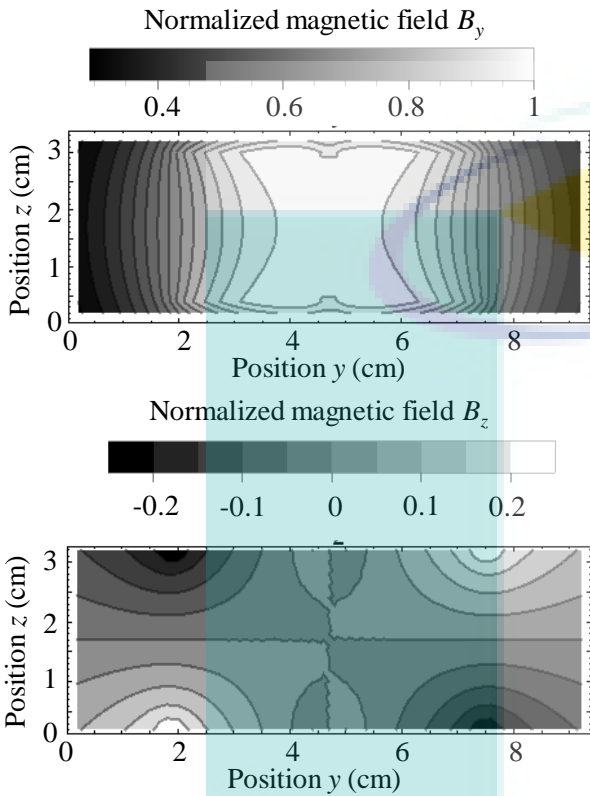


Figure 2: The distribution excitation magnetic field  $B_y$  and  $B_z$  inside the excitation coil.

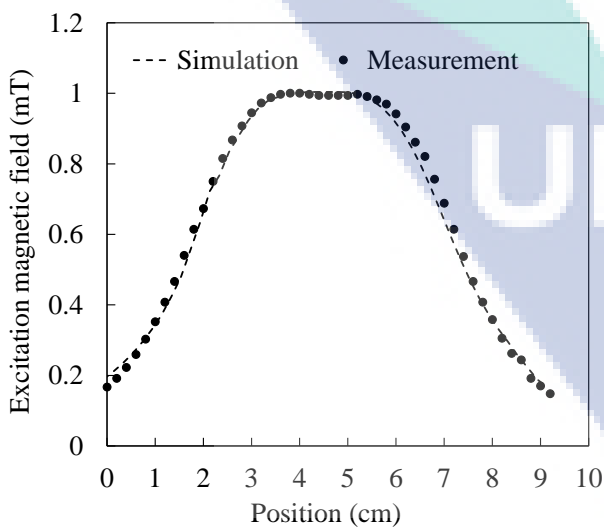


Figure 3: The distribution line of excitation magnetic field with respect to the position along the axis of the excitation coil.

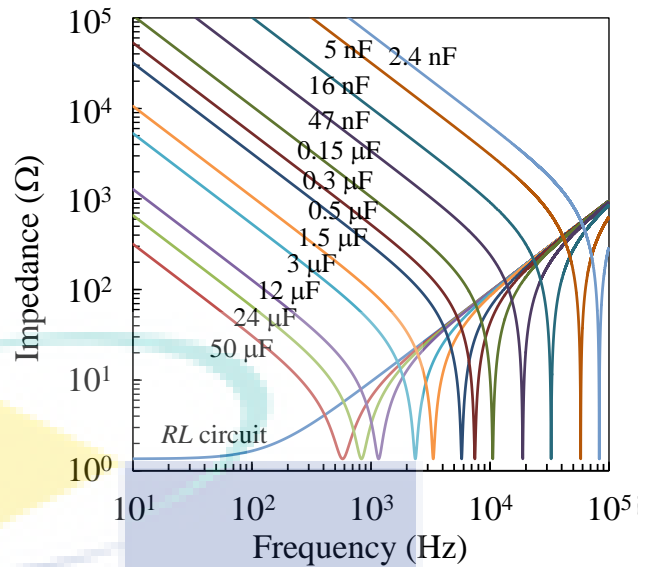


Figure 4: The impedance of the series *RCL* circuit.

when the frequency is larger than 100 Hz. When the *RL* circuit is connected to capacitors, the impedance due to the capacitance is dominance in the region below the resonant frequency. The impedance reaches a minimum value when the circuit is at resonance. As the frequency becomes larger than the resonant frequency, the impedance increases due to inductance. As shown in Fig. 4, the impedance demonstrated a characteristic of a narrow-band filter where a maximum current can be obtained at the resonant frequency.

The calculated and measured resonant frequencies are shown in Figure 5. The resonant frequency was determined by measuring the flowing current to the excitation coil while sweeping the frequency of power supply in constant voltage mode. The resonant frequency was determined when the flowing current reached a maximum value. From Figure 5, it can be shown that the measured resonant frequency agreed to the calculated frequency. The measured resonant frequency was slightly larger compared to the calculated resonant frequency. This could result in slight differences of capacitance in the fabricated capacitor networks.

The measured current of the *RCL* circuit in resonance mode at different capacitor values is shown in Figure 6. The current was measured when the power supply was operated in the constant voltage mode. The magnitude of the current could be maintained without significant decrease until 32.5 kHz when the excitation coil was operated in the resonance mode. In the region higher than 10 kHz, a rapid decrease of current's magnitude was observed, and this might be caused by the significant increase in resistance and core losses. As a comparison, the flowing current of the *RL* circuit was also shown in Figure 6. The flowing current decreased inverse-proportionally with the frequency. The current in the *RL* circuit was reduced by 100 times at 32.5 kHz compared to the *RCL* circuit in the resonance mode. From this, it can be shown that the benefit of the resonant circuit to drive the excitation coil at high frequency.

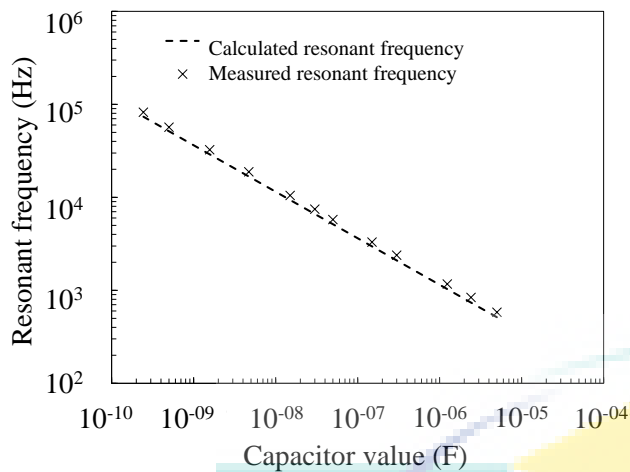


Figure 5: Resonant frequency of series  $RCL$  circuit with respect to capacitor values.

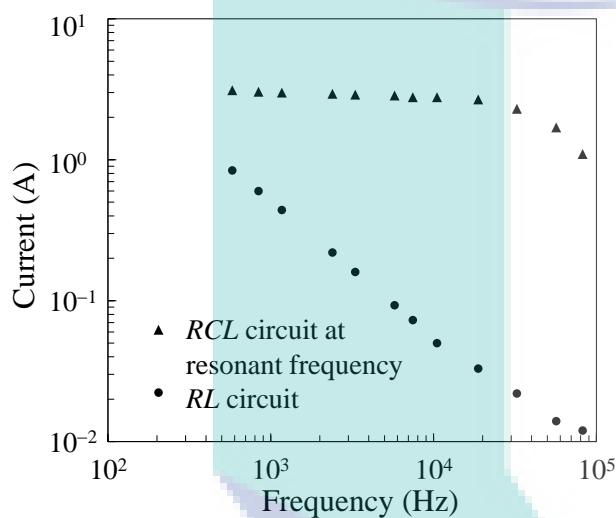


Figure 6: The current at the excitation coil when the power supply was operated in the constant voltage mode.

#### IV. CONCLUSION

A high-homogeneity of excitation coil with a resonant circuit for AC magnetometer has been developed for evaluation of the magnetic response of the MNPs. The excitation coil was fabricated from a Litz wire to reduce AC resistance at high frequency. The fabricated excitation coil showed a non-uniformity of 6% within a 30-mm region, which was sufficient for the size of a 1-mL sample. A resonant circuit consists of multiple capacitor values was designed and fabricated. The magnitude of the flowing current from the power supply was successfully maintained until 32.5 kHz when the excitation coil was operated in the resonance mode. Improvement of the current at a higher frequency can be expected by taking into consideration of coil's AC resistance and core losses during the design of the excitation coil. It is expected that the developed excitation coil system can be utilized for harmonics and magnetic relaxation measurement of MNPs.

#### ACKNOWLEDGMENT

This work was supported by Ministry of Higher Education of Malaysia under grant number of RDU 160115 and Research Management Center of Universiti Malaysia Pahang under grant number of RDU 170377.

#### REFERENCES

- [1] M. M. Saari, K. Sakai, T. Kiwa, T. Sasayama, T. Yoshida, and K. Tsukada, "Characterization of the magnetic moment distribution in low-concentration solutions of iron oxide nanoparticles by a high-Tc superconducting quantum interference device magnetometer," *J. Appl. Phys.*, vol. 117, no. 17, p. 17B321, May 2015.
- [2] Y. Higuchi, S. Uchida, A. K. Bhuiya, T. Yoshida, and K. Enpuku, "Characterization of Magnetic Markers for Liquid-Phase Detection of Biological Targets," *IEEE Trans. Magn.*, vol. 49, no. 7, pp. 3456–3459, Jul. 2013.
- [3] K. Enpuku, T. Tanaka, Y. Tamai, and M. Matsuo, "AC susceptibility of magnetic markers in suspension for liquid phase immunoassay," *J. Magn. Magn. Mater.*, vol. 321, no. 10, pp. 1621–1624, May 2009.
- [4] F. Ahrentorp *et al.*, "Sensitive high frequency AC susceptometry in magnetic nanoparticle applications," *AIP Conf. Proc.*, vol. 1311, no. 2010, pp. 213–223, 2010.
- [5] A. Guillaume, J. M. Scholtyssek, A. Lak, A. Kassner, F. Ludwig, and M. Schilling, "Magnetorelaxometry of few Fe<sub>3</sub>O<sub>4</sub> nanoparticles at 77K employing a self-compensated SQUID magnetometer," *J. Magn. Magn. Mater.*, vol. 408, pp. 46–50, 2016.
- [6] F. Ludwig, E. Heim, S. Mäuselein, D. Eberbeck, and M. Schilling, "Magnetorelaxometry of magnetic nanoparticles with fluxgate magnetometers for the analysis of biological targets," *J. Magn. Magn. Mater.*, vol. 293, no. 1, pp. 690–695, May 2005.
- [7] H. C. Bryant *et al.*, "Magnetic Properties of Nanoparticles Useful for SQUID Relaxometry in Biomedical Applications," *J. Magn. Magn. Mater.*, vol. 323, no. 6, pp. 767–774, Mar. 2011.
- [8] A. Tsukamoto *et al.*, "Improvement of sensitivity of multisample biological immunoassay system using HTS SQUID and magnetic nanoparticles," *Phys. C Supercond.*, vol. 445–448, pp. 975–978, Oct. 2006.
- [9] A. Tsukamoto *et al.*, "Reduction of the magnetic signal from unbound magnetic markers for magnetic immunoassay without bound/free separation," *Phys. C Supercond.*, vol. 463–465, pp. 1024–1028, Oct. 2007.
- [10] A. Prieto Astalan *et al.*, "Magnetic response of thermally blocked magnetic nanoparticles in a pulsed magnetic field," *J. Magn. Magn. Mater.*, vol. 311, no. 1 SPEC. ISS., pp. 166–170, 2007.
- [11] P. Baranov, V. Baranova, S. Uchaikin, and Y. Pisarenko, "Creating a uniform magnetic field using axial coils system for calibration of magnetometers," pp. 0–4, 2010.
- [12] M. M. Saari *et al.*, "Optimization of an AC/DC High-Tc SQUID Magnetometer Detection Unit for Evaluation of Magnetic Nanoparticles in Solution," *IEEE Trans. Appl. Supercond.*, vol. 25, no. 3, pp. 1–4, Jun. 2015.
- [13] K. Enpuku *et al.*, "Performance of Pickup Coil Made of Litz Wire and Coupled to HTS SQUID," *Phys. Procedia*, vol. 36, pp. 400–404, Jan. 2012.
- [14] V. Connord, B. Mehdaoui, R. P. Tan, J. Carrey, and M. Respaud, "An air-cooled Litz wire coil for measuring the high frequency hysteresis loops of magnetic samples - A useful setup for magnetic hyperthermia applications," *Rev. Sci. Instrum.*, vol. 85, no. 9, 2014.
- [15] P. W. Goodwill, G. C. Scott, P. P. Stang, and S. M. Conolly, "Narrowband magnetic particle imaging," *IEEE Trans. Med. Imaging*, vol. 28, no. 8, pp. 1231–7, Aug. 2009.
- [16] K. Enpuku, S. Hirakawa, R. Momotomi, M. Matsuo, and T. Yoshida, "Performance of HTS SQUID using resonant coupling of cooled Cu pickup coil," *Phys. C Supercond.*, vol. 471, no. 21–22, pp. 1234–1237, Nov. 2011.
- [17] T. Q. Yang and K. Enpuku, "SQUID magnetometer utilizing normal pickup coil and resonant-type coupling circuit," *Phys. C Supercond.*, vol. 392–396, pp. 1396–1400, Oct. 2003.

# A Sensitive AC Magnetometer using A Resonant Excitation Coil for Magnetic Fluid Characterization in Nonlinear Magnetization Region

Mohd Mawardi Saari<sup>1</sup>, Nazatul Sharreena Suhaimi<sup>1</sup>, Nurul Akmal Che Lah<sup>2</sup>, Kenji Sakai<sup>3</sup>, Toshihiko Kiwa<sup>3</sup>,  
*Member, IEEE*, and Keiji Tsukada<sup>3</sup>, *Member, IEEE*

<sup>1</sup>Faculty of Electrical & Electronic Engineering, Universiti Malaysia Pahang, 26600 Pekan, Pahang, Malaysia

<sup>2</sup>Innovative, Manufacturing, Mechatronics and Sports Lab (iMAMS Lab), Faculty of Manufacturing Engineering, Universiti Malaysia Pahang, 26600 Pekan, Pahang, Malaysia

<sup>3</sup>Graduate School of Natural Science and Technology, Okayama University, 700-8530 Okayama, Japan

In order to tailor the magnetic nanoparticles (MNPs) properties for intended applications, it is crucial to unravelling their fundamental dynamics with respect to excitation magnetic field. In this work, we report on the development of a sensitive AC magnetometer using a resonant excitation coil for this purpose. The excitation coil fabricated from a Litz wire is connected to a capacitor network to reduce the impedance of the circuit efficiently. The high efficiency showed by the excitation coil enables investigation of MNP's dynamics in the nonlinear magnetization region. We demonstrate the sensitivity of the developed system by measuring the harmonics distribution of multi-core iron oxide nanoparticles suspended in solutions with the iron concentration down to 300 ng/ml. We experimentally show that the first harmonic component is not entirely 'transparent' to the diamagnetic background of the carrier liquid compared to the higher harmonics. We also demonstrate the complex magnetization measurement of the iron oxide nanoparticles in solution and immobilized states from 3 Hz to 18 kHz. A highly sensitive exploration of MNPs' dynamics can be expected using the developed AC magnetometer.

**Index Terms**—Magnetometer, AC susceptibility, harmonics, magnetic nanoparticles.

## I. INTRODUCTION

Properties characterization of magnetic nanoparticles (MNPs) is essential for their standardization and optimization to ensure continuous improvement and performance for specific applications [1]–[3]. One of the magnetic characterization methods of MNPs is the AC susceptibility measurement where this method can provide fast and abundant information on their dynamics such as harmonics, size distribution, magnetic anisotropy and hysteresis loop [1], [2], [4]–[6]. Moreover, the AC susceptibility measurement can also be used to monitor the interaction between MNPs and their environment such as binding reaction in magnetic bio-detection application [7], [8] and viscosity of suspension liquid [6], [9]. To serve these purposes, various developments of AC magnetometers have been reported. In fact, depending on the applications of MNPs, the intensity and the frequency of the excitation magnetic field, as well as the concentration of MNPs, are different. Therefore, a sensitive AC magnetometer that can cover wide ranges of field intensity and excitation frequency is much desired to serve as a characterization tool.

One of the technical issues in constructing an AC magnetometer is the rapid increase of the impedance of excitation coil at the high-frequency region besides the direct feedthrough of the excitation field at the detection unit [10], [11]. The increase of the impedance will limit the field intensity range at the high-frequency region. A superior current supply can be used to overcome the impedance and to maintain a high field intensity at the expense of high cost. Alternatively, since the increase of the impedance is mainly due to the inductance, the impedance can be reduced by

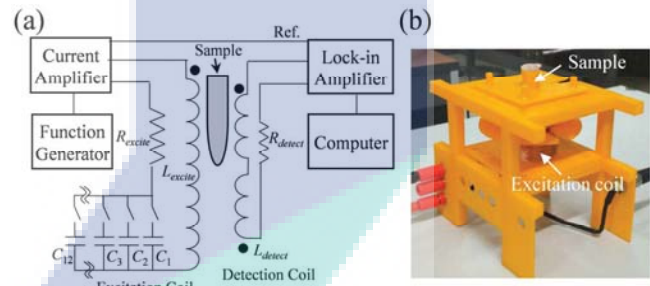


Fig. 1 (a). The schematic diagram of the AC magnetometer using a resonant excitation coil. (b) Picture of the excitation and detection unit setup.

miniaturization of the excitation coil [11]. However, this may reduce the homogeneity region of the excitation field. Moreover, the reactance due to the inductance can be cancelled out based on the electrical resonance of a series  $RCL$  circuit at a narrow bandwidth frequency. In the case of an induction coil is used to sense the magnetization of MNPs, the direct feedthrough can be reduced by using a gradiometer configuration and/or a filter [10], [11]. However, introduction of the filter may reduce the detection bandwidth and the response linearity, depending on the filter characteristics.

In this work, we report the development of a sensitive AC magnetometer using induction coils for MNPs characterization in the nonlinear magnetization region. To reduce the impedance of the excitation coil at the high-frequency region, we use a resonant capacitor network which is connected in series to an excitation coil fabricated from a Litz wire. The capacitor network is designed to achieve resonance at discrete frequencies on a logarithmic scale. A first-order axial differential coil is used as the detection sensor to realize



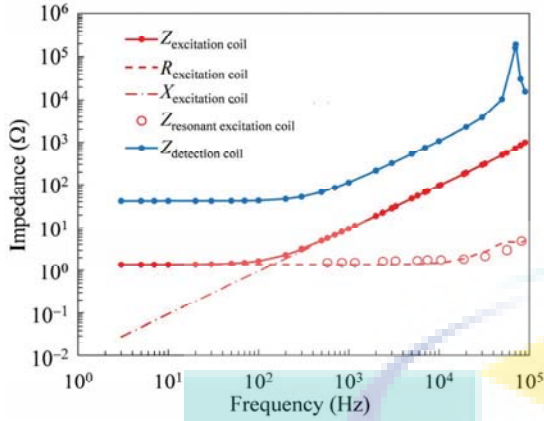


Fig. 2. Impedance  $Z = \sqrt{R^2 + X^2}$  of the excitation and detection coils with respect to frequency. Here  $R$  and  $X$  are the resistance and reactance of the coil, respectively.

attenuation of the direct feedthrough and high sensitivity. We demonstrate the sensitivity of the developed system by evaluating the harmonics of multi-core iron oxide nanoparticle solutions at different concentrations. We also show the capability of the developed system to assess the complex magnetization of the iron oxide nanoparticles in a wide frequency range.

## II. EXPERIMENTAL

### A. AC Magnetometer using Resonant Excitation Coil

Fig. 1 (a) shows the schematic diagram of the developed AC magnetometer which consists of two main parts: magnetic field excitation and magnetic response detection units. Using a cylindrical surface current model [12], an excitation coil was designed to produce a high homogeneity and strong excitation magnetic field for a 1-ml cylindrical sample. To prevent voltage breakdown and sparks between the winding layers, and mitigate the temperature rise during the excitation of a high magnitude and frequency of electric current, the excitation coil was separated into two identical coils by a 4-mm gap. Each identical coil had a 24-mm length ( $I_{\text{Excite}}$ ) and 30-mm inner diameter and was fabricated to be 150 turns using a Litz wire composed of 60 strands of 0.1-mm Cu wires. The excitation coil was connected to the capacitor network to form an  $RCL$  circuit, which was constructed from multiple values of polypropylene film capacitors. The resonant frequency was determined from the selected value of capacitance. The resonant frequency  $f_R$  of the  $RCL$  circuit is given by

$$f_R = \frac{1}{2\pi\sqrt{LC}}, \quad (1)$$

where  $L$  and  $C$  is the inductance of the excitation coil and capacitance of the capacitor network. The resistance and inductance of the excitation coil measured by an LCR meter (GW INSTEK LCR-816) were 1.352  $\Omega$  and 1.518 mH at 1 V and 1 kHz.

For the magnetic response detection unit, an induction detection coil was fabricated using a 0.25-mm Cu wire. The

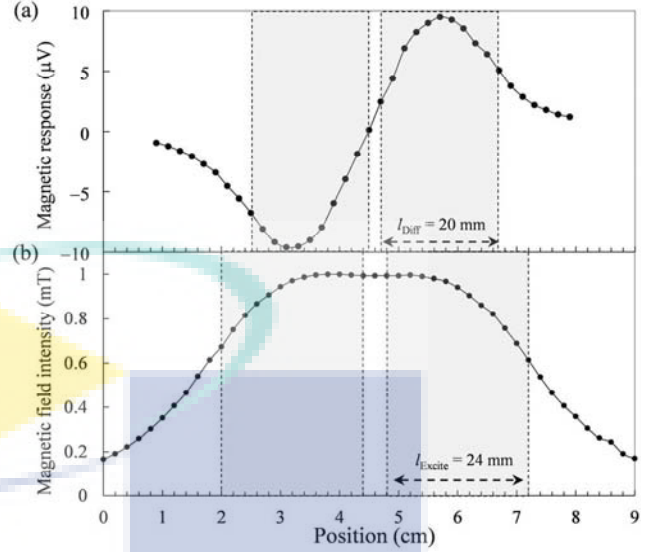


Fig. 3. (a) Gradient characteristic of the detection coil and (b) magnetic field distribution produced by the excitation coil with respect to position. Shaded areas show the regions covered by the lengths of the detection and excitation coils, respectively.

detection coil was configured to be a first-order axial differential coil, whose inner diameter was 15 mm and one coil had 1000 turns and length  $I_{\text{Diff}} = 20$  mm. A 3-mm gap separated the two identical coils which were connected in opposite-series configuration. The detection coil was placed inside the excitation coil, and the cancellation rate of the excitation magnetic field was improved by manually tuning the position of the detection coil at the axis of the excitation coil. The detection coil was connected to a lock-in amplifier (LI5640, NF Corporation) for a phase-sensitive detection. The picture of the excitation and detection unit setup is shown in Fig. 1 (b). The resistance and inductance of the detection coil measured by the LCR meter were 41.46  $\Omega$  and 16.76 mH at 1 V and 1 kHz.

### B. Multi-Core Iron Oxide Nanoparticle Solutions

The sensitivity of the developed system was demonstrated by measuring the harmonics of a commercial multi-core iron oxide nanoparticle, namely nanomag-D-spio D100 (Micromod Partikeltechnologie GmbH, Rostock-Warnemuende, Germany). The particles have the mean hydrodynamic and core sizes of 100 nm and 12 nm, respectively [3], [13]. Solutions of different iron concentrations were prepared from 0.24 mg/ml to 300 ng/ml by diluting the stock solution with purified water.

## III. RESULTS AND DISCUSSIONS

### A. Resonant Excitation Coil

Fig. 2 depicts the complex impedance of the excitation coil measured by the lock-in amplifier using a 4-point terminal measurement. The resistance  $R_{\text{excitation coil}}$  of the excitation coil showed a constant value of 1.3  $\Omega$  until 10 kHz and gradually increased in a higher frequency region. The measured reactance  $X_{\text{excitation coil}}$  of the excitation coil increased linearly

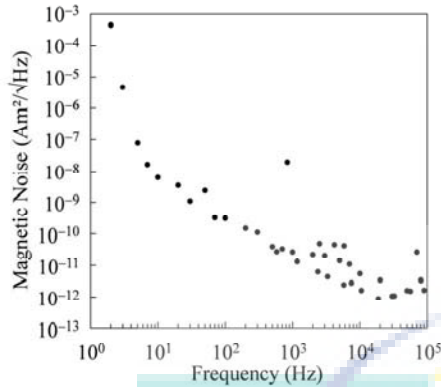


Fig. 4. Magnetic noise of the developed system during the excitation of 834-Hz and 15.6-mT<sub>pp</sub> magnetic field.

with respect to frequency, showing that, the inductance largely contributed the increase of the impedance at high frequency. The effectiveness of the resonant technique was evaluated by measuring the current and voltage of the *RCL* circuit when it was connected to a current supply, operated in a constant voltage mode. The open circles in Fig. 2 show the impedance of the *RCL* circuit derived from the resonant current and voltage. The impedance could be maintained at a low constant value up to 18 kHz. Compared to the case when the resonant technique was not applied (the closed red circles in Fig. 2), the impedance was effectively reduced and showed a close value to  $R_{\text{excitation coil}}$ . Fig.3 (b) depicts the magnetic field distribution of the excitation coil produced by a current amplitude of 0.2 A at 50 Hz along the axis of the excitation coil. The distribution was measured by a Teslometer. The homogeneity of the excitation field for a region from 30 to 42 mm was calculated to be 94%. A sample could be placed within this region to obtain a high uniformity of magnetization. The excitation coil showed a high efficiency of 5.2 mT/ampere at the high homogeneity region, enabling characterization of MNPs in the non-linear magnetization region [11].

### B. Detection Coil

The impedance of the detection coil is shown in Fig. 2. The impedance increased when the frequency was more significant than 1 kHz and a self-resonant characteristic was observed at 70 kHz. The self-resonant characteristic was due to the parasitic capacitance between the winding layers, which its value was calculated to be 300 pF. Using a small 30-turn coil, the gradient characteristic which is shown in Fig. 3 (a), and the sensitivity of the detection coil were measured. From the gradient characteristic, the detection sensitivity of a sample can be improved when the sample is placed at an optimized position relative to the detection coil. Furthermore, the peak of the gradient resided near the edge of the high-homogeneity region of the excitation field where a slight reduction in sensitivity can be expected when the sample is at the centre of the high-homogeneity region. Fig. 4 shows the magnetic noise of the developed system during the excitation of 834-Hz and 15.6-mT<sub>pp</sub> magnetic field. The harmonic spectrums were observed due to the direct feedthrough of the excitation field. The cancellation rate of the first-order differential coil was

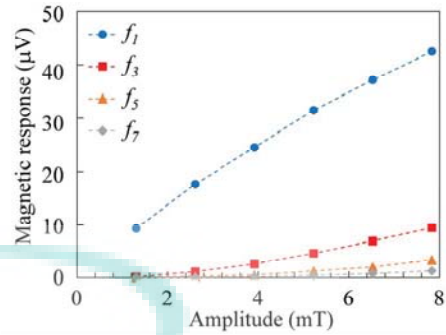


Fig. 5. The first  $f_1$ , third  $f_3$ , fifth  $f_5$  and seventh  $f_7$  harmonic components of the iron oxide nanoparticle solution during the excitation of 30-Hz magnetic field at different amplitudes.

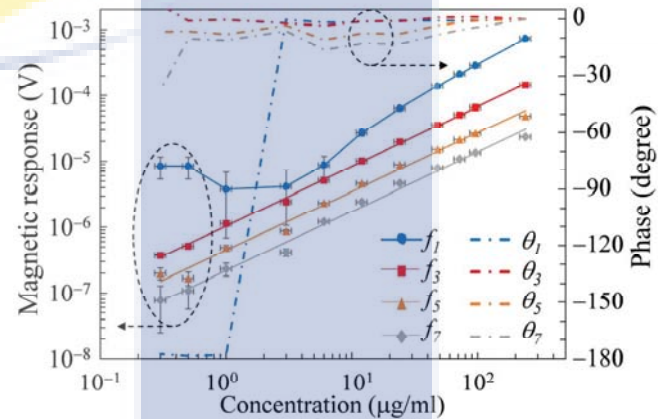


Fig. 6. Intensity (solid markers) and phase (dashed lines) of harmonics during the excitation of 834-Hz and 15.6-mT<sub>pp</sub> magnetic field with respect to iron concentration.

calculated to be  $B_{\text{detect}}/B_{\text{apply}} = 5 \times 10^{-3}$  and a sensitivity of  $5 \times 10^{-10}$  Am<sup>2</sup>/√Hz was shown at 100 Hz.

### C. Magnetic Response of Iron Oxide Nanoparticle Solution

Fig. 5 shows the odd harmonics of the 0.24-mg/ml iron oxide nanoparticle solution with respect to the amplitude of the 30-Hz excitation field. It is shown that the harmonic intensity increased with respect to the excitation amplitude, reflecting the non-linear magnetization of the iron oxide nanoparticles [13]. The non-linear magnetization characteristic of the iron oxide nanoparticles became more apparent when the excitation amplitude was greater than 2.6 mT.

Fig. 6 shows the intensity and phase of the harmonics with respect to different iron oxide concentrations during the excitation of 834-Hz and 15.6-mT<sub>pp</sub> magnetic field. The phases of the various concentration solutions were referenced to the phase of the 0.24-mg/ml solution. The first harmonic component  $f_1$  was observed to decrease rapidly when the iron concentration was reduced. The  $f_1$  gradually became constant in the concentration region that lower than 3 μg/ml with the phase shift of 180 degree due to the domination of the diamagnetic signal from the water [14]. The higher harmonics were observed to be linearly proportional to the iron concentration with a slight deviation in their phases due to noise. The harmonics and the phases outcomes were consistent to our previously reported result in ref. [13]. This

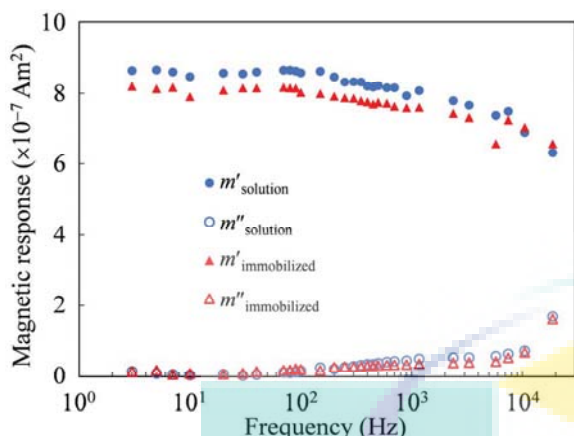


Fig. 7. Real (closed markers) and imaginary (open markers) components of magnetizations of the iron oxide nanoparticles in solution (blue markers) and immobilized (red markers) states during the excitation of 3.1-mT<sub>pp</sub> magnetic field.

experimentally proved that  $f_i$  could be affected by the diamagnetic background of the carrier liquid and the effect of the diamagnetic background to the observed  $f_i$  depended on the iron concentration. Corrections for the diamagnetic background resulted from the eddy currents' susceptibility of the solution must be introduced if the observed  $f_i$  is utilized to determine the iron concentration. Therefore, it could be concluded that  $f_i$  was not entirely 'transparent' to the diamagnetic background compared to other higher harmonics.

The complex magnetization of the iron oxide nanoparticles in solution and immobilized states measured with respect to frequency is shown in Fig. 7. The iron concentration for both states was 0.24 mg/ml. An agar gel was used to immobilize the iron oxide nanoparticles. Both the solution and immobilized states of the real component of magnetization  $m'$  exhibited a decay characteristic when frequency was larger than 100 Hz while the imaginary component  $m''$  increased with increasing frequency. The same qualitative characteristic of the solution and immobilized states reflected that the iron oxide nanoparticles were not highly affected by the Brownian relaxation, *i.e.*, the magnetic moments were not thermally blocked. Although the  $m''$  peak was not obviously observed in the frequency measurement range, it could be inferred that the Neel relaxation was dominant in the iron oxide nanoparticles. Measurement at frequency above 18 kHz could not be achieved since the direct feedthrough had saturated the input dynamic range of the lock-in amplifier.

#### IV. CONCLUSION

An AC magnetometer using the induction coils was developed for a sensitive magnetic characterization of MNPs. The resonant coil technique was implemented in the excitation unit to reduce its impedance at high frequency and an efficiency of 5.2 mT/A was obtained. The developed system successfully measured the harmonics distribution of the iron oxide nanoparticle solutions with the iron concentration down to 300 ng/ml. The results demonstrated the significant effect of diamagnetic carrier liquid to the observed harmonics. The complex magnetization of the iron oxide nanoparticles in the

solution and immobilized states showed that they were not mainly affected by the Brownian relaxation mechanism. Further improvement in the design of the detection unit could reduce the direct feedthrough and its parasitic capacitance. As a result, a sensitive characterization of magnetic fluid in a non-linear magnetization region can be achieved by using the developed system.

#### ACKNOWLEDGMENT

This work was supported by Ministry of Higher Education of Malaysia under grant number of RDU 160115 and Research Management Center of Universiti Malaysia Pahang under grant number of RDU 170377.

#### REFERENCES

- [1] J. Wells *et al.*, "Standardisation of magnetic nanoparticles in liquid suspension," *J. Phys. D: Appl. Phys.*, vol. 50, no. 38, p. 383003, Sep. 2017.
- [2] K. Enpuku, T. Sasayama, and T. Yoshida, "Estimation of magnetic moment and anisotropy energy of magnetic markers for biosensing application," *J. Appl. Phys.*, vol. 119, no. 18, p. 184902, 2016.
- [3] M. M. M. Saari, K. Sakai, T. Kiwa, T. Sasayama, T. Yoshida, and K. Tsukada, "Characterization of the magnetic moment distribution in low-concentration solutions of iron oxide nanoparticles by a high-Tc superconducting quantum interference device magnetometer," *J. Appl. Phys.*, vol. 117, no. 17, p. 17B321, May 2015.
- [4] F. Ahrentorp *et al.*, "Sensitive high frequency AC susceptometry in magnetic nanoparticle applications," *AIP Conf. Proc.*, vol. 1311, no. 2010, pp. 213–223, 2010.
- [5] V. Connord, B. Mehdaoui, R. P. Tan, J. Carrey, and M. Respaud, "An air-cooled Litz wire coil for measuring the high frequency hysteresis loops of magnetic samples - A useful setup for magnetic hyperthermia applications," *Rev. Sci. Instrum.*, vol. 85, no. 9, 2014.
- [6] D. Cabrera *et al.*, "Unraveling viscosity effects on the hysteresis losses of magnetic nanocubes," *Nanoscale*, 2017.
- [7] F. Ahrentorp *et al.*, "Sensitive magnetic biodetection using magnetic multi-core nanoparticles and RCA coils," *J. Magn. Magn. Mater.*, vol. 427, no. September 2016, pp. 14–18, 2017.
- [8] M. Ura, K. Noguchi, Y. Ueoka, and K. Nakamura, "Improved Liquid-Phase Detection of Biological Targets Based on Magnetic Markers and High-Critical-Temperature Superconducting Quantum Interference Device," vol. 1, no. 6, pp. 669–675, 2016.
- [9] V. L. Calero-DdelC, D. I. Santiago-Quiñonez, and C. Rinaldi, "Quantitative nanoscale viscosity measurements using magnetic nanoparticles and SQUID AC susceptibility measurements," *Soft Matter*, vol. 7, no. 9, p. 4497, 2011.
- [10] M. M. Saari *et al.*, "Optimization of an AC/DC High-Tc SQUID Magnetometer Detection Unit for Evaluation of Magnetic Nanoparticles in Solution," *IEEE Trans. Appl. Supercond.*, vol. 25, no. 3, pp. 1–4, Jun. 2015.
- [11] Z. W. Tay, P. W. Goodwill, D. W. Hensley, L. A. Taylor, B. Zheng, and S. M. Conolly, "A High-Throughput, Arbitrary-Waveform, MPI Spectrometer and Relaxometer for Comprehensive Magnetic Particle Optimization and Characterization," *Sci. Rep.*, vol. 6, no. March, p. 34180, 2016.
- [12] N. S. Suhaimi, M. M. Saari, A. I. Mohamed, N. A. C. Lah, and M. Samykan, "Development of a compact and sensitive AC magnetometer for evaluation of magnetic nanoparticles solution," in *2017 IEEE 8th Control and System Graduate Research Colloquium (ICSGRC)*, 2017, no. August, pp. 221–224.
- [13] M. M. Saari, N. A. Che Lah, K. Sakai, T. Kiwa, and K. Tsukada, "Harmonics distribution of iron oxide nanoparticles solutions under diamagnetic background," *J. Magn. Magn. Mater.*, vol. 452, pp. 145–152, Apr. 2018.
- [14] T. Mizoguchi *et al.*, "Highly Sensitive Third Harmonic Detection Method of Magnetic Nanoparticles using AC Susceptibility Measurement System for Liquid Phase Assay," *IEEE Trans. Appl. Supercond.*, vol. 8223, no. c, pp. 1–1, 2016.